Enschede, 14th February 2024

Towards Defect-Free Printing of High-Strength Aluminium Alloys

Master Thesis, Mechanical Engineering

T.L. van Rooijen

COMMITTEE
dr.ir. T.C. Bor
dr. M. Luckabauer
prof.dr.ir. M.B. de Rooij
S. Sayyad Rezaeinejad, MSc

UNIVERSITY OF TWENTE.
Faculty of Engineering Technology,
Chair of Production Technology

Acknowledgement

Dear reader,

Before you lies the work I performed to obtain the academic Master of Science degree in mechanical engineering. It is not only the result of my thesis period, but also the conclusion of my time as a student at the University of Twente since September 2018.

It takes a village to raise a child, and so it takes a university faculty to graduate a student. Therefore, I would like to use this opportunity to thank the people that made this thesis work possible:

First of all, I would like to give a very big 'thank you!' to my daily supervisor Ton Bor. I enjoyed our conversations and I highly appreciate your never-ending willingness to provide new ideas and insights and to help me out where it was needed, even when your health was providing challenges.

Furthermore, I would like thank Saed Sayyad Rezaeinejad for helping with performing the large amount of experiments and for our interesting conversations about Iranian and Dutch culture. Many thanks to Bert Vos, providing technical support as well to the Horst workshop men, especially to Kai Wissink of Geerdink for often repairing broken components of the setup.

Thanks to Bart, Henryk, Feije and Yde for working along side me in the Horst basement, which became at times my second home. Thanks for being around at the moments we enjoyed life together and also at the moments I needed a coffee break. Thanks to my colleagues from the Royal Netherlands Army Reserves for being my second family throughout my student time and supporting me as brothers.

I would like to thank my parents for supporting me wherever possible and Jaime for being around since we were 8 years old.

Lastly, I would like to give my special thanks to Talitha, my fiancée. Thank you for your endless love and support and for giving colour to my life.

I hope you enjoy reading.

Kind regards,
Tom van Rooijen
Enschede, February 2024

Summary

Additive Manufacturing (AM) has emerged as a novel promising manufacturing technique and is considered the backbone of the fourth industrial revolution. AM is praised for advantages on material waste, low demand on post-processing, ecofriendliness and the lack of human interference needed compared to traditional production methods. Aluminium-magnesium (Al-Mg) alloys are a very popular metal alloy group used mainly for applications that demand a high strength-to-weight ratio, excellent corrosion resistance, high thermal and electrical conductivity and good processibility. However, Al-Mg alloys are prone to solidification defects, making most popular fusion-based AM techniques less suitable for these alloys.

At the University of Twente, the Friction Screw Extrusion Additive Manufacturing (FSEAM) method is developed as a Solid State Additive Manufacturing technique to overcome the solidification problems. Recent research has successfully produced wall-like structures, but the system is prone to unsteady varying material outflow speed affecting the product's geometrical stability. Furthermore, a research gap lies in the knowledge of the influence of the tool gap parameter and tool rotation rate on the system's temperatures, tool torque, feed force and normal force applied on the substrate by outflowing material. This knowledge is crucial for further optimisation of FSEAM to a full-grown production technique that is promising to be applied in aerospace products and beyond.

In this master thesis, an extensive systematic experimental study is performed with a modified Friction Screw Extrusion (FSE) setup to map the influence of the tool gap parameter and tool rotation rate to the mentioned system parameters and to measure and be able to predict the varying material outflow speed from system data.

The analysis of the parameter results give clear insight into parameter behaviour and reveals a clear set of system parameters to omit for avoiding varying material outflow speed in the current FSE(AM) setup. Furthermore, calculations lead to the proposal of an alternative mass balance for flow analysis. Also, ideas and suggestions are proposed to improve an existing FSE material flow analysis model.

During the FSE experiments, outflowing extrusion material is video recorded. An advanced video processing method based on the Farneback method is developed that successfully retrieves material outflow speed data. Correlation analysis based on the Pearson correlation coefficient reveals clear linear correlation between the outflow speed data and normal force data on micro-variation level in the case of significant material outflow speed variation. The developed correlation method is found to be a clear indicator in predicting the occurrence of material outflow speed variation. Severity coefficients are proposed as a first step to indicate the severeness of this variation, although improvements in the experimental setup must be made first to let them be fully applicable. A cleaner data retrieving method for the torque data would most likely let the torque data correlate to the normal force and material outflow speed data as well. This improvement makes the developed correlation method suitable to be applied in FSEAM experiments in which video recording of outflow material speed is not possible. This would enable the prediction of unwanted material outflow variation during FSEAM and indication of its severity.

Contents

1 Introduction

This first chapter is used to explain the research motivation of this master thesis and to explain and place the Friction Screw Extrusion Additive Manufacturing (FSEAM) technology at the University of Twente (UTwente) in context. Furthermore, current FSEAM research hurdles are mentioned. The chapter is closed off with the research questions that form the basis for this thesis' research and the thesis' outline.

1.1 Research Motivation

Aluminium-magnesium (Al-Mg) alloys are a very popular group of metal alloys used mainly for applications that demand a high strength-to-weight ratio, excellent corrosion resistance, high thermal and electrical conductivity and good processibility [1–3]. This makes aluminium the second most important metal in the world economy [1]. Typical applications can be found in domestic products, automotive industry, marine industry, electrical products and predominantly in the aerospace industry as the most important metal [1].

Besides, Additive Manufacturing (AM) has emerged as a novel and very promising manufacturing technique (mostly) based on layer by layer joining as the backbone of the fourth industrial revolution, also called Industry 4.0 [4]. AM for plastics is currently used in mainstream industry as an alternative for conventional methods for its advantages on material waste, low demand on post-processing, ecofriendliness and the lack of human interference needed [4]. However, metal-based AM for aluminium-magnesium alloys remains less successful due to challenges in processing metals to high quality products with techniques suitable for plastic processing [4].

For metals in general and for aluminium specifically, defects related to solidification such as voids, cavities, corrosion, shrinkage upon cooling, inclusion of contaminations and high residual stresses are known problems that often prevent metal printing in mainstream melting-based production lines [2,4]. Besides, the resulting cast microstructure (when cooling rates are not sufficient) in melting based AM, which is less strength efficient than a wrought microstructure due to its larger grain size, makes such a process less attractive.
These melting based defects in combination with the automotive and aerospace industry seeking for strength, structural and environmental efficiency as provided in the AM technique for plastic products makes the wish for a successful solid-state additive manufacturing (SSAM) method for metals an interesting improvement over melting based AM.

Friction Stir Additive Manufacturing (FSAM)

As a first solution, White patented a Friction Stir Welding (FSW) technique in 2002 in which layers of sheet metal can be joined together by a rotating pin moving through the interface of two sheet metal layers and joining these together by the induced friction [4]. The resulting product is characterised by a fine equiaxed grain structure with properties typically observed with wrought microstructures [5].

In the search for more economic material usage and more freedom in product design for aluminium, Airbus and Boeing adapted this AM-FSW technique in order to produce aluminium wing ribs in 2006 and 2012 respectively. The advantage of this implementation included higher production speeds, less material waste and overall less environmental impact [4, 6]. The method has been implemented in their production facilities in addition to conventional methods, but still faces challenges for extreme demanding applications such as launching platforms [7].

Within the large development of different (SS)AM techniques, the ASTM F2792 gives a clear overview with classification based on material usage, heat source and material phase. This overview is presented in Figure 1. It can be seen that the FSAM technique (of which AM-FSW is a subtechnique) can be found under the metal based solid-state / non-beam sheet lamination AM techniques with friction as

heating source [4].

The extensive review paper of Kumar Srivastava et al (2021) [8] estimates that in 2020 28% of engineering products would have been applicable for production by FSAM. Their exponential estimation for the year 2030 states that 50% of engineering products could be (re)designed towards production with further developed FSAM variants by then.

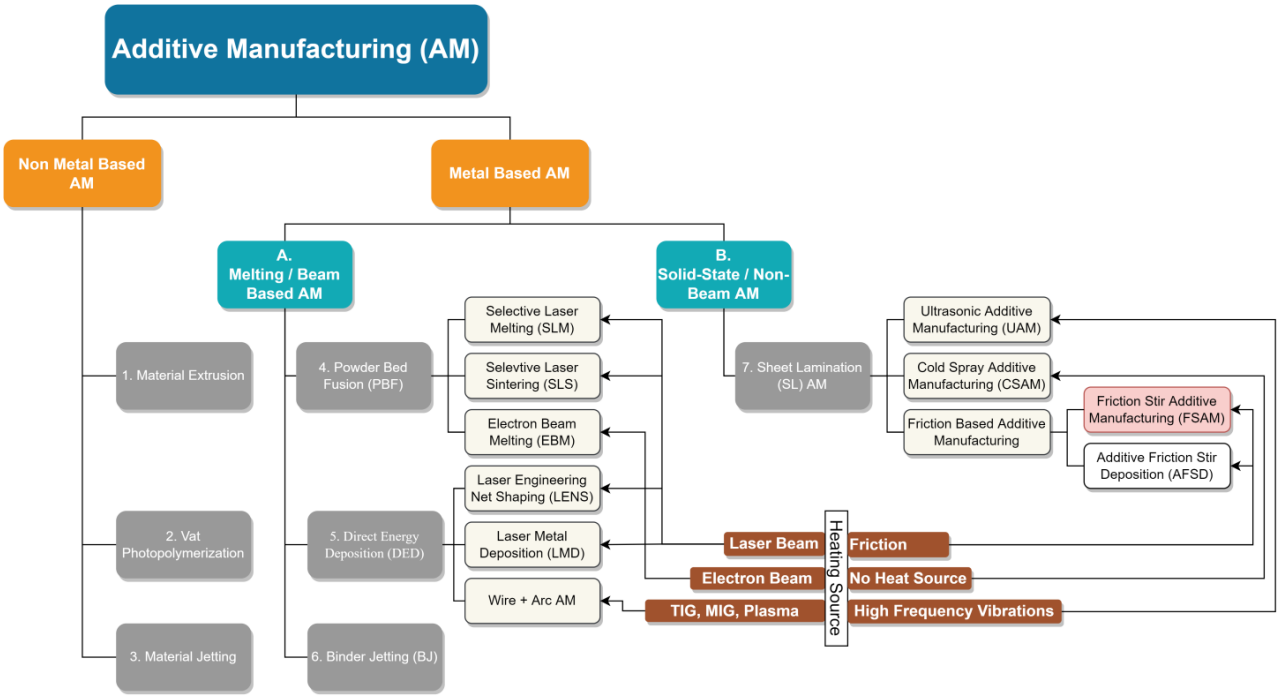

Figure 1: Additive Manufacturing process tree according to ASTM F2792 [4]

Additive Friction Stir Deposition (AFSD)

Based on the principles of FSAM, Additive Friction Stir Deposition has gained increasing interest in the last few years as a novel AM method [5]. However, still in an early stage of development and lacking geometrical accuracy and flexibility in freedom of design [5].
The method is a truly AM method in the sense that feed material is added onto a substrate instead of joining existing material pieces together as in FSW / FSAM. This promises increased freedom of geometry, feed material choice, processing speeds and product size (for producing large parts), applying coatings and making local repairs [5].

Examples of different process variants of AFSD are presented in Figure 2. It can be seen in the figure that AFSD is based on the addition of feed material either in powder form or as a rod onto a substrate by adding friction (and thus heat) and pressure by rotation of a hollow tool, the feed material itself or in some cases by an extrusion-like screw inside a hollow tool [2,5]. This combination of pressure, heat and the large plastic deformation of the feed material provide the circumstances for a bond between the feed material and the substrate.

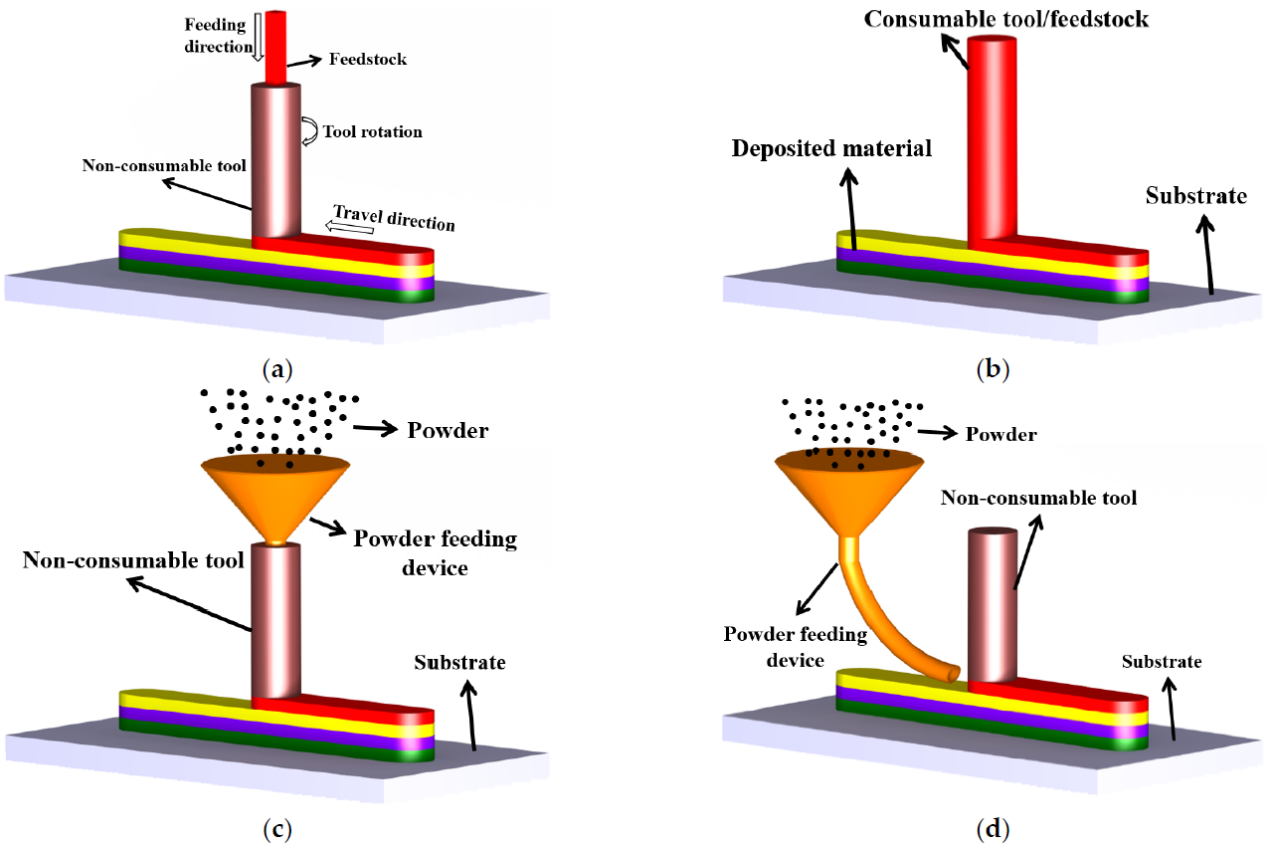

Figure 2: Different AFSD process concepts [5]

Researchers in AFSD have successfully processed alloys of aluminium, titanium, magnesium and also steels [5], providing thus a promising range of material applications. However, microstructural challenges are found in kissing-bonds, cavities and hook defects, which need more understanding of tooling and process parameters to solve and to make AFSD feasible for mainstream manufacturing [5].

Furthermore, the microstructural development characterised by the combinations of grain growth due to elevated temperatures, phase transformations, precipitate development, high plastic deformation rates and dynamic recrystallization is not yet fully understood [5]. This needs further research to provide full control of microstructural and thus mechanical properties of the printed product. In order to still obtain the desired mechanical properties, post-processing heat treatments are attempted in research but also need further research for full understanding of the microstructural effects [5].

From AFSD to FSEAM at the University of Twente

First research on AFSD at the University of Twente started with Friction Surface Cladding (FSC) in 2013 in order to gain in-house process understanding with experiments by Van der Stelt et al [9]. FSC at that time was a technique generally used for coating FSW welded aluminium alloys in the AA2xxx and AA7xxx series with pure aluminium for corrosion resistance enhancement [9]. These experiments consisted of cladding a AA1050 layer onto an AA2024-T351 substrate with different process parameters and subsequent investigation of microstructure and hardness change. A sketch of the FSC setup is presented in Figure 3.b.

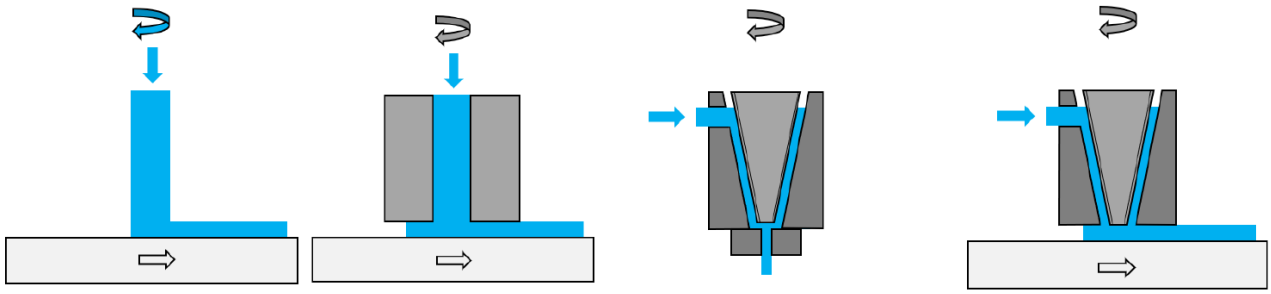

(a) FS (b) FSC (c) FSE (d) FSEAM

Figure 3: Research history at the UTwente towards FSEAM [10]

Further experiments on gaining insight in process parameters and microstructural results on FSC were conducted with the help of Phd student Liu and published in 2015 [11]. More attention was paid to the influence of tool rotation rate, table moving speed and process temperatures on hardness, microstructure and bonding quality. Materials used were the same as mentioned above. The experiments have resulted in defect free clad layers with smooth surface finish that have bonded well with the substrate. Besides, the built in-house setup was proven to be a successfully functioning cladding machine [11].

Research moved on with several master students via a bonding study to Friction Surfacing (FS) (Figure 3.a) of AA2024 onto AA2024 aluminium [12] to re-building the FSC setup towards a Friction Screw Extrusion (FSE) setup in the search for a more continuous material feeding system. Eventually, Lind managed to produce the first extruded rods of AA6060 in 2018 [13] with a semi-continuous material feed system. In this process, material is fed via a hydraulic piston into a housing with a rotating threaded tool, introducing plastic deformation, friction and thus heat. A sketch of this concept is presented in Figure 3.c.

The FSE setup was modified to prepare it for Friction Screw Extrusion Additive Manufacturing (FSEAM) by Smit [10] in 2020, in which the extruded rod is used to clad multiple layers on top of each other. First prints were successfully made by Ariës [14] in 2021.

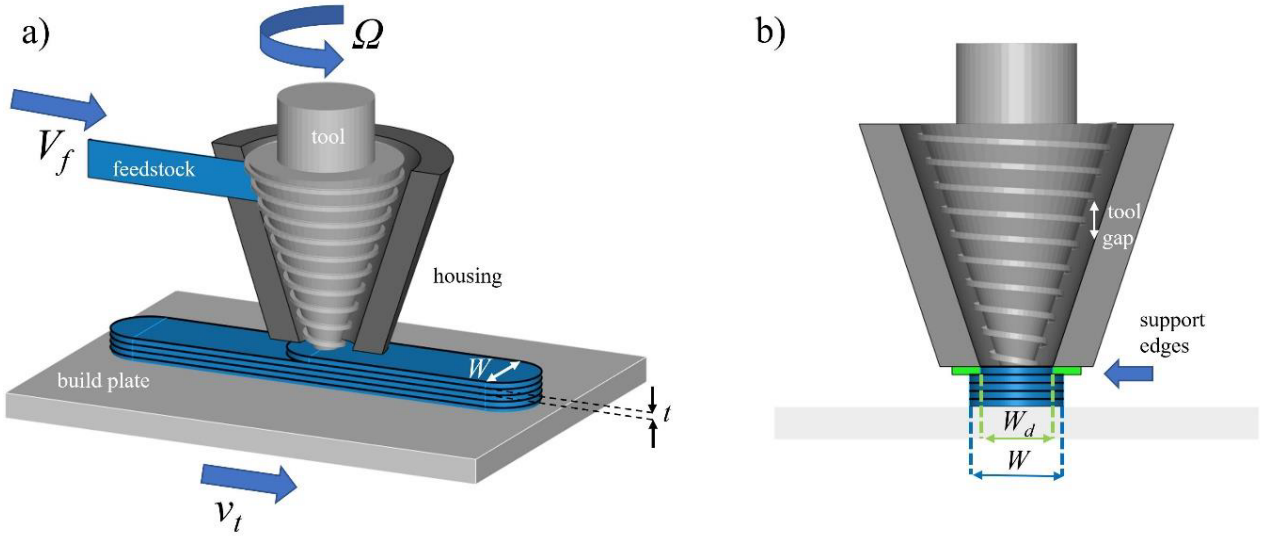

Figure 4: Simplified schematic of the current FSEAM process at UTwente, including important system parameters [15]

The concept sketch of FSEAM is shown in Figure 3.d and in more detail in its current form in Figure 4. It can be seen that (similar to FSE) the feed material is pressed against a tapered threaded screw,

which produces the heat, pressure and plastic deformation needed to process the material and secure proper bonding with the substrate. It can be seen in Figure 4.b that support edges are applied to fix the width W_d of a printed layer for better geometrical stability.

Since then several master students spent their thesis on further exploring the influence of process parameters and post heat treatments on microstructural effects, hardness and layer bonding quality [16,17]. Furthermore, it was tried to lower forces needed to process material by altering the tool design by adding a cylindrical part with milling features above the conical tool part to develop towards a small-scale FSEAM setup for higher resolution products [18].

Recent research consists of a master thesis performed by Strik [17] and on-going PhD research performed by Sayyad Rezaeinejad [15] on gaining insight on the effects of FSEAM input parameters on microstructural and mechanical properties of prints made from AA6060-T6 feed material on a AA2024-T351 substrate. In addition, an extensive paper with FSEAM progress at the UTwente so far is very recently published in May 2023 by Bor et al [19].

Future promises of FSEAM contain improvements in material processing volumes and speeds, active cooling control in the substrate surface, a continuous material feed supply possibly in other forms than rods or processing of other materials that show problems in fusion based processes [19]. Furthermore, FSEAM is promising for scaling to enable printing large or small light-weight products with complex 3D geometry [18]. Also, FSEAM could be used for local repairs of products instead of solely producing new parts [5].

1.2 Comparable Research to FSEAM

To give an overview of the position of FSEAM at the UTwente in global research, a brief introduction is given to recent comparable research in the aluminium AFSD research field.

W-FSAM

The Chinese research group of Chen developed an AM method called Wire-based Friction Stir Additive Manufacturing (2023) [2]. A schematic presentation of their setup is given in Figure 5.
A continuous wire feeding system using AA4045 is used (comparable to what is often used in polymer AM) in which the rotating conical threaded screw pulls the material based on demand. The tool nozzle contains three 2 $[mm]$ long conical pins stirring the current and previous material layer to enhance dynamic fluidity (shear thinning), which eventually prevents kissing bonds. A typical rotational speed of 2000 $[rpm]$ is used, with a traverse velocity of 1000 $[mm/min]$ and wire feeds up to 6000 $[mm/min]$ can be realised. The research group succeeded in printing a dome, without applying supports. Mechanical destructive testing revealed increased strength (UTS 111% at 177% elongation) with respect to the base material in trade of a hardness decrease (86%). Microstructure is comparable to FSEAM (3.5 $[\mu m]$ grains) with excellent material properties of printed products.

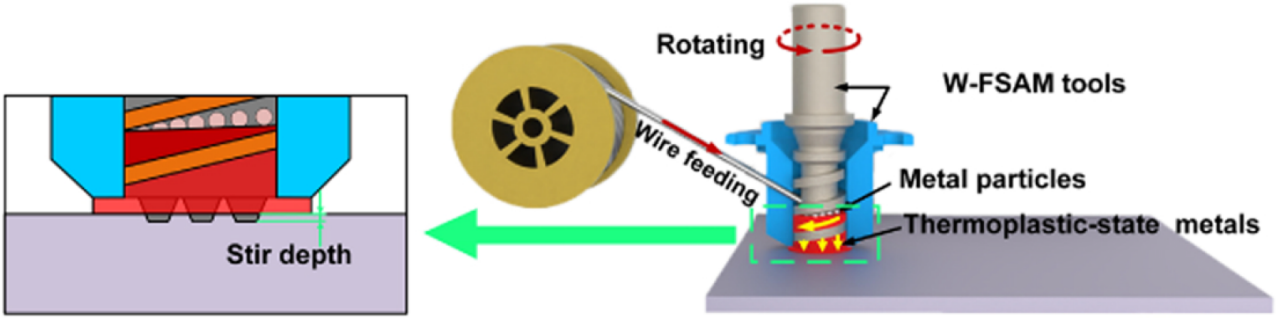

Figure 5: W-FSAM setup overview, taken from [2]

SolidStir Additive Manufacutring: SSAM

The research group of Haridas in Texas, USA, developed the SSAM technique published in 2023 [20]. The process is almost identical to FSEAM at the UTwente. A schematic representation of the SSAM setup is shown in Figure 6. The method uses a threaded tapered tool to process AA6061-T6 and results in very comparable microstructural benefits with fine equiaxed grains in a wrought-like microstructure. Increase in corrosion resistance was found as well.
The only differences with FSEAM are that SSAM uses two semi-continuous feed channels operated in turn to guarantee a 'continuous' feed material flow. Also, the tool tip consists of pins stirring the currently and previously printed layer to break up oxide layers, working similar as in W-FSAM. As a result, no layer bonding defects were reported. Lower strength properties than the feed material were reported, in combination with an increase of ductility. Walls were successfully printed, however a lack of geometrical guiders in the tool nozzle as used in FSEAM (see Figure 4) results in very inconsistent printing geometry.

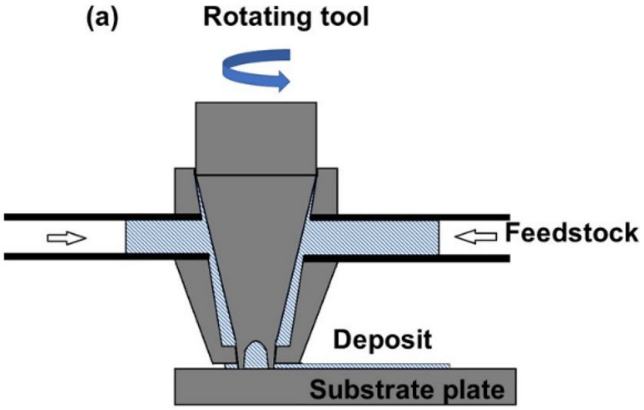

Figure 6: SSAM setup overview, taken from [20]

Tooling in Friction Stir Additive Manufacturing (FSAM)

With FSAM, layers of metal are one by one welded together with a rotating tool using the principle of Friction Surface Welding (FSW). A rotating pin-shaped tool is inserted in the layer interface that generates enough frictional heat to weld the layers together. If layers are stacked, one can make printed products. A schematic of the process is presented in Figure 7.

As the material flow processes in this AM-method are comparable with FSEAM, a brief literature study is performed to learn from advice stated in that research field. Focus is laid on the used tooling with layer bonding difficulties in FSEAM in mind.

Generally, a conical threaded pin is used for producing aluminium in FSAM, comparable to tooling in FSE. Non-weldable variants of AA2xxx and AA7xxx series are successfully processed for aerospace applications [7]. Also, the FSAM prove of concept holds for the AA5xxx series and magnesium alloys [21]. The same principle of a threaded FSAM pin is used to process AA5xxx and AA7xxx in microstructural and mechanical research by Jha et al (2023) [22] and for research to produce magnesium alloys [6]. Conical threaded pins are found to successfully weld two plates of AA5083 and AA6061 together without bonding defects [23]

An extensive review paper of Hassan et al (2023) [4] compares the state-of-the-art FSAM research and a.o. compares different tool designs for Friction Stir Lap Welding (FSLW), which is FSW performed from two layers of material placed overlapping eachother. Tool pins are often cylindrical of shape with convex features, flatted edged, (concaved) arced grooves or simply cylindrical.
Threaded pins are often recommended for their ability to drive vertical material flow whilst mixing material of two material layers. In this

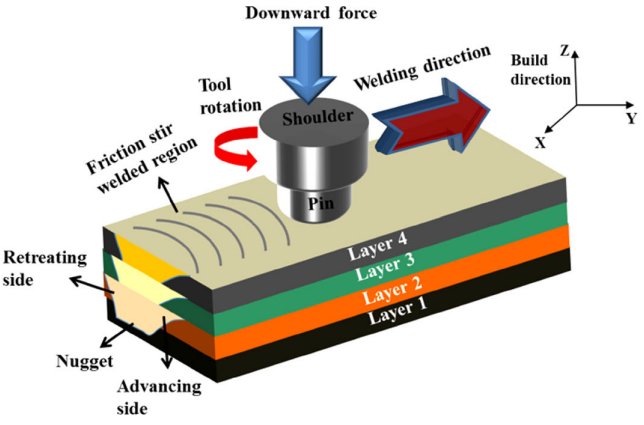

Figure 7: FSAM process overview, taken from [21]

way, a defect-free bond is well-possible [24]. The same conclusion is drawn after analysing different tool options in butt-joined FSW [25].

1.3 Research Problem

Below, the research questions of this master thesis are formulated after introduction of recent challenges encountered during FSEAM research.

Research Challenges

The recent master thesis performed by Strik [17, 26] and parallel research by Sayyad Rezaeinejad [15] combined in a paper by Bor et al (2023) [26] show successful results of FSEAM with AA6060-T6 as feed material on a AA2024-T351 substrate. Experiments were performed by building rectangular walls of multiple layers of 1 $[mm]$ thick and 15 $[mm]$ wide with varying table speed of 100 to 250 $[mm/min]$ with a corresponding feed ratio (i.e. feed volume rate with respect to volumetric demand) of 1.3 and a tool rotation speed of 400 $[rpm]$. Promising mechanical properties (yield and tensile strengths) and fine microstructure (grain size $< 10\mu m$) were found.

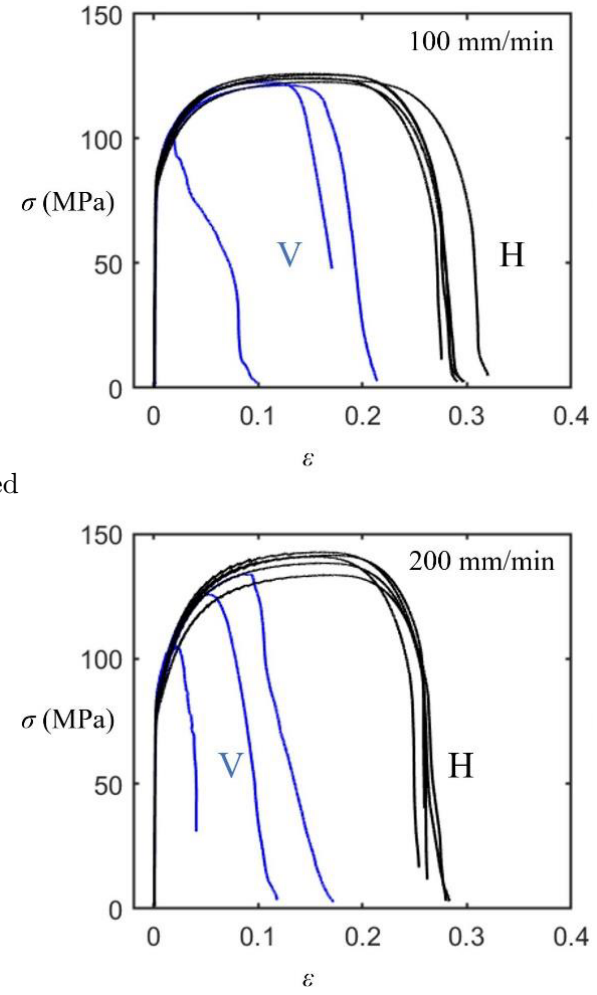

Figure 8: Stress/strain curve of successful (in black) and failed (in blue) FSEAM tensile tests [15]

However, the following challenges have been encountered in recent research:

- Poor bonding has been found at lower table speeds in the form of strings of small cracks in the microstructure of layer interfaces, resulting in premature cracking during tensile tests. Especially in specimens made out of the vertical direction of a print i.e. the direction through the printing layers. Stress/strain curves showing this premature cracking are presented in Figure 8 in the blue lines indicated with 'V' compared to specimens made along the printing direction ('H') in black.

- Wave-like patterns on printed walls made with a low printing speed of 100 $[mm/min]$ are shown in Figure 9. These occurred due to irregular material outflow speed as also observed during FSE experiments [18]. It is found that this behaviour tends to decrease with higher table speeds [15]. However, no explanation or method to quantify this effect is found yet. Solving this issue is important for acceptable product quality and to enable printing of higher resolution products with narrower layers. Additionally, it is important for enabling printing of stronger materials where excessive normal forces have to be avoided for controllability of the system.

- A research gap can be identified in the knowledge of the effects of the tool gap parameter on the system, which is defined as the vertical distance between the threaded tool and its tool housing as shown in Figure 4.b. This parameter is never systematically researched, but is suspected to significantly influence the normal force on the substrate induced by material outflow and the problematic varying material outflow speed as an altered tool gap directly alters the material flow geometry in the tool housing [19].

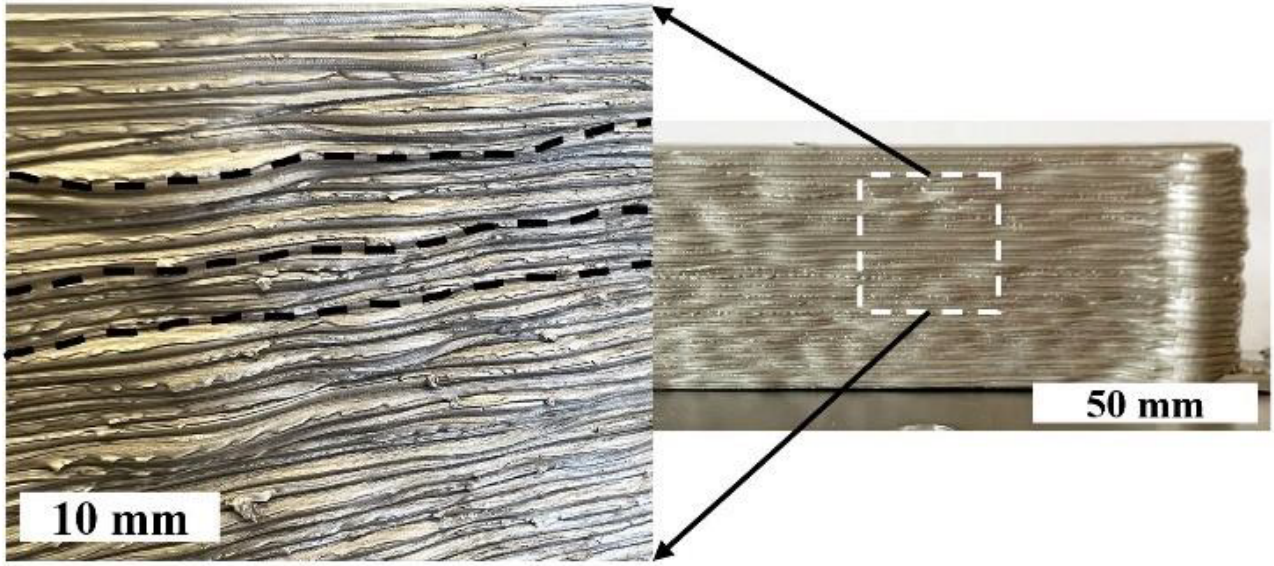

Figure 9: An FSEAM print made with table speed of 100 $[mm/min]$ showing inconsistent wave-shaped geometry [15]

Research Questions

The following two research questions for this master thesis are formulated from the research challenges:

1. How do changes in tool gap and tool rotation rate influence the measurable FSE(AM) system parameters (normal force, feed force, tool torque and temperatures) in the FSE(AM) setup?
2. Can the observed material outflow speed variation in FSE(AM) be measured and predicted from system data and how do tool rotation rate and tool gap influence this varying speed?

1.4 Thesis Outline

To answer these research questions, literature study is performed in combination with extensive systematical FSE experiments (2 experiment series) and data analysis. The organisation of the performed work is as follows:

Chapter 1 of this thesis consists of an **introduction**, outlining the context of this research. A **literature study** is presented in Chapter 2, giving more in-depth background to the subjects mentioned in the introduction. Furthermore, information from other studies is presented that help answer the research questions. The **setup** used for the FSE experiments is outlined in Chapter 3. There, an overview is given about modifications made with respect to preceding FSE research. The **results and discussion** are separated for both research questions. Chapter 4 presents them for the system parameter research and Chapter 5 for the material outflow speed variation. The last part of this thesis consists of the **conclusions** to the research questions in Chapter 6 and the **recommendations** for further research in Chapter 7.

Besides the FSE experiments, a series of new FSEAM tool designs is developed to alter material flow in the nozzle region to help improve layer bonding quality and reduce normal forces in FSEAM. The design process of these alternative tools is presented in the Appendices C.1, C.2 and C.3 as these are not further used in the experimental work due to time limitations of this thesis.

2 Literature

In this chapter, relevant literature is mentioned to provide context and to help understand the research process and the results of this thesis. Literature on the used material is presented, on varying extrusion flow, on earlier research to the UTwente FSEAM setup and on research of other groups comparable to the UTwente FSEAM.

2.1 Material

In order to understand material behaviour in the FSE and FSEAM experiments of this thesis, an introduction to the material used, its properties and known phenomena are presented below.

Material Properties

The material dominantly used in FSE and FSEAM experiments at the UTwente is AA6060-T6. A widely used and well-available aluminium-magnesium-silicium alloy in peak hardened state with circa 0.3-0.6 Si% and circa 0.35-0.6 Mg%. The material is widely used in applications requiring good machinability, weldability, heat conduction, ductility and corrosion resistance and found its way in the automotive, machinery and electronics/robotics industry [1].

The popularity of this kind of aluminium alloys is largely due to their high strength to weight ratio, costs and availability. A typical density of 2700 $[kg/m^3]$ (about a third of regular steel [1]) and yield and tensile strength of respectively 150 and 190 $[MPa]$ [27] (roughly half of low carbon steels [1]) with elongation at break of 8% [1,27], makes this kind of aluminium alloys a fair competitor in light-weight designs requiring medium strength. Furthermore, this alloy has typically a Young's modulus of 69.5 $[GPa]$ and a melting point between 610 to 655 $[°C]$ [1].

AA6060 obtains most of its strength from precipitation hardening [28]. These precipitates are small magnesium-silicon particles in out-of-equilibrium state that hinder the movement of dislocations in the aluminium lattice, thus increasing the material's strength properties [28]. The procedure of precipitation hardening is explained below.

Specific numeric and more in-depth material composition data of this specific aluminium alloy can be found in the material data sheet [27] in Appendix A.

Precipitation Hardening

To understand the thermal material behaviour of the AA6060 alloy during FSE(AM) experiments and resulting material properties and microstructure, the phase diagram and T6 heat treatment is elaborated on. A sketch of both are combined in Figure 10, which displays the thermal path in the current FSEAM setup at the University of Twente connected to the pseudo-binary $Al - Mg_2Si$-phase diagram.

It can be seen on the left in Figure 10 that the $Al - Mg_2Si$-phase diagram consists of a fairly simple pseudo-binary phase diagram [3, 29–32] of which the AA6060 chemical composition used in FSEAM research [15] is indicated with the vertical line in the phase diagram on the left in Figure 10. It can be seen that the alloy can exist in a solid $\alpha + \beta$ state, which are in the case of the $Al - Mg_2Si$-system Al and Mg_2Si, respectively.

Due to the AA6060 composition, the alloy can be (in equilibrium conditions) in solid state in a saturated α state (saturated Al) at elevated temperatures and an $\alpha + \beta$ state ($Al + Mg_2Si$ precipitates) at all lower temperatures. This creates the ability to influence the material structure by cooling the material from elevated temperatures in the α region in a non-equilibrium state, creating non-equilibrium precipitates in the α-matrix dependent on the cooling rate. The type of precipitates (shape, size and Al/Mg-composition [33]) influences the increase of strength properties

and is dependent on cooling speed and subsequent ageing treatments [3, 34].

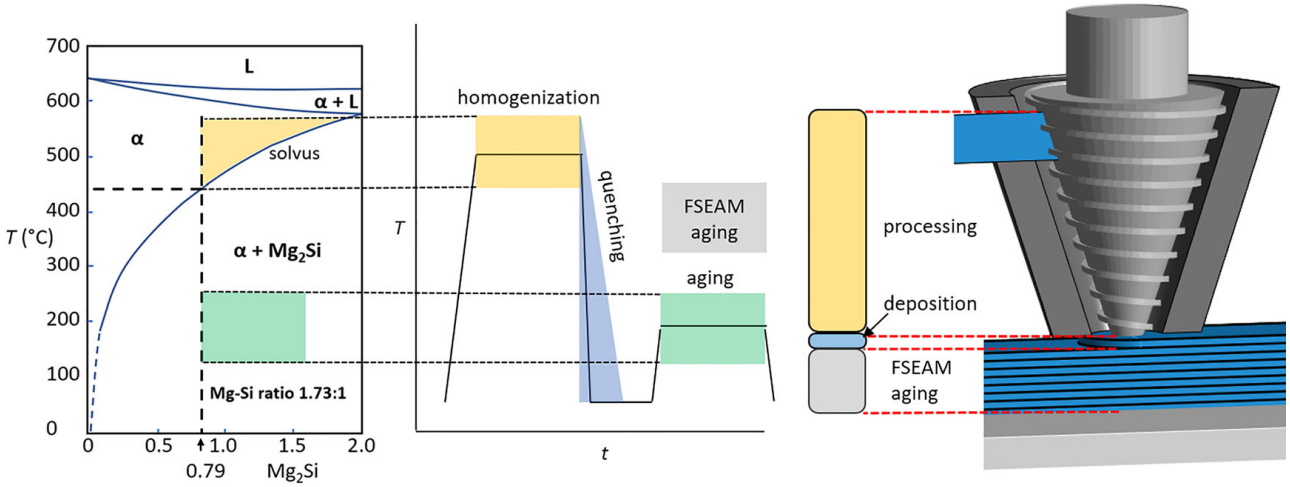

Figure 10: AA6060 phase diagram linked to the thermal path of FSEAM [15]

This effect is applied in the T6 heat treatment [3], which has the same thermal path shape as shown in the middle graph in Figure 10. In this heat treatment, the material is heated into the α-phase to circa 520-550 [$^{\circ}C$] [35] until all Mg_2Si is dissolved in the aluminium. Next, the material is quenched to room temperature into a super saturated solid solution (SSSS) and subsequently artificially aged with the help of an elevated temperature of circa 160-180 [$^{\circ}C$] [35] within the $\alpha + \beta$ region of the phase diagram. This results in Mg and Si clustering together in different compositions depending on the ageing conditions [33].
In can be seen in Figure 10 that currently the temperatures experienced by previously printed layers due to a newly printed layer are above the typical T6 ageing temperatures, causing overageing in the prints with subsequent strength loss.

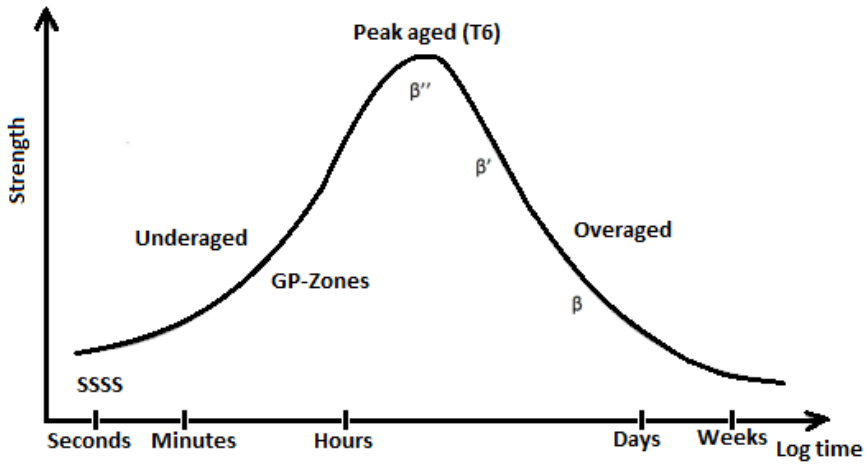

Figure 11: Sketch presenting effect of precipitation development with respect to material strength [28], in correspondence with [3, 34]

The development of precipitate types compared to material strength is presented in Figure 11. The goal of the T6 heat treatment is to optimise the precipitation type with respect to strength, thus resulting in the β"-shape [28, 33]. The β"-shape precipitates have a fine needle-shape structure and have a composition of Mg_5Si_6 [28, 33, 36].

The precipitates occurring before and after the peak aged state have more rounded shapes than the β" precipitates [28] and are therefore less efficient in matrix slip resistance as can be concluded from Figure 11.

Considering the hardness gain with respect to natural ageing time was found to be asymptotic in comparable alloys AA6005 and AA6082; i.e. the hardness increases in a more or less linear way and reaches a plateau [37] as can be seen in Figure 12. This is an important detail for performing mechanical analyses on FSEAM prints as natural ageing effects on the comparable AA6060 alloy can influence the results in a significant amount of time after printing.

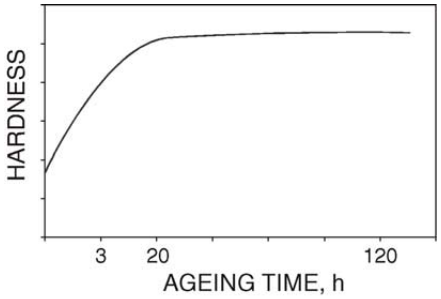

Figure 12: Hardness development to natural ageing time of AA6008 and AA6082 [37]

Fracture Behaviour

Researched fracture behaviour on the very comparable alloy AA6061-T6 [1, 35] at different strain rates from 10^{-4} to 10^{-1} $[s^{-1}]$ and different temperatures from 25 to 300 $[°C]$ show that full ductile fracture behaviour can be clearly identified by microscopic dimples in microstructural analysis [38]. Even more useful is that the depth of these dimples should give an indication of the grade of ductility of the material [38]. An example of such a surface is presented in Figure 13.

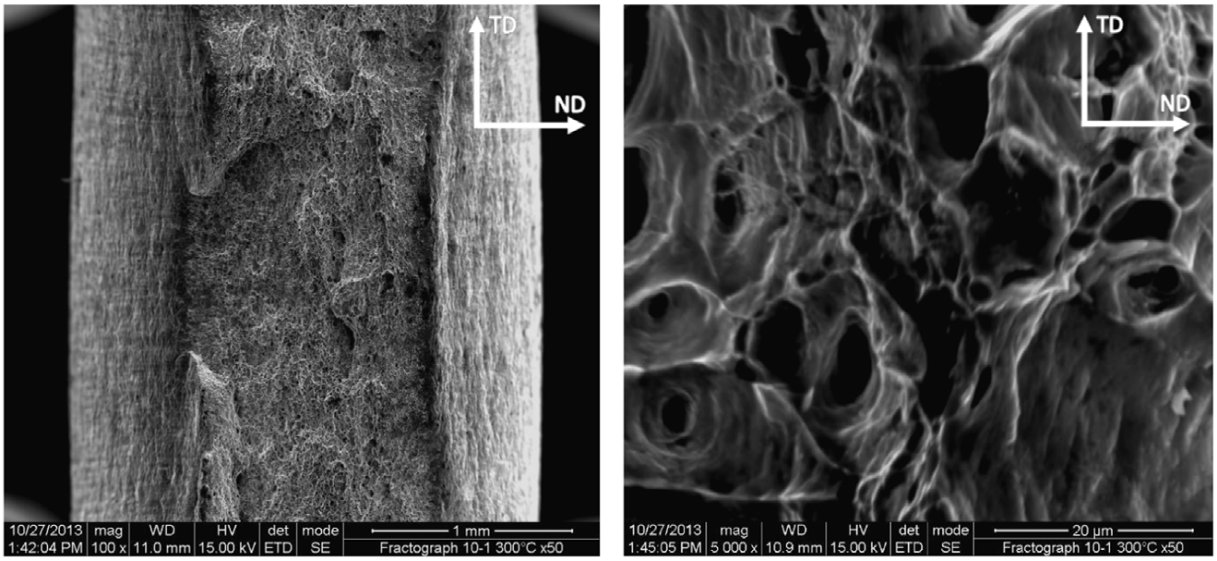

Figure 13: SEM image of dimpled cracked surface in AA6061 [38]

These dimples occur due to nucleation and coalescence of micro-voids around particles in the aluminium matrix, eventually leading to a micro-crater-like surface. These are in the case of AA6061-T6 found to be iron rich particles in microscopic research, but considering the occurrence of this phenomenon could also be β" precipitation hardening particles in the case of AA6060-T6 [38].

This recognisable microstructure fracture behaviour can be used as an indication of ductility on a cracked surface in for example tensile tests of FSEAM samples. Logically, it can thus be used as a valuable indication of bonding quality in the FSEAM process, as significant bonding defects would result in non-ductile cracking giving non-dimpled surfaces.

Flow Behaviour

Solid state metals are generally treated as non-Newtonian fluids with high viscosities in flow simulations. The flow field is generally assumed to belong to the laminar regime and the viscosity is taken as a

function of temperature and strain rate [39].

The extensive book of Sheppard (1999) [40] states that the Zener-Hollomon method is mostly used to describe aluminium material flow, which was indeed still widely seen across this literature research. This concept is furthermore mostly used in FSEAM flow modelling so far, for example in the work of Masselink [16] and Lind [13]. The method takes the dynamic recovery and recrystallization process into consideration [39]

The formula stated according to Sheppard and Wright [39, 40] is:

$$\bar{\sigma} = \frac{1}{\alpha} ln \left(\left(\frac{Z}{A} \right)^{\frac{1}{n}} + \sqrt{\left(\frac{Z}{A} \right)^{\frac{2}{n}} - 1} \right) \tag{1}$$

in which $\bar{\sigma}$ represents the effective stress and Z the Zener–Hollomon parameter. The other parameters are linked to flow geometry and are not further elaborated on. Z is formulated as [40]:

$$Z = A \ [sinh(\alpha \bar{\sigma})]^n = \dot{\bar{\epsilon}} \ exp \left(\frac{\Delta H}{GT} \right) \tag{2}$$

in which $\dot{\bar{\epsilon}}$ is the effective shear rate, ΔH the deformation activation energy, G the gas constant and T the temperature.

Viscosity modelling used in combination with the Zener-Holloman method is commonly based on the effective viscosity, which is constructed from the effective normal stress and effective normal strain rate by applying Von Mises stress. The derivation is based on pure shear stress in uniaxial tensile tests [39]. This gives:

$$\mu = \frac{\bar{\sigma}}{3\dot{\bar{\epsilon}}} \tag{3}$$

in which μ represents the effective viscosity, $\bar{\sigma}$ the effective stress and $\dot{\bar{\epsilon}}$ the effective strain.

2.2 AFSD at the University of Twente: FSEAM

Below, attention is paid to previous research on the University of Twente that can provide a basis for answering the research questions. Only research efforts are mentioned. The current FSE(AM) setup is described in detail in Chapter 3.

Brief FSEAM Characteristics

From the most recent UTwente research sources [15,17,19,26], the FSE(AM) process can be characterised by its solid-state process temperatures, generally a factor of 0.6 to 0.9 times the material's melting temperature. This is combined with high material processing pressures, which cannot be measured directly but are needed as basic requirement for this process. These pressures result in normal forces on the substrate in FSEAM in the order of magnitude of 10 $[kN]$. These pressures and temperatures are induces by a threaded tool generally rotating with rates between 400 and 600 $[rpm]$ combined with a tool torque in the range of 40 $[Nm]$.

A table moving speed between 100 and 500 $[mm/min]$ combined with a volumetric material supply of a factor 1.3 times the material demand (based on table velocity) results in successful printing of AA6060-T6 in wall-shape structures with near net-shape without macro-defects. Geometrical guides in the nozzle of 10.5 $[mm]$ wide are used for geometrical stability.

Furthermore, the prints have low residual stresses as no stress-related deformation is observed. The prints have few solidification defects and lack chemical changes due to the solid-state nature of

FSE(AM). First mechanical tests on prints without post-processing show a hardness reduction from 80 $[HV]$ to 40 $[HV]$ and a UTS of 100 $[MPa]$, which is circa 200 $[MPa]$ for AA6060 in T6-state [1]. Microscopy revealed a wrought equiaxed grain structure with fine grain size (< 10 $[\mu m]$), due to severe plastic deformation and complex dynamic recrystallization effects.

Tool Gap Influence on FSE(AM) parameters

In recent master thesis, the following conclusions were drawn on how FSE(AM) would be influenced by altering the tool gap:

- Masselink [16] and Strik [17] both state with the same reasoning that increasing the tool gap would have a significant effect on cylinder force and torque. They state that cylinder force will decrease with increasing tool gap as less pressure is needed to press a flowing substance with the same speed through a wider space. They state further that a larger tool gap means more material rotates round the tool and thus torque should increase.
- Lind [13] states from simulations and experiments that the cylinder force and normal force pressure will increase the tool gap as a result of lower temperatures and thus higher material viscosity.

It is seen in earlier experiment results [16] that material output is directly linked to material input. In other words: when material input stops, the output stops simultaneously. This means that the screw is not dominant on material transport in the tool housing region [41]. This observation is contrary to what is common in polymer extrusion in which material transport is coupled to tool rotation rate due to small tool gaps [42]. The used tool gap in FSE(AM) might thus be too big to generate this coupling effect. This can be seen as beneficial for FSE(AM) as it makes the system far better controllable.

Furthermore, back-flow of material in the tool housing area is found empirically and via simulations as seen in the aluminium cross section in Figure 15 [16] and in the scale model compared to simulations in recent work by Visser [18]. Pressurised material surplus in a narrowing volume tends to flow back to a location providing more 'space', which is in this case the higher regions of tool housing.

Thermal Research

Different thermal analyses were performed to better understand FSE(AM) in order to improve printing quality. This is for example done with a simple FEM-model to determine thermal conductivity in FSEAM prints whilst new layers are still added [17]. In this way, the ageing behaviour (and thus precipitate development and printed product strength properties) can be predicted.

Worth noting is the serrated yielding behaviour (jagged edges in stress/strain-curve) found in tensile tests samples of FSEAM prints made with different printing velocities [15]. It was observed that prints made with higher temperatures (at higher velocities) above the solvus line of AA6060 experienced serrated yielding and ones made at lower temperatures, which stayed below the solvus line, experienced smooth yielding behaviour.
Such effects are known in carbon steels as the Portevin–LeChatelier (PLC) effect, due to the interaction of solute atom diffusion with stress fields around dislocations [15]. It is out of the scope of this thesis to provide an extensive theoretical layout of this effect. However, practical consequences are that FSE(AM) is apparently successfully able to process AA6060 at relatively low temperatures, whilst not being in a homogeneous α phase and that predicting and controlling thermal behaviour is of key importance for controlling yield behaviour of printed products made with FSEAM.

Print Layer Adhesion

Besides unwanted varying extrusion rate, bonding defects are found in recent FSEAM-experiments [19]. It is known that the oxide layer between the new and previously printed layer must be broken

by a high enough pressure (supported with sufficient temperatures) to ensure proper atomic bonding [4, 19, 43]. Insufficient bonding is called a 'kissing-bond' and is well known to occur during FSW of AA6xxx series [43].
In FSEAM, the needed pressures are applied in the form of a normal force induced by tool rotation and material movement. Small voids and cracks on layer interfaces were found in microscopy analysis [19]. Logically, these can explain pre-mature failure in the tensile tests presented in Figure 8.

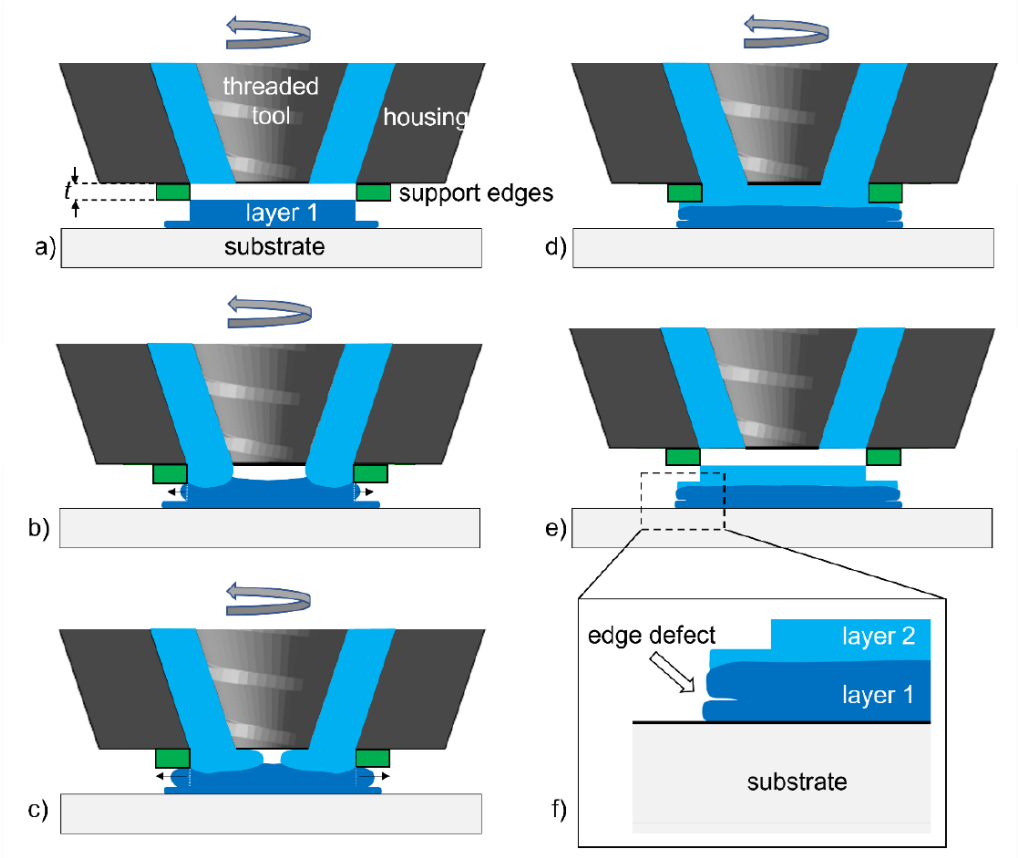

Figure 14: FSEAM print process in phases, taken from [41]

Improper bonding could also be found in the nature of material flow around the current FSEAM tooling. Different stages of the FSEAM printing process are shown in Figure 14, where uneven pressure distribution can logically be derived from the uneven material outflow upon the substrate, resulting in above-mentioned defects. A solution proposed by Bor [19] is to experiment with different tool designs in the nozzle area. Ideas for different tool designs can be found at other research groups, as discussed in Chapter 1.

In the work of Masselink [16], cross sections of the material flow around the tool (Figure 15) are made of aluminium with contrast material coming out of the tool housing and nozzle area in FSE experiments. Different material flow effects can clearly be seen due to the used contrast material. Different flow rate regions (slow or fast) substantiate the observations made from Figure 14. Besides, a clear vortex zone is present characterised by low normal forces applied in substrate direction.
Furthermore, the indicated dead zones in the nozzle region and back flow seen along the FSE-tool (for example at the area indicated with 'FSE-tool screw surface') and tool housing are flow features further researched by Visser [18]. In his master thesis, a transparent enlarged scale model of the extrusion head is made to be able to observe and analyse flow behaviour. This scale model can be used to test flow behaviour of alternative tooling to improve pressure distribution.

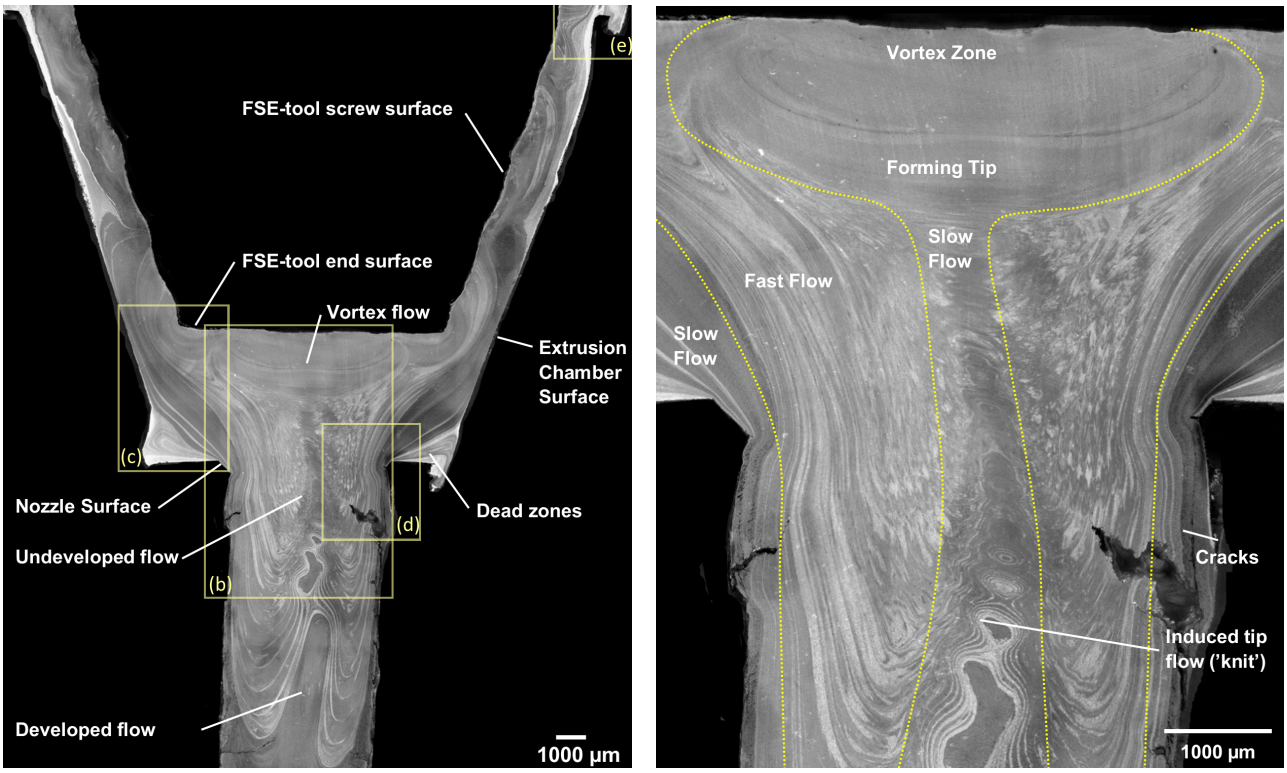

15.a. Overview **15.b.** Zoom (b)

Figure 15: FSE typical material flow at the exit region, taken from [16]

2.3 Varying Material Outflow Speed in FSE(AM)

As introduced earlier, recent FSEAM experiments [17, 19] produced at low printing speeds are prone to inconsistent material outflow speed, resulting in inconsistent geometry of printed walls as shown in Figure 9. No explanation is found yet for the cause. However, it is known from earlier FSE experiments and available FSE extrudate samples that varying material outflow speed occurs in FSE as well [16,18]. A brief literature study on varying material outflow speed well-known from polymer extrusion processes is presented and (where possible) compared to observations from earlier FSE experiments.

The extensive book of Rauwendaal (2013) [44] on polymer extrusion presents clear examples of different polymer rod extrusion defects, of which a schematic illustration is presented in Figure 16.

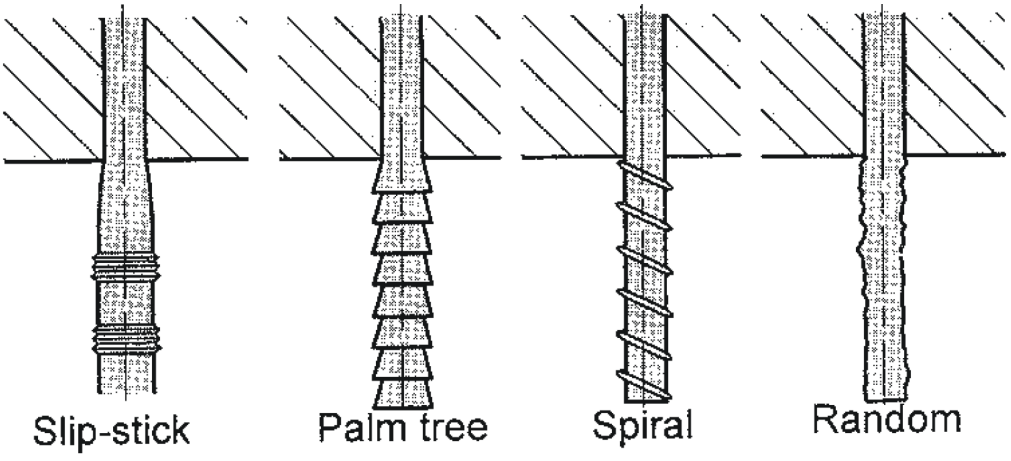

Figure 16: Common melt fracture defects in polymer rod extrusion, taken from [44]

All of the shown defects occur in FSE as well, based on observations of available FSE-samples from earlier master theses [16] and of which an overview is presented in Figure 17 with different feed

velocities (v_f). Rauwendaal states that the presented defects in Figure 16 are not solely surface defects, but defects related to the entire extrudate volume. An exception is the shark skin defect, which looks like a very local piece of palm tree and is stated to be a surface defect only. It is stated that an explanation of the cause is still part of debate between researchers and that the mechanisms may vary per polymer type. However, Rauwendaal mentions that literature agrees that defects are most likely triggered by excessive shear stress behaviour in the polymer at the die interface.

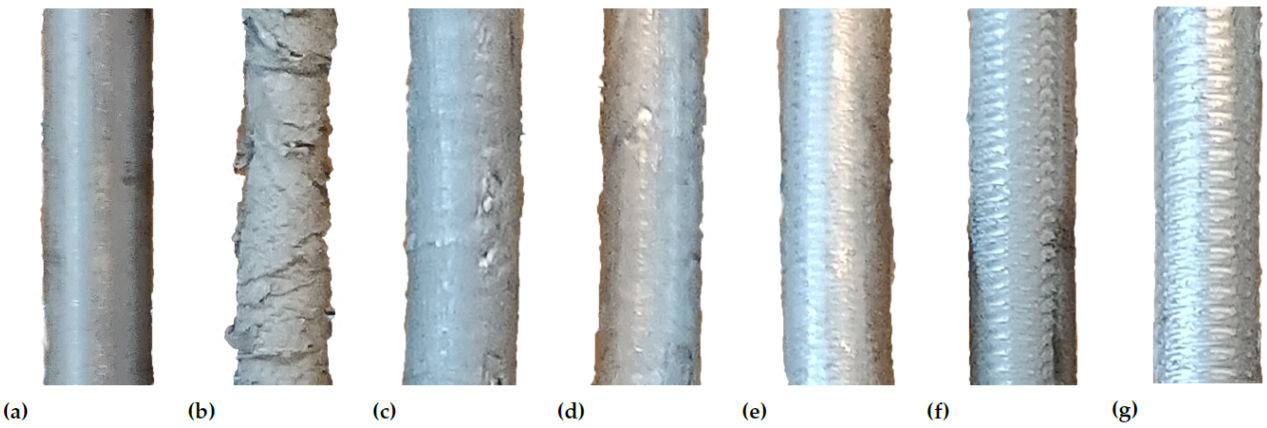

Figure 17: Typical FSE extrudate appearances, taken from [16]. With a) feed material, b) at the starting up phase, c) with $v_f = 0.25$ $[mm/s]$, d) with $v_f = 0.75$ $[mm/s]$, e) with $v_f = 1.25$ $[mm/s]$, f) with $v_f = 1.75$ $[mm/s]$, g) with $v_f = 2.25$ $[mm/s]$.

According to Rauwendaal [44], the stick-slip effect was introduced by Benbow, Charley, and Lamb to explain extrudate distortions and flow instability. They state that polymer melt material will intermittently slip when a critical shear stress between polymer melt and die wall is exceeded in combination with a lack of adhesion between polymer and die wall. This to relieve excessive deformation energy in the material. Rauwendaal states that this effect is widely observed by extrusion workers in a range of polymer extrusion techniques.

Additionally, Rauwendaal explains the term 'superextrusion' in which the polymer melt slips uniformly and constantly with respect to the die wall. No clear proof is found whether a loss of contact between polymer and die wall takes places or that the polymer shears over a thin polymer layer that sticks to the die wall.

Rauwendaal states that a general solution of the presented melt defects in Figure 16 can be found in changing the die design to be more streamlined, in increasing temperatures, applying lower extrusion velocities, using lubricant or changing polymer material characteristics. Another option is mentioned by permanently performing the process in the superextrusion phase, which is commonly already applied in polymer extrusion to reach high production rates.
Early research conducted by Benbow et al (1961) [45] finds that for extrusion defects for polythene, surface roughness is not of influence for a solution but rather the material composition.

An extensive study on polymer extrusion defects conducted by Vergnes (2015) [46] learns that defect behaviour in FSE as described above is comparable with behaviour seen in molten polymers with a linear molecular structure. It is stated that defects like shark skin originate at the exit region of a nozzle due to sharp shear stress gradients at the die corners in combination with large elongation rates. The shark skin effect is found temperature sensitive in a way that higher temperatures postpone it to higher flow velocities and that the effect can almost be completely omitted at processing close to the melting temperature. Vergnes states further that changing the die material to one with lower surface energy would promote macroscopic wall slip (thus the earlier mentioned superextrusion).

Furthermore, Vergnes presents Figure 18, in which pressure is set out to flow rate for typical linear polymer rod extrusion including domain indications of the mentioned extrusion defects. It is stated that the stick-slip behaviour takes places in between points Q1 and Q2, where pressure is unstable but oscillated periodically. Extrudates made in this region typically have altered sharkskin and smooth appearance. Vergnes mentions that the oscillating nature is highly sensitive to flow geometry, but that the effect is not yet understood. The solutions presented are complex stress/strain mechanisms that are part of debate between researchers.

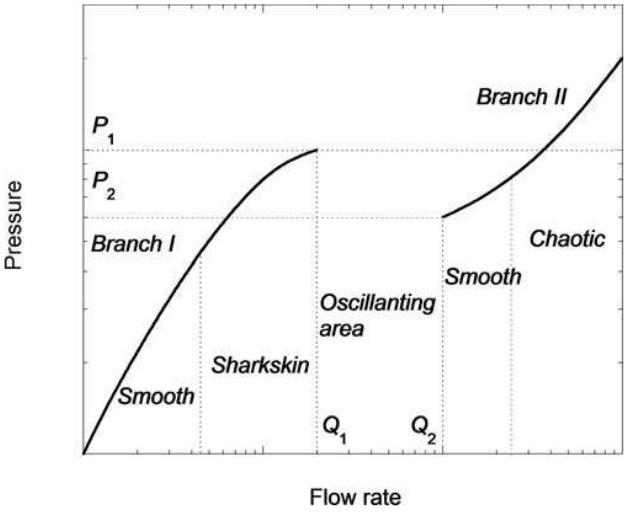

Figure 18: Pressure versus flow rate in linear polymer rod extrusion, taken from [46]

Solutions according to Vergnes are for example temperature increase, where the effects are moved to higher pressure values and oscillation amplitude is reduced. Besides changes in polymer molecular properties, it is stated that die surfaces made from low-energy surfaces (a.o. deoxidized brass) severely reduce the oscillating effects or let is completely disappear, leading to Vergnes strong empirically based evidence that the oscillation is related to the stick-slip mechanism.
Several models are pointed out by Vergnes that are based on the polymer molecular nature of entanglements. However, the most robust solution seems to induce permanent wall slip (thus superextrusion) and so completely omit the region of oscillating flow pressure. Practical solution implementations focused on system control for temperature regulation can be found in Campbells book on "Analyzing and Troubleshooting Single-Screw Extruders" (2013) [47].

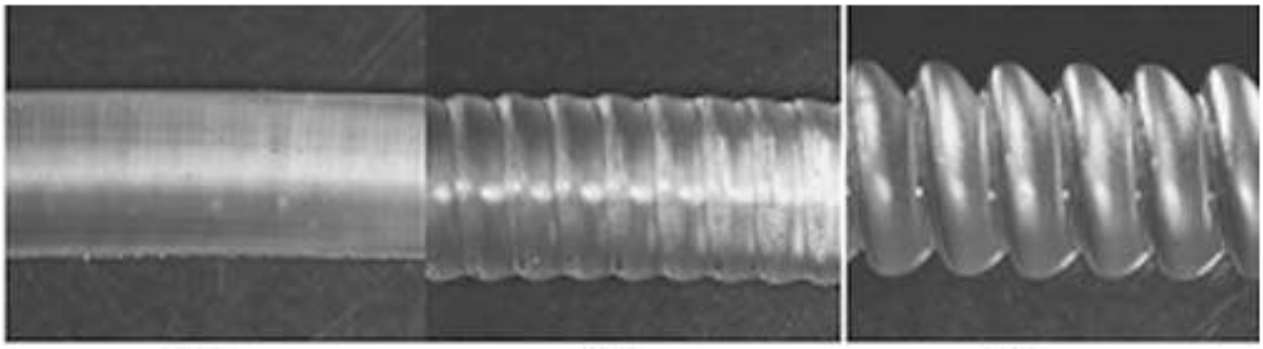

Figure 19: Helical shape due to volume defect with increasing severity with increasing flow rate [46]

In FSE at the UTwente, samples made with higher feed velocities show characteristic helical patterns in their surface as seen in Figure 17. This effect is widely seen in polymer rod extrusion as shown in Figure 19. In polymer rod extrusion, it is known that the severity of the effect increases (eventually to chaotic deformations) and the frequency remains the same whilst increasing flow rates [46]. In available FSE samples, the frequency seems related to the tool rotation rate and feed velocity. An explanation for the effect in polymer rod extrusion is not yet found and the effect is hard to capture in data [46].

For stick-slip behaviour at a tool steel-AA6063 interface, Ma et al (2012) [48] performed extrusion experiments with a slit die and successfully developed a tribological model matching the experimental results. It is seen in their results that the die length in flow direction displays a zone were stick occurs and a zone were slip occurs depending on the local normal pressure experienced by the extrudate

material. Ma states that sticking occurs when the nominal friction stress is larger than the shear strength of the process material. When this is the case, the extrudate material shears over a very thin layer of its own material that sticks to the die wall. The shear stress to nominal pressure behaviour than follows a shape similar as presented in Figure 20. It is stated that surface topography is of minor influence in determining the transition point of stick-slip and that the presence of sufficient pressure is the major factor.

Widerøe et al (2012) [50] finds in AA6060 to tool steel rheology experiments that the pressure needed for stick is decreased significantly at higher temperatures.
The conditions for tool-workpiece stick-slip conditions is believed to determine the torque and heat input to the workpiece in comparable FSW according to Wang et al (2021) [49]. They state that quantitative experiments to the tool-workpiece stick-slip conditions are rare and that numerical methods that are compared to general experiment results dominate.

Although no robust explanation is found in literature for the mechanisms behind the varying outflow speed found in FSE, suggestions of avoiding the effect are presented and entries for empirical evidences are given that can be compared to FSE experimental results.

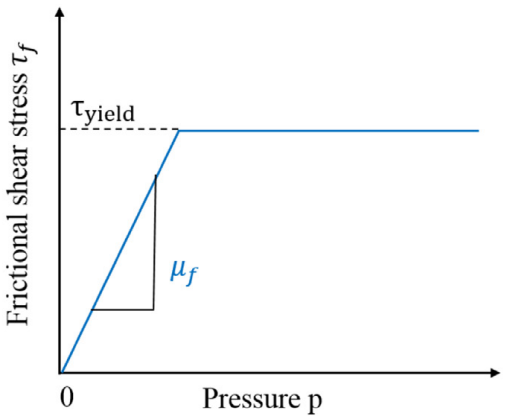

Figure 20: Shear stress versus pressure in stick slip behaviour assuming Coulomb friction [49]

3 Experimental Setup & Method

To answer the research questions of this thesis, FSE setups are performed. Below, argumentation is presented first on why FSE is chosen as the research platform of this thesis. Then a more detailed overview of the FSE(AM) setup currently used at the University of Twente is presented. Furthermore, setup modifications needed for answering the research questions are explained, including changes made in between the first and second experiment series. Lastly, the experimental method is elaborated on.

3.1 Choice for FSE experiments

FSE experiments were found suitable for finding an answer to the research questions as FSE is a much simpler and better controllable process to perform than FSEAM. Furthermore, FSE can be performed on the FSEAM setup with minor setup changes.
A key difference between FSE and FSEAM is that in FSEAM the processed material presses against a previously printed layer resulting in a normal force, whilst this previous layer is absent in FSE and so this normal force as well. It is profitable to be able to measure normal force (F_n) data during FSE to be able to extend experimental FSE results to usefull predictions for FSEAM as well. Therefore, the current FSE setups needs changes to mimic this normal force.

Furthermore, FSE experiments give the advantage of being able to capture the extruded material exit flow speed in video data to be able to capture any variations in material outflow speed. This would not be possible with FSEAM.

3.2 Current FSE Setup

A more detailed view of the FSE printing setup currently used at the University of Twente is presented in the cross-section in Figure 21. The only difference with FSEAM being another nozzle part. The setup consists of a modified Waldrich Coburg Planar Machine with a $13kW$ electric motor attached overhead. To this motor, a printing head assembly is attached as presented in Figure 21.

The printing assembly consists of a hydraulic cylinder pushing feed material into the indicated extrusion head assembly, of which the force is measured with a Lorenz K13-50kN force transducer (strain based). The cylinder displacement is measured with a displacement sensor attached to the load cell holder and travels over a guiding rail. In FSEAM, the normal force applied onto the substrate by outflowing material can be measured by three HBM KMR 100kN force sensors. This is not possible for FSE as no substrate is present to apply a normal force on by outflowing material.
In Figure 22.b., the currently used tool is presented in the nozzle head for FSE(AM). The only difference in setup between FSE and FSEAM is the nozzle region, which consists of a straight nozzle with holder plate for FSE (close-up in Figure 23) and for FSEAM of a part combining the tool housing and nozzle, giving an open nozzle with geometrical guiders (shown as green support edges in Figure 4).

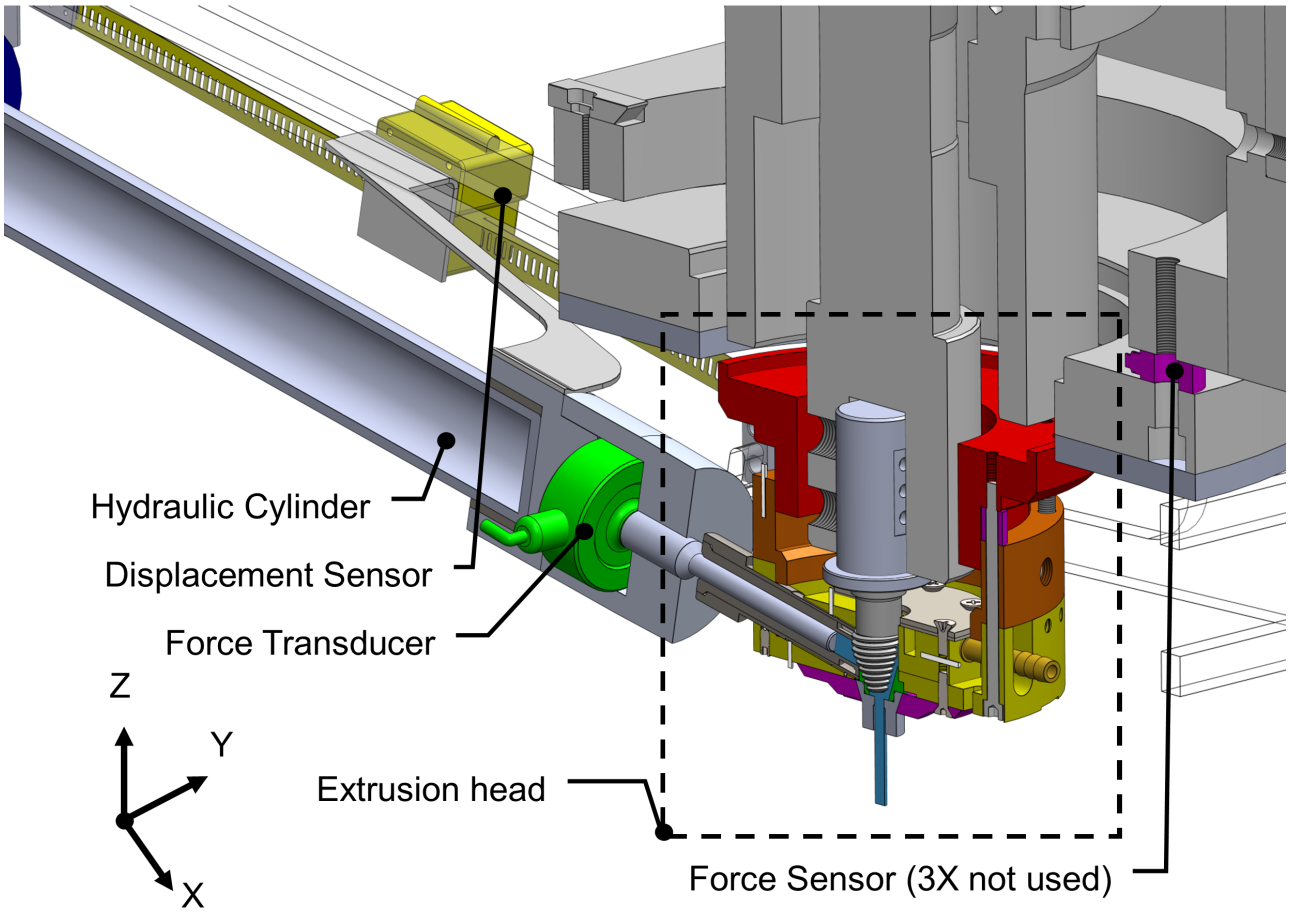

Figure 21: Overview of current FSE setup, with only the printing nozzle being different from FSEAM, taken from [16]

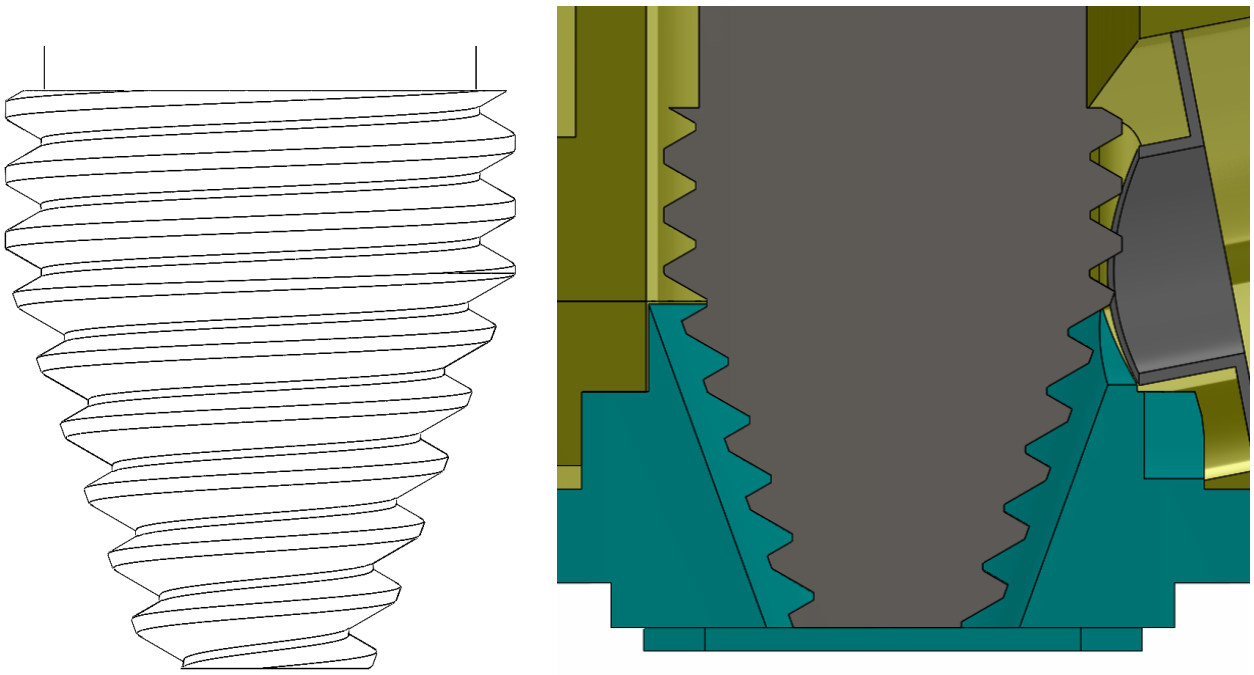

22.a. Sketch

22.b. In FSEAM assembly

Figure 22: Sketch of tool head design in FSEAM setup used in recent UTwente research [15, 17]

The current tool design used in FSE(AM) is presented in Figure 22. The tool consists of a conical and tapered section and is completely threaded with M20 ISO965 thread [19]. Technical drawings of the tool are presented in Appendix C.2.

The tool gap (TG) and end gap (EG) in the extrusion head are important parameters for successful FSE(AM) [10], as these significantly influence pressures and temperatures in the material flow path. Definitions of both TG and EG are presented in Figure 23. A tool gap of 3.2 $[mm]$ was used in most recent FSEAM work of Strik [17].

As can be seen in Figure 23, the tool gap and end gap in the current FSE setup cannot be altered separately. They can be adjusted together by adjusting the spacer height in the mounting head. This spacer is indicated in pink in Figure 21 between the orange and red part in the extrusion head area. By changing the spacer size, the whole extrusion head assembly is lowered or lifted with respect to the tool.

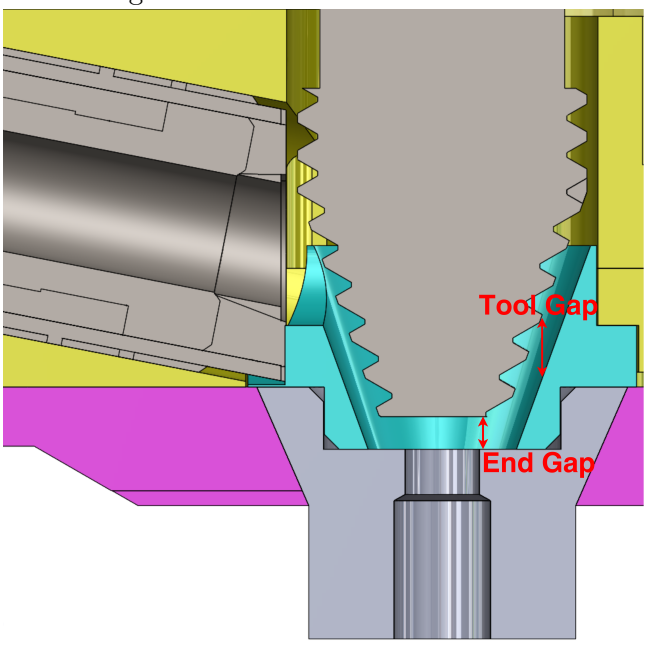

Figure 23: Close up of FSE setup from earlier research [16, 18] with tool gap and end gap definition

Cooling of the system is realised by two water cooling channels. One channel in the feed tube and one in the mounting head shaped around the rotating tool [18]. Cooling water is provided from a bulk water tank with a simple aquarium pump with adjustable volumetric supply rate.

3.3 Setup Modifications

The FSE setup from the recent master theses of Visser [18] and Masselink [16] is taken as the starting point for modifications. New parts are designed such that the normal force (F_n) experienced in FSEAM can be imitated. Besides, it is wished for to retrieve temperature data more closely to the material flow than in the current setup. Especially the temperature in the nozzle area, as this would be the maximum temperature of the material flow based on flow simulations [16].

To do so, a new **nozzle plate** with **guiding plate** are designed which are schematically presented respectively in green and grey in Figure 24. Technical drawings can be found in Appendix B.

The two parts are designed such that a translating vertical Degree of Freedom (DoF) remains between the green nozzle plate (which rests on the hatched supports) and the grey guiding plate, which is bolted to the present yellow mounting head. More simply, the nozzle plate and guiding plate can move up and down to each other. Furthermore, small holes are present in the grey nozzle plate such that the material flow temperature can be measured directly measured in the material.

The DoF is realised by making a circular flange onto the guiding plate, which slides into a circular slot of the green nozzle plate with a loose fit. Three aligning holes are drilled in both the nozzle plate and guiding plate. The nozzle plate holes are threaded and the guiding plate holes are smooth. Simple bolts can be used as dowel pins, such that pure vertical movement is guaranteed. A schematic close-up of one 'dowel bolt' is presented in Figure 25.

The whole mounting head assembly with the tool can now move up and down while the green nozzle plate keeps resting on the support frame (hatched in Figure 24). Doing so, the tool gap can be adjusted by fixing the mounting head with different spacer size. Available spacers of 1 $[mm]$ thick

can be placed between the nozzle plate and the guiding plate around the dowel pins to guarantee a desired end gap of 2.4 $[mm]$, which is in correspondence with earlier FSE(AM) research [19].

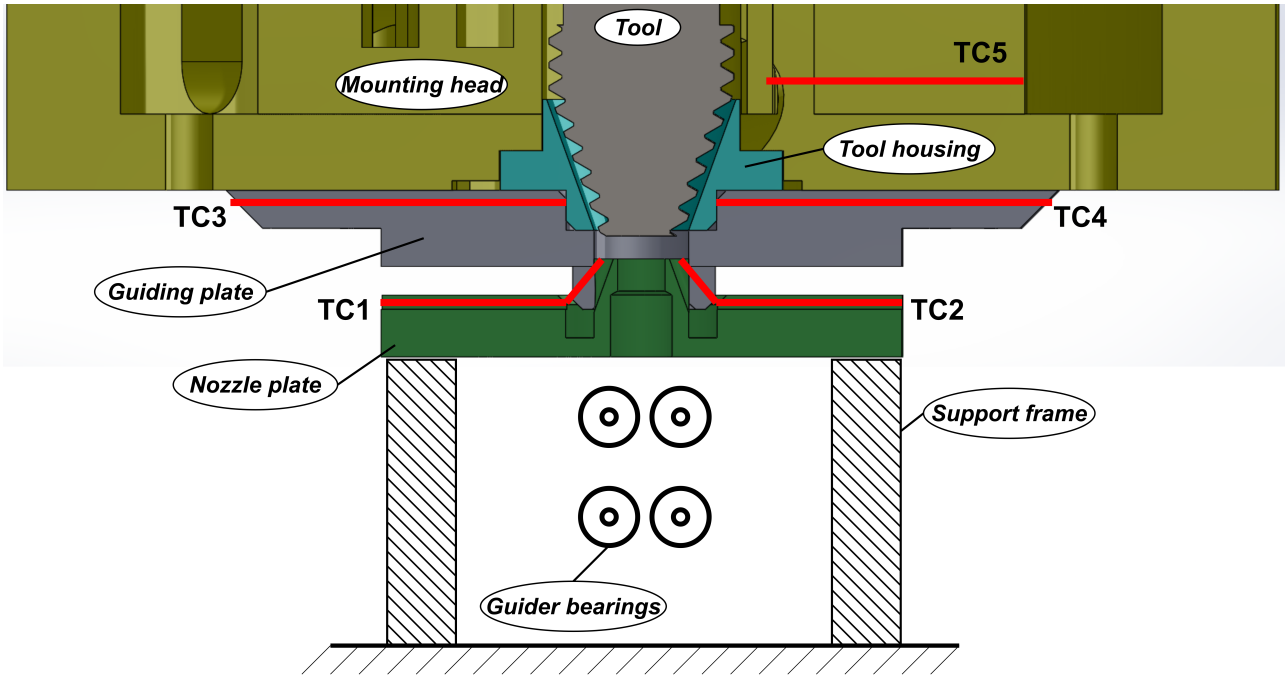

Figure 24: Sketch of the modified FSE-setup with part identification in text balloons. Thermocouples placed in slots and indicated with red lines, with measuring point at the line end closest to the tool.

By doing so, material flow can apply force on the nozzle plate, of which the reaction force can be measured by the three force sensors (placed axisymmetric) in the existing setup as presented in Figure 21. In this way, the normal force occurring in the FSEAM-setup by outflowing material pressing onto a previously printed layer is imitated and can be measured.

Two sets of tool housing (blue), tool housing holder (grey) and extrusion die (green) are produced by the UTwente's laboratory workshop out of H13 steel without post treatment.

The correct **tool gap** is ensured by using the correct combination of a self-made 9.8 $[mm]$ bushing and 1 $[mm]$ spacers to bolt the mounting head over the tool. The bushing (with extra spacers) location is indicated in Figure 21 by the pink bushing between the red and orange parts.

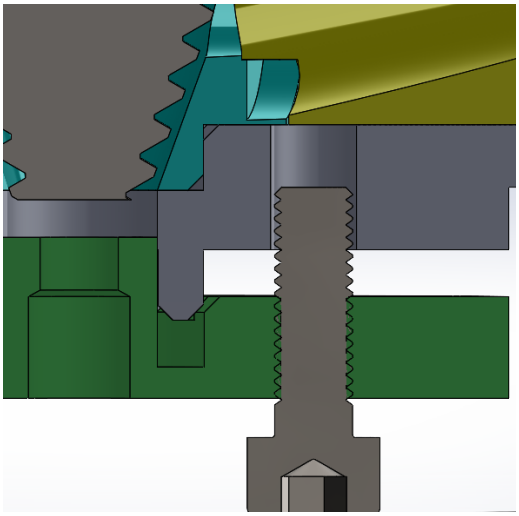

Figure 25: Modified FSE-setup: close-up of hexagonal bolt placed in the nozzle plate acting as dowel pin in the guiding plate

A **support frame** is produced out of extruded aluminium profiles to improve the support structure for the second experiment series. It contains two sets of bearing pairs that guide the extrudate vertically to prevent horizontal motion. The design of the aluminium frame support is elaborated on in Appendix D as well as the support construction of the first experiment series, which was found to be insuffient.

The plan for **thermocouple placement** is listed below and schematically presented in Figure 24. Thermocouples are placed opposite to each other in pairs. Thermocouples are manually made from thermocouple type-K 0.5mm wires, with on one side a type-K connector connected to a data processing

laptop and on the other side welded into the correct temperature measuring position. Welding was realised by stripping a piece of thermocouple wire and using that as an improvised welding electrode to weld a thermocouple to the desired position on the nozzle plate or guiding plate. A Labfacility L60+ thermocouple welding device under protection of argon shielding gas was used as power supply.

- TC1&2 are placed in the nozzle plate through a slot and hole in the nozzle plate to measure the temperature at the extrusion area directly in the material flow.
- TC3&4 are placed in the guiding plate through a slot in the circular edge in order to measure the temperature half way the material flow.
- TC5 is already available from earlier research [17] and placed in the mounting head (yellow in Figure 24) at the tool cooling exit channel in order to measure the water temperature at the material inlet.

With this thermocouple plan, the thermal path of processed material and cooling water temperature (giving an indication of heat and thus energy input) can be tracked whilst providing a backup for failing thermocouples. Also, it can serve as in indicator whether or not the temperature distribution in the setup is axisymmetric.

The **feed force** (F_{feed}) load cell was replaced with a new K-13 type load cell with a maximum allowable force of 50 $[kN]$. Feed force is induced by a hydraulic cylinder pushing a push-pin into a feed tube with a maximum $F_{feed} = 25$ $[kN]$ with a hydraulic pressure relieve valve for safety reasons. The feed velocity (v_f) is adjusted by a rotatable knob altering the cylinder pressure. As the knob holds a key to unlock its motion, v_f is expressed in 'key' values according to the numbers that indicate the scaling on the knob.

3.4 Experimental Method

The experiment series will be performed according to the FSE settings as indicated in Table 1. Parameters are chosen as such, that the maximum range of known suitable parameters [15, 16, 18, 26] of the setup is used in order to gain maximum data acquisition and subsequently process knowledge.

Table 1: FSE parameters of performed tool gap experiments

Experiment tag	TG [mm]	EG [mm]	Tool rotation [rpm]	Input speed [key]									
TG1.5_400_x	1.5	2.4	400	2	2.5	3	3.5	4	4.5	5	5.5	6	10
TG1.5_500_x	”	”	500	”	”	”	”	”	”	”	”	”	”
TG1.5_600_x	”	”	600	”	”	”	”	”	”	”	”	”	”
TG2.5_400_x	2.5	2.4	400	2	2.5	3	3.5	4	4.5	5	5.5	6	10
TG2.5_500_x	”	”	500	”	”	”	”	”	”	”	”	”	”
TG2.5_600_x	”	”	600	”	”	”	”	”	”	”	”	”	”
TG3.5_400_x	3.5	2.4	400	2	2.5	3	3.5	4	4.5	5	5.5	6	10
TG3.5_500_x	”	”	500	”	”	”	”	”	”	”	”	”	”
TG3.5_600_x	”	”	600	”	”	”	”	”	”	”	”	”	”
TG4.5_400_x	4.5	2.4	400	2	2.5	3	3.5	4	4.5	5	5.5	6	10
TG4.5_500_x	”	”	500	”	”	”	”	”	”	”	”	”	”
TG4.5_600_x	”	”	600	”	”	”	”	”	”	”	”	”	”

Available AA6060-T6 aluminium rods of 8mm diameter with a length varying between 45 and 50mm were used as feed material. Also half-length rods were used.

An experiment has a pre-set tool gap and tool rotation rate. The correct sets of bushings and spacers are installed for a tool gap, then the machine is lowered onto the nozzle plate and support frame with

a pre-tension of 3 to 5 $[kN]$. The machine remains lowered in that position until experiment runs for all three tool rotation rates for that tool gap setting are performed. In this way, most reliable data is obtained.

An experiment run starts with a single feed rod at key 2 to warm-up the system. This is repeated until the system is at a steady-state temperature (typically 3 cycles from a cold start). Then experiment runs are performed with 1.5 feeds starting at key 2 and increased to key 10 according to Table 1. An experiment is closed with 1 feed at key 2 in order to check repeatability.

After the hydraulic feed cylinder makes a full range of travel, the hydraulic cylinder with push pin is retrieved, the feed cylinder velocity is altered with the rotatable knob. After this, 1.5 new feed material pieces are inserted in the feed tube. Then the next experiment run can start.

The resulting extruded rods are labelled with the experiment tag according to Table 1: 'TG' stands for 'Tool gap experiment', the first number indicates the tool gap in millimetres, the second number indicates the tool rotation rate in rotations per minute and the last number (x in Table 1) indicates the material input speed expressed in 'key' that complies with the numbering on the rotatable knob used for adjusting the hydraulic feed cylinder pressure.
For example: TG4.5_500_6 indicates tool gap experiment with parameter settings; $tool\ gap = 4.5\ [mm]$, $tool\ rotation\ rate = 500\ [rpm]$ and $feed\ velocity = key\ 6\ [-]$.

A second series of extrusion experiments was performed with the same input settings as mentioned in Table 1. The second series is numbered with the same experiment tag structure as explained above, but with 2 in front of the tag. For example: 2TG4.5_500_6.

A conversion table from the key values to feed velocity (v_f) is presented in Table 2. Note that the conversion values of v_f do not perfectly align across the experiments as the rotatable knob is sensitive and key values are set by hand.

Table 2: Conversion table of feed velocity from key number to v_f in $[mm/s]$. Values taken from experiment results of 2TG3.5_400_x

Key	2	2.5	3	3.5	4	4.5	5	5.5	6	10
$v_f\ [mm/s]$	0.23	0.38	0.57	0.75	1.0	1.3	1.5	1.9	2.2	2.3

Furthermore, cooling water rate is set to 3.0 to 3.5 $[l/min]$ for both cooling channels for all experiments.

Video recordings will be made of the extrudate for all extrusion runs. This will be realised by placing a smartphone (Samsung Galaxy A54) in a clamp close to the extrusion region whilst using its in-build light, the 9:16 ratio 30FPS HD mode with the 2x zoom option.

The experiments will be performed by two operators; one monitoring the data acquisition laptops, cooling flows and extrudate labelling. The other operating the hydraulic feed cylinder, feed resupply and preventing extrudate material hitting the Waldrich-Coburg planar table.

4 Parameter Analysis

In this section, FSE experiments are be performed to empirically answer the research question about the effects of the tool gap and tool rotation rate parameters on the measurable FSE(AM) system parameters. This is realised by designing and installing new parts on the existing FSE setup and performing experiments with varying tool gap and varying tool rotation rate over a feed velocity window as described in Chapter 3. Results are presented, discussed and coupled to earlier research and literature where possible. Calculations are presented to help clarify flow behaviour of aluminium in the tool housing.

4.1 Data Processing

Data is obtained from three data retrievers; normal force (F_n), feed force (F_{feed}) , cylinder travel (x_f), and thermocouple temperature (TC) data directly from the corresponding sensors in the setup via a LabView 2016 programme made by Axel Lok at the UTwente, including a separate data file transformer to obtain a .dat file, which could be used as input for MATLAB data processing. The torque data was video recorded from the Waldrich-Coburg's control panel display with a webcam connected to a second laptop. Video recordings of the extrudate were made with a smartphone as explained in Chapter 3.

In MATLAB (version R2023b), all data processed via LabView was labelled, normalised where needed and further processed. The following processing steps were taken:

- The total normal force F_n was determined from the sum of the three load cells. Normalisation was applied by setting the first data point to zero when extrusion was not performed.
- The cylinder travel data was smoothed for plotting purposes by using the function *movmean* with a window width of 25 data points, assuming the travel during extrusion occurs in a linear manner.
- The average values of F_n, F_{feed}, all temperatures and the cylinder travel velocity per extrusion run (v_f) were determined as follows:
  - The effective cylinder travel window bounds [x_{eff}] in which effective extrusion takes place was determined manually by comparing x_f to F_n data. F_n logically reacts at the start or stop of an experiment run as material flow changes.
  - The last 50% of window length [x_{eff}] was assumed to be 'steady-state'. The average values of F_n, F_{feed} and temperature data were determined including standard deviations in this time window.
  - v_f was determined by taking the slope of [x_{eff}] with respect to time. Here, v_f is assumed linear, which visually holds.
  - The most suitable thermocouple of the TC-pairs was chosen for macro-analysis, generally the one with consistently the highest values and least sudden variations.

The **torque (M) data** was processed separately using the following method:

- Videos were recorded from the torque display with a webcam on the Waldrich-Coburg control panel.
- Videoframes were read into MATLAB. Using the functions *adapthisteq* and *histeq* from the Computer Vision Toolbox, the lightning and contrast settings were optimised. The function *imbinarize* was used to make the frame binary and the function *imopen* for eliminating remaining noisy pixels.
- Using the function *ocr* with the 'seven-segment'-option, the torque values were read from the optimised image frame. Due to light reflections on the display during recording, only integers were possible to retrieve correctly.

- Resulting data appeared to be noisy as the webcam recording rate did not match the refresh rate of the display and the *ocr* function is known to be sensitive to image imperfections. Noise was removed with the following conditions based on manual data interpretation. Deleted points were replaced by linear interpolation of surrounding data points:
  - Empty cells (*ocr* function returns no value)
  - Negative torque values (suggests reverse tool direction)
  - Torque values higher than 70 *[Nm]*
  - Sudden jumps higher than a factor 10 between adjacent data points, higher than 10 *[Nm]* between neighbouring data point, higher than 20 *[Nm]* between the second neighbouring data points and higher than 35 *[Nm]* between third neighbouring data points.
- Averages and standard deviations per experiment run were determined in correspondence with the forces and temperatures approach.

4.2 Results

Below, a selection of the obtained data is presented with a first interpretation step. For future research reference, all data graphs of the raw forces, temperatures and torque data are added in Appendix E & F. Data files are available on request.

Two series of experiments were performed. Both containing the full set of parameters as displayed in Table 1. After first processing and analysis of the first series data, it was concluded that the setup did not show sufficient repeatability and too much noise. The setup was improved and the experiment series was repeated. Setup improvements between the series are elaborated on in Appendix D. Furthermore, figures presenting the results from the first experiment series can be found in Appendix E.

Working Order

Below in Table 3, the chronological working order of the second experiment series is presented including date, which parts in the setup were changed and other peculiarities that are worth mentioning.

Table 3: Working order of second experiment series including factors of influence

Experiment Tag	Date	Parts Changed (beforehand)	Peculiarities
2TG4.5_400_1_x	8th nov '23	-	Jammed at key 6. Video too unfocused for video analysis
2TG4.5_600_x	15th nov '23	Fan added at nozzle location for forced cooling and buckle prevention	-
2TG4.5_500_x	15th nov '23	-	Buckling at key 5, restart experiment from key 4.5
2TG4.5_400_2_x	15th nov '23	-	Jammed at key 6. Redoing 2TG4.5_400_1_x of 8th nov
2TG3.5_600_x	21th nov '23	Fan broken and removed. TC3&4	From now pure vertical extrusion and cutting after each experiment run instead of bending extrudate away.
2TG3.5_500_x	21th nov '23	-	Buckling at key 4.5, restart experiment from key 4
2TG3.5_400_x	21th nov '23	-	Control panel of Waldrich fallen over before experiment
2TG2.5_600_x	21th nov '23	-	-
2TG2.5_500_x	21th nov '23	-	-
2TG2.5_400_x	21th nov '23	-	-
2TG1.5_600_x	23th nov '23	-	-
2TG1.5_500_x	23th nov '23	-	-
2TG1.5_400_x	23th nov '23	-	-

Typical Appearance

Typical extrudate appearance is presented in Figure 26. Figure 26.a is taken from video recordings of experiment 2TG3.5_400_x and presents the extrudate surface development from key 2 (outer

left) gradually increasing towards key 10 (outer right) within a single experiment. Such a surface development was uniformly found in all experiments and can be described as follows:

1. A completely smooth surface can be seen for the lowest key settings.
2. Helical shaped rings start to occur slightly, but the surface remains mostly smooth with occasional light patches of shark skin.
3. The surface is prone to clear shark skin defects and helical rings are more dominantly present. A close-up of shark skin is presented in Figure 26.b on the right.
4. The surface smoothens again (reduces shark skin) and shows clear helical shaped rings.
5. The surface remains without other defects and the ring distance increases with feed rate.

26.a. 2TG3.5_400_x: From left to right increase in feed velocity with gradually changing appearance within the same experiment. Key numbering in red.

26.b. Close-up of palm tree (left) and shark skin (right) extrusion defects

Figure 26: Typical FSE extrudate appearances

Severe extrusion speed variation was observed in experiment run 2TG3.5_400_2, but this did not leave traceable deviations on the extrudate surface. Besides the appearance transition explained above, palm tree defects as shown in Figure 26.b on the left were commonly found in the first part of an extrudate whilst starting up the setup from a cold start.

4.2.1 Typical Raw Data

In Figure 27, a typical raw data set is presented of the 2TG3.5_400_x experiment to give a first overview of the course of an experiment. General observations that hold for all experiments are presented.

It can be seen clearly from the forces and temperatures that the experiment consists of 12 runs, of which the first run (key 2, 1 feed) is used to warm up the system and the last run (key 2, 1 feed) is used as a control run to test repeatability. The key velocities are sequentially increased from key 2 to key 10 as indicated in Table 1.
The figure is divided in three subfigures displaying (from top to bottom) the force data, the temperature data and the feed cylinder position with its average velocity in *[mm/s]*. The average feed velocity values could differ slightly between experiments as the key value is set manually with the rotating knob.

The start and end of an experiment run is indicated with a vertical dashed line with a horizontal dashed line in between indicating average values taken over the last 50% of an experiment run time window.

Looking at F_{feed}, a peak force in the beginning can be seen due to a 'cold start' of the feed material, as the hardness and viscosity of AA6060 drops with temperature rise. A force drop and peak at two-third of an experiment run can be clearly seen at for example key 3. This is due to the transition of feed material from the first full feed to the last half-feed, which has a different temperature as it was still stored and unused in the feed tube till that point.

It holds for the temperature data that after a small heating-up period, the data seems to stay more or less constant with small variations present. Contrary, it can be seen that F_n keeps rising slightly during an experiment run, even whilst temperatures are in steady-state. Note the difference in small variations between the three different load cells.
The cooling water temperature TC_{water} shows slight rising as well during an experiment run instead of reaching a steady-state.

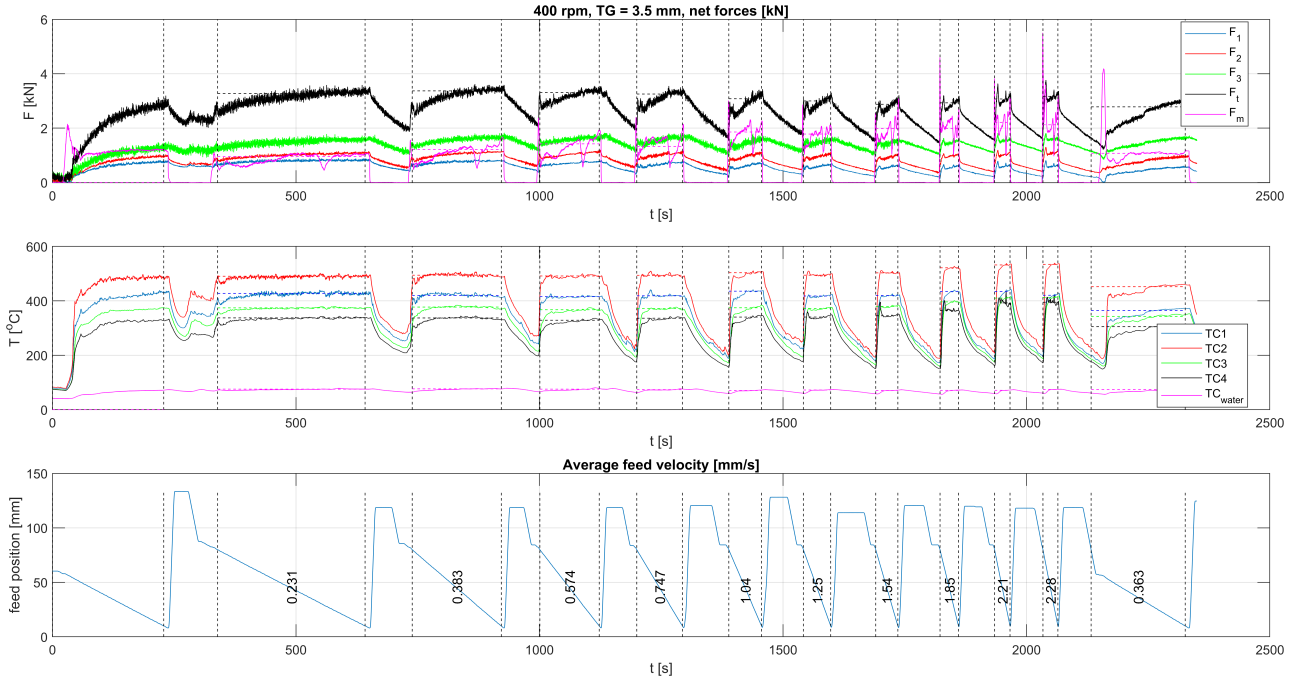

Figure 27: Typical data set of FSE experiments with varying tool gap and tool rotation rate. 2TG3.5_400_x

Thermocouple differences occur whilst being placed on the same location, but opposite to each other. This means that either the temperature profile in the setup is not axisymmetric, which is unlikely, or the placement of thermocouples is very sensitive to slight positioning variations or very small damages into the thermocouple wire. From the first experiment series, the latter can be assumed to be true.

A roughly linear decrease of F_n can be seen in between experiment runs exactly at the end of extrusion in combination with a slowing decrease of temperature values, whilst tool rotation is still present. This,

instead of a sharp drop in F_n at the moment material flow is observed to stop. This means that new feed material is a requirement for elevated F_n and temperatures. The reducing F_n learns that material pressure on the nozzle plate must be present after stopping extrusion, which can only come from the tool rotation as being the only active force-inducer present in that time window. This only holds if the threaded tool is actively providing pressure downward onto the aluminium, thus being (at least partly) responsible for material flow. This is discussed further in Section 4.3.

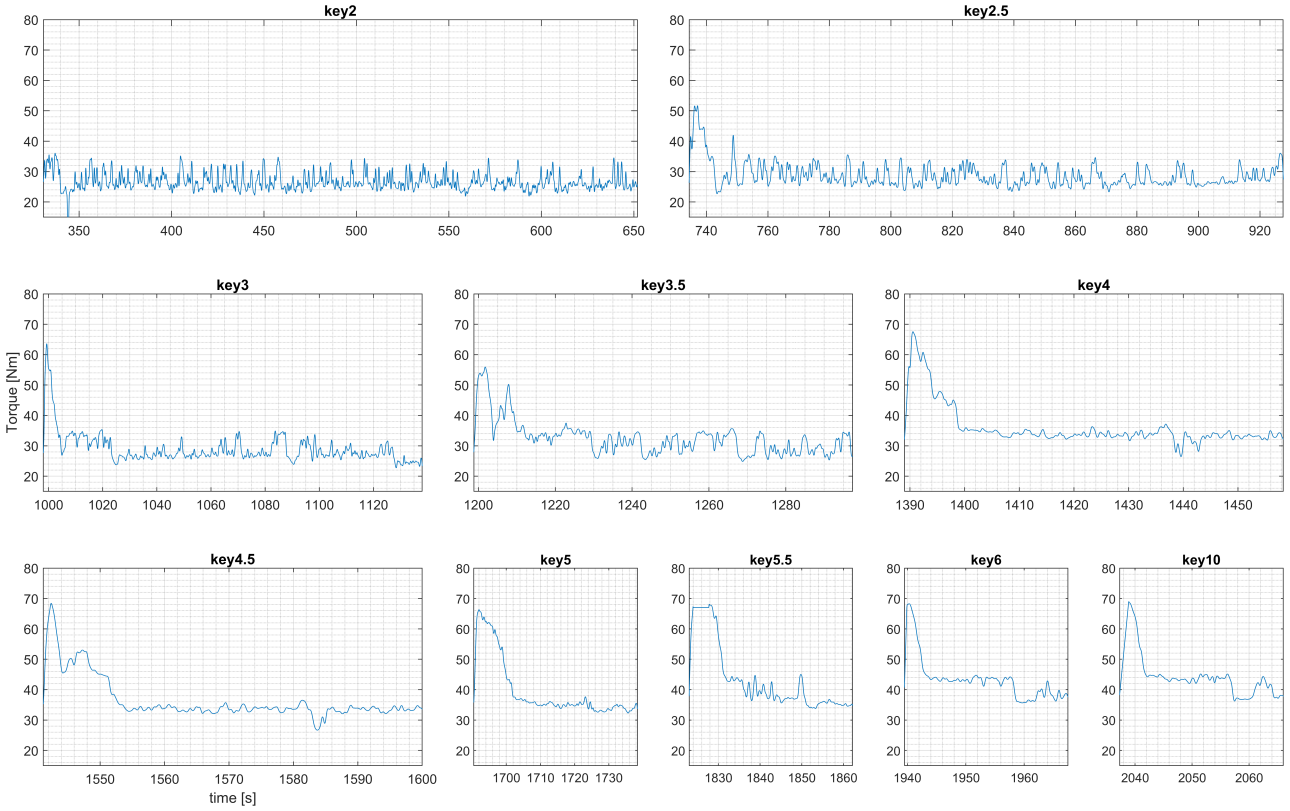

Figure 28: Raw torque data cut per experiment run, smoothed with function *smoothdata* for readability. 2TG3.5_400_x

Raw torque data of experiment 2TG3.5_400_x smoothed with MATLAB function *smoothdata* and cut per experiment run is presented in Figure 28. Torque data is presented in a different figure as it is retrieved with a separate method from other data and doing so enables a more detailed magnified view.

It can be seen that for all key settings, the torque data first shows a peak comparable with F_{feed} in Figure 27 and then stays roughly at a 'steady-state' value of circa 25 $[Nm]$ for the lowest key and 45 $[Nm]$ for the highest key. Small variations are present during the steady-state phase.
In correspondence with F_{feed} data, the initial peak is more significantly present at higher key settings. As explained, torque data is topped of at maximum 70 $[Nm]$ for noise reduction reasons, so peaks showing a plateau at that value (like at key 5.5) can be interpreted higher. It was observed that experiment runs showing (near) jamming showed initial peaks towards 100 $[Nm]$, which can thus be considered as the maximum torque value before jamming occurs.

Load Cell Drift

During experiments and first data processing, it was observed that load cell data did not behave as logically suspected. In Figure 29, raw, non-normalised data from the F2 load cell from experiments 2TG1.5_600_x, 2TG1.5_500_x and 2TG1.5_400_x is placed in chronological order and severe drift with respect to time can be observed. A third-degree polynomial is plotted through the data points to help visualise the trend.

It can be seen that the F2-data shows a clear trend, mostly negative over time. The shape of the trend shows roughly a negative parabolic shape in the 400rpm-section, a negative linear trend in the 500rpm-section and a flattened shape in the 600rpm-section of the graph. The other load cells show drift in this level of severity as well, but each load cell shows a very different trend line (even opposite to the trend shown in Figure 29).

As this drift issue forms a significant distortion in the normal force data over time and as no solution is found yet to eliminate this drift effect, the normal force data is not further analysed in the next section of overview graphs.

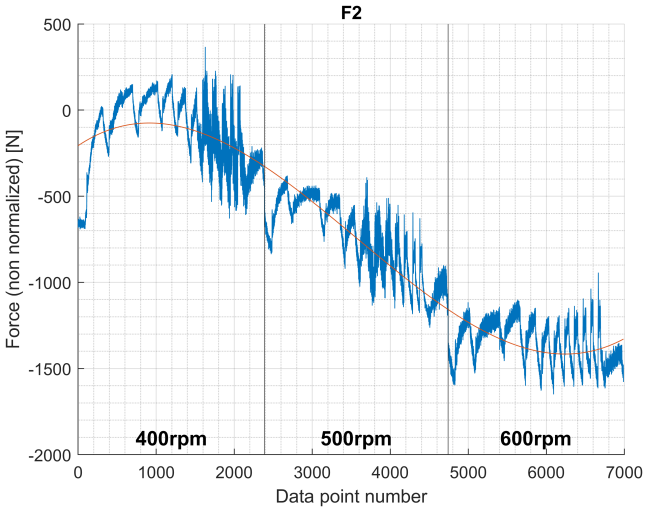

Figure 29: Load cell F2 drift example at $TG = 1.5\ [mm]$

Elaboration on the cause of this drift and possible solutions are presented in Section 4.3.

4.2.2 Macro-analysis

Below, the results of the macro-analysis are presented sorted in Figures per data type. Macro-level is defined as the time window of a complete experiment run. Some figures are sorted per tool gap, whilst others are sorted per tool rotation rate depending on the trends the data shows. Note that experiments that have a restart of the recordings are plotted in two sections for data processing reasons. The experiments 2TG4.5_400_1 and 2TG4.5_400_2 where both full experiments, but both jammed at key 6.

Temperature Data

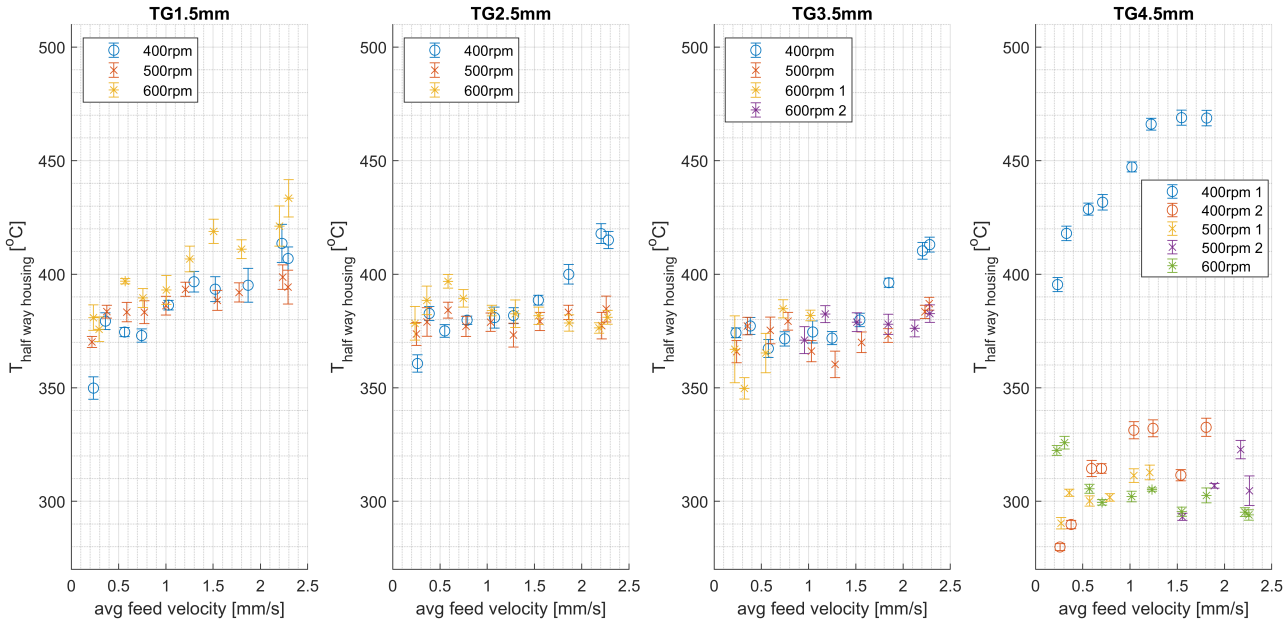

Figure 30: Average temperature half way the tool housing (TC3&4) sorted per tool gap. Standard deviation shown in errorbars.

In Figure 30, the data of TC's 3&4 (see Figure 24 for thermocouple placement) is presented sorted per tool gap. For $TG = [1.5\ 2.5\ 3.5]\ [mm]$ temperatures lay roughly around $380°C$. A subtle decrease with increasing tool gap is seen for these tool gaps. For $TG = [2.5\ 3.5]\ [mm]$, $\omega = 400\ [rpm]$ data increases comparable to all $\omega's$ at $TG = 1.5\ [mm]$, while the rest remains indifferent of changing v_f. Temperatures for $TG = 4.5\ [mm]$ differ significantly from the other tool gaps, which is due to faulty thermocouples, which are replaced according to Table 3. The difference between correctly installed thermocouples and faulty/noisy ones can give differences exceeding $100°C$, as repeatedly experienced in the first experiment series.

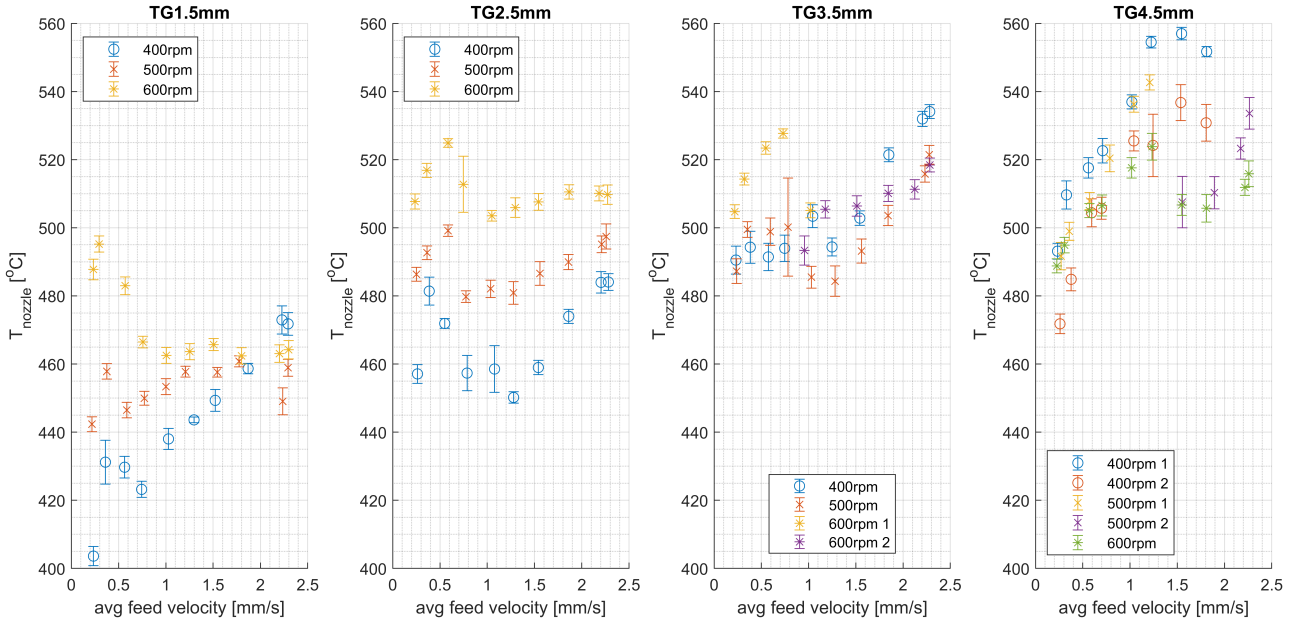

Figure 31: Average temperature in the nozzle (TC1&2) sorted per tool gap. Standard deviation shown in errorbars.

Figure 31 presents the T_{nozzle} data of TC's 1&2. The following can be seen while observing the data within the same tool rotation rate vale:

- $\omega = 400\ [rpm]$: T_{nozzle} increases over v_f for all tool gaps. T_{nozzle} also increases with increasing tool gap.
- $\omega = 500\ [rpm]$: T_{nozzle} increases less over v_f than at $\omega = 400\ [rpm]$ or even remains constant. T_{nozzle} increases slightly over TG.
- $\omega = 600\ [rpm]$: T_{nozzle} varies over v_f and shows slight increase over TG.

Besides, T_{nozzle} increases for higher ω especially for lower v_f values for $TG = [1.5\ 2.5\ 3.5]\ [mm]$. This relation is inverted for higher v_f values at $TG = [3.5\ 4.5]\ [mm]$. Towards settings likely to cause jamming, T_{nozzle} start to increasingly deviate with respect to ω, with $\omega = 400\ [rpm]$ showing the highest values.

Looking over increasing TG, a general increase in T_{nozzle} can be seen. A higher tool gap means a slower throughput time of feed material in the tool housing, thus logically providing the aluminium more time to warm up.
Furthermore, T_{nozzle} remains under $T_{solvus} \approx 440°C$ of AA6060 [15] at $TG = 1.5\ [mm]$ for $\omega = 400rpm$, which means that precipitates in the feed material are not dissolved into a homogeneous α-state, but do only age further during FSE. Microstructural and mechanical analysis must prove if this is observation is true.

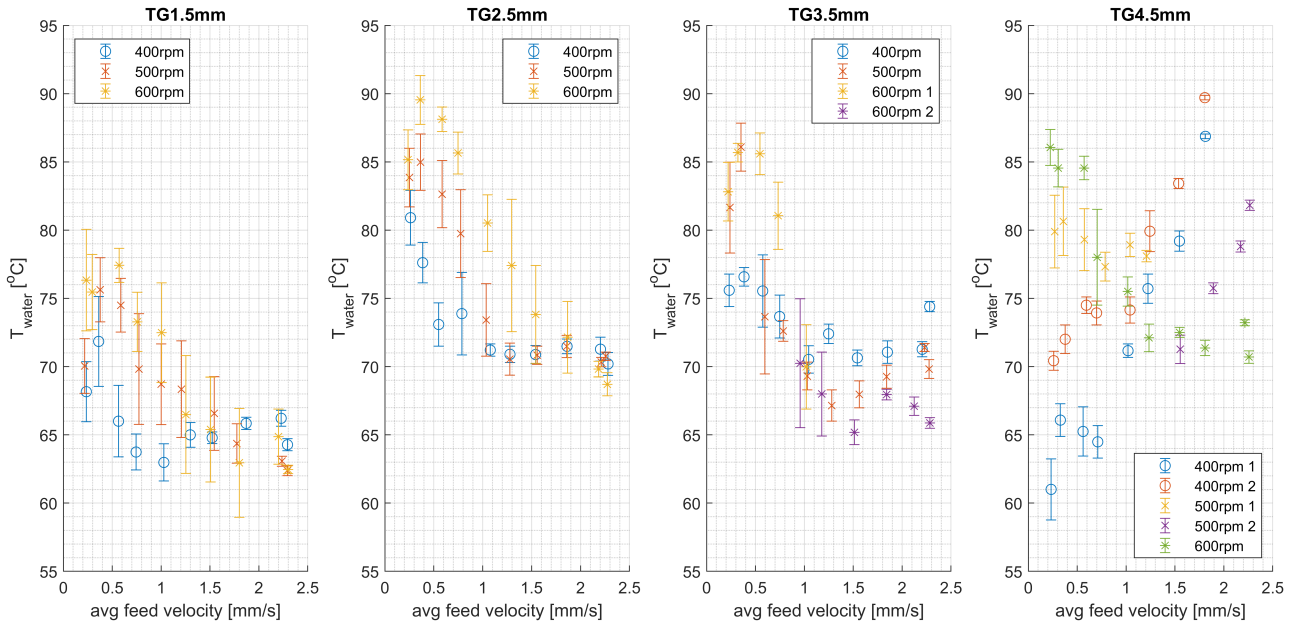

Figure 32: Average temperature at water cooling (TC5) sorted per tool gap. Standard deviation shown in errorbars.

The results of the tool cooling channel exit temperature T_{water} are shown in Figure 32, which is highly related to the heat input E_{in} into the system.
The graphs show that within experiments that were not prone to jamming, a clear decreasing trend with increasing v_f is present, whilst T_{nozzle} shows the opposite relation and $T_{halfway}$ does not comply either. As presented later, torque data does also not comply, whilst being the main energy input. Furthermore, the lower ω, the lower T_{water} is. The higher v_f, the less spread between ω changes for $TG = [1.5\ 2.5\ 3.5]\ [mm]$. Also here, some 'likeliness of jamming'-factor plays a role.

Force & Torque Data

In Figure 33, F_{feed} results are presented sorted per tool rotation rate ω, which for all setup settings shows a slowing increase with respect to v_f and indifference to changing TG. Torque values are

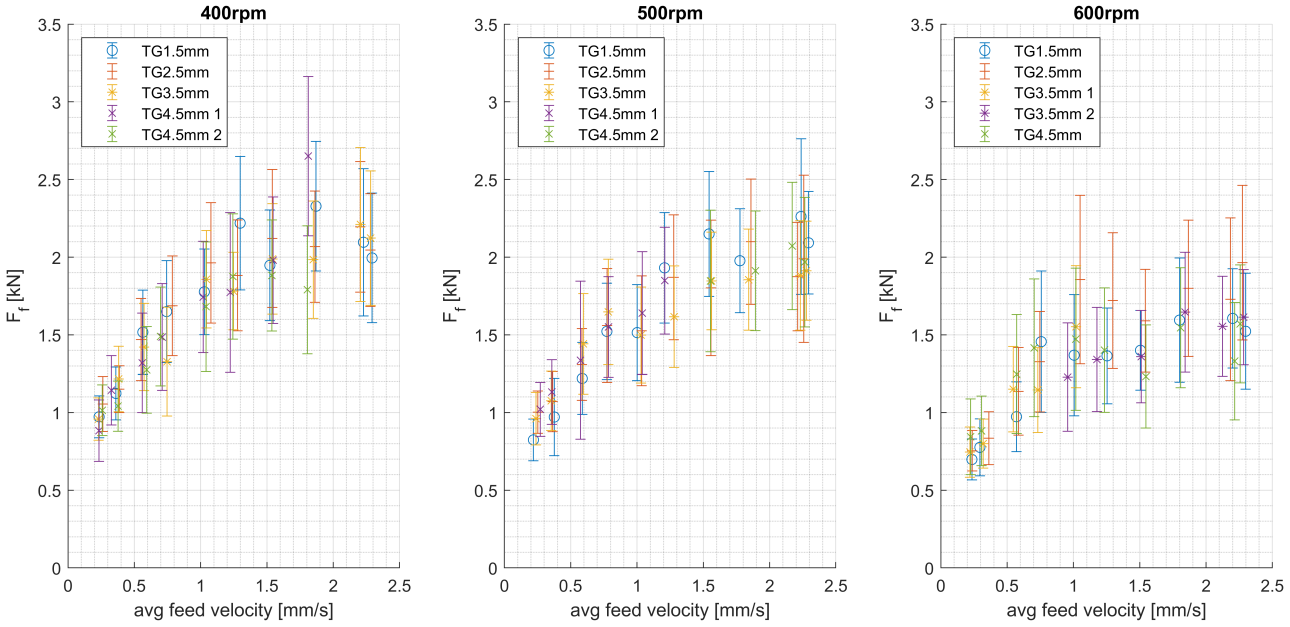

Figure 33: Average feed force sorted per tool rotation rate. Standard deviation shown in errorbars.

roughly similar for the lowest v_f settings irrespective of TG or ω. For higher ω, the slowing effect of the increase is stronger present and seems to happen at lower v_f.

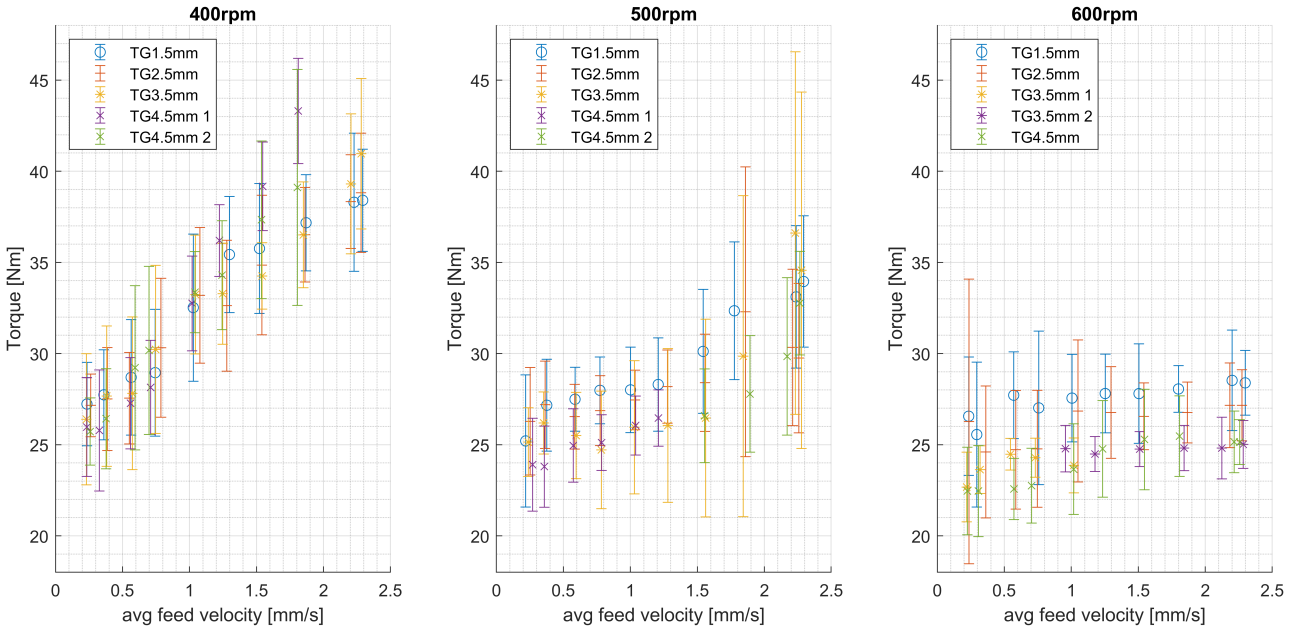

Figure 34: Average tool torque sorted per tool rotation rate. Standard deviation shown in errorbars.

Torque (M) data is shown in Figure 34. M does not show clear dependence to TG for $\omega = 400$ $[rpm]$ and shows linearly shaped increase with respect to v_f there.
A transition seems to take place at $\omega = 500$ $[rpm]$ towards $\omega = 600$ $[rpm]$ in which the increase with respect to v_f flattens and eventually disappears. For $\omega = 600$ $[rpm]$, M increases with lower TG.

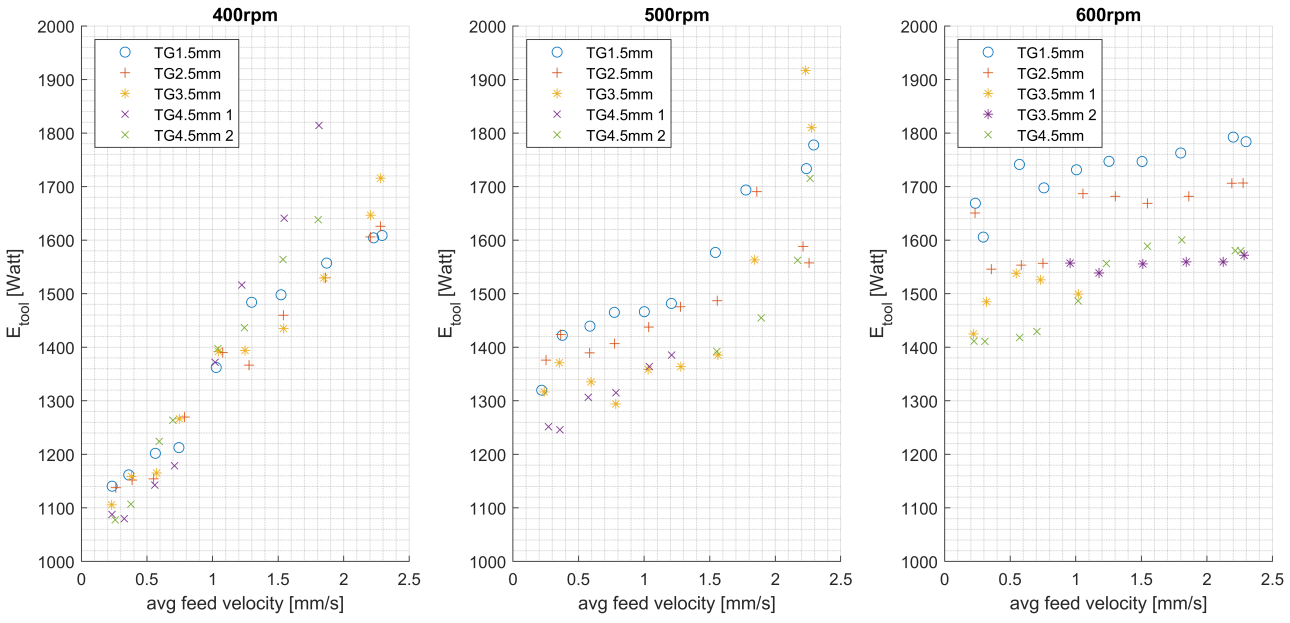

Figure 35: Average tool power input sorted per tool rotation rate.

The conversion to power input by the tool is presented in Figure 35 without standard deviations for better readability. The conversion from torque to power input is performed according to:

$$\dot{E}_{tool} = \omega M \tag{4}$$

with M indicating the torque in $[Nm]$ and ω the tool rotation rate in $[rad/s]$.

It can be seen that the power input increases with v_f at lower ω with the same behaviour as with the torque. The power input shows at higher v_f a maximum plateau at $\omega = 600$ $[rpm]$ of circa 1800 $[Watt]$ for $TG = 1.5$ $[mm]$, of circa 1700 $[Watt]$ for $TG = 2.5$ $[mm]$ and of roughly 1600 $[Watt]$ for $TG =$ [3.5 4.5] $[mm]$. Outliers at the highest v_f at $\omega = 500$ $[rpm]$ are found to have excessive standard deviation if compared to torque data in Figure 34.

4.3 Discussion

To put the experimental results into context, a coupling with earlier FSE(AM) research or polymer extrusion literature is provided were possible. To create more understanding of the behaviour seen in the figures above, some elementary calculations are presented. The report structure of the results section above is followed as much as possible.

Surface Appearance coupled to Literature

All extrusion defects from polymer extrusion presented in Figure 16 are found very similar in FSE extrudates as presented in Figure 26. This means that mechanisms that cause these defects in polymer extrusion are likely to be present in FSE(AM) as well. It is therefore recommended to perform a more extensive literature study on the possible extrusion defect mechanisms in polymers and their prevention solutions.

Unfortunately, no explanation can be given on the cause of defects found in the FSE experiments based on the analogy with polymer extrusion defects as causes for these defects are not yet known in polymer extrusion. However, as excessive polymer shear forces at the die wall interface are likely the trigger for defects as explained in the literature section, further research to the shear stress behaviour of aluminium at the tool housing wall (and possibly at the tool surface as well) can help further understand the occurrence of the observed extrusion defects in FSE.

Further coupling of surface appearance features to the window of FSE settings was not performed as the focus of this thesis lies on data study. However, coupling surface appearance features to specific FSE-settings to gain insight in any possible relation is recommended for further research.

Load cell drift

Severe normal force load cell drift prevented macro-analysis of this data. A logical cause could be that the whole setup heats up over time, causing metal parts expanding and influencing the load cell compression. Especially the aluminium support (which has a relative large thermal expansion coefficient compared to steel [1]) was felt to heat up significantly after a few hours of performing experiments to be nearly too hot to touch.

Besides, the used load cells are already extensively used in previous research. It can not be guaranteed that they were not damaged in the past.

Furthermore, the maximum allowable force of the load cells is 100 $[kN]$ each, so 300 $[kN]$ for the total setup. The maximum pretension of 5 $[kN]$ during FSE-experiments does not exceed 2% of the maximum allowable force. The typical maximum F_n of roughly 4 $[kN]$ as seen in Figure 27 gives a total of 3% usage of the maximum normal force capacity of the load cells. Although the load cells should be sensitive enough to measure accurately at such low loads, it is wise to replace the current load cells with ones with lower maximum allowable loads to reduce any sensitivity noise. Typical F_n values are not expected to exceed 15 $[kN]$ during FSEAM at regular settings [17, 19].

Solutions for correcting and investigating load cell drift during FSE-experiments are:

- Post-experiment drift compensation can be applied in MATLAB by applying a trend analysis as shown in Figure 29.
- The voltage signal of the load cells is converted to a force value by the LabView data retrieving programme. Recalibration of this conversion factor would be a wise first step in trouble-shooting.
- Measuring the temperature of the aluminium support frame can be used for determining material expansion that results in change of the pretension. The same can be applied for other metal parts that influence pretension.
- Another way of frame expansion compensation can be performed by pretensioning the system, but instead of performing FSE, only heat the support frame to verify if and how frame temperature affects load cell drift.
- A load cell creep analysis can be performed by pretensioning the setup onto the support frame and record F_n over time, whilst not performing any actions. This information can be used for post-experiment compensation of F_n-data.
- A more extreme solution is to completely redesign the support frame and F_n measuring method to another concept. The work of Lind (2018) [13] shows an alternative.

Macro-analysis

Below, a discussion on the macro-analysis figures is presented and sorted per data flow.

T_{nozzle}**:**
An increase of T_{nozzle} over the tool gap is described. A higher tool gap means a slower throughput time of feed material in the tool housing, thus logically providing the aluminium more time to warm up. However, this effect is not measured as strongly in TC's 3&4 location half way the tool housing, which suggests that temperature differences with respect to TG and ω would increase at or around the nozzle area in FSE. This is further confirmed by TC3&4 data in Figure 30 showing less deviation with respect to ω change (for $TG = [1.5\ 2.5\ 3.5]$ $[mm]$) than for T_{nozzle} data. Further research with different tool shapes at the nozzle location would prove if this suspicion is true.

It was furthermore observed that T_{nozzle} remains under the solvus temperature of AA6060 at $TG = 1.5$ $[mm]$, $\omega = 400$ $[rpm]$ at the lowest v_f values. Starting from the T6-state means that the resulting extrudate is suspected to be (heavily) overaged. If this is true, this means that a homogeneous state is not a strict requirement for FSE to process AA6060, but that overaged material (with generally decreased hardness) at elevated temperatures is suitable as well. If so, this would open doors for 'low temperature'-FSE(AM) with promises to be less energy demanding than the current process. Further research on microscopical and mechanical tests on that extrudate is advised to confirm if this.

T_{water}**:**
The results of T_{water} are influenced by the cooling water in the bulk tank warming up after series of experiments. Therefore, one must not rely closely on the height of the temperatures between tool gap series, but rather roughly on trends within experiments.

It is seen that the lower ω, the lower T_{water}, whilst experiments are performed chronologically the other way around (600 towards 400 $[rpm]$). This means that heating of bulk water is not a dominant factor.
The higher v_f, the less spread between ω changes for $TG = [1.5\ 2.5\ 3.5]$ $[mm]$ is seen. Also here, some 'likeliness of jamming'-factor seems to play a role. It can be seen that the steep increase in torque values (thus energy input) is a logical explanation.
The decreasing spread of data with increasing v_f and contradictory relations with T_{nozzle} & $T_{halfway}$ suggest that the height of T_{nozzle} is primarily determined by the time aluminium stays in the tool housing until a threshold of heat input due to high torque (and secondary the ω) near jamming is

passed.

M:
As the feed force is applied perpendicular on the tool surface, the friction between the feed and tool rotation could be simplified to basic Coulomb friction as a first start for further understanding. The Coulomb equation is shown in Equation 5:

$$F_{feed} = \mu_f \cdot F_T = \mu_f \cdot \frac{M}{r_{tool}} \tag{5}$$

in which F_{feed} relates to the tool torque M via the friction coefficient μ_f.

In correspondence with the basic Coulomb friction, M does not show clear dependence to TG for $\omega = 400$ $[rpm]$ in Figure 34 and shows linearly shaped increase with respect to v_f. As Equation 5 does not simply represent the relation between F_{feed} and M for higher ω (generally for higher relative velocity v_{rel} of processed material with respect to tool surface), a different friction relation than simply the Coulomb dynamic friction (slip based) is expected for these setup settings.

T_{water} is known to rise towards jamming, which corresponds with high M and high $\dot{E}_{tool}$ for the settings prone to jamming. This means that an exceptional amount of heat is put into the aluminium before jamming, possibly expanding the feed material in the feed tube too much to be processed by the feeding cylinder.

$\dot{E}_{tool}$:
A maximum plateau of $\dot{E}_{tool}$ at $\omega = 600$ $[rpm]$ seen in Figure 35 can be an evidence of the processed aluminium approaching (or even just exceeding) the solidus temperature locally at the tool interface due to conduction of heat to the rest of the material being not fast enough to dissipate it. The result is that viscosity (and thus heat generation due to friction) drop severely until the material is again sufficiently below the solidus temperature. In this way, the FSE-system shows 'self-balancing' behaviour.

Comparison with earlier FSE experiments

The results of above macro-analysis are compared to AA6060-T6 FSE-experiment results performed by Masselink (2021) [16] on the setup as shown in Figure 21. Masselink used: $TG = 4$ $[mm]$, $EG = 2.8$ $[mm]$ and the same windows of ω and v_f as in this thesis' FSE experiments. The following can be said from comparing the work:

- Sample appearances are similar with identification of the same extrusion defects.
- Masselink experienced jamming at the key 6 at $\omega = 400$ $[rpm]$, comparable to this thesis' experiments.
- The torque path within an experiment run is found to be similar: an initial peak followed by a more or less steady-state plateau. The torque values in Masselink's work are generally 10 $[Nm]$ lower than in this thesis' work. The slowing increase of torque over v_f when ω is increased is found similar.
- F_{feed} in this thesis' experiments was found to be higher at roughly 1 to 2.2 $[kN]$ with an increasing shape compared to values of 0.6 to 1.1 $[kN]$ with a general flatter shape at Masselink's experiments.
- T_{nozzle} is generally 150 $[°C]$ lower in Masselink's work and show much less increase over v_f. This can be explained by position of thermocouples as they are directly in contact with material in the modifies setup of this thesis, whilst Masselink's are placed not directly in contact and thus face a conductive thermal barrier. This applies in general for other thermocouple comparisons as well, although the differences in temperature values are less extreme.

In general, FSE experiment results show large overall similarities, but also significant differences in parameter data. This can be explained by slight differences in TG and EG geometry or by the setup being very sensitive to thermocouple placement. Besides, Masselink experienced severe wearing of tooling.
It can be concluded from this comparison that the FSE(AM) setup shows qualitative repeatability (although there are differences in used setup), but does not show acceptable quantitative repeatability yet. It is recommended to perform a repeatability analysis of the FSE experiments and improve the setup to increase this repeatability.

Tool Gap predictions in earlier theses

In Chapter 1, predictions on the effect of the tool gap parameter on other system parameters from earlier FSE(AM) master theses are presented.

To summarise, Masselink (2021) [16] states that tool gap is an important parameter that affects torque and F_{feed}. As TG increases, F_{feed} would decrease as it is easier to press material through a wider opening. As TG increases, torque would increase as well as more material is present around the rotating tool that must be turned around. Strik (2023) [17] does the same predictions based on the same argument.
Lind (2018) [13] states from a flow modelling analysis that an increasing TG would lead to higher F_n as material flow temperatures would be lower resulting in lower material viscosity.

From the results in Section 4.2, the torque was found to be indifferent to TG at $\omega = 400$ $[rpm]$ and showed to be decreasing with TG towards $\omega = 600$ $[rpm]$. F_{feed} was found indifferent to TG. This shows that simple flow reasoning as from Masselink and Strik does not hold in FSE(AM).
T_{nozzle} was found to be increasing in the results in Section 4.2, contrary to Lind's modelling results. Statements about F_n could not be judged because of load cell drift reasons as explained before.

Judging the cause of contradictory results from Lind's modelling is difficult, as his modelling approach uses several assumptions that are acceptable for programmability reasons, but deviate from reality. This holds for the assumption that strain hardening/softening effects are rejected in his model and that new feed material is introduced at the top of the tool in the flow direction of the tool housing (i.e. vertical direction) instead being fed horizontally as in the experimental setup.

The statements from Strik and Masselink seem to show oversimplifications, although based on empirical results. It is very likely that the differences seen between Masselinks experiments and the ones from this thesis originate from the end gap being variable with TG in Masselink's work and being fixed in this thesis. This means that the EG plays an important role in the final setup parameter values. It is therefore recommended to perform a systematic study to the EG parameter.
As the end gap was constant in the experiments from this thesis, it can be said (with caution on repeatability) that the results from this systematic parameter study can be interpreted more reliable when it comes to the influence of the tool gap.

Feed/tool-interface: volumetric displacement

To gain some more understanding on the aluminium material flow, the feed/tool-interface is looked at. A schematic drawing is presented in Figure 36 with relevant system parameters. To get an indication of the volumetric display the tool can handle ideally, a steady-state case with significant elevated temperatures for FSE processing (as seen during the experiments) is assumed. It is also assumed that the tool thread is the only transport mechanism. Furthermore, it is assumed that F_{feed} is high enough to press the feed material fully plastically into the M20 thread on the tool, so that the material can be sheared off and processed by the thread.

The amount of feed material that is provided is:

$$\dot{V}_{feed} = \pi R_{feed}^2 v_f \tag{6}$$

with $\dot{V}_{feed}$ being the volumetric supply rate of the feed material, R_{feed} the feed material radius and v_f the feed velocity. As $R_{feed} = 4$ $[mm]$ and v_f is in the range of circa [0.2 2.3] $[mm/s]$:

$$\dot{V}_{feed} = [10.1 \; to \; 115.6] \; [mm^3/s] \tag{7}$$

The volumetric rate transportable by the tool is determined with ISO 724 metric M20 thread standard dimensions. The situation from Figure 36 is considered with the simple ideal case of feed material being pressed fully plastically into the thread grooves. Then the aluminium is sheared off from the feed rod and transported downwards to the nozzle area. This means that the effective transport volume rate consists of one groove spinning round.

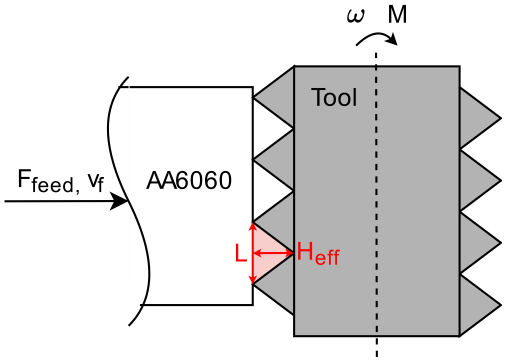

Figure 36: Schematic drawing of feed/tool interface with system parameters.

To determine this tool transport volume rate ($\dot{V}_{thread}$), the cross-sectional area A shaded in red in Figure 36 is considered. A triangular shape is taken with the properties from ISO 724 metric M20 thread (note that the figure is oversimplified compared ISO 724); thread angle $\alpha = 60°$, pitch $P = 2.5$ $[mm]$, thread height $H = \frac{1}{2}\sqrt{3}P$, effective height $H_{eff} = 3/4H$ and triangle base length $L = \frac{3}{2}tan(\frac{1}{2}\alpha)$. This results in:

$$A = \frac{9}{16} H_{eff}^2 tan(\frac{1}{2}\alpha) = 1.52 \; [mm^2] \tag{8}$$

Now determining the volumetric rate:

$$\dot{V}_{thread} = v_{tool,cyl} \cdot A = \sqrt{(2\pi R_{cyl})^2 + P^2} \cdot \omega \cdot A = [621 \; to \; 932] \; [mm^3/s] \tag{9}$$

in which $v_{tool,cyl}$ is the tool surface speed at the cylindrical part of the tool, R_{cyl} is the tool radius at the cylindrical part and the resulting value window of $\dot{V}_{thread}$ depends on the window of $\omega = [400 \; 600]$ $[rpm]$.

Considering the tip of the conical part of the tool (see Appendix C.2 for measurements) which has the least amount of thread volume in one revolution yields:

$$\dot{V}_{thread,end} = v_{tool,end} \cdot A = [226 \; to \; 339] \; [mm^3/s] \tag{10}$$

in which $v_{tool,end}$ is the tool surface speed at the tip of the conical part of the tool, R_{end} is the tool radius at the tip of the conical part.

It holds that $\dot{V}_{thread} > \dot{V}_{thread,end} >> \dot{V}_{feed}$, so the used tool is very well capable of processing the offered feed material in the full range of feed velocity under these assumptions. This is a logical result, as the opposite outcome would logically result in failure of the FSE(AM) process as feed material can then not be processed quick enough.

Stating that the tool thread is the only mechanism transporting the feed material would mean that the outflow velocity would be independent of the feed velocity. This would mean that when the feed cylinder stops providing material to the tool, the tool would continue extruding until all material volume is processed. Considering that in practise some material will be left in the housing, the extrusion would stop after a critical minimum amount of material is left in between the tool and its housing. Furthermore, this statement would mean that extrusion velocities are related to tool rotation

rate.
However, the opposite results of the statement are observed, namely that extrusion speed is fully depended on feed velocity and independent of tool rotation rate. This means that material processing is not fully performed by the rotating tool, but some other mechanism is responsible for material flow between tool and housing. This result corresponds with the conclusion of the raw data analysis.

The only other mechanism available for transporting material through the volume between the tool and its housing is the force provided by the feed cylinder, simply forcing the material through the tool housing regardless of the screw geometry. Stating that the feed cylinder is the only mechanism that forces the feed material through the tool housing volume makes the threads on the tool redundant for this usage, but solely useful for increased surface area for frictional heat supply.
It is known from experiments in the master thesis of Lind (2018) [13] that performing FSE experiments with a non-threaded conical section of the tool was impossible. From this, it can be concluded that both material processing mechanisms must be present in the FSE setup. The following conservation of mass equation must then hold:

$$\dot{V}_{feed} = n_{thread}\dot{V}_{thread} + n_{forced}\dot{V}_{forced} \tag{11}$$

$$with \quad n_{thread} < \frac{\dot{V}_{feed}}{\dot{V}_{thread}} \quad and \quad n_{forced} > 0$$

of which n_{thread} and n_{forced} are scaling factors determining how much the volumetric rate induced by either the thread or the feed cylinder is present. This equation can be used as a starting point for future FSE(AM) flow analyses.

Coupling to Flow Simulations by Masselink

In the master thesis performed by Masselink [16], extensive material flow modelling is performed, in which several advanced material flow models are compared to his experimental FSE results. A sketch of the flow model is presented in Figure 37. Key in his analysis is the significant influence of the factor δ used by Masselink to determine the amount of 'grip' that the rotating tool performs on the aluminium. $\delta = 1$ results in aluminium having the same velocity at the tool interface ($v_{Al} = v_{tool}$) and $\delta = 0$ results in no effect of v_{tool} onto v_{Al}.

Furthermore, additional step-functions are introduced into the used material models in order to be able to influence flow models to resemble Masselink's FSE results.

The modelling results show quantitative similarities to Masselink's FSE results but deviate qualitative regarding flow fields. Masselink concludes that more attention has to be paid to boundary conditions. His boundary condition for feed material is formulated such that his feed material is fed from a top inlet between the tool and tool housing with a material

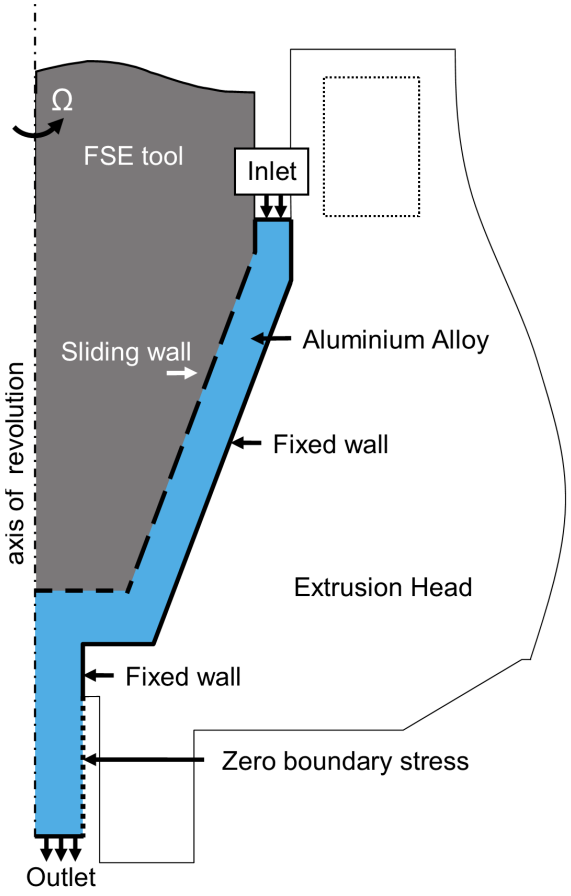

Figure 37: Sketch of the thermo-mechanical FSE flow model as presented by Masselink [16]

volume rate corresponding with FSE-experiments.
Analysing his results in the form of velocity, temperature, and pressure profiles learns:

- v_f is only defined at the inlet boundary location line without a driving pressure, which is present in the real setup. Furthermore, this boundary condition directly interferes with a boundary condition assigned to flow velocity on the aluminium-tool interface.
- v_f is not seen back in temperature profiles, which would be expected at the inlet boundary condition line as new material is colder than material already directly prone to heat input. Temperature of new material entering the area between tool and housing is not mentioned.
- F_{feed} could not be found as driving force or pressure behind v_f at the inlet boundary, which is found to be a key factor in determining outflow speeds. It seems that the mentioned pressure and temperature profiles are fully due to tool rotation.

Furthermore, this inlet boundary condition lacks the friction effect of F_{feed} on the rotating tool with a feed rod, which is suspected to provide a large part of the generated heat in the system. Jamming of the FSE setup during this thesis' experiments happened at the start of an experiment run, although the volume between tool and housing was fully filled with aluminium from an earlier experiment run. This means that the interface between feed rod and tool is dominant for inducing flow and thus for successful FSE(AM).

Comparing quantitative results of this thesis' to results from Masselink's is therefore not reliable without improving his model. An improved flow model could be made by changing the material feed boundary condition in Masselink's model to have the inlet from the side with additional friction effects, similar to real-life FSE experiments and considering implementing realistic F_{feed} and feed temperature (T_{feed}) as boundary conditions at the feed/tool-interface. Furthermore, Equation 11 can be considered for implementing the two identified material flow effects.

Using Masselink's flow model as a basis with the above-mentioned improvements would result in a promising more realistic and useful flow model.

5 Material Outflow Speed Variation

The goal of this chapter is to quantify and predict the inconsistent geometry seen in FSEAM experiments at lower table speeds [17,19] from experimental system data and to indicate how this behaviour relates to tool gap and tool rotation rate settings. This new knowledge will open doors for better volumetric supply control which will increase FSEAM product quality.

To do so, a method is presented and performed to extract this behaviour from experimental FSE data. Furthermore, the results are coupled to the parameter analysis results, to earlier research and to literature to better understand the results.

5.1 Brief Method Description

The following method is be applied to reach the goal of this chapter. More details will be provided along the presentation of the results in Section 5.2 were needed for better understanding. A schematic flow chart is presented in Figure 38 to help understand the method structure described below.

- To give a first rough quantitative indication of material output variation, the order of magnitude of the geometrical variation frequency is determined by **manually counting** the number of geometrical 'waves' in an available FSEAM print that clearly shows varying outflow speed.
- As described in Chapter 4, **video recordings** of the extrudate were made during experiments.
- In MATLAB, the *estimateFlow* function was used with the Farneback method to **extract video velocity data** from the video frames. To obtain reliable data, the following aspects were applied:
  - *Noise reduction*: velocity data 'back ground' noise was observed. After analysis, a threshold value of 0.2 [pixels/frame] was determined for the absolute pixel velocity. Values under the threshold were rejected and above were allocated to the moving extrudate.
  - *Memory management*: Flow data is determined for all pixels for every video frame, which causes memory storage issues. Therefore, a Region of Interest (RoI) is selected within the video frames. Besides, resulting velocity data per pixel is stored as a mean value per frame. This results per video frame in an average absolute flow velocity value (V) with velocity direction (φ) and components in vertical (or extrusion) direction (V_y) and in horizontal direction (V_x) .
- In MATLAB, the system data from the FSE setup and the optical flow data results were combined for **visual data analysis**. The data was plotted and inspected in a time window of 30 seconds from experiment run 2TG3.5_400_2 with known significant variation as visually seen in the video recording. Basic analysis tools (like FFT) were applied to find relations between the different data flows.
- **Correlation analysis** based on the Pearson correlation coefficient was applied on the last halve of an experiment run to identify linear correlation between data of one F_n load cell (F_2) and V_y. Time window steps of 5 seconds had to be used used to omit the effects of load cell drift. Results were visually compared to the video recordings. Important applied intermediate steps are:
  - Cross-correlation was applied using MATLAB function *xcorr* to obtain the data lag resulting in optimal linear correlation (non-normalized). This lag value is used to align the two data flows per time window step using function *circshift*.
  - The MATLAB function *corrcoef* is used to determine the Pearson correlation coefficient between the two aligned data flows per time window step. The median value from the different window steps per experiment run r_{med} was taken as the final value to discriminate outliers.

- A **severity analysis** is performed to try to quantify the severity of V_y variation related to F_2 variation on system settings found to be prone to severe material outflow speed variation. This is based on ratios between the standard deviations and/or coefficient of variation of F_2 and V_y data determined as by-product in the correlation analysis.

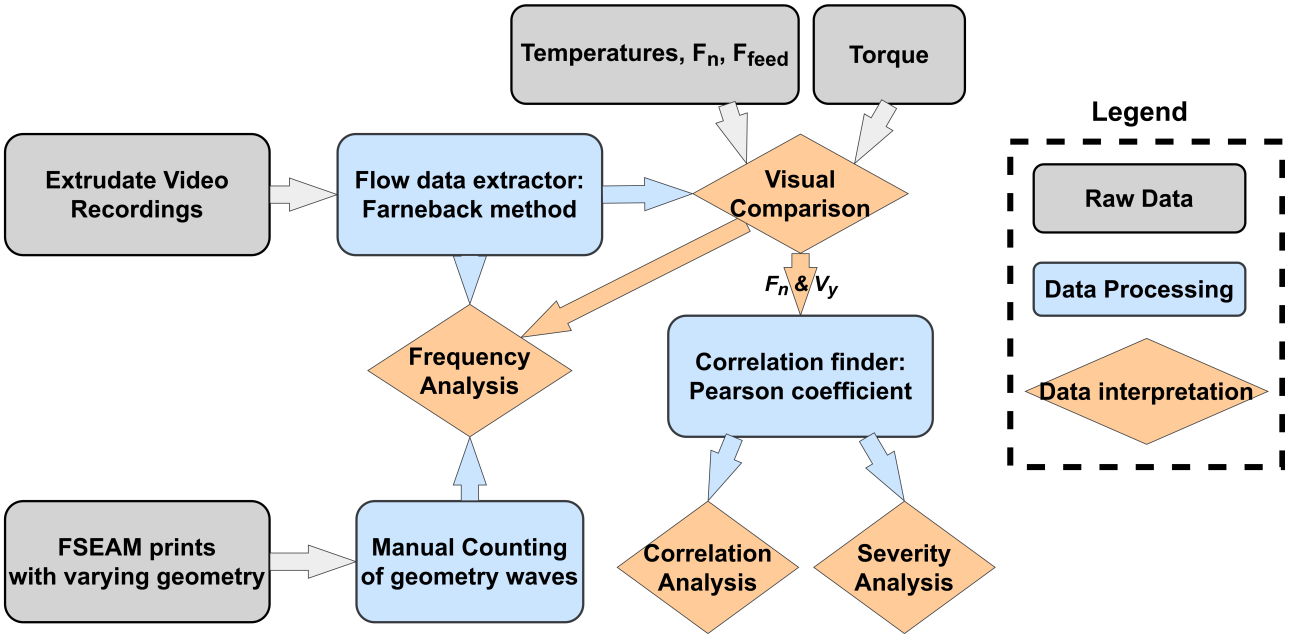

Figure 38: Schematic flow chart of the applied method used in Section 5

5.2 Results

In the following section, the results of the described method are presented along with methodical details were beneficial for better understanding of the results.

5.2.1 Manual Counting

To obtain a first quantification at which geometrical variation occurs, remains from an FSEAM print from earlier research [15, 17] are visually inspected. The print remains used are shown in Figure 39 and are made with a table speed (v_t) of 100 $[mm/min]$ (which corresponds with a feed velocity (v_f) of 0.453 $[mm/s]$) a tool gap (TG) of 3.2 $[mm]$ and a tool rotation rate (ω) of 400 $[rpm]$ [17].
The considered area for counting the variations over the printing layers is indicated in red in Figure 39.b. The green area is omitted as the printing table was stationary there. The distance between the two red lines is 60 $[mm]$. Additionally, the surface of the sawed side of the print is shown in Figure 40 with a red dashed centre line.

The following observations can be made in Figure 39:

- Geometric variations can be clearly seen in the form of waves. This suggests periodical behaviour, although the wave length is not constant.
- 2 to 5 wave bulges per printing layer can be observed.
- A varying amplitude per printing layer can be observed: hardly visible small bulges up to relatively large clear bulges.
- Bulges can be clustered on multi-layer level up to circa 5 printed layers. A likely cause would be that excess material would plastically deform previously printed layers, bulging them further out of plane.

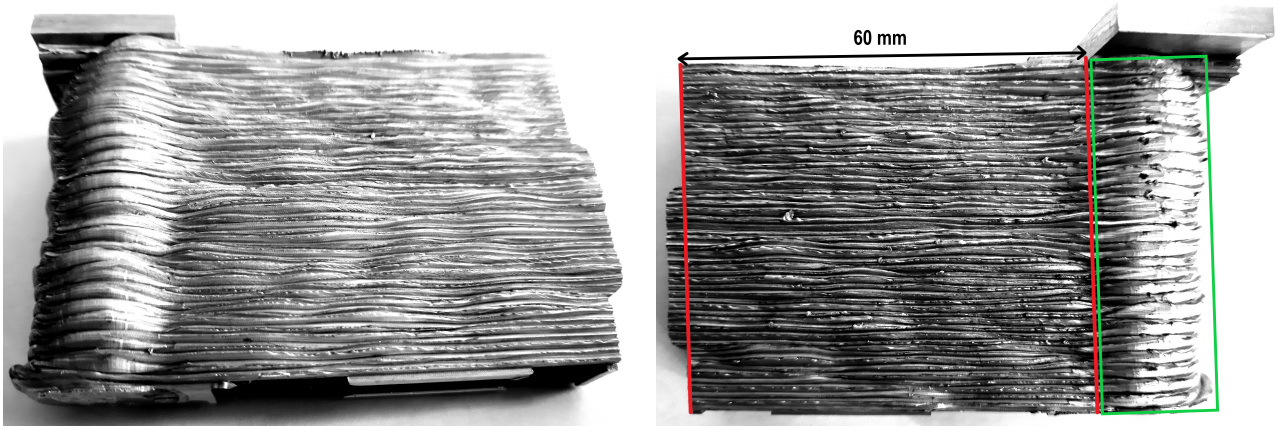

39.a. Front **39.b.** Back

Figure 39: FSEAM print with typical 'waviness' made with table speed of 100mm/min [15]

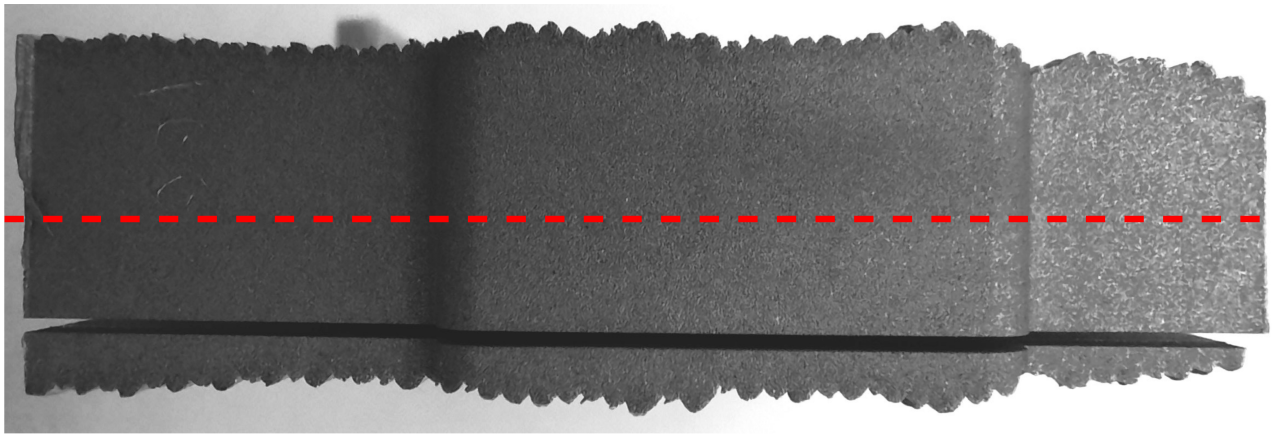

Figure 40: View of sawed edge of FSEAM print of Figure 39 with symmetry indication line

- Additionally, it can be seen from the red centre-line in Figure 40 that waves occur in a symmetric way on both outer sides of the surface.

Knowing the number of wavy bulges occurring per printing layer at a known table velocity gives a rough indication of the frequency at which this behaviour occurs. Using the following equation yields:

$$f_{wave} = \frac{v_t \cdot N}{L} = 0.05556 \; till \; 0.1389 \; [Hz] \tag{12}$$

in which $v_t = 100$ $[mm/min]$, N is the number of counted waves in a printed line from 2 to 5 and L is the length of 60 $[mm]$ between the two red lines.

To conclude: a first frequency indication of varying material outflow speed lays in the order of magnitude of 0.1 Hz.

5.2.2 Video Recording Results

The extrudates of all experiment runs are successfully video recorded. An example of a typical video frame is shown in Figure 41. It can be seen in the figure that the extrudate is filmed in the support as shown in Figure 63.a (Appendix D) between the top two bearing pairs. The markings on the rotating bearings can be used for rough extrusion speed reference. As the extrudate would often temporarily slip along the bearings instead of rotating them, the rotary bearing movement is not suitable for detailed velocity extraction. The RoI used for video velocity extraction in MATLAB is indicated by the red rectangle.

5.2.3 Extracting Video Velocity Data

To extract the extrusion velocity from the video recordings, the Farneback optical flow method is used from MATLAB Computer Vision toolbox, that determines the velocity of each pixel between two adjacent video frames. The Farneback optical flow algorithm has the following characteristics [51] important for interpreting the results:

- A quadratic polynomial approximation of the pixel intensity (i.e. pixel brightness in grey-scale) field variations over the neighbourhood of each pixel is applied.
- Iteratively applying a finer grid over the video frame enables the algorithm to handle larger displacements.
- Multiple iterations are used with a feedback loop to compensate for parasitic background motion of the recording device.
- The algorithm uses the assumption that changes in the displacement field over the stated neighbourhood around a pixel are small. This makes the algorithm less suitable for videos with sharp velocity changes within a video frame. This is not expected to cause problems in this specific application.
- Points in the neighbourhood of evaluated pixels are weighed on the basis of 'certainty', which is coupled to pixel intensity values in the neighbourhood, and on 'applicability', which is the relative weight of points in the neighbourhood based on their position (e.g. points outside of the video frame are not applicable).

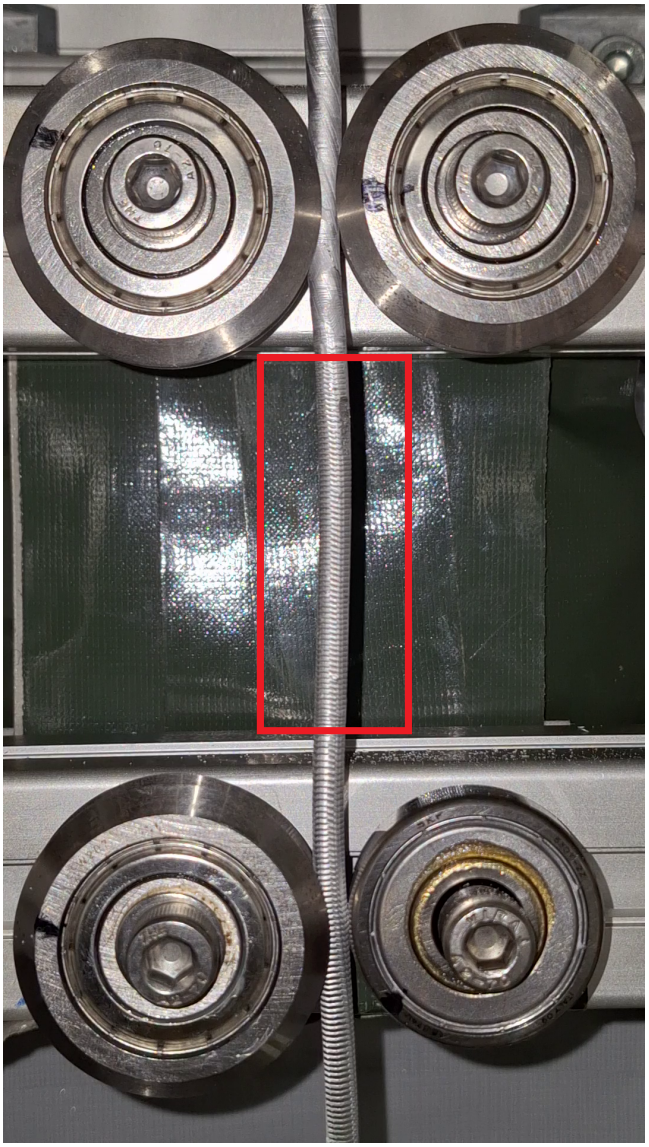

Figure 41: Typical raw input video frame with Region of Interest (ROI) indicated in red rectangle. Note the helical rings on the extrudate surface. 2TG3.5_400_x.

Although more computationally expensive, it was chosen to apply algorithm settings with higher precision than default for this MATLAB analysis to obtain very detailed results. The specific syntax with parameter settings used in MATLAB is:

opticalFlowFarneback('NumPyramidLevels',5,'NeighborhoodSize',7,'NumIterations',5,'FilterSize',30)

For the MATLAB function *estimateFlow*, also the Hurn-Schunck method, the Lucas-Kanade method and the Lucas-Kanade derivative of the Gaussian method were available to calculate optical flow data. Comparing the available information in the MATLAB software documentation presenting dummy results, observing that the Farneback method is the only method in MATLAB that provides a multi-level grid calculation 'resolution pyramid' for enhanced accuracy and taking into consideration an extensive numerical fluid mechanics comparison study for the mentioned methods [52], the Farneback method was chosen to be used in the *estimateFlow* function in this analysis.

Typical results for the velocity in extrusion direction (V_y) are displayed per key setting in Figure 42. V_y-figures of the other experiments are presented in Appendix F.

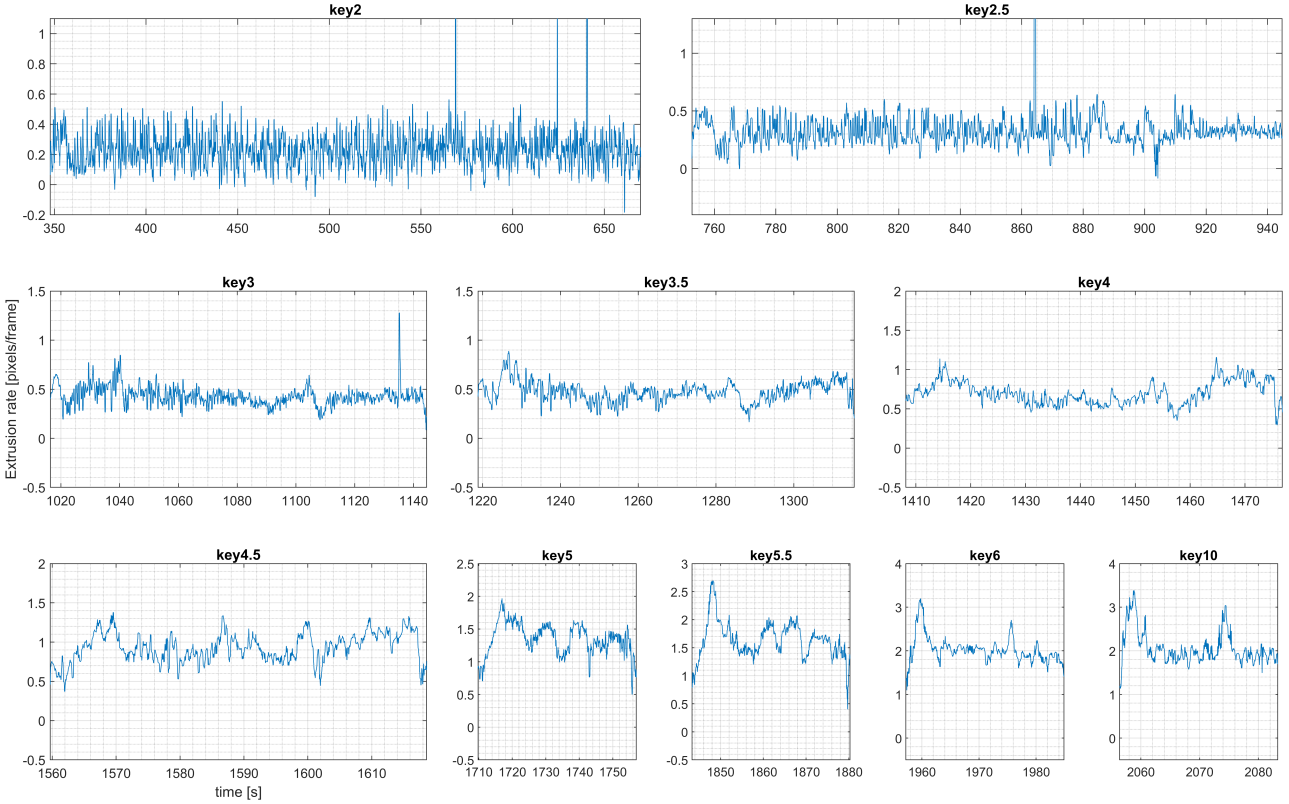

Figure 42: Typical extrusion speed in y-direction V_y after using *smoothdata* function in Matlab, cut per key: 2TG4.5mm_400rpm_x

Typical features seen for all experiments in these figures are:

- The average velocity increases with increasing feed rate. Which is very logical and corresponds with visual inspection of the recorded videos.
- Micro-variations can be seen for all feed rates. These variations seem increasingly severe (i.e. percentage of the mean velocity) for lower feed rates.
- For higher feed rates, a peak at the start of the experiment run is visible. Also a peak at about three-quarters of the experiment run duration can be found at the point where the first full feed rod is completely processed and the remaining half feed rod is introduced in the machine. In both cases, the temperature of the feed material at the start of processing a feed rod is very likely not sufficient enough (thus too high viscosity) to be processed by the rotating tool. Similar peak characteristics can be found in F_{feed} and torque data, although time lag between them can not be evaluated due to lack of a time stamp in the different data recording devices.
- Irrespective of characteristic peaks at higher feed rates and micro-variations, the velocity is roughly constant. This corresponds with the recorded videos.

Three characteristics in Figure 42 that seem contradictory, but which can be generally found across the experiments, are:

- Negative velocity values, which are not seen in the recorded videos. This could be noise or some peculiarity from the algorithm. This was not further analysed as it did not significantly influence further results.
- Videos with flow vectors that indicate faulty results at the edge of the video frame due to the present repetitive rings at the surface of the extrudate as for example seen in Figure 41. The

algorithm very occasionally confuses rings at the bottom edge of the video frame with each other which results locally in higher velocity.

- Subpixel accuracy can be seen, whilst a video frame consists of discrete pixels. This is possible because the Farneback optical flow method uses a quadratic polynomial approach of the intensity field of pixels in a video frame. Furthermore, it is possible due to Gaussian filtering over pixel neighbourhood and polynomial expansion used in the Farneback algorithm. [51]

In order to capture any periodic behaviour of the extrusion speed, a Fast Fourier Transform (FFT) analysis was performed on all experiments on V_x and V_y data with MATLAB function *fft*.
An example of the FFT analysis of V_y is presented for 2TG3.5_400_2 in Figure 43. It is known from video observation that extrusion speed variation was severe at this specific experiment. Two particularities from the figure are worth mentioning:

- At the tool rotation rate of $\omega = 400$ $[rpm]$ ($f_{tool} = \frac{400}{60} = 6.67$ $[Hz]$), a peak can be found. In all FFT graphs, this tool rotation rate peak was found increasing with feed rate, which corresponds with video observations. This effect was especially strong in V_x data as tool rotation made the extrudate vibrate slightly in the horizontal plane.

- Slight low-frequency activity can be found in the window of [0 1] Hz. This effect is less present for experiment runs in which variation could not be observed from the video analysis.

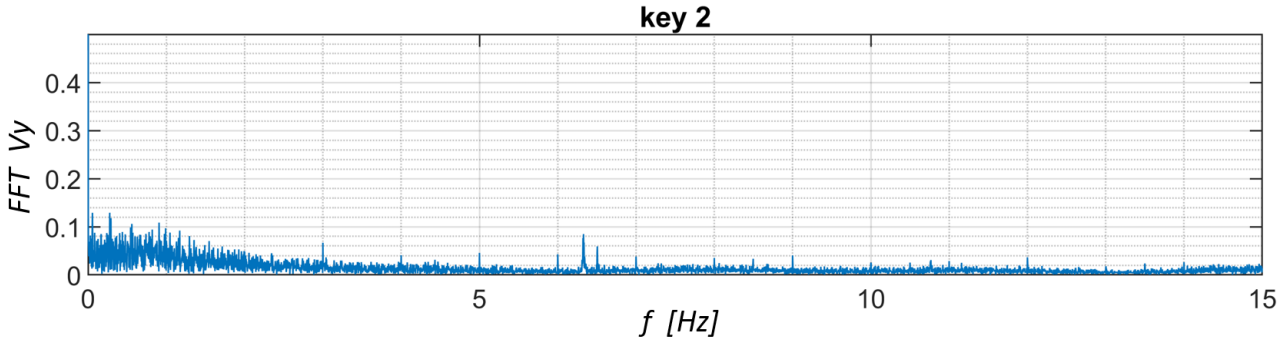

Figure 43: Fast Fourier Transform (FFT) analysis of V_y normalised to $f = 0$ $[Hz]$ (average velocity): 2TG3.5_400_2

5.2.4 Visual Data Comparison

Analysis of V_y data on macro-level (time window of a full experiment run) did not give much information about the observed extrusion velocity variations. To try to gain more understanding, comparison of all available data flows is performed on meso- (time window of circa 5 seconds) and micro-level (time window under 1 second) on a small piece of data from 2TG3.5_400_2.
Clear severe extrusion speed variation could be observed in the recorded video in the time domain $t = [530\ 560]$ $[s]$, thus $dt = 30$ $[s]$. Comparable settings also gave wavy geometry in recent FSEAM printing research [17] (Figure 39). Therefore, this piece of data was chosen to visually compare on this fine level.

The video was visually analysed in this time frame and extrusion speed variations were counted. It was observed that the extrudate tends to move in a faltering manner with at some points hardly any movement. The amount of variations was observed to be $N = 20$, which corresponds with a frequency of $f_{vid} = \frac{N}{dt} = \frac{20}{30} = 0.67$ $[Hz]$.

In Figure 44, all available data flows are presented for the mentioned time frame. All data flows are time-aligned to the video time, i.e. the time scale of V_x and V_y. For the normal force data, the load cell F_2 was chosen as this load cell seemed to have the lowest noise from the three load cells. $T_{halfway}$ is omitted as this data flow is less relevant for temperature tracking than the presented T_{nozzle} as

discussed in Chapter 4.

V_x was found to be only present at points with a significant V_y value from video observation. It can be seen that V_x shows circa 5.5 periodic amplitude increases with a corresponding frequency of $f_{Vx} = 0.18\ [Hz]$, which is within the order of magnitude of the manual counting of the waviness in the FSEAM print.

Counting the variations V_y data gives the same frequency result as f_{vid}. The amount of variations in F_2 data corresponds as well.

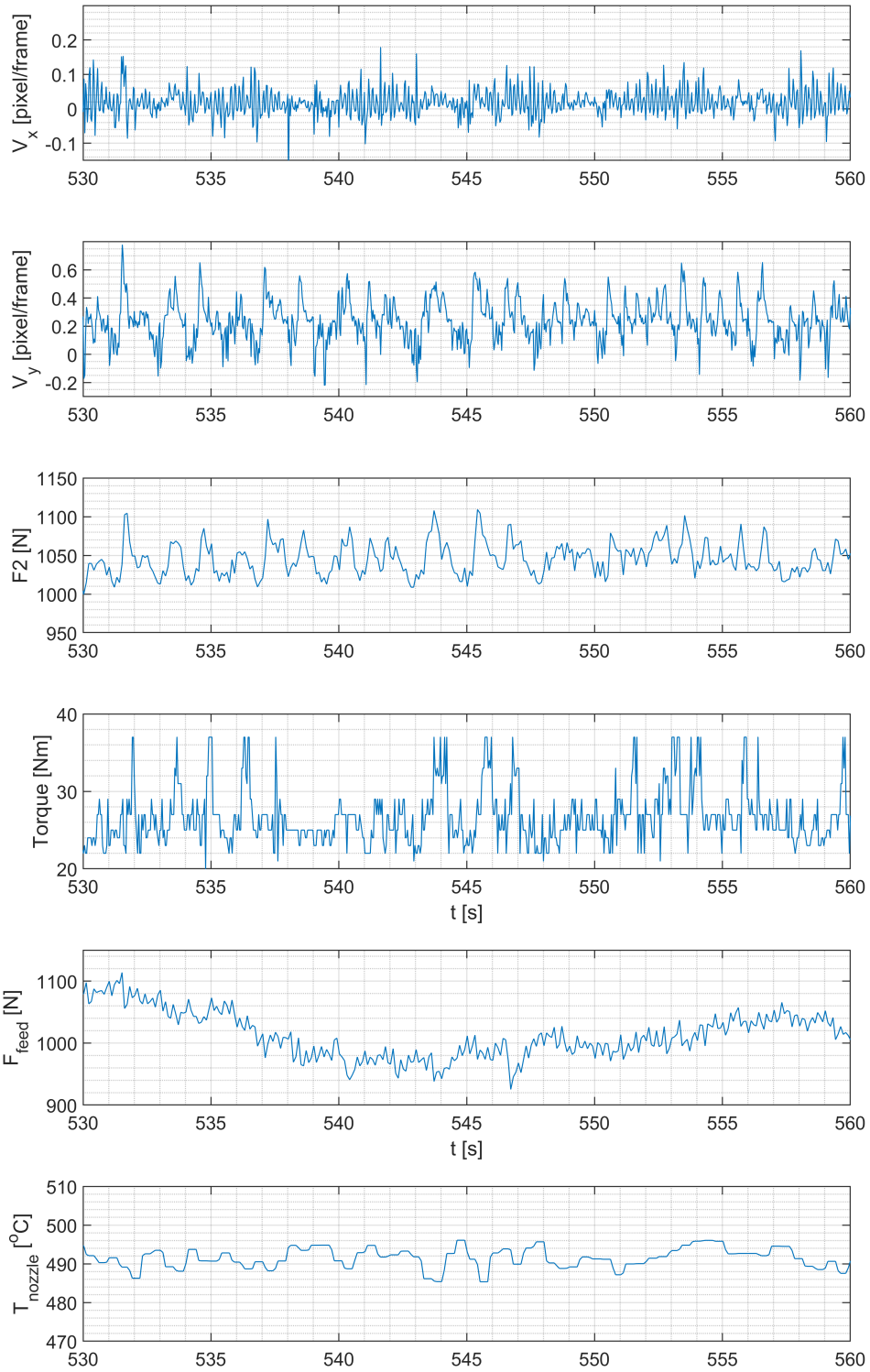

Figure 44: 2TG3.5_400_2 data flows in 30 $[s]$ time frame with known severe V_y-variation

Figure 45: F_2 and V_y data from Figure 44 scaled and plotted over eachother.

It is clear that the data flows of V_y, F_2 and torque show great similarity in micro-variation. Laying F_2 and V_y data over each other gives a high degree of similarity as shown in Figure 45. Note that the difference in data recording frequency (30 $[Hz]$ for V_y and 10 $[Hz]$ for F_2) can be seen clearly in Figure 45 as V_y shows a much higher resolution than F_2. This suspected correlation is used for further correlation analysis as worked out in the next section. Torque data seems to show similarity as well, but not as clean as between V_y and F_2. This could be due to the cumbersome torque retrieving method.

The remaining parameters from Figure 44 do not show this clear similarity in micro-variations and are therefore omitted for correlation analysis.

A Fast Fourier Transform analysis is performed in MATLAB on V_y and F_2 on the presented time window to find any periodical behaviour. No clear peak could be identified in the frequency domain, but only a wide spread of low-frequency behaviour. This means that the variations shown do not obey to a periodical effect with a fixed frequency.

F_{feed} and F_2 data show different characteristics in micro- and meso-variations, whilst both data flows are logically directly influenced by each other. This means that the variations in F_2 is not caused by variations in F_{feed} and must thus be found in the aluminium flow behaviour inside the tool housing.

5.2.5 Correlation & Severity Analysis

In search for correlation, a simple but effective tool is the Pearson correlation coefficient, which is available with the function *corrcoef* in MATLAB. The Pearson correlation coefficient indicates a linear correlation between two data sets [53]. It displays a value between -1 and 1 with 0 meaning no correlation, 1 meaning full positive linear correlation and -1 meaning full negative linear correlation. For this analysis, a Pearson correlation coefficient above 0.6 is seen as a significant good correlation [53].

The analysis is performed on data of F_2 and V_y. Note that the Pearson correlation coefficient can never be 1 in this case, due to the difference in data retrieving frequency (10 and 30 fps respectively) between the two data flows. The F_2 data needed to be interpolated linearly to provide a similar number of data points with V_y for the correlation analysis.
The torque data is left out of scope of this correlation analysis as the data retrieving method of the torque is seen as not robust enough for micro-variation analysis, because of the heavy noise-reduction post-processing and the cumbersome data retrieving method as explained in Chapter 4.

The mathematical equation to calculate the Pearson correlation coefficient is displayed below [54]. In essence, it is the covariance between two data sets divided by the product of the standard deviations of both data sets:

$$r(V_y, F_2) = \frac{\sum_i (V_{yi} - \bar{V}_y)(F_{2i} - \bar{F}_2)}{\sqrt{\sum_i (V_{yi} - \bar{V}_y)^2} \sqrt{\sum_i (F_{2i} - \bar{F}_2)^2}} \tag{13}$$

in which the index i goes over all data points in the available time window.

The parameter r is calculated for all time window steps of 5 seconds for all experiment runs. The median per experiment run was taken as the final r-value for an experiment run to discriminate outlying values. This r_{med} is taken as the final indication of correlation between F_2 and V_y for that specific experiment run.
Besides the r_{med}-value, the standard deviations of F_2 (σ_{F2}) and V_y (σ_{Vy}) and the coefficient of variation of V_y (CV_{Vy}) were calculated per time window frame as a by-product. The average for these values was taken over the time window frames as these values are a property of the individual data sets and not of the relation between the two.

To try to quantify the **severity** of the extrusion speed variation, two parameters are constructed from σ_{F2}, σ_{Vy} and CV_{Vy} and proposed below:

The ratio between the standard deviations of V_y and F_2 is taken to quantify the amplification between variation in the normal force and extrusion speed:

$$n_{std} = \frac{\bar{\sigma}_{Vy}}{\bar{\sigma}_{F2}} \tag{14}$$

in which $\bar{\sigma}_{Vy}$ is the mean standard deviation of V_y of an experiment run, subsequently $\bar{\sigma}_{F2}$ for F_2.

The average coefficient of variation of V_y and of the standard deviation of F_2 is taken for an experiment run. Doing so, the severity of variation in V_y (dimensionless ratio) due to variation in F_2 can be determined:

$$n_{cv} = \frac{\bar{CV}_{Vy}}{\bar{\sigma}_{F2}} = \frac{(\frac{\bar{\sigma}_{Vy}}{\bar{V}_y})}{\bar{\sigma}_{F2}} \tag{15}$$

The difference between n_{std} and n_{cv} is that the first provides a degree of direct amplification between variations in V_y caused by variations in F_2 and the second provides a degree of severity amplification of severity of variations in V_y caused by variations in F_2.

The correlation method is applied on all experiment runs mentioned in Table 3 whilst parallel visually analysing the recorded videos for validation of the results. This yields that three experiment runs show $r_{med} > 0.6$, meaning a reliable correlation between F_2 and V_y. The correlation and severity parameter results from these experiment runs are presented in Table 4:

Table 4: Significant correlation results

TG [mm]	2.5			3.5		
Key	r_{med}	n_{cv}	n_{std}	r_{med}	n_{cv}	n_{std}
2	-	-	-	0.72	0.035	0.0094
2.5	0.63	0.019	0.0056	0.68	0.026	0.0097

The following can be stated from the MATLAB process and the results in Table 4.

- High r_{med}-values only occur at low key settings at intermediate tool gap settings at a tool rotation rate of 400 [rpm]. These settings are so far most used during FSEAM experiments [19].
- The corresponding videos were visually inspected parallel to running the MATLAB script for each experiment run. Significant variations in V_y were visually only observed for the FSE-settings with $r_{med} > 0.6$ as presented in Table 4.

- Looking at $TG = 3.5$ $[mm]$, it seems that n_{cv} decreases whilst n_{std} stays roughly constant. This would indicate that the severity of speed variation decreases for higher key settings, whilst the amplitude ratio between the variation of V_y and F_2 would remain the same. More experiments and elaborate analyses are needed to confirm this and to provide reference to which n_{std} and n_{cv} can be judged, as this is now lacking and only relative changes can be interpreted.
- Looking at $Key = 2.5$, it seems that n_{cv} and n_{std} both decrease with decreasing tool gap. This would mean that the variations in F_2 amplify less variation in V_y and cause less severe V_y variation over decreasing tool gap. Also here, more experiments and elaborate analyses is needed to confirm this.

In order to put the results of Table 4 in perspective to the other experiment runs, contour maps are made and presented in Figure 46 and 47. Note that the heat maps are only a visual guide and that colour interpolation between the plotted data points must not be treated as such.
Only contour maps for $\omega = 400$ $[rpm]$ are presented as this is the only tool rotation rate yielding significant correlation. Contour maps for 500 and 600 $[rpm]$ can be found in Appendix G.

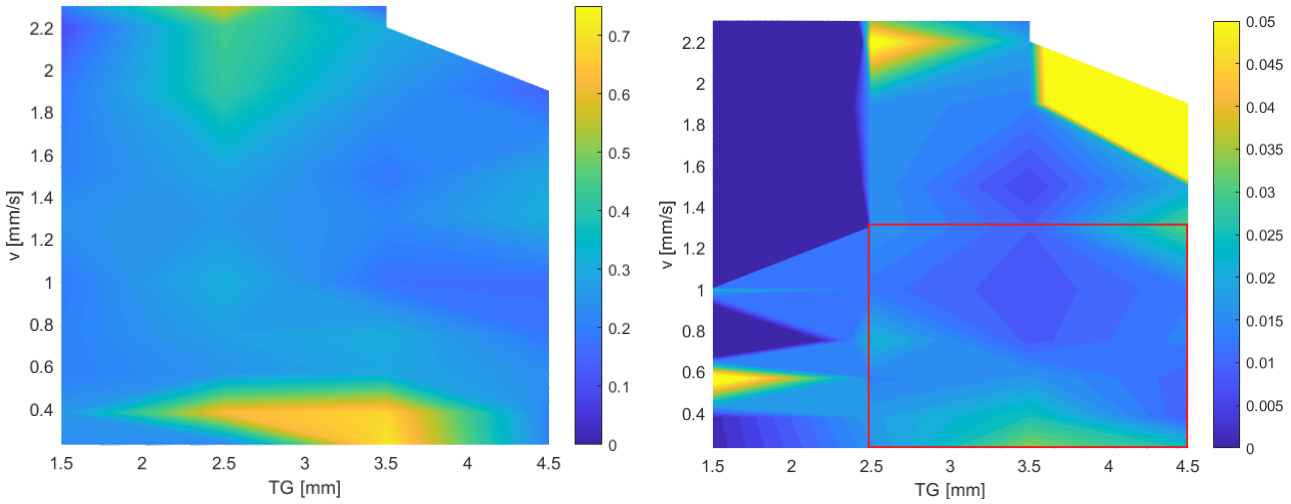

46.a. Correlation coefficient r_{med}

46.b. Severity ratio n_{cv}

Figure 46: Correlation & severity analysis contour maps at 400rpm. The red rectangle indicating the region with most reliable data.

The r_{med} values at 400 $[rpm]$ are presented in Figure 46.a. The extrusion velocity v on the y-axis for all contour maps is taken from the average feed velocity values from experiment 2TG3.5_400_x for programmability reasons in MATLAB. This indices a small error on the y-axis as the feed velocities are not exactly the same for all experiment runs although performed at the same key settings, but this does not disturb the contour maps in a qualitative way. Note that data lacks in the top right corner due to jamming at these system settings.

It can be seen that the correlation coefficients from Table 4 lighten clearly from the surrounding area. The remaining area of the contour map remains more or less between r_{med}-values of 0.2 and 0.3, meaning no significant correlation [53]. Also for 500 and 600 $[rpm]$, the contour maps in Appendix G show no significant correlation with all r_{med} values remaining between 0.2 and 0.3 with occasionally local maxima around 0.45 at the highest key settings.

At the highest feed velocity values at $TG = 2.5$ $[mm]$, an increased r_{med}-value of 0.59 can be noted. However, this can be named a peculiarity after manual inspection of the r_{med}-values of all time video windows of this experiment, due to excessive lag shift differences in the cross-correlation step (see method) between subsequent time windows within the same experiment run. Additionally, the low number of time windows available at these higher speeds does not provide enough reference to judge

the different lag shifts from this cross-correlation step.

Expanding this manual inspection of r_{med}-value and lag data to more experiment runs shows that, in general, results at higher extrusion speed values are increasingly noisy due to this excessive lag shifts and low number of window steps. This typically starts to occurs at $v > 1.3$ $[mm/s]$ corresponding to $Key > 4.5$.

The contour map of n_{cv} in Figure 46.b. seems chaotic and inconsistent at first glance. This means that either this n_{cv} is not reliable when calculated as byproduct from the correlation analysis using time windows in this order of magnitude, or that the data contains a lot of noise.
Ignoring the noisy data of $TG = 1.5$ $[mm]$ and $v > 1.3$ $[mm/s]$ shows an area (indicated in red) of n_{cv} being roughly constant at 0.015 with a small area lightning up to roughly 0.035 at the settings showing highest r_{med} values according to Table 4 and Figure 46. The n_{cv} can therefore carefully be seen as a promising value to eventually be used for indicating severity of V_y variation due to variation in F_2, but further research is needed to confirm this.

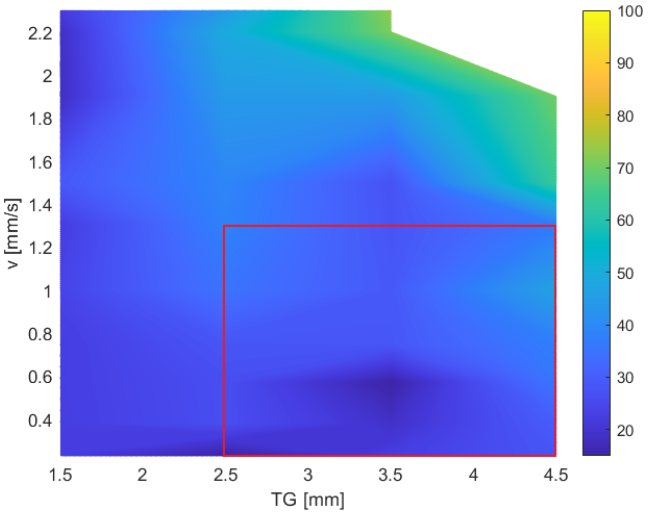

Figure 47: Severity analysis contour map: σ_{F2} @ 400rpm. The red rectangle indicated the region with most reliable data.

Values of n_{std} were found to be roughly constant over the whole domains of ω and TG, which suggests a direct relation between variations in V_y to variations in F_2. The correlation graphs are further omitted as these provide no further information. They can be found in Appendix G.

It would be interesting to search for trends in system data for the case when no video data is available to perform correlation analysis with as in FSEAM. Therefore, the contour map of σ_{F2} at $\omega = 400$ $[rpm]$ is presented in Figure 47. Note the red rectangle that indicates the most reliable data as explained above. Presenting a contour map for the coefficient of variation of F_2 is not possible due to drift problems explained in Chapter 4.

It can be seen that σ_{F2}-values show a minimum in the area where significant correlation is found. This is contradictory to what would be expected from this area that shows the highest variation in V_y from visual video analysis.
Furthermore, higher standard deviation values are found towards the settings prone to jamming around the top right corner of Figure 47. This would suggest again that some 'likeliness to jamming'-factor is present in system parameter behaviour.

5.3 Discussion

Below, a discussion is presented to improve understanding of the results and to provide context. At first, the results are discussed according to the section structure as presented above. Then, couplings are made to earlier research and to literature.

Visual Data Comparison

The torque data was find to be not clean enough for correlation analysis. This is very likely due to its cumbersome retrieving method of video recording the display screen on the Waldrich-Coborg machine control panel and than retrieving the numbers from video analysis in MATLAB. However, it is found promising to show similar correlation with F_2 and V_y as could be seen in Figure 44.
This means that V_y can be omitted for indicating varying outflow velocity if correlation of torque data shows indeed the same level of correlation. The developed correlation analysis method can then be applied in FSEAM data as well, as video recording outflowing material is not possible there.

Evaluation of Correlation & Severity analysis

It was seen in Figure 46.a in combination with visual video analysis that the parameter r_{med} works as a good indicator of significant extrusion speed variation. In the case when torque data can be used for identifying correlation, an advanced application would be to implement the r_{med} parameter directly in the LabView data acquisition programme. Varying material outflow speed could then be detected live during FSEAM experiments and the operators could be warned.
It is necessary that torque data is retrieved directly from the electric motor to realise the necessary data accuracy. Alternative wiring and a data converter are already available to be installed in the FSE(AM) setup so that torque data can be read from the LabView programme.

It was shown in Figure 47 that a region of minimal σ_{F2} was found in the region with maximum r_{med}. This is contrary to expectations, as significant varying V_y is highly likely to lead to significant varying F_2. An explanation would be that the some 'likeliness of jamming'-factor introduces extra variation in the normal force data. It must be kept in mind here as well that σ_{F2} is determined as a byproduct in the correlation analysis with a relative large time window for higher values of v, which is not optimal as explained before. It could well be the case that the area with minimal σ_{F2} is just a random event. A repeatability analysis is recommended to prove if this is indeed the case.
A better method for retrieving σ_{F2}, σ_{Vy} and CV_{Vy} would be to use MATLAB functions like *movmean* and *movstd* in an analysis separate from the correlation analysis to determine these values more precisely with a moving average window.

Coupling to Macro-Analysis

No outstanding data points were found in the macro-analysis in Chapter 4 that could identify occurrence of varying outflow speed at specific system settings.

The experiment runs that show the highest r_{med} values were found to have clearly the lowest $\dot{E}_{tool}$ values. However, experiment runs that do not show varying outflow speed whilst having the same ω, but a different TG also show these lowest $\dot{E}_{tool}$ values.

A recommendation would be to lower the ω domain in the experiment window as varying extrusion speed was only found at $\omega = 400$ $[rpm]$. Lowering to 300 or 350 $[rpm]$ would give more insight to the shift of varying extrusion speed towards other values of v_f and TG. This new information would help judging future flow modelling efforts.

Coupling to Earlier Research

F_n data from FSEAM prints made by Strik (2023) [17] is presented in Figure 48. The x-axis shows the travel of the printing table and the y-axis shows the height of the prints. This results in a heat map displaying F_n data for all 50 printed layers. The print from the left figure (experiment E1) was prone to severe geometrical waves, the right (experiment E2) was not.

The prints were made with $TG = 3.2$ $[mm]$, $EG = 2.8$ $[mm]$, $\omega = 400$ $[rpm]$ and with $v_f = 0.453$ $[mm/s]$ for E1 (between key 2.5 and 3) and $v_f = 0.685$ $[mm/s]$ for E2 (between key 3 and 3.5).

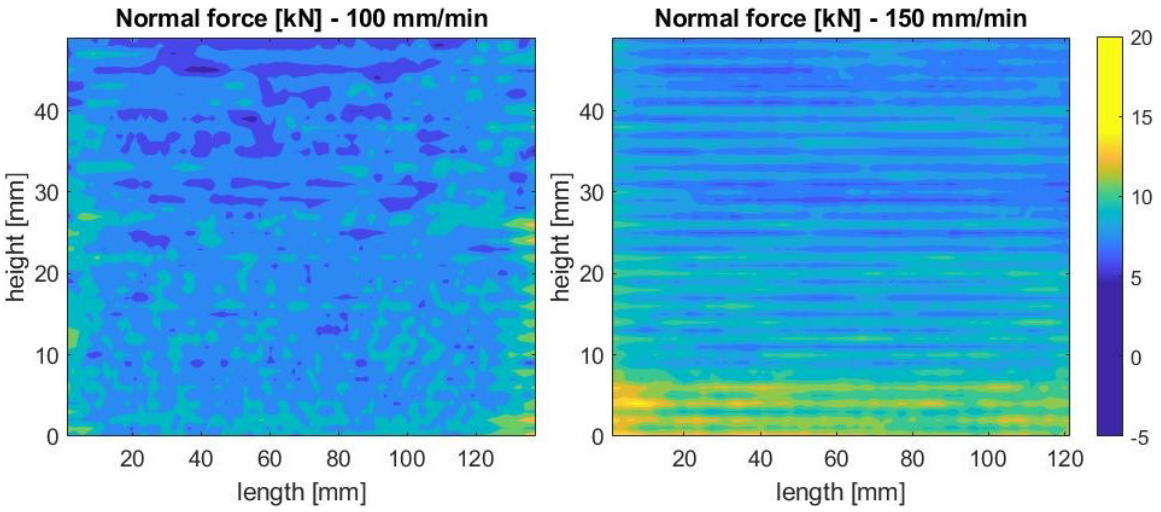

Figure 48: F_n results from FSEAM prints as presented by Strik (2023) [17]. Printing table velocity (length direction) shown in the titles.

The varying material outflow speed corresponds roughly with the r_{med} results found in Figure 46.a with E1 laying on the edge of the significant correlation domain and E2 laying out of it.

It can be clearly seen that the normal force profile through the print is much more irregular for E1 (left) compared with E2 (right). A similar irregular F_n profile was also found in the work of Ariës (2021) [14] of an FSEAM print that shows irregular geometry made with comparable system settings as Strik.
It would be of added value to geometrically scan the outside of print E1 and compare it to the F_n data to find any correlation. It can also be compared to the torque data. It is recommended for further research to add such geometrical data in the developed correlation analysis method.

FSEAM experiments with increasing printing table velocity (v_t) to print height performed by Bor (2023) [19] with the same setup settings as Strik shows that geometrical variation is present in the printing table velocity domain of $v_t = [50\ 150]$ $[mm/s]$. The variation effect reduces from $v_t = 125$ $[mm/s]$ towards the upper domain bound and is absent from $v_t > 150$ $[mm/s]$ onwards. This also corresponds with the results found for r_{med} in Figure 46.a. This means that the reduction of the r_{med} value would also indicate a reduction in the severity of the geometric waves effect in FSEAM prints. In other words: the height of the r_{med} value is promising in giving an indication of the severity of varying material outflow speed. It is therefore recommended to perform an analysis to the possible relation between the height of r_{med} and the deviations in print geometry. Print geometry data would furthermore provide reference and context to judge n_{cv} and n_{std} values to.

Coupling to Literature

The observed alternating F_2 seen during experiment runs with significant varying material outflow speed corresponds with oscillating extrusion pressure seen in polymer stick-slip behaviour between points Q1 and Q2 in Figure 18. However, the appearance of extrudates prone to varying outflow speed does not show altering sharkskin/smooth surface as is the case for polymers, but remain smooth. The different regions of extrusion speed can therefore not easily be identified. Sharkskin is generally observed on extrudate surface as explained in Chapter 4, but occurs later in the v_f window.

A research-worthy recommendation for FSE(AM) would be to try different die wall materials, as so far only H13 steel is used for the tool housing. It is explained in the literature section that low surface energy die materials would smoothen the polymer flow in the die and (completely) reduces the oscillating pressure behaviour as it reduces sticking behaviour. Repeating the experiment series from

this thesis with different die wall materials (or coatings) having significantly different surface energies would gain more knowledge on the varying material outflow velocity behaviour seen in FSE(AM) from a tribological perspective.
One could think of the same suggestion for die wall roughness. However, as discussed earlier in the literature section, Ma et al (2012) [48] found in tribological-based extrusion research that surface topography does not influence this behaviour due to large normal pressures in the extrusion process. This effect can therefore be omitted in future experiments.

As mentioned in the literature section, the cause of varying polymer extrusion speed is tried to be explained by complex stress/strain-relations, but are part of debate within that research field. From above correlation analysis, varying extrusion speed can be successfully detected and predicted from the obtained data and shows similarities with polymer extrusion behaviour, but a clear explanation of the cause could not be identified yet. However, the similarities with polymer extrusion literature and conclusions from tribological/rheological research suggests that the cause of observed varying material outflow speed in FSE(AM) can be found in the aluminium/die-interface.
It is therefore recommended to further understand this interface in FSE(AM) in a more tribological manner. This can be achieved by developing an FSE(AM) flow model that includes the tribological effects of the aluminium/die-interface (and perhaps then the tool interface as well). The flow modelling approach used by Ma et al (2012) [48] could be used as a starting point as the modelled friction is fully plastic based and a similar material combination was used in modelling their interface, namely AA6063 and tool steel.

6 Conclusion

In this master thesis, the following two research questions were addressed:

1. How do changes in tool gap and tool rotation rate influence the measurable FSE(AM) system parameters (normal force, feed force, tool torque and temperatures) in the FSE(AM) setup?
2. Can the observed material outflow speed variation in FSE(AM) be measured and predicted from system data and how do tool rotation rate and tool gap influence this varying speed?

Literature research was performed to provide context on the used feed material during experiments, on the development of the FSEAM technique on the University of Twente and on comparable Additive Friction Stir Deposition methods and tooling. Furthermore, relevant literature and results from comparable research were presented.

As part of this thesis' work, two series of FSE experiments with varying tool gap and tool rotation rate were performed. Extensive data analysis was performed, explanatory calculations were provided and a coupling to relevant literature and earlier research was made.

The following conclusions were drawn from above research, sorted per research question and per topic:

6.1 FSE System Parameter Relations

- An existing FSE(AM) setup at the UTwente was successfully modified to an FSE setup that was able to measure flow-induced normal force (F_n) comparable to the normal force in FSEAM acting on substrate material, but in a better controllable way providing a more straightforward parameter analysis and which enabled video recording of extrudates for extrusion velocity analysis.
- A torque data extraction method was developed in MATLAB using video recordings from the setup's torque display screen that successfully returned reliable data for macro- (time scale of whole experiment run) and meso-analysis (time scale of circa 5 seconds). The data was not clean enough to be used for micro-analysis (time scale less then 1 second).
- Severe load cell drift with respect to time was observed that prevents reliable macro-analysis of F_n data. Solutions are proposed to solve this issue.
- Parameter analysis on macro-scale was successfully performed of the data flows of all experiment runs to identify parameter relations with respect to changing tool gap (TG) between 1.5 and 4.5 $[mm]$, tool rotation rate (ω) between 400 and 600 $[rpm]$ and feed velocity (v_f) between 0.2 and 2.3 $[mm/s]$. The following was found:
  - The nozzle temperature increased with TG and generally increased with feed velocity, although exceptions were present at the highest ω values with the lowest TG values. Furthermore, the nozzle temperature remained under the solvus temperature for $\omega = 400$ $[rpm]$ and $TG = 1.5$ $[mm]$ at the lower halve of the v_f window. This suggests that FSE is able to process AA6060 in a non-homogeneous state throughout the whole material flow path.
  - The temperature half way the material flow path stayed more or less constant with in a few cases a slight increase with respect to feed velocity. Furthermore, it was roughly constant to changes in tool gap and indifferent to ω for the lower half of the feed velocity window. The placement of these thermocouples provided a conductive thermal barrier that hindered perfect temperature measurement.
  - Differences in temperature in the material flow with respect to changes in TG and ω seem to increase towards the nozzle region, which suggests that the nozzle region is dominant in determining temperature differences with respect to TG and ω.

  - The cooling water temperature at the cooling channel exit was higher for higher ω at lower v_f. Furthermore, it decreased with v_f, but increased where jamming is near to occur. This shows that the time aluminium stays in the tool housing is dominant for determining the cooling water temperate unless heat input exceeds a threshold due to high torque values.
  - The feed force was found indifferent from TG. The feed force has shown a slowing increase with respect to feed velocity and a slight decrease over ω. The flattening effect became stronger with increasing ω.
  - At $\omega = 400$ $[rpm]$, torque (and thus the heat input by the rotating tool) increased with feed velocity and was indifferent for TG. Towards $\omega = 600$ $[rpm]$, torque became indifferent to feed velocity and stayed at a plateau which increases slightly with decreasing TG. This shows that the FSE setup is self-balancing if a maximum heat input by the tool is met.

- The FSE-setup was prone to jamming for large tool gaps in combinations with low tool rotation rates ($TG = 4.5$ $[mm]$ and $\omega = 400$ $[rpm]$). High torque values and increasing cooling water temperature were indicators for (near) jamming conditions, i.e. torque values approaching 100 $[Nm]$ and cooling water temperatures rising above $90°C$.

- Feed material flow in the tool housing is caused both by tool thread transport and forced by feed cylinder force as derived from stick-slip calculations and empirical results from earlier FSE research. An alternative conservation of mass equation is proposed that can be used in future flow simulation analyses.

6.2 Material Outflow Speed (V_y) Variation

Manual Geometry Analysis

- Manual geometry calculations on an earlier produced FSEAM build with severe geometrical variation has shown roughly periodical V_y variations in the order of magnitude of 0.1 $[Hz]$

Extracting V_y data

- A MATLAB method based on the Farneback method was developed and successfully applied for retrieving the extrudate outflow velocity (V_y) in FSE experiments from video recording made with a basic smartphone. The data was detailed enough to perform correlation analysis based on micro-variations.

- Frequency analysis with Fourier transformation has shown that observed variations in V_y lack a fixed frequency, but show a broad bandwidth in the frequency domain indicated by the manual geometry analysis.

Correlation Analysis

- A correlation analysis method was developed and successfully applied in MATLAB using the Pearson correlation coefficient. The developed correlation coefficient r_{med} is able to clearly indicate linear correlation on micro-variation level between F_n and V_y data, which is validated with visual analysis of the extrusion video recordings.

- Significant linear correlation ($r_{med} > 0.6$) was found in experiment runs with $TG = [2.5,\ 3.5]$ $[mm]$, $\omega = 400$ $[rpm]$ and at lowest feed velocities i.e. experiment tags 2TG3.5_400_2, 2TG3.5_400_2.5 and 2TG2.5_400_2.5. These settings are the most common settings used in FSEAM research so far.

- The correlation value r_{med} has shown to work as a clear indicator of significant extrusion speed variation with values of 0.6 indicating correlation and values between 0.2 and 0.3 indicating a lack of correlation between F_n and V_y.

- Linear correlation between F_n, V_y and torque data is suspected from visual data inspection. If so, V_y can be omitted and the correlation method can be implemented in FSEAM and used during experiments.
- Two severity parameters (n_{cv} and n_{std}) were proposed to quantify the severity of V_y variations scaled to F_n variations based on standard deviations or coefficient of variation of F_n and V_y. However, F_n drift prevented clear determination of n_{cv} and n_{std} within the correlation method and prevented practical use of the severity parameters.
- Comparison with earlier FSEAM research showed that FSEAM settings prone to material outflow speed variation are comparable to the FSE settings found in this research. The correlation value r_{med} seems to scale with geometrical variation severity found in FSEAM prints.
- Clear similarities are found between FSE extrudate surface defects and polymer extrusion volume defects described in literature. The roughly periodical behaviour of F_n also complies with the stick-slip polymer extrusion defect from literature. Unfortunately, polymer extrusion literature did not provide a comprehensive explanation for varying material outflow speed.

To summarise: FSE experiments have successfully resulted in structural mapping of FSE system parameter behaviour to changing tool gap and tool rotation rate. Additionally, variations in material outflow speed are successfully captured in data and system settings prone to this behaviour can be clearly identified through correlation between normal force and extrudate outflow speed. However, experimental data nor literature study provided an explanation for the cause of the varying material outflow speed.

7 Recommendations

In the last chapter of this thesis, recommendations are given for further research. A separation is made between recommendations related to the FSE setup with the parameter analysis, the material outflow speed variation research and other recommendations. The recommendations are sorted per topic and then organised by importance where possible.

7.1 FSE Setup & Parameter Analysis

Below, recommendations are made to improve the FSE(AM) setup for further empirical or modelling research. Besides, a few recommendations are made following from the parameter analysis results:

General

- Perform a repeatability analysis. Repeat all experiments preferably three times or more to validate repeatability of the setup and the resulting data.
- It is recommended to perform microstructural and mechanical analyses to structurally map resulting material characteristics of extrudates to the TG, ω and v_f windows for increasing general FSE knowledge. This also provides a data set that can judge the credibility of the parameter analysis results of this thesis.
- Severe drift with respect to time caused the normal force data to be unusable for parameter analysis between experiment runs. It is recommended to implement the mentioned solutions from Chapter 4 as the normal force is a crucial tool in bonding quality analysis in FSEAM.
- It is recommended to include a time stamp in the different data recording devices as this helps placing data variations occurring in multiple data flows in perfect chronological order. Data time synchronisation had to be done manually in this thesis without a perfect time reference.

Setup Assembly

- A spare mounting head assembly is recommended. Cleaning parts after a (jammed) experiment run takes significant amount of time. Experiments could not continue in the next two days after jamming. Continuing the experiments by replacing the whole head with a spare would enable efficient time management.
- The height of the hydraulic feeding cylinder must be manually aligned with the position of the feed tube for every tool gap alteration. The degree of alignment differed per experiment from perfect play of the feed tube for the whole cylinder travel to free play at the start of travel with little to none at the end of travel. The amount of feeding force needed to overcome this alignment imperfection was tested and identified as negligible. Redesigning the alignment system into a more fool-proof solution would be an improvement.
- After years of use by different students, the system shows clear signs of geometrical wear. This was excessively found in the fixation and alignment solution of the hydraulic feeding cylinder, where screw threads sheared off or bolts broke. Furthermore, the mounting head shows clear signs of geometrical wear. Replacing worn parts is recommended for enhanced data accuracy.
- Setting the tool gap height was done by self-made steel bushings in combination with steel spacers of 1 $[mm]$ thick. Due to applied pretension, it was observed that the spacers tended to bend slightly over the bushings, which does not give ideal geometrical stability. A set of sturdy bushings per tool gap setting would solve this.

Thermocouples

- The thermocouples were found very vulnerable. Often wires would break or wire insulation would strip resulting in unwanted wire contact and faulty data. Thicker wire diameter and welding of the thermocouples was an improvement and resulted in a clean data set, but was still not ideal. Extra protection for wire insulation on vulnerable points and an improved way of thermocouple welding is recommended.
- An extra thermocouple in the water tank measuring the bulk water temperature would enable calculation of ΔT_{water} between cooling inlet and outlet of the tool housing and so an indication of heat energy 'lost' in cooling. Additionally, adding a thermocouple in the cooling outlet of the feed tube cooling channel would give insight in heat entering the feed material in the feed tube, giving more insight in jamming conditions.
- Making a hole in the tool housing and welding TC3&4 in the tool housing itself will obtain more reliable temperature half way the material flow path without the current conductive thermal barrier.

7.2 Material Outflow Speed (V_y) Variation

Below, ideas for further analysis and improvements for the experimental setup are presented. The points are sorted per subject from the above section.

General

- Whilst performing FSEAM experiments when geometrically constant products are desired, omit the FSE settings that have shown to give significant variations in V_y. This can easily be accomplished by increasing the tool rotation rate to 600 $[rpm]$.
- Physical appearance of the resulting extrusion samples is not investigated in this thesis. It is worth analysing the extrudate surface (repetitive rings), which might give more information about the extrusion speed variation and extrusion defect behaviour with respect to TG, ω and v_f.
- Perform FSEAM experiments with settings prone to inconsistent material outflow speed and analyse optical geometry variations of the print layers with F_n data to gain better understanding of the relation between the two. Furthermore, a comparison between these results and the developed correlation & severity method from this thesis would gain more insight in the method's applicability.
- As significant outflow speed variation was only found at the lowest tool rotation rate of 400 $[rpm]$, an extra experiment series performed at a lower tool rotation rate of 300 $[rpm]$ would show whether or not the severity of material outflow variation would increase with reducing the tool rotation rate.
- It is recommended to perform the experiment series of this thesis with other tool housing materials with significantly different surface energies. This, because the FSE(AM) process and resulting FSE sample appearances show similarity with polymer extrusion literature and aluminium tribilogy and rheology research suggesting such a solution for altering friction behaviour at the die wall.
- It is recommended to include tribological behaviour of the aluminium-die wall interface in future flow analyses as material flow shear stress behaviour there is suggested in literature to be highly likely the trigger for varying material outflow speed.

Extrusion Velocity Data Extraction

- A professional camera mounted into a fixed stand with manually adjustable focus will help obtaining more stable video data. Now using an available smartphone on a removable stand with auto-focus did provide programmability challenges in the MATLAB video analysis.
- Recording the extrusion speed video and other data flows with the same feed rate would make correlation analysis more reliable. Now these differences in recording frequency introduced unnecessary imperfections in the correlation analysis making it impossible for the Pearson correlation coefficient to be its theoretical maximum value of 1.

Correlation Analysis

- Torque data is suspected to show the same micro-variations as extrusion speed and normal force data. Torque data retrieved directly from the electric motor can be used to find correlation with normal force data. In this way, video recording can be omitted to trace material outflow variation and the developed correlation analysis can be extended to track material outflow variation in FSEAM. To realise this, available electronic hardware should be reconnected and available LabView software should be reprogrammed on the data-retrieving laptop in the current setup.
- Instead of using the time window of a whole experiment run in the correlation method, time window steps had to be embedded to omit normal force load cell drift effects. This resulted in a less suitable analysis method for higher feed velocity settings. Solving the drift issue with the proposed solutions would thus give more reliable correlation analysis results.
- A more reliable method for further severity analysis would be to separately determine standard deviation and coefficient of variation values with *movmean* and *movstd* functions in MATLAB in a separate programming path, instead of retrieving these as a byproduct from the correlation analysis. The relatively large window steps needed for the correlation analysis caused errors in the used values for n_{cv} and σ_{F2}.
- The standard deviation of F_n seemed to increase towards setup settings prone to jamming. Further research could be interesting to validate if there exists an 'likeliness to jamming'-effect on the normal force variation.
- Scanning the geometry deviations in FSEAM prints layer by layer gives data that can be added in the correlation analysis method. Doing so, one gains more knowledge on the relation between variations in the normal force, torque and the resulting effect on print geometry.

7.3 Other

- An alternative conservation of mass is formulated in Equation 11, which can be used as a starting point for further flow simulation studies. A material flow model performed by Masselink [16] with improved inlet boundary conditions can be used as a promising basis to implement this new insight.
- FSEAM experiments can be performed with the alternative tool designs presented in Appendices C.3, C.1 and C.2 in combination with the recommended system settings for consistent material outflow speed to investigate alternative tool nozzle design on layer bonding quality in FSEAM and to enable temperature measurement in the tool tip.

References

[1] Ansys, "Granta EduPack 2022 R2, Material Science Software," 2022.

[2] H. Chen, X. Meng, J. Chen, Y. Xie, J. Wang, S. Sun, Y. Zhao, J. Li, L. Wan, and Y. Huang, "Wire-based friction stir additive manufacturing," *Additive Manufacturing*, vol. 70, p. 103557, 5 2023. [Online]. Available: https://linkinghub.elsevier.com/retrieve/pii/S2214860423001707

[3] W. D. Callister and D. G. Rethwisch, *Materials Science and Engineering, SI version*, 10th ed. John Wiley & Sonds Pte Ltd, 2018.

[4] A. Hassan, S. R. Pedapati, M. Awang, and I. A. Soomro, "A Comprehensive Review of Friction Stir Additive Manufacturing (FSAM) of Non-Ferrous Alloys," *Materials*, vol. 16, no. 7, 4 2023.

[5] H. Dong, X. Li, K. Xu, Z. Zang, X. Liu, Z. Zhang, W. Xiao, and Y. Li, "A Review on Solid-State-Based Additive Friction Stir Deposition," 10 2022.

[6] S. Palanivel, P. Nelaturu, B. Glass, and R. S. Mishra, "Friction stir additive manufacturing for high structural performance through microstructural control in an Mg based WE43 alloy," *Materials and Design*, vol. 65, pp. 934–952, 1 2015.

[7] M. M. Ahmed, M. M. El-Sayed Seleman, D. Fydrych, and G. Çam, "Friction Stir Welding of Aluminum in the Aerospace Industry: The Current Progress and State-of-the-Art Review," 4 2023.

[8] A. Kumar Srivastava, N. Kumar, and A. Rai Dixit, "Friction stir additive manufacturing – An innovative tool to enhance mechanical and microstructural properties," 1 2021.

[9] A. A. Van Der Stelt, T. C. Bor, H. J. Geijselaers, R. Akkerman, and A. H. Van Den Boogaard, "Cladding of advanced Al alloys employing friction stir welding," in *Key Engineering Materials*, vol. 554-557. Trans Tech Publications Ltd, 2013, pp. 1014–1021.

[10] H. J. Smit, "FRICTION SCREW EXTRUSION: TOWARDS SOLID STATE ADDITIVE MANUFACTURING OF HIGH-STRENGTH ALUMINIUM ALLOYS," 2020.

[11] S. Liu, T. C. Bor, A. A. Van Der Stelt, H. J. Geijselaers, C. Kwakernaak, A. M. Kooijman, J. M. Mol, R. Akkerman, and A. H. Van Den Boogaard, "Friction surface cladding: An exploratory study of a new solid state cladding process," *Journal of Materials Processing Technology*, vol. 229, pp. 769–784, 11 2015.

[12] M. De Leede, "SOLID STATE ADDITIVE MANUFACTURING A STUDY TO UNDERSTAND THE BONDING PROCESS OF FRICTION SURFACING US-ING AA2024-T351 ONTO AA2024-T351," Tech. Rep., 2017.

[13] J. B. Lind, "Towards continuous solid state additive manufacturing of aluminium alloys," 2018.

[14] R. C. G. Arïens, "Exploratory research of friction stir extrusion additive manufacturing using AA6060 T6," 2021.

[15] S. Sayyad Rezaeinejad, D. H. Strik, R. M. Visser, T. C. Bor, M. Luckabauer, and R. Akkerman, "Solid-State Additive Manufacturing of AA6060 employing Friction Screw Extrusion Additive Manufacturing," Tech. Rep., 2023.

[16] N. Masselink, "Friction Screw Extrusion: An exploratory research to the relations between process parameters, microstructure and mechanical properties," 2021.

[17] D. H. Strik, "Influence of print speed on the microstructure and mechanical properties of AA6060 FSEAM builds," 2023.

[18] Visser R, "Friction Screw Extrusion- Towards mall scale H-FSE - an efficient material feed."

[19] T. Bor, M. d. Leede, F. Deunk, J. Lind, W. Lievestro, H.-J. Smit, R. Ariës, V. Dolas, N. Helthuis, M. Luckabauer, and R. Akkerman, "Friction screw extrusion additive manufacturing of an Al-Mg-Si alloy," *Additive Manufacturing*, vol. 72, p. 103621, 6 2023. [Online]. Available: https://linkinghub.elsevier.com/retrieve/pii/S2214860423002348

[20] R. S. Haridas, A. Gumaste, P. Varshney, B. R. Manu, K. Kandasamy, N. Kumar, and R. S. Mishra, "SolidStir Additive Manufacturing: A Novel Deformation-Based Additive Manufacturing Using Friction Stir Technology," *JOM*, 2023.

[21] S. Palanivel, H. Sidhar, and R. S. Mishra, "Friction Stir Additive Manufacturing: Route to High Structural Performance," *JOM*, vol. 67, no. 3, pp. 616–621, 3 2015.

[22] K. K. Jha, R. Kesharwani, and M. Imam, "Microstructure and Mechanical Properties Correlation of FSAM Employed AA5083/AA7075 Joints," *Transactions of the Indian Institute of Metals*, vol. 76, no. 2, pp. 323–333, 2 2023.

[23] ——, "Microstructure, texture, and mechanical properties correlation of AA5083/AA6061/SiC composite fabricated by FSAM process," *Materials Chemistry and Physics*, vol. 296, 2 2023.

[24] R. Cojocaru, L. Boţilă, C. Ciucă, H. Daşcău, and V. Verbiţchi, "Friction stir lap welding of light alloy sheets," in *Advanced Materials Research*, vol. 814, 2013, pp. 187–192.

[25] S. Emamian, M. Awang, F. Yusof, P. Hussain, M. Mehrpouya, S. Kakooei, M. Moayedfar, and A. Zafar, "A review of friction stir welding pin profile," *Lecture Notes in Mechanical Engineering*, pp. 1–18, 2017.

[26] T. C. Bor, D. H. Strik, S. S. Rezaeinejad, N. G. J. Helthuis, G. S. Vos, M. Luckabauer, and R. Akkerman, "A feasibility study on friction screw extrusion additive manufacturing of AA6060," 2023.

[27] *Material Data Sheet EN AW-6060*. Essen, Germany: thyssenkrupp Materials Services GmbH, 2017.

[28] M. Baruah and A. Borah, "Processing and precipitation strengthening of 6xxx series aluminium alloys: A review," *International Journal of Materials Science*, vol. 1, no. 1, pp. 40–48, 1 2020.

[29] A. Malekan, M. Emamy, J. Rassizadehghani, and M. Malekan, " Effect of Isothermal Holding on Semisolid Microstructure of Al–Mg 2 Si Composites ," *ISRN Metallurgy*, vol. 2012, pp. 1–7, 6 2012.

[30] J. L. Murray and A. J. Mcaiister, "The AI-Si (Aluminum-Silicon) System," Tech. Rep., 1984.

[31] B. Milkereit, C. Schick, O. Kessler, L. Jonas, and O. Keßler, "The continuous cooling precipitation diagram of an aluminum alloy en AW-6005A Ultrafast calorimetry of nonequilibrium systems View project," Tech. Rep. 3, 2012. [Online]. Available: https://www.researchgate.net/publication/231520606

[32] I. J. Polmear, D. StJohn, J.-F. Nie, and M. Qian, *Light alloys : metallurgy of the light metals*.

[33] R. Vissers, M. A. van Huis, J. Jansen, H. W. Zandbergen, C. D. Marioara, and S. J. Andersen, "The crystal structure of the β phase in Al-Mg-Si alloys," *Acta Materialia*, vol. 55, no. 11, pp. 3815–3823, 6 2007.

[34] G. Dieter, *Mechanical Metallurgy. SI Metric Edition*, 1988.

[35] P. Mukhopadhyay, "Alloy Designation, Processing, and Use of AA6XXX Series Aluminium Alloys," *ISRN Metallurgy*, vol. 2012, pp. 1–15, 4 2012.

[36] A. K. Gupta, D. J. Lloyd, and S. A. Court, "Precipitation hardening in Al-Mg-Si alloys with and without excess Si," Tech. Rep., 2001. [Online]. Available: www.elsevier.com/locate/msea

[37] G. Mrówka-Nowotnik and J. Sieniawski, "Influence of heat treatment on the microstructure and mechanical properties of 6005 and 6082 aluminium alloys," in *Journal of Materials Processing Technology*, vol. 162-163, no. SPEC. ISS., 5 2005, pp. 367–372.

[38] A. Dorbane, G. Ayoub, B. Mansoor, R. Hamade, G. Kridli, and A. Imad, "Observations of the mechanical response and evolution of damage of AA 6061-T6 under different strain rates and temperatures," *Materials Science and Engineering A*, vol. 624, pp. 239–249, 1 2015.

[39] X. Liu, G. Chen, J. Ni, and Z. Feng, "Computational Fluid Dynamics Modeling on Steady-State Friction Stir Welding of Aluminum Alloy 6061 to TRIP Steel," *Journal of Manufacturing Science and Engineering, Transactions of the ASME*, vol. 139, no. 5, 5 2017.

[40] T. Sheppard, *Extrusion of Aluminium Alloys*. Springer US, 1999.

[41] T. Bor, M. De Leede, F. Deunk, J. Lind, W. Lievestro, H.-J. Smit, R. Ariës, V. Dolas, N. Helthuis, M. Luckabauer, and R. Akkerman, "Friction screw extrusion additive manufacturing of an Al-Mg-Si alloy," Tech. Rep., 2023.

[42] C. Rauwendaal, *Polymer Extrusion*, 5th ed. Carl Hanser Verlag}, 2013.

[43] A. Oosterkamp, L. Djapic Oosterkamp, and A. Nordeide, "'Kissing Bond' Phenomena in }Solid-State Welds of Aluminum Alloys," WELDING JOURNAL, Tech. Rep., 8 2004.

[44] C. Rauwendaal, *Polymer extrusion*, 5th ed. München: Calrl Hanser Verlag, 2013.

[45] J. Benbow, R. Charley, and P. Lamb, "Unstable flow of Molten Polymers," 1961.

[46] B. Vergnes, "Extrusion Defects and Flow Instabilities of Molten Polymers," Tech. Rep., 2015. [Online]. Available: www.hanser-elibrary.com

[47] G. A. Campbell and M. A. Spalding, "Analyzing and Troubleshooting Single-Screw Extruders," Tech. Rep., 2013.

[48] X. Ma, M. B. De Rooij, and D. J. Schipper, "Friction conditions in the bearing area of an aluminium extrusion process," *Wear*, vol. 278-279, pp. 1–8, 3 2012.

[49] X. Wang, Y. Gao, X. Liu, M. McDonnell, and Z. Feng, "Tool-workpiece stick-slip conditions and their effects on torque and heat generation rate in the friction stir welding," *Acta Materialia*, vol. 213, 7 2021.

[50] F. Widerøe and T. Welo, "Conditions for sticking friction between aluminium alloy AA6060 and tool steel in hot forming," in *Key Engineering Materials*, vol. 491. Trans Tech Publications Ltd, 2012, pp. 121–128.

[51] G. Farnebäck, "Two-Frame Motion Estimation Based on Polynomial Expansion," Tech. Rep. [Online]. Available: http://www.isy.liu.se/cvl/

[52] L. P. Mendes, A. M. Ricardo, A. J. Bernardino, and R. M. Ferreira, "A comparative study of optical flow methods for fluid mechanics," *Experiments in Fluids*, vol. 63, no. 1, 1 2022.

[53] P. Schober and L. A. Schwarte, "Correlation coefficients: Appropriate use and interpretation," *Anesthesia and Analgesia*, vol. 126, no. 5, pp. 1763–1768, 5 2018.

[54] W. H. Press, *Numerical recipes in C : the art of scientific computing*. Cambridge University Press, 1992.

[55] W. Lievestro, "Friction Screw Cladding, Een prototype als stap naar het continu-cladden van aluminiumlegeringen." 2019.

A AA6060 Material Properties

On the next pages, the material data sheet [27] of the used AA6060-T6 aluminium alloy feed material is presented for consulting exact properties. It also gives a comparison between feed material properties and material properties of FSE and FSEAM products.

Material Data Sheet

Aluminium alloy

Materials Services
Technology, Innovation
& Sustainability

Material designation:	EN-Material No.	DIN-Material No.
	EN AW-6060 [EN AW-Al MgSi]	3.3206

Scope

This data sheet applies to cold drawn and extruded rod/bar, tubes and profiles made of aluminium-silicon alloy EN AW-6060.

Application

Among the heat treatable aluminium alloys the material EN AW-6060 shows medium mechanical properties and a good atmospheric and seawater corrosion resistance. The material is good weldable and is used for example in the automotive and railway industry.
The alloy EN AW-6060 is heat treatable and it is suitable for decorative anodizing.

Chemical composition in %

Si	Fe	Cu	Mn	Mg	Cr	Zn	Ti	Al
0.30–0.6	0.10–0.30	≤ 0.10	≤ 0.10	0.35–0.6	≤ 0.05	≤ 0.15	≤ 0.10	Rest

Others[a]: Each: max. 0.05 % Total[b]: max. 0.15 %

[a] „Others“ includes listed elements for which no specific limit is shown as well as unlisted metallic elements. The producer may analyze samples for trace elements not specified in the registration or specification. However, such analysis is not required and may not cover all metallic „Other“ elements. Should any analysis by the producer or the purchaser establish that an „Others“ element exceeds the limit of „Each“ or that the aggregate of several „Others“ elements exceeds the limit of „Total“, the material shall be considered non-conforming.

[b] The sum of those “Others” metallic elements 0,010 % or more each, expressed to the second decimal place before determining the sum.

Mechanical properties at room temperature (cold drawn rod/bar and tube)

Temper	Dimensions			Yield strength	Tensile strength	Elongation		Hardness[1]
	D[a]	S[b]	t[c]	$R_{p0,2}$	R_m	A	A_{50}	
	[mm]	[mm]	[mm]	[N/mm²]	[N/mm²]	[%]	[%]	HBW
T4	- ≤ 80	- ≤ 80	≤ 5 5 < t ≤ 20	≥ 65 ≥ 65	≥ 130 ≥ 130	≥ 12 ≥ 15	≥ 10 ≥ 13	50 50
T6	≤ 80	≤ 80	≤ 20	≥ 160	≥ 215	≥ 12	≥ 10	75

thyssenkrupp Materials Services GmbH, thyssenkrupp Allee 1, 45143 Essen, Germany
T: +49 201 844-553019, F: +49 201 844-553017, www.thyssenkrupp-materials-services.com
Chairman of the Supervisory Board: Guido Kerkhoff
Executive Board: Joachim Limberg (Chairman), Markus Bistram, Hans-Josef Hoss, Dr. Klaus Keysberg
Commercial Register: Essen HRB 22760, Vat-No.: DE811154735

Mechanical properties at room temperature (extruded rod/bar and tube)

Temper	Dimensions			Yield strength	Tensile strength	Elongation		Hardness[1)]
	D[a)]	S[b)]	t[c)]	$R_{p0,2}$	R_m	A	A_{50}	
	[mm]	[mm]	[mm]	[N/mm²]	[N/mm²]	[%]	[%]	HBW
T4	≤ 150	≤ 150	≤ 15	≥ 60	≥ 120	≥ 16	≥ 14	50
T5	≤ 150	≤ 150	≤ 15	≥ 120	≥ 160	≥ 8	≥ 6	60
T6	≤ 150	≤ 150	≤ 15	≥ 150	≥ 190	≥ 8	≥ 6	70
T64	≤ 50	≤ 50	≤ 15	≥ 120	≥ 180	≥ 12	≥ 10	60
T66	≤ 150	≤ 150	≤ 15	≥ 160	≥ 215	≥ 8	≥ 6	75

Mechanical properties at room temperature (extruded profiles)

Temper	Wall thickness	Yield strength	Tensile strength	Tensile strength		Hardness[1)]
	t	$R_{p0,2}$	R_m	A	A_{50}	
	[mm]	[N/mm²]	[N/mm²]	[%]	[%]	HBW
T4	≤ 25	≥ 60	≥ 120	≥ 16	≥ 14	50
T5	≤ 5 5 < t ≤ 25	≥ 120 ≥ 100	≥ 160 ≥ 140	≥8 ≥ 8	≥ 6 ≥ 6	60 60
T6	≤ 5 5 < t ≤ 25	≥ 150 ≥ 140	≥ 190 ≥ 170	≥ 8 ≥ 8	≥ 6 ≥ 6	70 70
T64	≤ 15	≥ 120	≥ 180	≥ 12	≥ 10	60
T66	≤ 5 5 < t ≤ 25	≥ 160 ≥ 150	≥ 215 ≥ 195	≥ 8 ≥ 8	≥ 6 ≥ 6	75 75

[1)] For information only
[a)] D = Diameter for round bar
[b)] S = Width across flats for square and hexagonal bar, thickness for rectangular bar
[c)] t = Wall thickness for tubes

Reference data for some physical properties (for guidance only)

Density at 20 °C	Electrical conductivity	Thermal conductivity	Specific heat capacity	Young's modulus	Shear modulus
[kg/dm³]	[MS/m]	[W/m•K]	[J/kg•K]	[MPa]	[MPa]
2.70	34–38	200–220	898	69500	26100

Mean linear thermal expansion coefficient [10^{-6} K^{-1}]

-50–20 °C	20–100 °C	20–200 °C	20–300 °C
21.8	23.4	24.5	25.6

Guidelines on the temperatures for hot forming and heat treatment

Annealing		
Temperature	Time to heat up	Cooling conditions
360–400 °C	1.0–2.0 h	≤ 30 °C/h to 250 °C, below 250 °C on air

Precipitation heat treatment			
Solution heat treatment	Quenching	Natural ageing	Artificial ageing
525–540 °C	Water, air	5–8 days	Temperature: 155–190 °C Time: 4–16 h

Processing/Welding

The material is good weldable with the conventional processes (MIG and TIG). As welding filler metal is SG-AlMg5, SG-AlSi and SG-AlMg3 recommended. In annealed temper there may arise some difficulties during machining (for example ribbon or thread chips). The machinability improves with the grade of ageing.

Remarks

According to EN 602 the use of the material is allowed for the contact with food.
For decorative anodizing the material EN AW-6060 should be selected as anodizing quality acc. to DIN 17611 for quality reasons.

Editor

thyssenkrupp Materials Services GmbH
Technology, Innovation & Sustainability (TIS)
thyssenkrupp Allee 1
45143 Essen
Germany

Reference

DIN EN 485-2 : 2016-10 — Beuth Verlag GmbH, Postfach, D-10772 Berlin
DIN EN 573-3 : 2013-12
DIN EN 754-2 : 2017-02
DIN EN 755-2 : 2016-10
Aluminium-Werkstoff-Datenblätter — Aluminium-Verlag Marketing & Kommunikation GmbH
Aluminiumtaschenbuch Band 1 – 3 — D-40003 Düsseldorf

Important Note

Information given in this data sheet about the condition or usability of materials respectively products are no warranty for their properties, but act as a description.
The information, we give on for advice, comply to the experiences of the manufacturer as well as our own. We cannot give warranty for the results of processing and application of the products.

B Technical Drawings Parts

On the next pages, technical drawings are presented made and used for producing the newly designed parts as explained in Section 4.

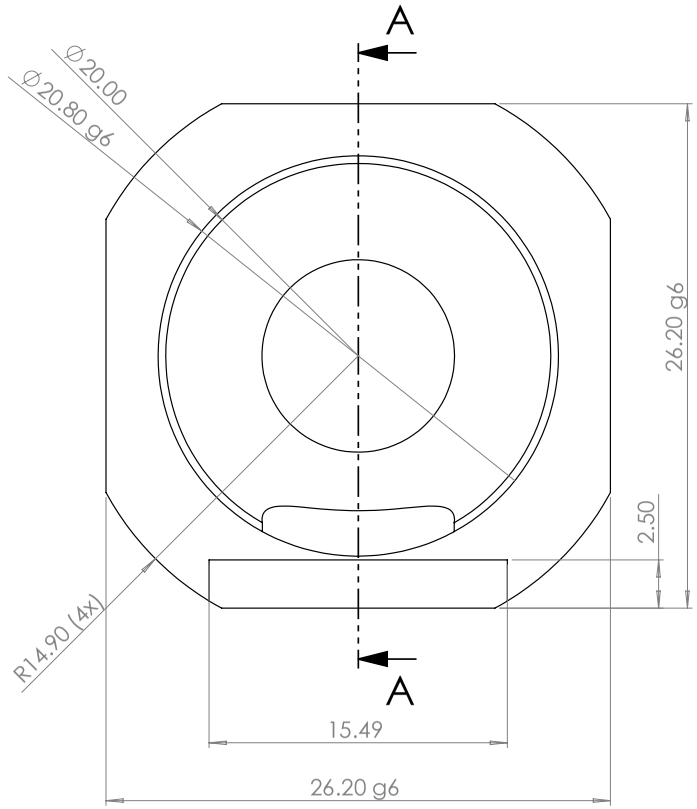

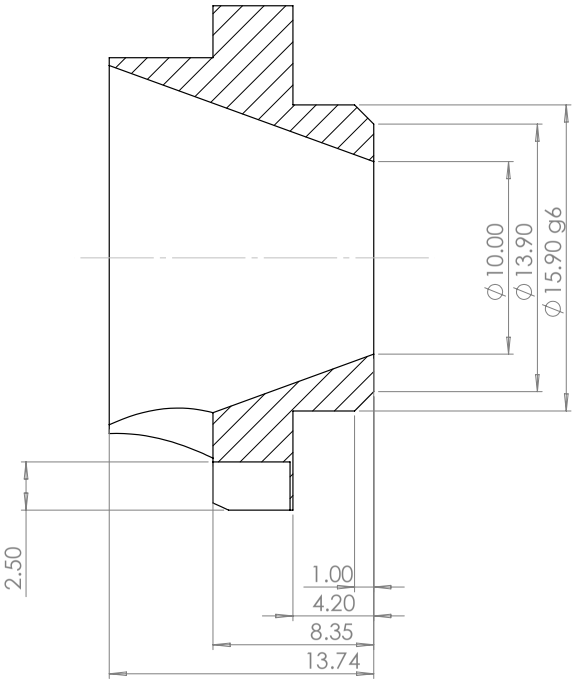

SECTION A-A

SCALE 4 : 1

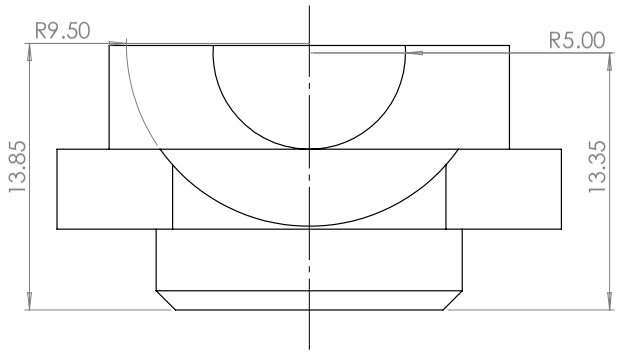

1.6

UNLESS OTHERWISE SPECIFIED: DIMENSIONS ARE IN MILLIMETERS SURFACE FINISH: TOLERANCES: LINEAR: ANGULAR:		FINISH:			DEBURR AND BREAK SHARP EDGES	DO NOT SCALE DRAWING	REVISION
	NAME	SIGNATURE	DATE			TITLE:	
DRAWN							
CHK'D							
APPV'D							
MFG							
Q.A				MATERIAL:		DWG NO. 2_7 Nozzel_v3	A3
				WEIGHT:		SCALE:2:1	SHEET 1 OF 1

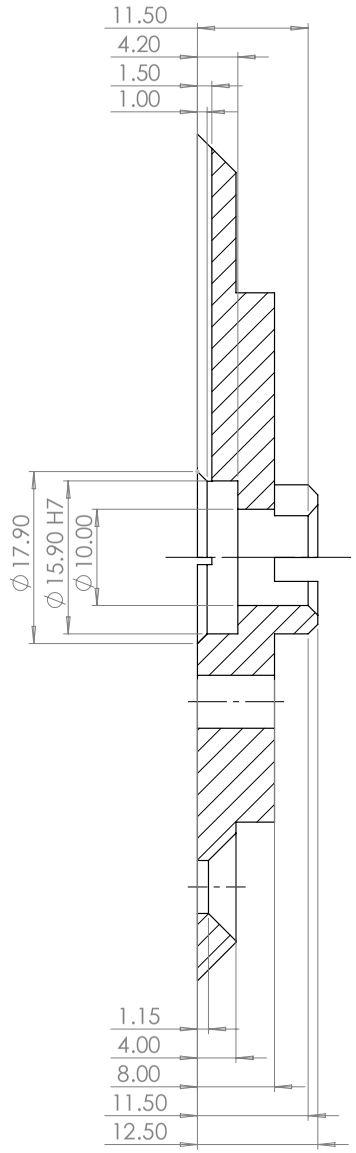

SECTION A-A

SCALE 2 : 1

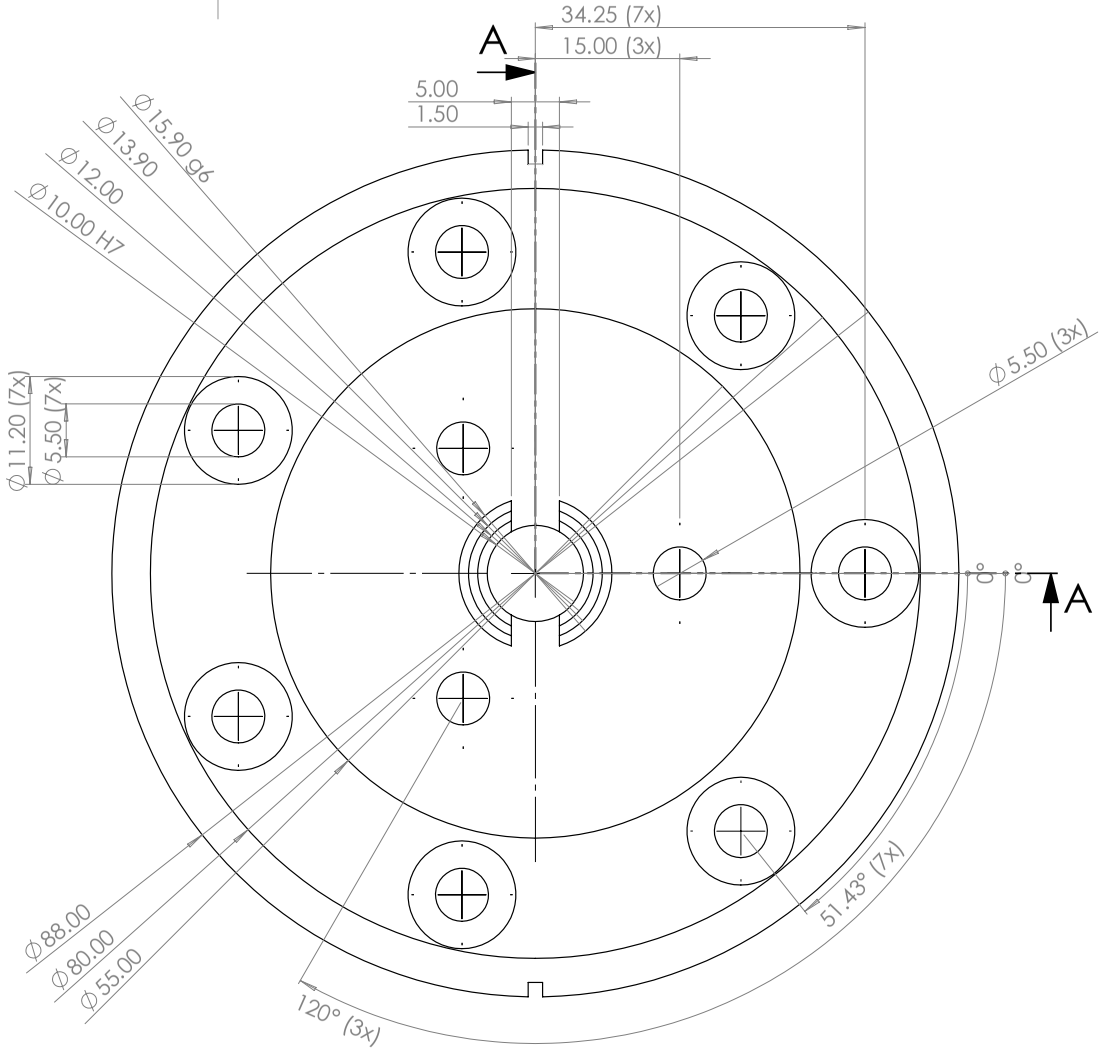

1.6

UNLESS OTHERWISE SPECIFIED: DIMENSIONS ARE IN MILLIMETERS SURFACE FINISH: TOLERANCES: LINEAR: ANGULAR:		FINISH:				DEBURR AND BREAK SHARP EDGES	DO NOT SCALE DRAWING	REVISION
	NAME	SIGNATURE	DATE				TITLE:	
DRAWN								
CHK'D								
APPV'D								
MFG								
Q.A								
				MATERIAL:			DWG NO.	A3
							2_6 Nozzle_holder_v2	
				WEIGHT:			SCALE:1:1	SHEET 1 OF 1

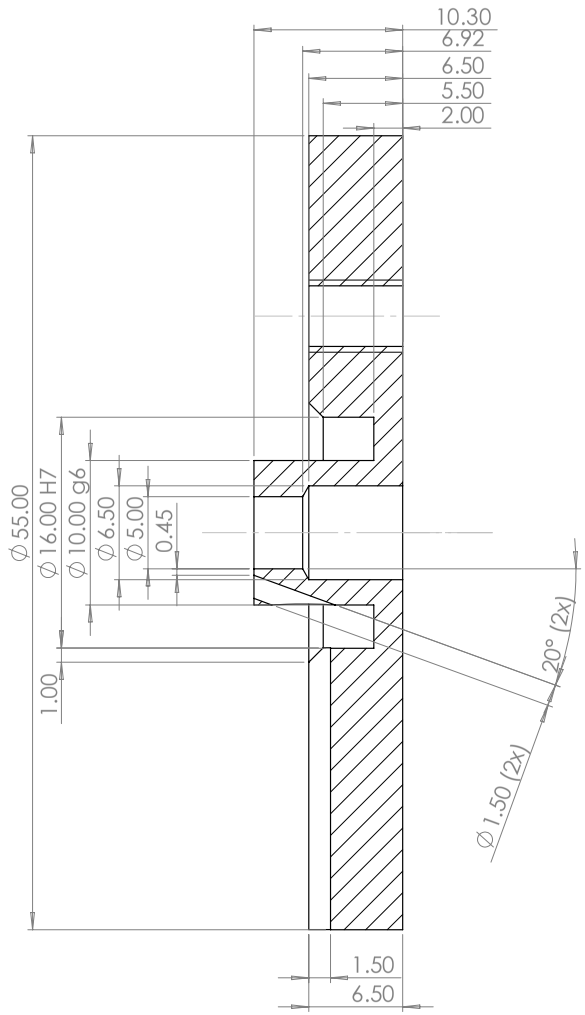

SECTION A-A

SCALE 3 : 1

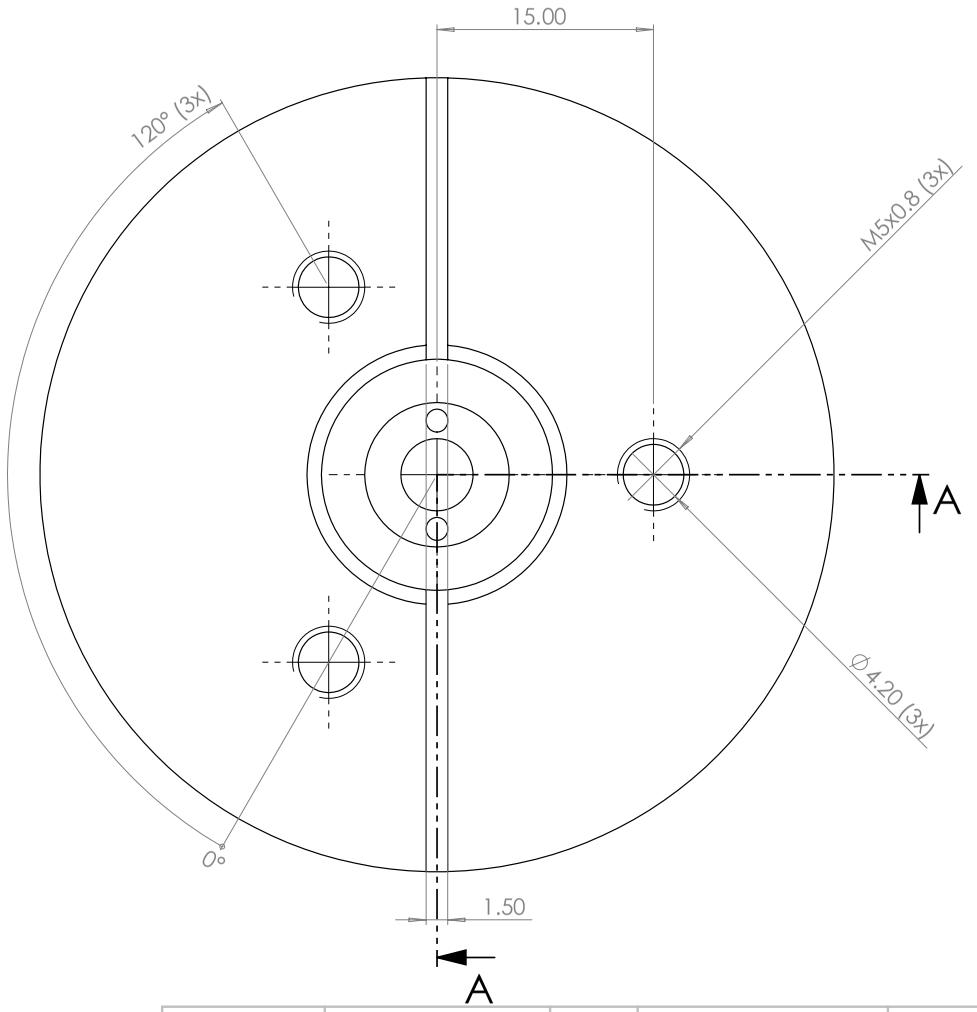

1.6

UNLESS OTHERWISE SPECIFIED: DIMENSIONS ARE IN MILLIMETERS SURFACE FINISH: TOLERANCES: LINEAR: ANGULAR:		FINISH:				DEBURR AND BREAK SHARP EDGES	DO NOT SCALE DRAWING	REVISION
	NAME	SIGNATURE	DATE				TITLE:	
DRAWN								
CHK'D								
APPV'D								
MFG								
Q.A				MATERIAL:			DWG NO.	A3
							nozzel_ext_die_TG_5mm	
				WEIGHT:			SCALE:2:1	SHEET 1 OF 1

C Alternative Tool Design

In this Appendix chapter, a first step towards an improvement of bonding quality is presented by the design of alternative FSEAM tools. A set of conceptual alternative tool designs is presented of which three designs were chosen and manufactured from W360 tool steel by Triton Tooling Ltd in Leighton Buzzard, England. The rejected tool designs are not elaborated on, but can be found in Appendix C.3 for further reference and can be used as inspiration for future research.
All proposed tool designs are based on the tool design used in recent research at the UTwente [15,17] as presented in Figure 22.
With the chosen tools, FSEAM experiments can be performed in order to qualitatively investigate the suitability of the proposed designs in solving the bonding quality issue of earlier research as explained in Chapter 1.

C.1 Approved Concepts

C.1.1 Pin based design

Inspired by the promising results of the W-FSAM setup of the Chinese research group of Chen [2], it is tried to implement pin features into the existing tool design. The design is based on the current tool with 3 pins placed symmetrically at the bottom of the tool in a circular way around the axisymmetry centre line as presented in Figure 49. The pins are 2mm long, which equals the thickness of two printed layers in the current FSEAM setup. The pins have a conical shape with a 20 degree angle, following the angle of the tapered part of the tool. The exact dimensions of the tool can be found in Appendix C.2. The SolidWorks file is available on request.

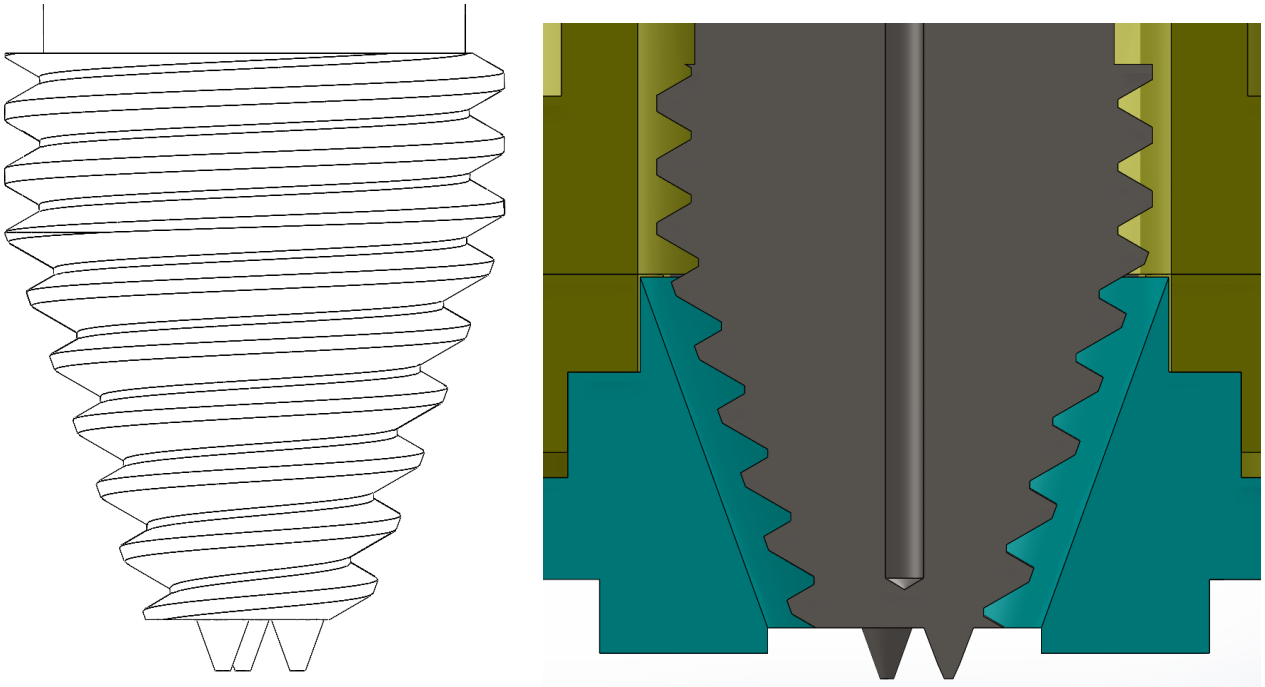

49.a. Sketch

49.b. Cross section view in FSEAM printing head

Figure 49: Tool design with pin feature

The goal of the pins is to break up the bonding interface between the previously printed layer and the currently printed layer in order to ensure better mixing of the print layers and so improve higher quality bonding of layers without kissing bonds. The rotating motion of the tool in combination with the translating motion of the table will logically result in a horizontal spiral-shape flow pattern of the

pins.

Whilst performing FSEAM experiments, it is possible to shave off a bit of pin length in between experiments on order to investigate the effect of pin length on bonding quality.

C.1.2 Flow based design

Besides the pin based design, two flow based alternative tool designs were found suitable to try FSEAM experiments with. The goal of these designs is to promote even distribution of processes material over the print width in order to improve bonding quality between printed layers. This, instead of a canalised flow as presented in Figure 14.b in the current situation, resulting in uneven pressure distribution of processed material on the previously printed layer and the discussed layer bonding problems.

As a starting point, Figure 15 from the analysis made in the master thesis of Niek Masselink [16] was taken. This analysis was performed on FSE experiments, whilst this tool redesign is for FSEAM experiments. It could therefore be subject of discussion whether or not this analysis is suitable for this purpose. But as these two methods have similar material flow in the tool housing, it was considered as a suitable starting point.

From Figure 50, two tool design features were indicated that can be altered to significantly improve the material flow to reach the stated goal above, which are encircled in red in Figure 50. These are:

- *Sharp tool edge:* causes an additional canalisation of the material flow away from the tool tip, resulting in material not being able to travel to the centre of the tool
- *Flat tip surface:* causes a vortex zone with low material travelling velocity. Processed material in FSEAM experiments can not reach the middle of the printed layer because of this.

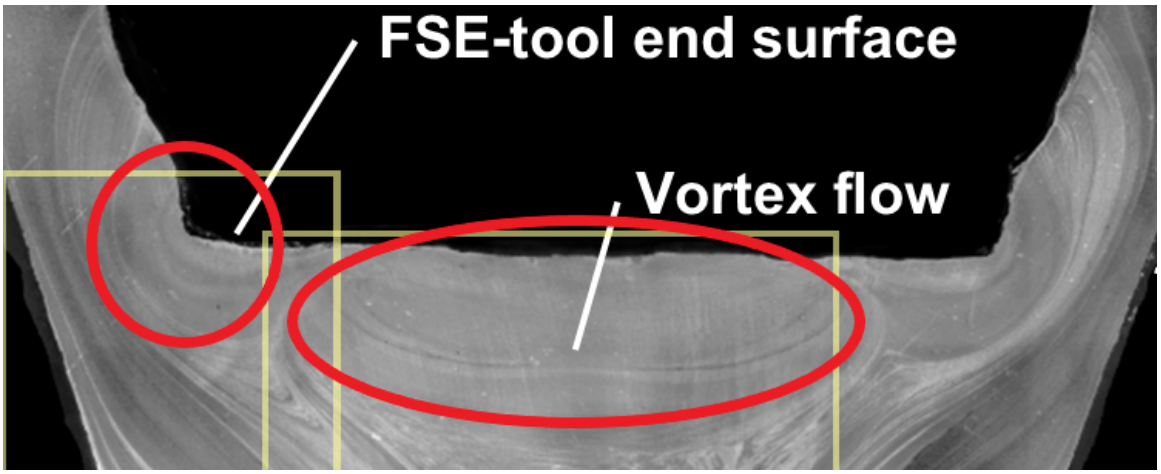

Figure 50: Cut and zoom of Figure 15.a with flow-influencing features indicated with a red circle

As the indicated sharp edge and flat surface do not contribute to even material distribution, chances on these features can be effective to alter bonding quality. From a selection of seven proposed concepts, the two designs below are chosen to perform experiments with. The rejected concepts with explanation can be found in Appendix C.3.

Edged design
By removing the sharp edge and flat surface as indicated in Figure 50 and replacing it by an edged tip, the material has more space to travel to the centre of the printed layer. Furthermore, the flow effects induced by the sharp edge and flat surface as described above will be minimised.

Furthermore, the tip of the edge is placed 1 $[mm]$ into the currently printed layer with a tool gap distance of 3.2 $[mm]$ in line with FSEAM experiments performed in latest research [15, 17]. This, in order to be able to more or less stir the currently and previously printed layer depending on the specified tool gap in the setup.

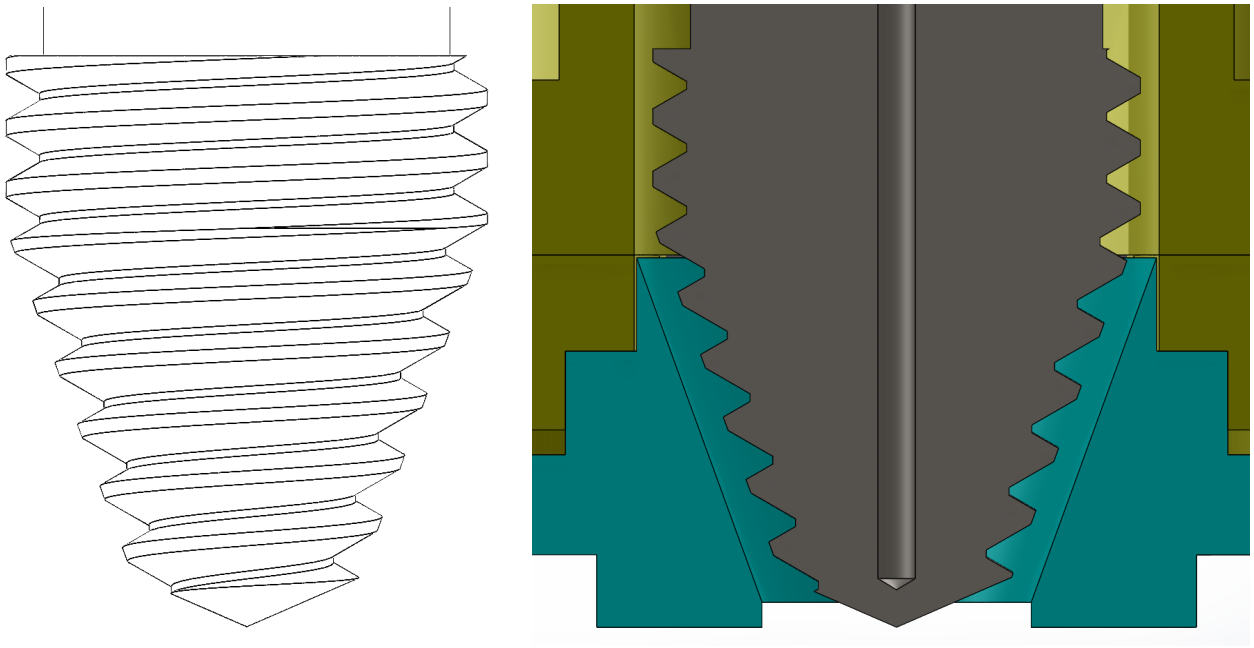

51.a. Sketch

51.b. Cross section view in FSEAM printing head

Figure 51: Tool design with edged feature

A sketch of the design is presented in Figure 51. The technical drawing of this design for production can be found in Appendix C.2. The SolidWorks file can be obtained on request.

Slotted design

Another way to give more space to let material travel to the centre of the tool tip is by making four slots into the tool design starting at the first full thread crest from the tip of the tool. A slotted design over the whole threaded tool length was already tried in the thesis of Lievestro [55], where severe material processing pressure losses in the tool housing caused unsuccessful material extrusion. With smaller slots as is presented in Figure 52, it is tried to keep the material flow pressure sufficient throughout the tool housing, but also to give material more space to travel to the centre of the tool tip. In other words reducing the negative effects of the sharp tool edge and flat tool tip with minimal changes to the existing tool design.
With a tool gap of 3.2 $[mm]$ as in recent research at the UTwente [15, 17], the tip of the tool levels with the top of the currently printed layer.

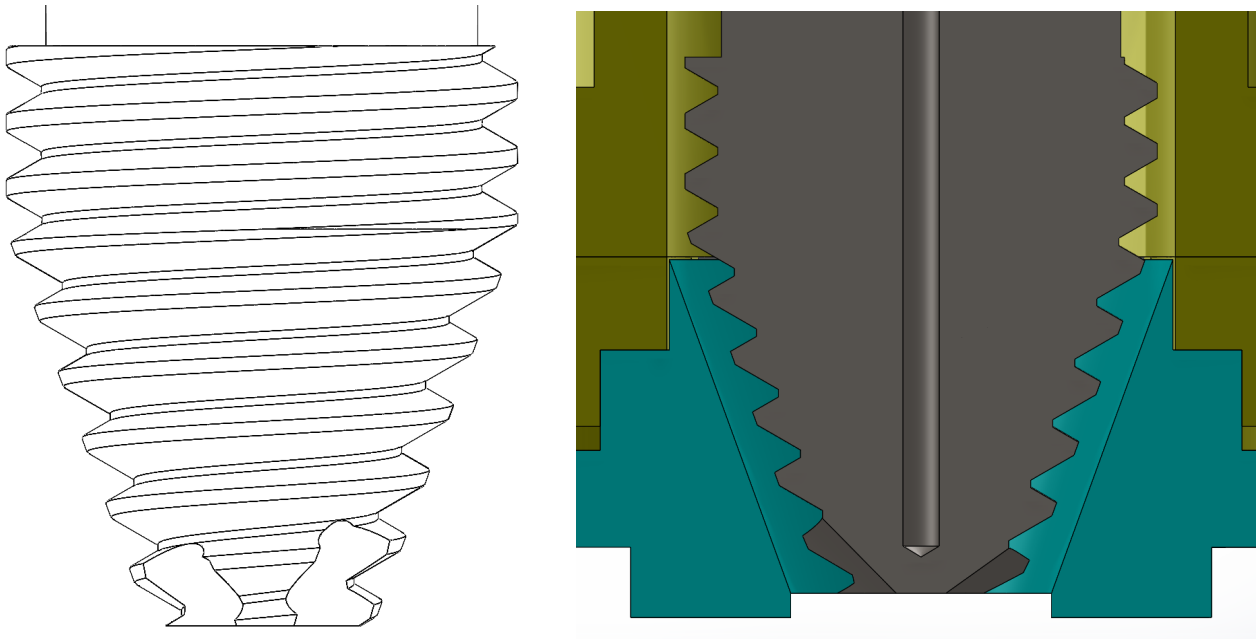

52.a. Sketch

52.b. Cross section view in FSEAM printing head

Figure 52: Tool design with slots feature

A sketch of the design is presented in Figure 52. The technical drawing of this design can be found in Appendix C.2. The SolidWorks file can be obtained on request.

C.1.3 Thermocouple placement

In order to be able to place a K-type thermocouple into the tool to get accurate temperature measurements of the material flow temperature at the tool tip in FSEAM, the following features had to be added to the tool design.

Blind holes
It can be seen in the sketches of the proposed tool designs in Figures 49, 51 and 52 that a blind hole of 1.5 $[mm]$ diameter is drilled that stops 1.5 $[mm]$ from the tool tip. In this hole, a thermocouple can be easily placed to give an indication of the printed material temperature at the tool tip.
In an ideal case, the thermocouple would be placed right at the tool tip as the current temperature measuring location is prone to a thermal gradient with respect to the tool tip itself due to the thermal conductivity of the tool material. However, placing the thermocouple closer to the tool tip with a blind hole was not possible for manufacturability reasons.

Through holes
In order to find a method to place a thermocouple closer to the tip of a tool in an experimental manner, a hole of 1.5 $[mm]$ diameter throughout the current design is made just through the tip such that the opening diameter in the tip is 1 $[mm]$ as can be seen in Figure 53. In this way a thermocouple can be placed tightly into the tip of the tool. By trying to weld it into place and flatten the tip surface to its original geometry, it the thermocouple can measure the true temperature of processed material at the tip location.

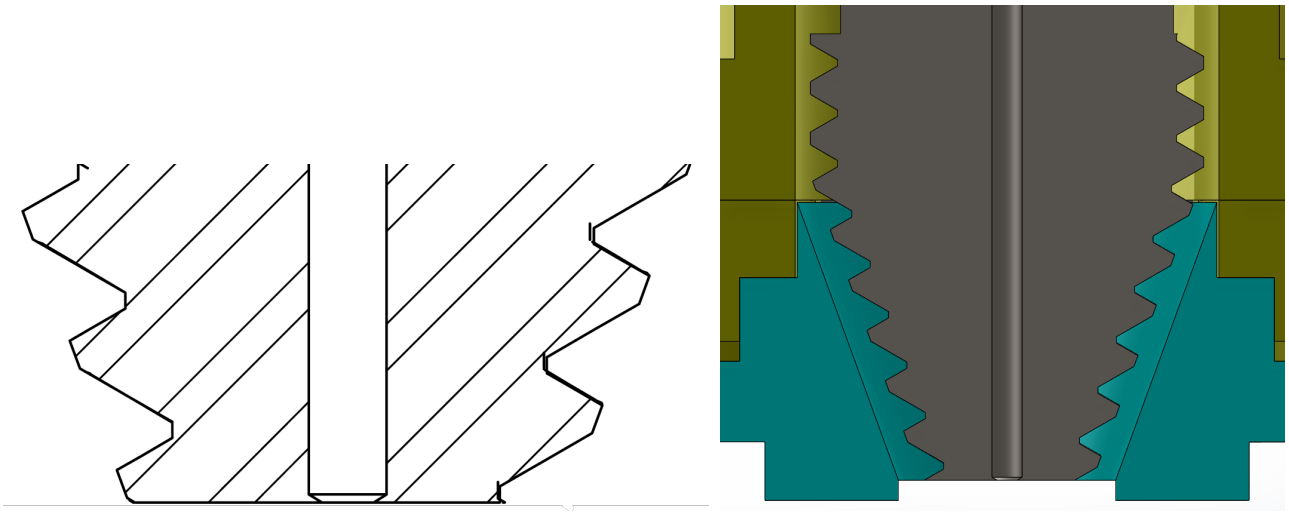

53.a. Cross section detail of through-out hole

53.b. Cross section view in FSEAM printing head

Figure 53: Tool design with hole trough-out tool

By doing so, an indication of the temperature difference between the true printing material temperature at the tip and the measured temperature by the thermocouple placed in a tool with a blind hole can be investigated.

Slots & Wireless device

The data measured with the thermocouple in the rotating tool cannot be transmitted to a data retrieving device with a fixed wired connection, simply because the tool is rotating in an electric motor. Therefore, a wireless data transmitting device based on WiFi was made by Rutger Visser (researcher at the UTwente at the time of writing) that can be attached to the rotating tool in order to solve this problem. The device imposes redesign of the mounting head, which is part for future work.

In order to guide the thermocouple wires to this wireless device, slots had to be implemented into the designed tools as shown in Figure 54. Details on dimensions can be found in the technical drawings in Appendix C.2

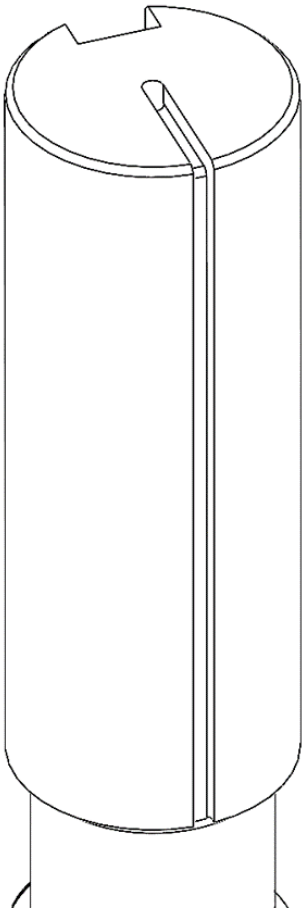

Figure 54: Guiding slot applied in all tool designs for guiding thermocouple wires to wireless sending device *van Rutger*

C.2 Technical Drawings

On the next pages, technical drawings are presented made and used for producing the newly designed tools as explained in Section C.1.

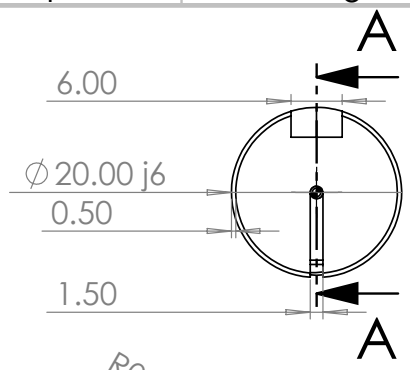

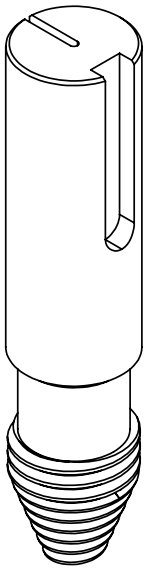

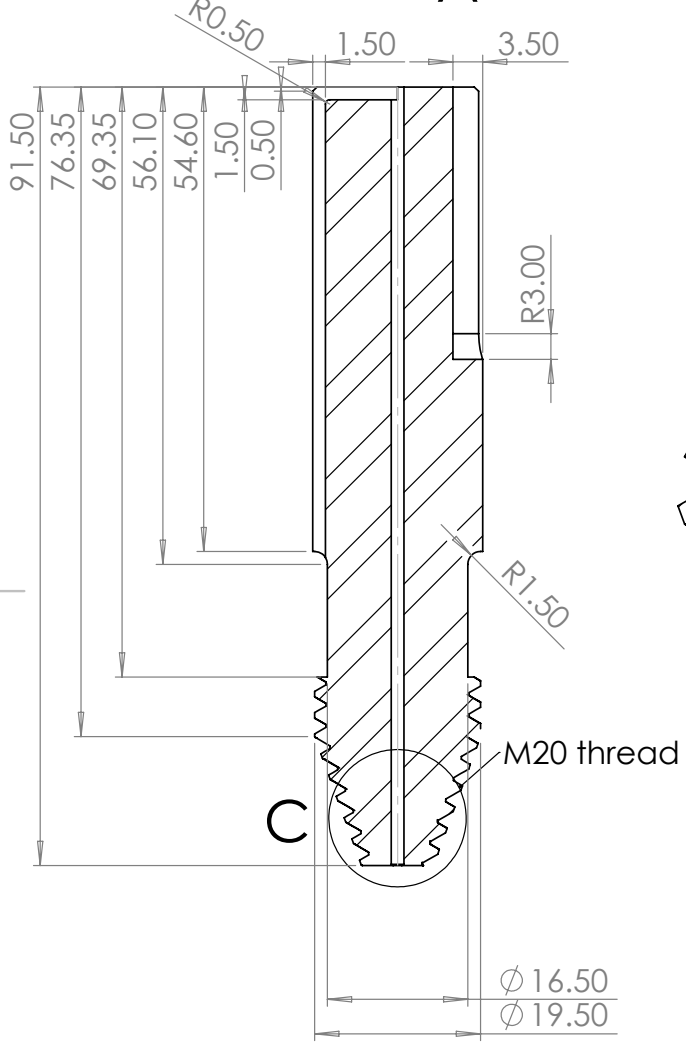

SECTION A-A

SCALE 1.25 : 1

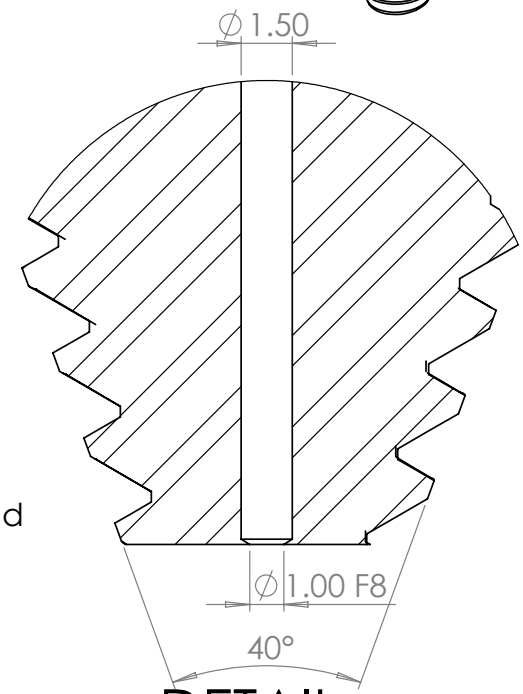

DETAIL C

SCALE 5 : 1

UNLESS OTHERWISE SPECIFIED: DIMENSIONS ARE IN MILLIMETERS SURFACE FINISH: TOLERANCES: LINEAR: ANGULAR:	FINISH:	DEBURR AND BREAK SHARP EDGES	DO NOT SCALE DRAWING / REVISION

	NAME	SIGNATURE	DATE
DRAWN			
CHK'D			
APPV'D			
MFG			
Q.A			

MATERIAL:	TITLE:	
WEIGHT:	DWG NO. Tool_v2	A4
	SCALE:1:1	SHEET 1 OF 1

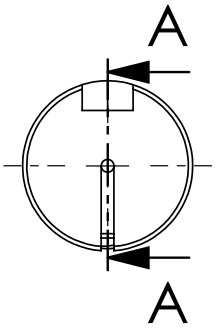

Tool dimensions identical to Tool_v2

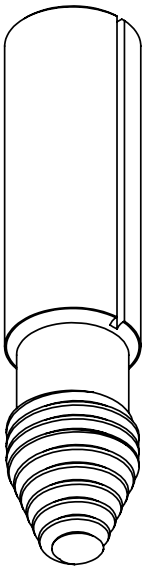

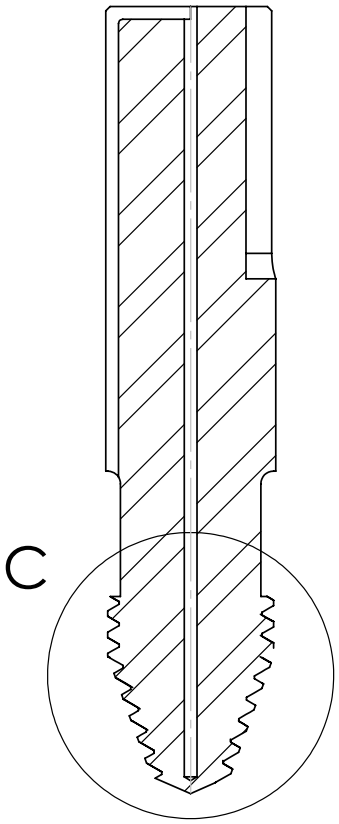

SECTION A-A

SCALE 1.25 : 1

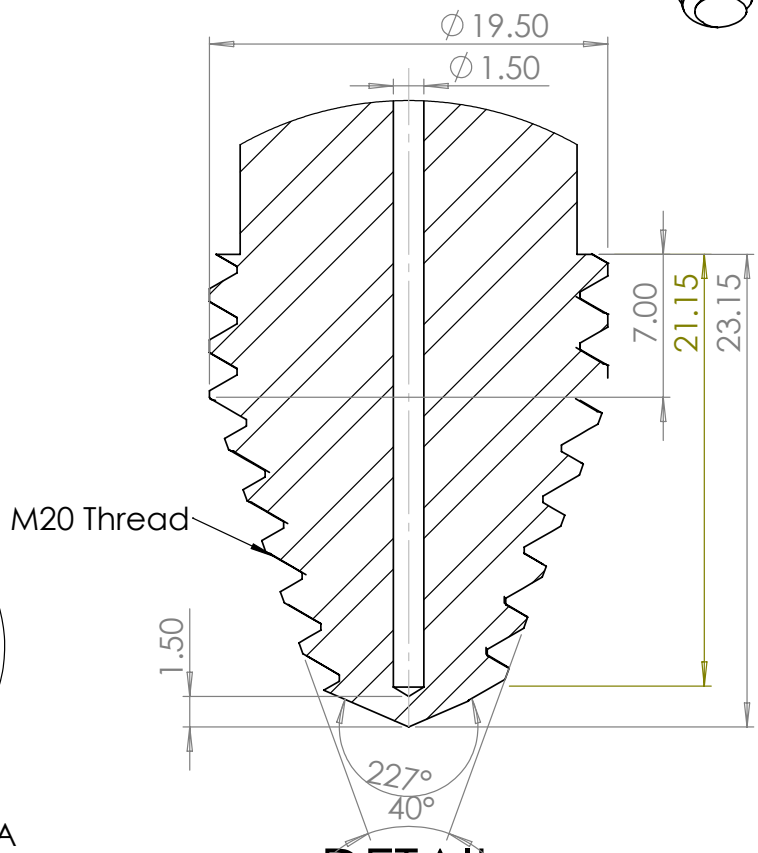

DETAIL C

SCALE 3 : 1

UNLESS OTHERWISE SPECIFIED: DIMENSIONS ARE IN MILLIMETERS SURFACE FINISH: TOLERANCES: LINEAR: ANGULAR:		FINISH:		DEBURR AND BREAK SHARP EDGES		DO NOT SCALE DRAWING	REVISION
	NAME	SIGNATURE	DATE				TITLE:
DRAWN							
CHK'D							
APPV'D							
MFG							
Q.A				MATERIAL:		DWG NO.	A4
						Tool_v2_long_pointy	
				WEIGHT:		SCALE:1:1	SHEET 1 OF 1

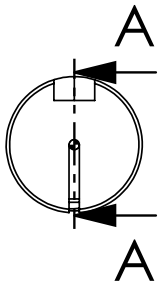

Tool dimensions identical to Tool_v2

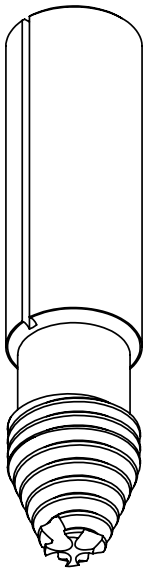

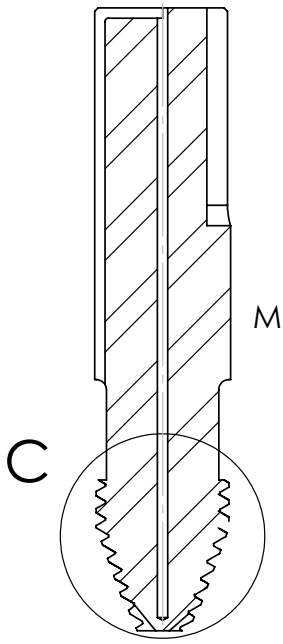

SECTION A-A

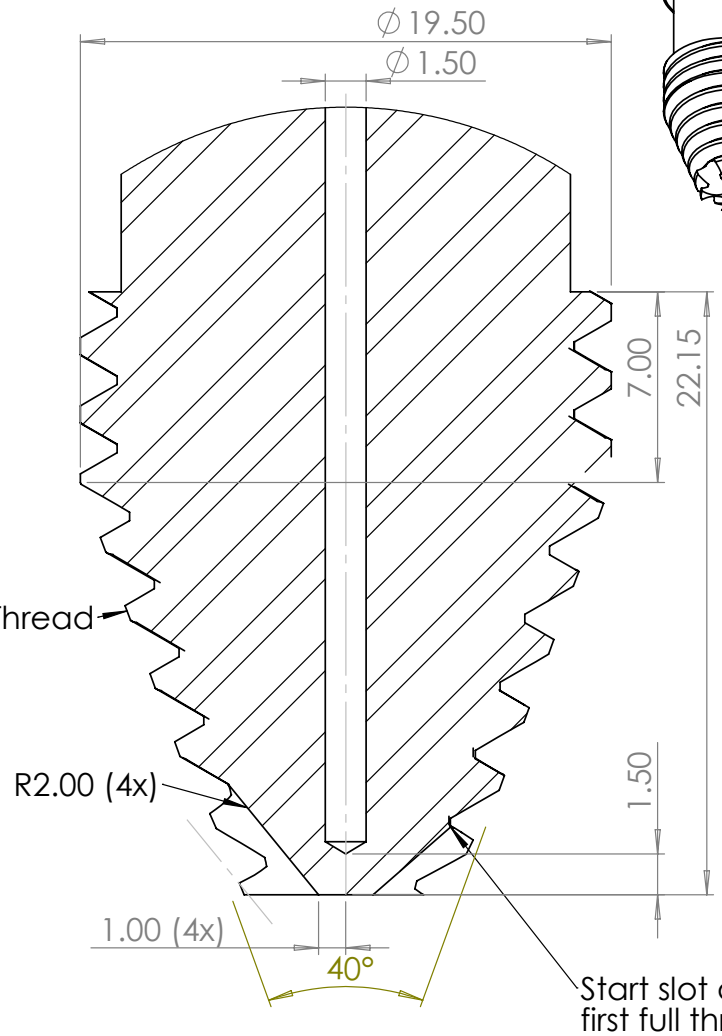

UNLESS OTHERWISE SPECIFIED: DIMENSIONS ARE IN MILLIMETERS SURFACE FINISH: TOLERANCES: LINEAR: ANGULAR:	FINISH:	DEBURR AND BREAK SHARP EDGES	DO NOT SCALE DRAWING / REVISION

	NAME	SIGNATURE	DATE
DRAWN			
CHK'D			
APPV'D			
MFG			
Q.A			

TITLE:

MATERIAL:

DWG NO. A4

Tool_v2_Slots_extra_Fine

WEIGHT:

SCALE:1:1

SHEET 1 OF 1

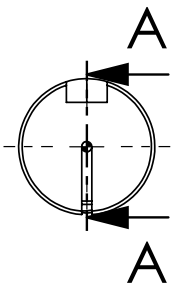

Tool dimensions identical to Tool_v2

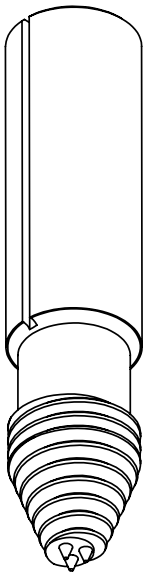

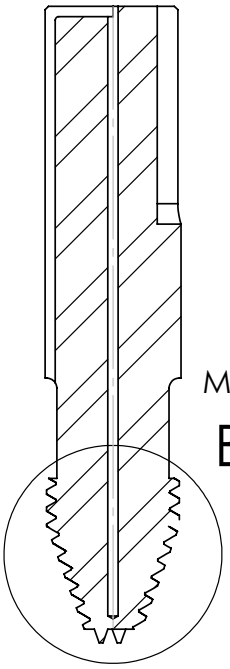

SECTION A-A

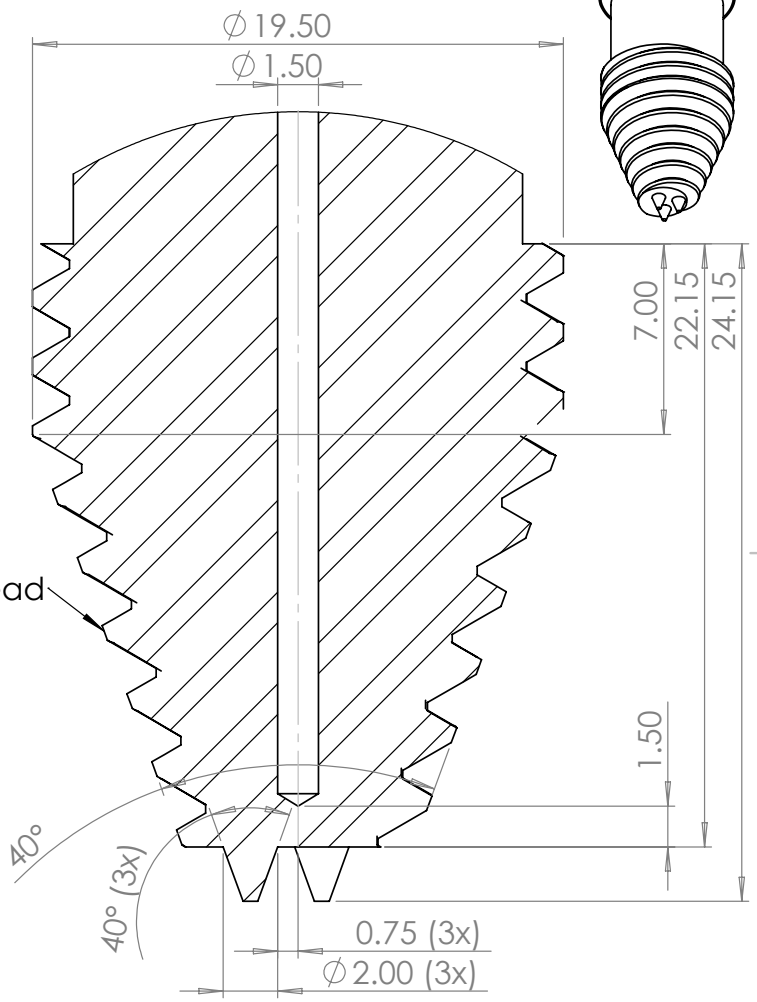

DETAIL B

SCALE 4 : 1

UNLESS OTHERWISE SPECIFIED: DIMENSIONS ARE IN MILLIMETERS SURFACE FINISH: TOLERANCES: LINEAR: ANGULAR:	FINISH:	DEBURR AND BREAK SHARP EDGES	DO NOT SCALE DRAWING / REVISION

	NAME	SIGNATURE	DATE
DRAWN			
CHK'D			
APPV'D			
MFG			
Q.A			

TITLE:

MATERIAL:

DWG NO. Tool_v2_Pins

A4

WEIGHT:

SCALE:1:1

SHEET 1 OF 1

C.3 Additional Concepts

Below, rejected tool design concepts for Section C.1 are presented with a short explanation. The rejected concepts can still serve as inspiration for future research. All concepts are derived from the available tool design used in earlier research [19] as presented in Figure 22. Attention must be paid to the principle of the features, rather than the exact dimensions. All SolidWorks files of the concept tools are available on request

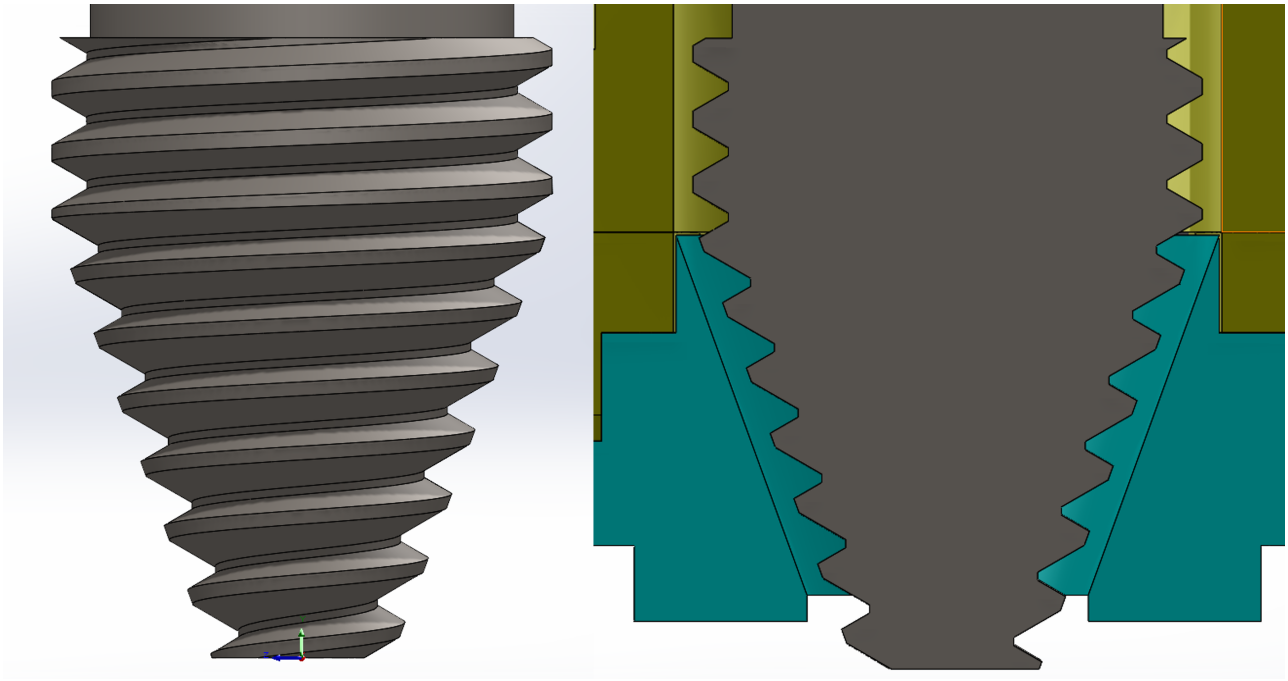

Figure 55: Rejected tool design concept with a long threaded feature with respect to the earlier used tool

In Figure 55, the rejected concept featuring a longer tapered threaded section is presented. A simple solution in order to mix the previously printed layer with the currently printed layer as seen in FSLW. Thread would induce a vertical material flow in mixing of the layers. The concept was rejected on concerns about deforming the geometry of the previously and currently printed layer too much.

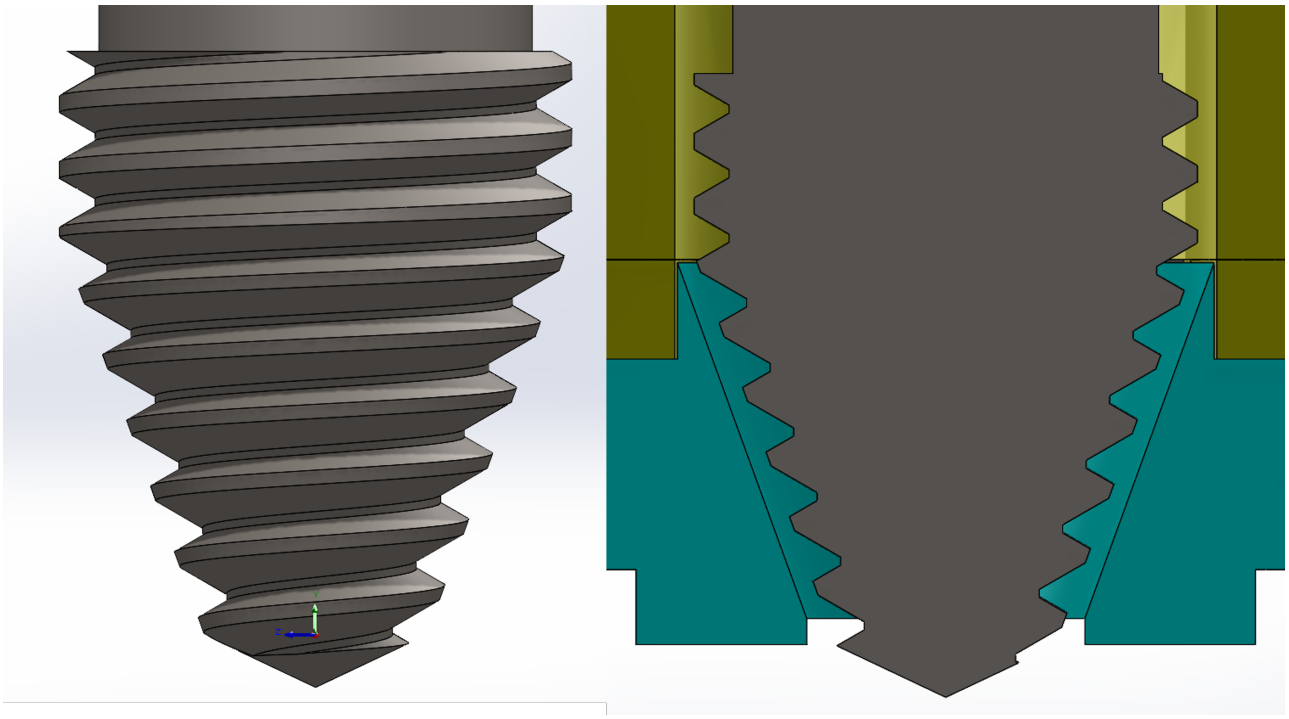

Figure 56: Rejected tool design concept with a long edged feature with respect to the earlier used tool

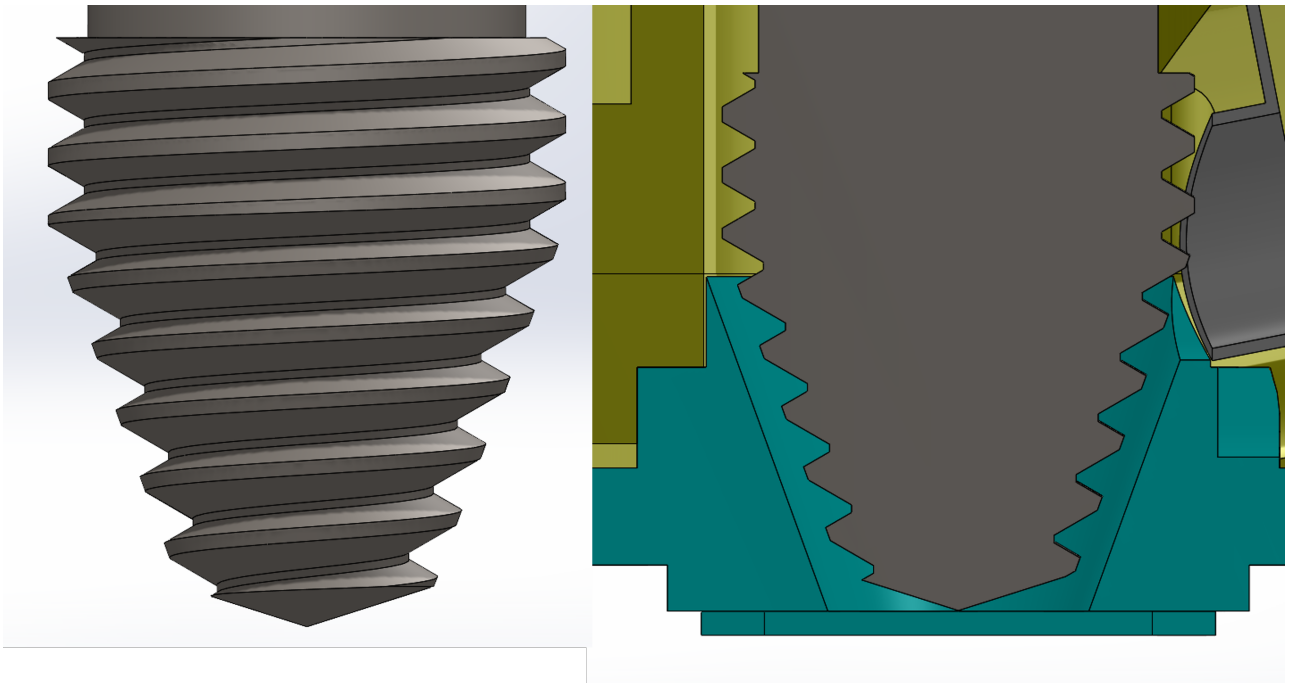

Figure 57: Rejected tool design concept with a short feature with respect to the earlier used tool

In Figures 56 and 57, the rejected concepts with an edged tip are presented. The design in Figure 56 is aimed on stirring the previously printed layer with the currently printed layer and solving the geometry problem from the design presented in Figure 55. The design in Figure 57 is aimed on giving the processed material more space to travel to the centre of the tool in order to even the pressure distribution of added material. The two concepts are combined in the tool design presented in Figure 51 balancing the two effects from both concepts in a hybrid design.

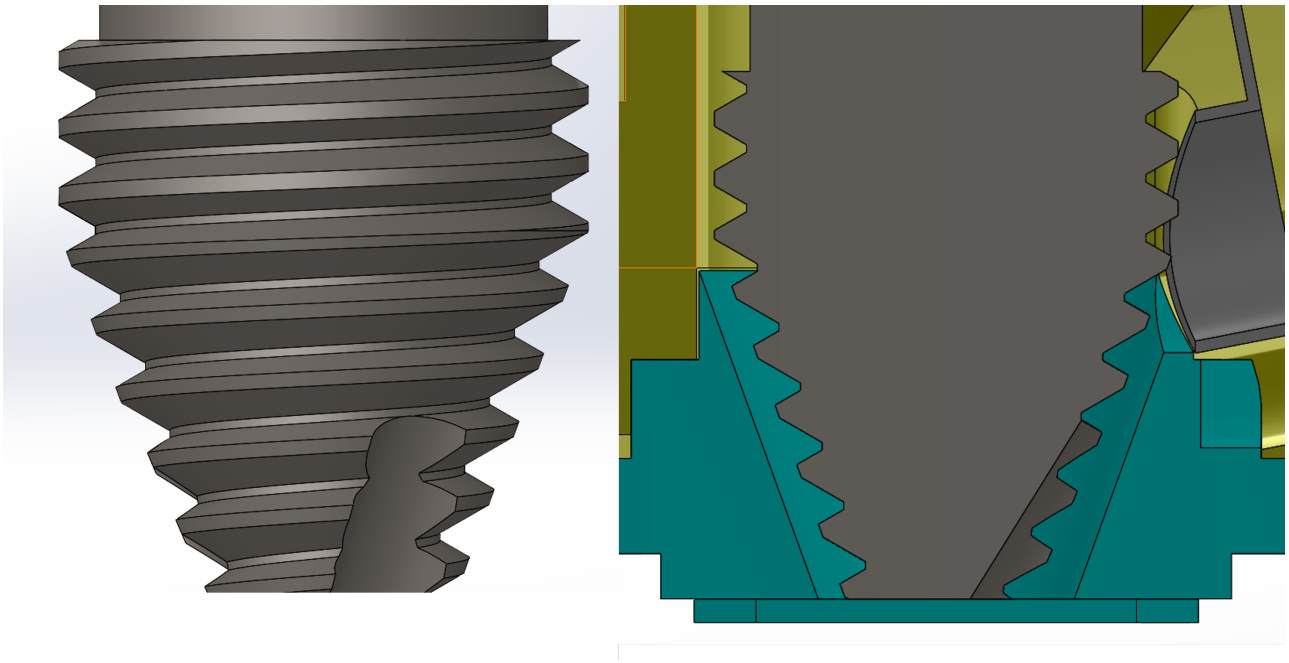

Figure 58: Rejected tool design concept with a rough slotted feature with respect to the earlier used tool

In Figure 58, the rejected concept with three evenly spaced slots over at least three thread pitches is presented. This concept was rejected as too large slots result in severe pressure loss whilst processing material with the screw as known from earlier experience with slotted tool designs [55]. Therefore, the smaller slots from the tool design presented in Figure 52 were chosen to try FSEAM experiments with.

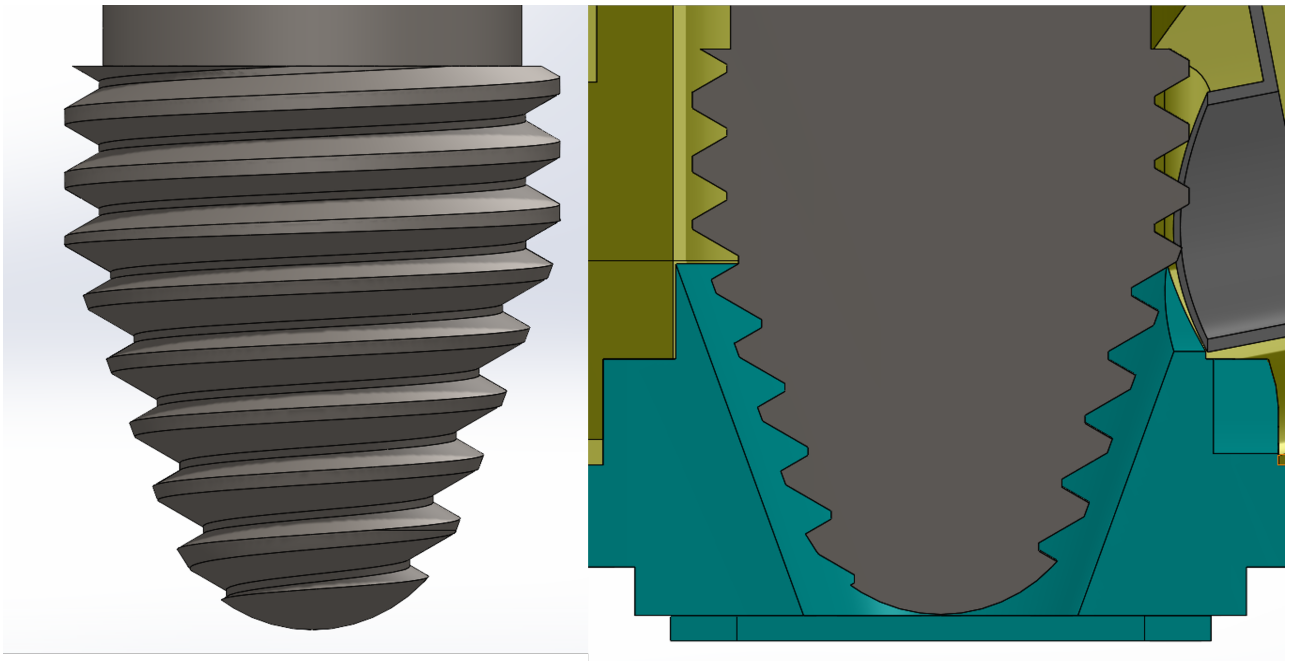

Figure 59: Rejected tool design concept with a rounded tip feature with respect to the earlier used tool

In Figure 59, the rejected concept with a rounded tip is presented. This concept also gives more space to let processed material travel to the centre of the tool for more even material and thus pressure distribution. As this concept is based on the same effect as the edged concept in Figure 57, it was chosen to further develop the more 'hybrid' edged design. Also, the edged design is simpler to produce and testing a feature effect with a single tool is beneficial for financial project management.

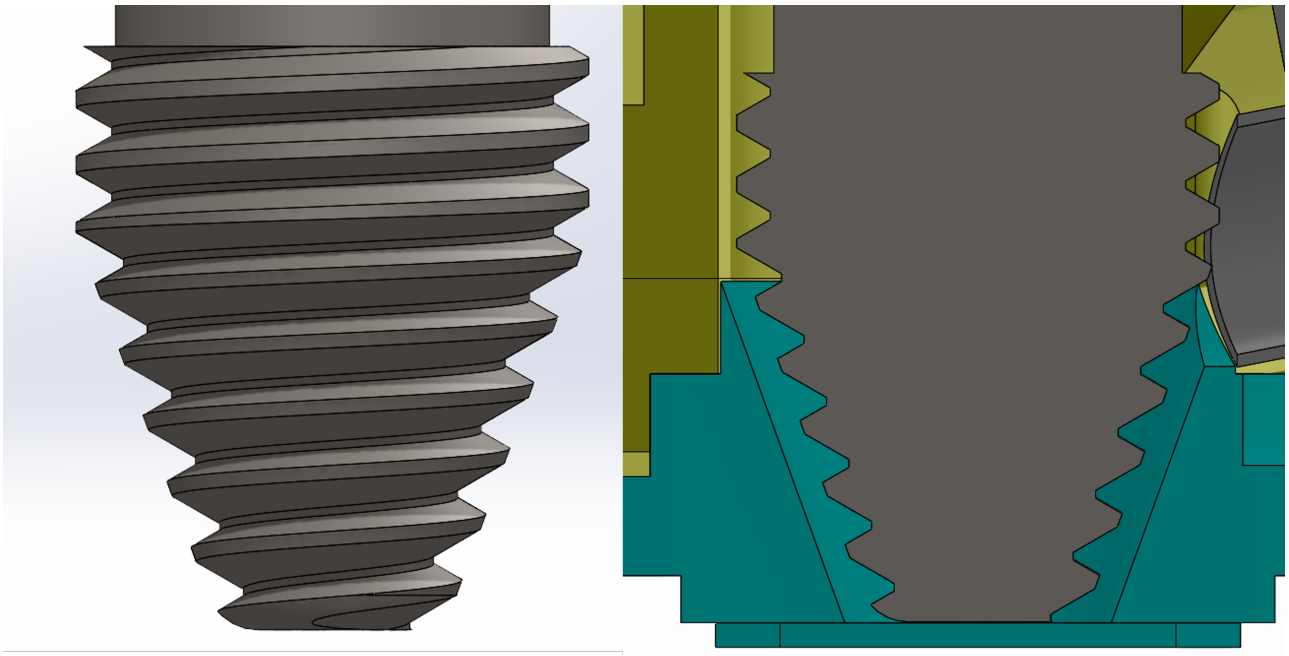

Figure 60: Rejected tool design concept with a filleted tip feature with respect to the earlier used tool

In Figure 60, the rejected concept with an filleted edge is presented. This concept is based on the same ideas and desired effects as the rounded rejected concept presented in Figure 59. This concept is thus rejected for the same reasons and because the fillet was seen as too subtle to have significant effects on the material flow.

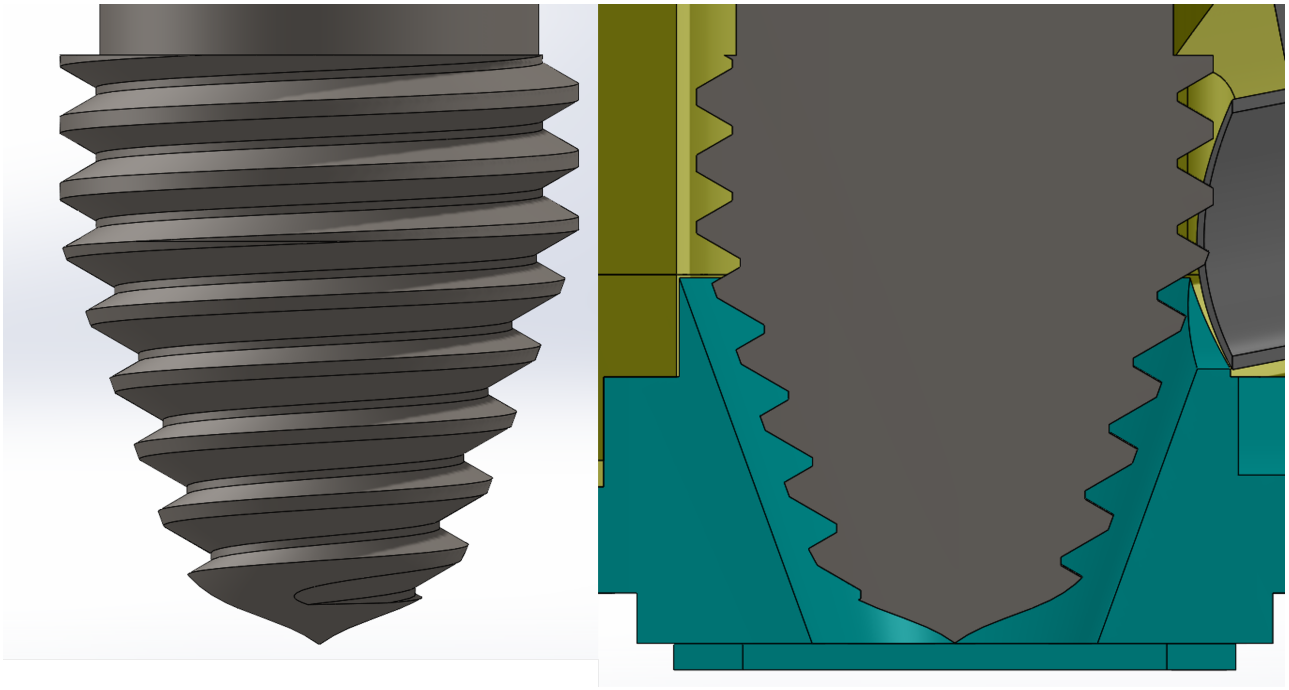

Figure 61: Rejected tool design concept with a smooth curved feature with respect to the earlier used tool

In Figure 61, the rejected concept with a more advanced smooth curved is presented. The curvatures were designed as such that material flow would not be affected by any edges and that processed material gathers needless in the middle of the tool. This concept is rejected as this design would likely not give significant material flow benefits over a more simple to produce edged concept as presented in Figure 51.

D Appendix: First experiment series & Modifications

Working order first series

Below in Table 5, the working order of the first experiment series is presented including date, when parts in the setup were changed and other peculiarities that were worth mentioning.

Table 5: Working order of first experiment series including factors of influence

Experiment Tag	Date	Parts Changed (beforehand)	Peculiarities
TG1.5_400_x	11th july '23	First run, all new parts	Uncalibrated feed force load cell Jammed at key 6
TG4.5_400_x	6th sept '23	TC's 1 to 4	Jammed at key 5; deformation of feed material sticking out of feed tube
TG3.5_400_x	12th sept '23	"	From now on 1.5 feeds used per run instead of 2
TG2.5_400_x	12th sept '23	"	-
TG4.5_400_x	15th sept '23	"	-
TG4.5_500_x	15th sept '23	-	-
TG4.5_600_x	15th sept '23	-	Excessive rattling and scraping sounds
TG1.5_400_x	26th sept '23	TC's 1 to 4	Redoing jammed experiment of 11th july
TG1.5_500_x	26th sept '23	-	-
TG1.5_600_x	26th sept '23	-	Excessive squeacking sounds
TG2.5_500_x	26th sept '23	TC's 1 to 4	"
TG2.5_600_x	26th sept '23	-	"
TG3.5_500_x	26th sept '23	TC's 1 to 4	"
TG3.5_600_x	26th sept '23	-	Using backup phone for filming (IPhone instead of Samsung)

Setup changes after first experiment series

Due to the reasons mentioned in Chapter 4, a second experiment series was needed to provide reliable data. For solving the problems encountered during the first series of experiments, the following alterations were made to the setup:

- A **new support frame** was made out of an available 40x40 $[mm]$ extruded aluminium profile system. The old and new support structures are presented in Figure 63. The old support consists of stacked steel parts that were available around the setup.
  The new support has a total height of 440 $[mm]$ and a footprint of 250x250 $[mm]$. The two profiles laying on the top of the frame can be easily adjusted to the required width for letting the nozzle plate rest on it. The frame contains two pairs of a grooved ball bearing combined with a regular ball bearing to function as a vertical guide for the extruded material. The bearing used are: a HepcoMotion W3X bearing and a

Figure 62: Tool housing at nozzle area with dismantled nozzle plates. Arrows indicating aluminium pushing out thermocouples.

SKF 6301-2Z single row deep groove ball bearing. With this design compared to the earlier setup, more stiffness is secured in the support construction and linear guiding of the extrudate is ensured for improved video analysis results of the outflow speed. Figure 63.a shows the new support installed for a FSE experiment.

- **Thermocouples** were welded onto the applicable parts in order to prevent TC1&2 being pressed away by the extruded aluminium. Figure 62 shows the extruded material after dismantling of the nozzle plates. The two red arrows indicate aluminium forced into the 1.5 $[mm]$ diameter thermocouple holes of the nozzle plate, pushing away the thermocouples. Note the difference in penetration depth, explaining temperature data differences between TC1 and TC2.
  Welding of TC1&2 was done by stripping thermocouple wire and using that as an improvised welding electrode. A Labfacility L60+ thermocouple welding device under protection of argon shielding gas was used for welding. Furthermore, thicker K-type thermocouple wire of 0.5 $[mm]$ diameter was used to reduce failure by wire fatigue.

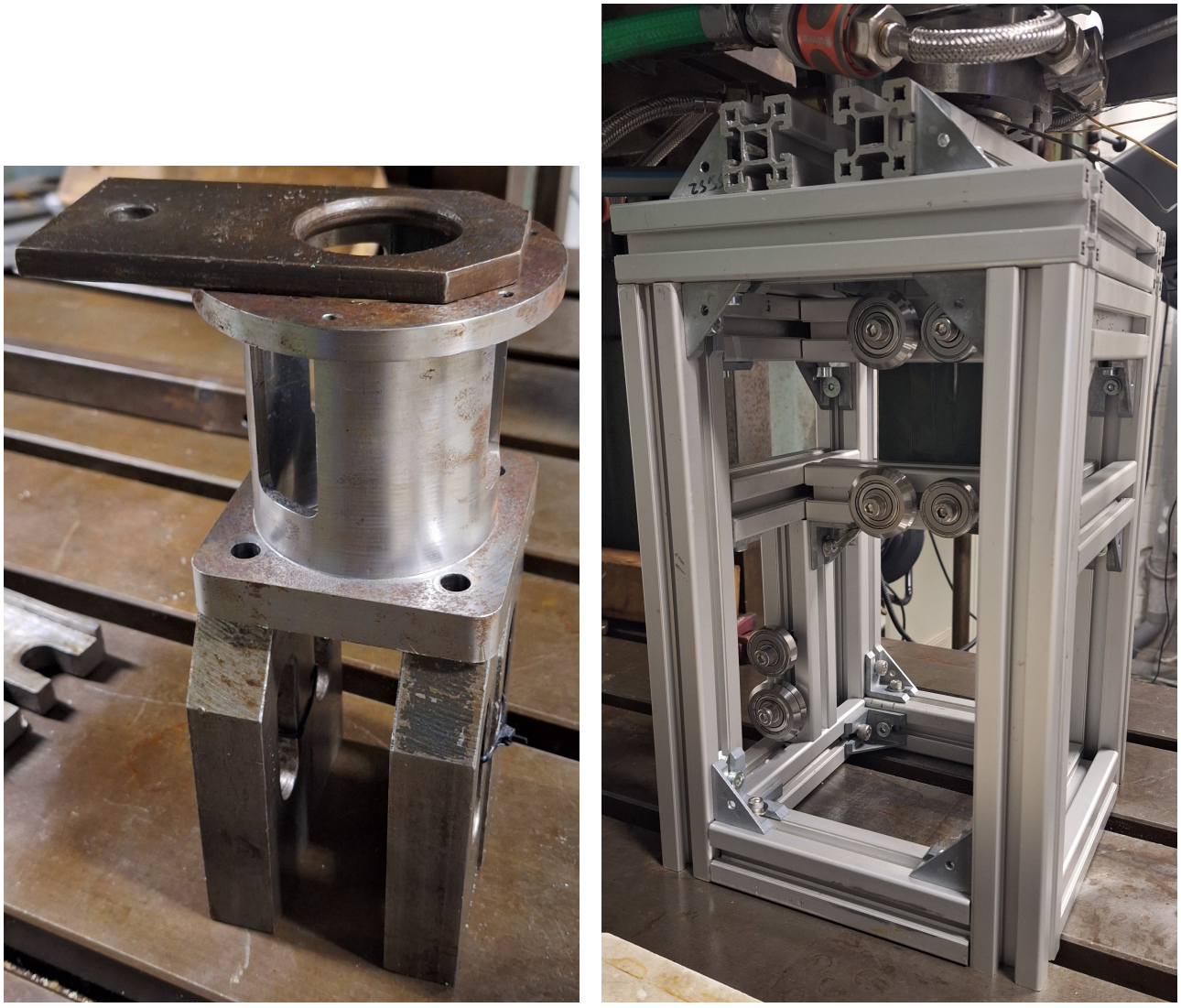

63.a. First series **63.b.** second series

Figure 63: Support frames used in FSE experiments

E Experiment Data Figures: Series 1

On the next pages, additional data figures are presented from the tool gap experiments series 1 as described in Chapter 4. This in order to give a complete and comprehensive overview of all experimental data for future reference.

The experiments are performed in the working order as presented in Table 5.

At first, the overview graphs of average forces, temperatures or torque are presented sorted per tool gap or tool rotation rate with 1 standard deviation in errorbars.
Next, the raw data per experiment is presented in three figures per experiment;

1. The raw data straight from the mentioned Labview programme. This includes normal forces, feed force, thermocouple data and hydraulic cylinder travel with average velocity.
2. The averaged forces and thermocouple data per key setting. Averages taken from the last halve of an extrusion run.
3. The raw torque data cut per key section.

E.1 Overview Figures

The remaining of this page is left blank intentionally to maximise figure size on the next page.

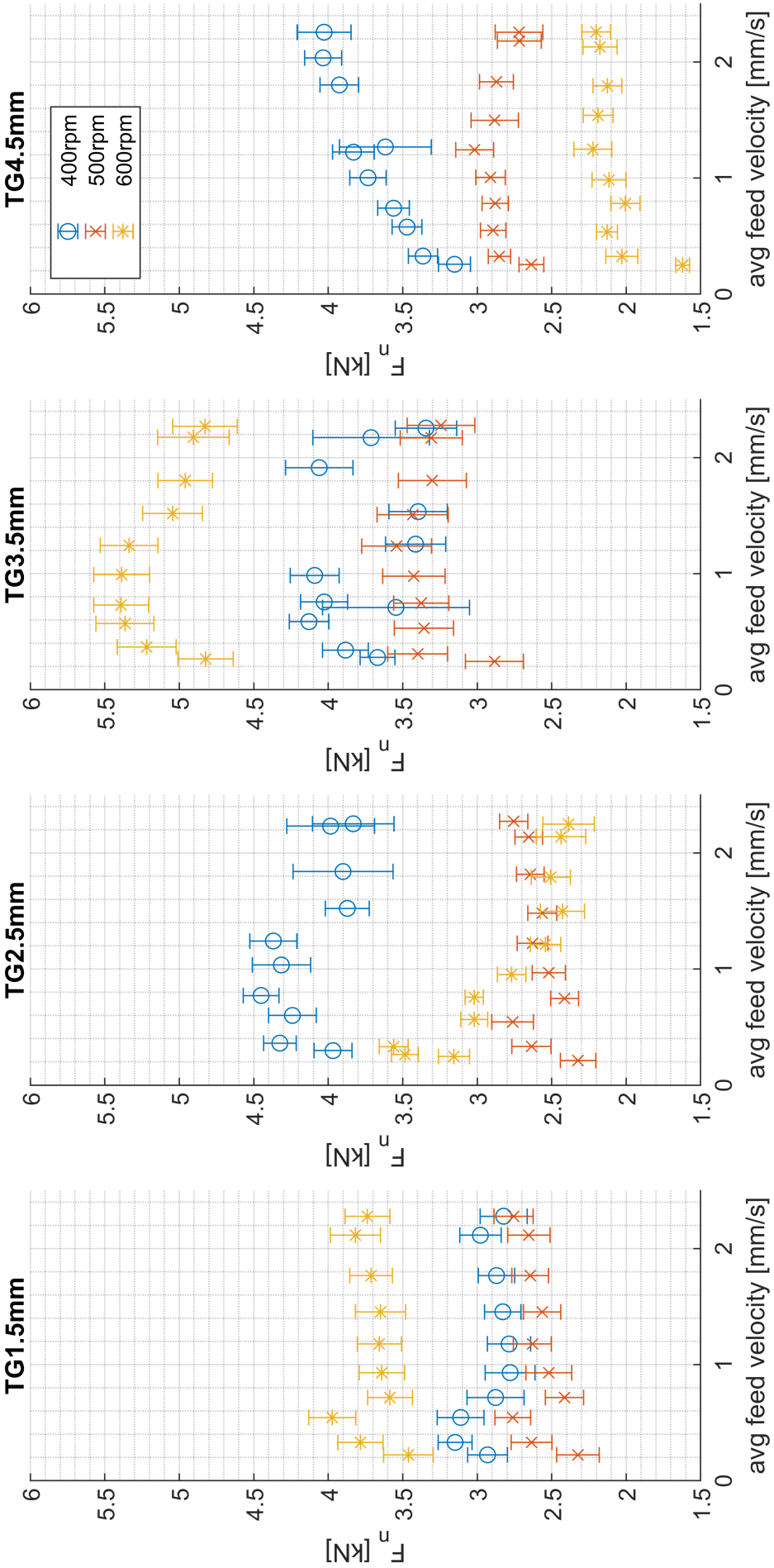

Figure 64: Average normal force sorted per tool gap.

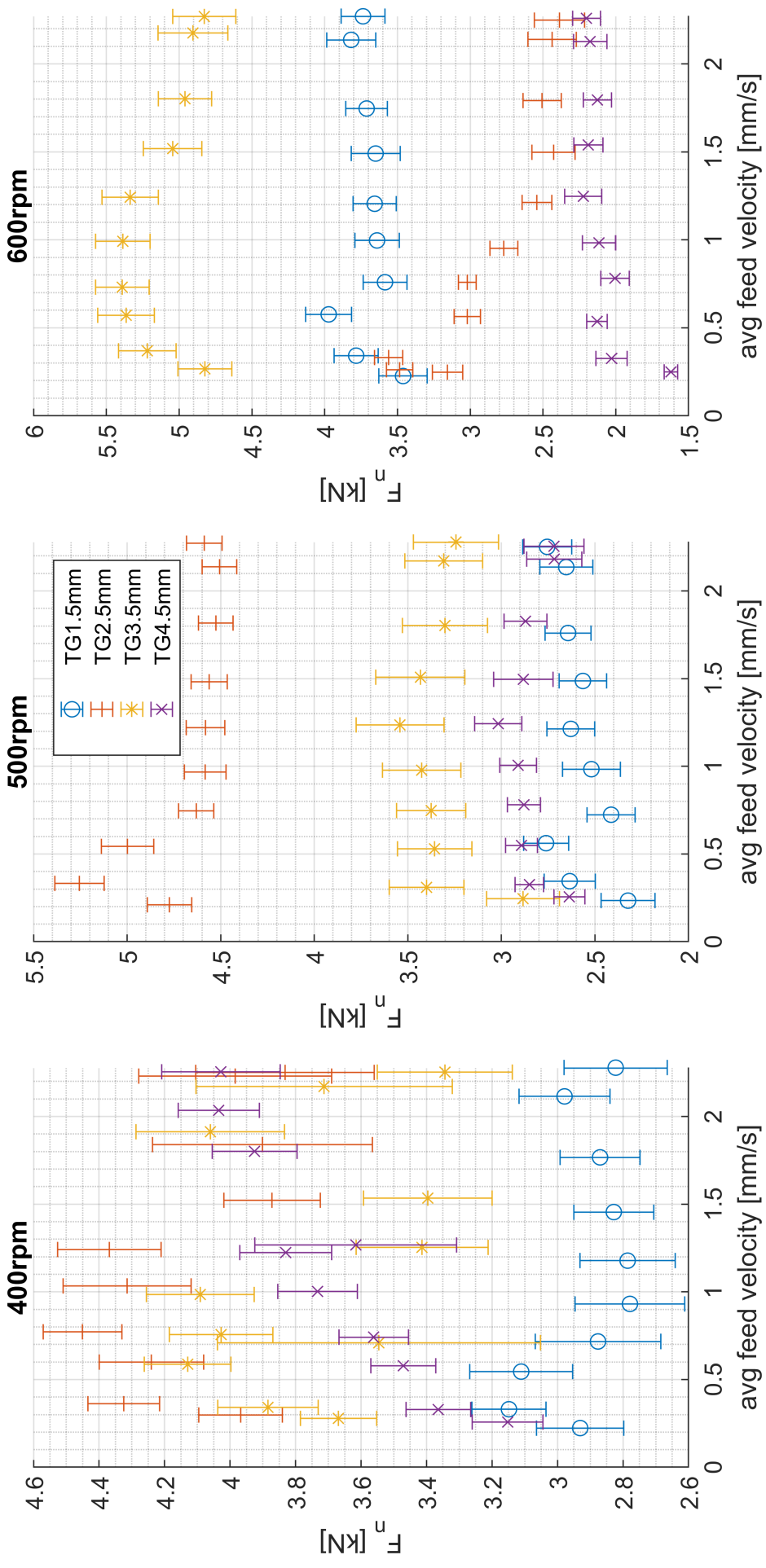

Figure 65: Average normal force sorted per tool rotation rate.

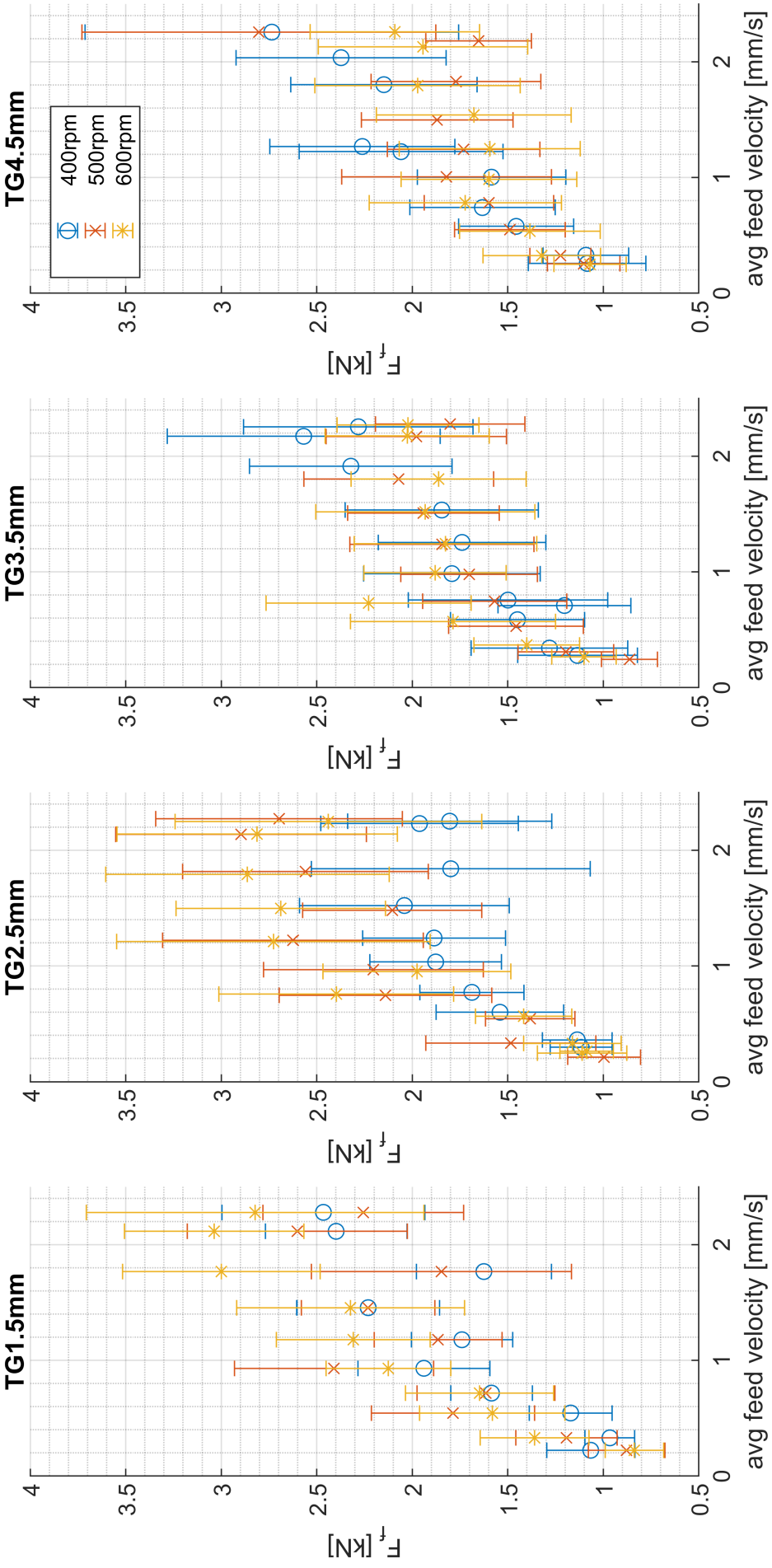

Figure 66: Average feed force sorted per tool gap.

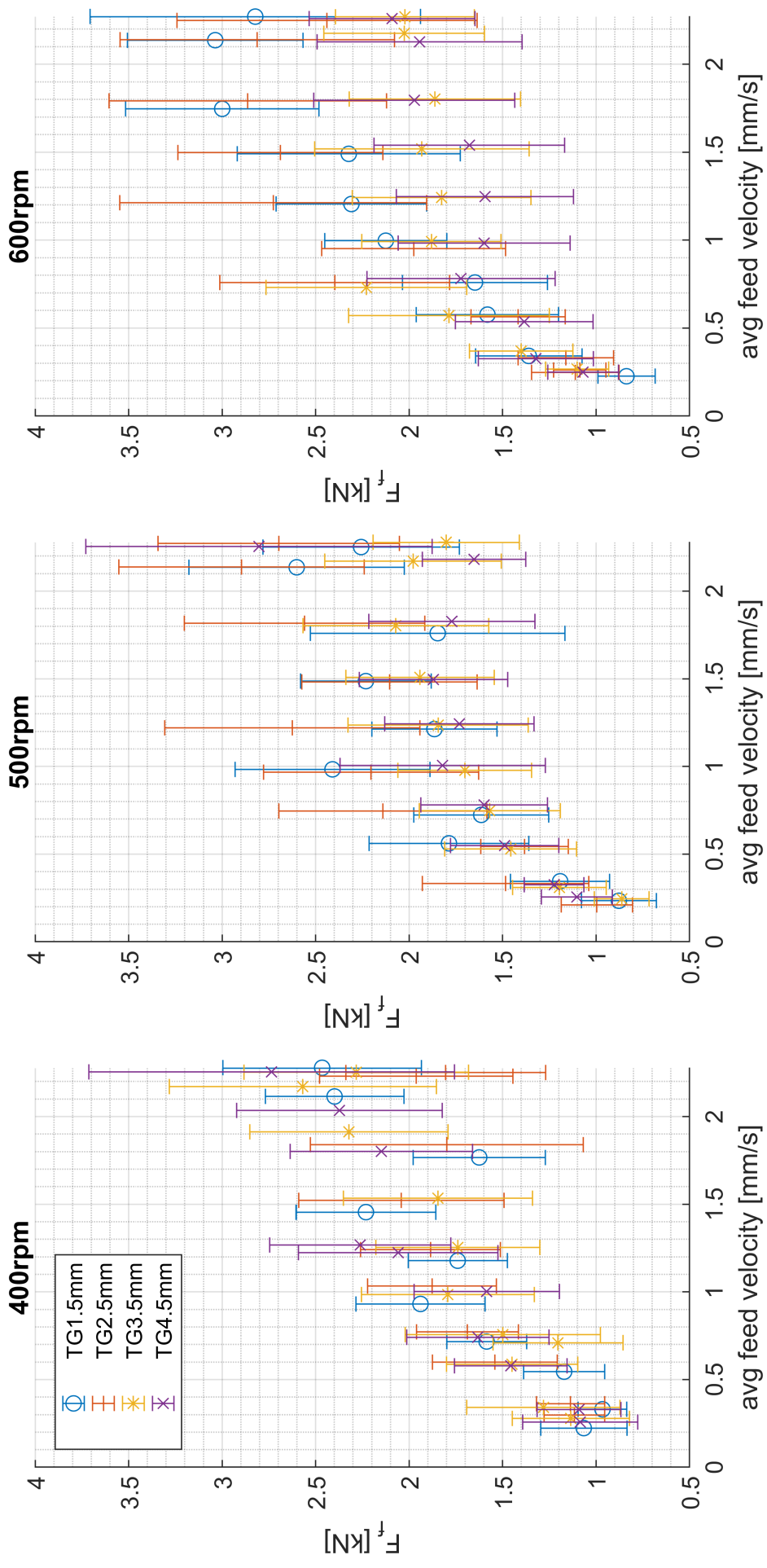

Figure 67: Average feed force sorted per tool rotation rate.

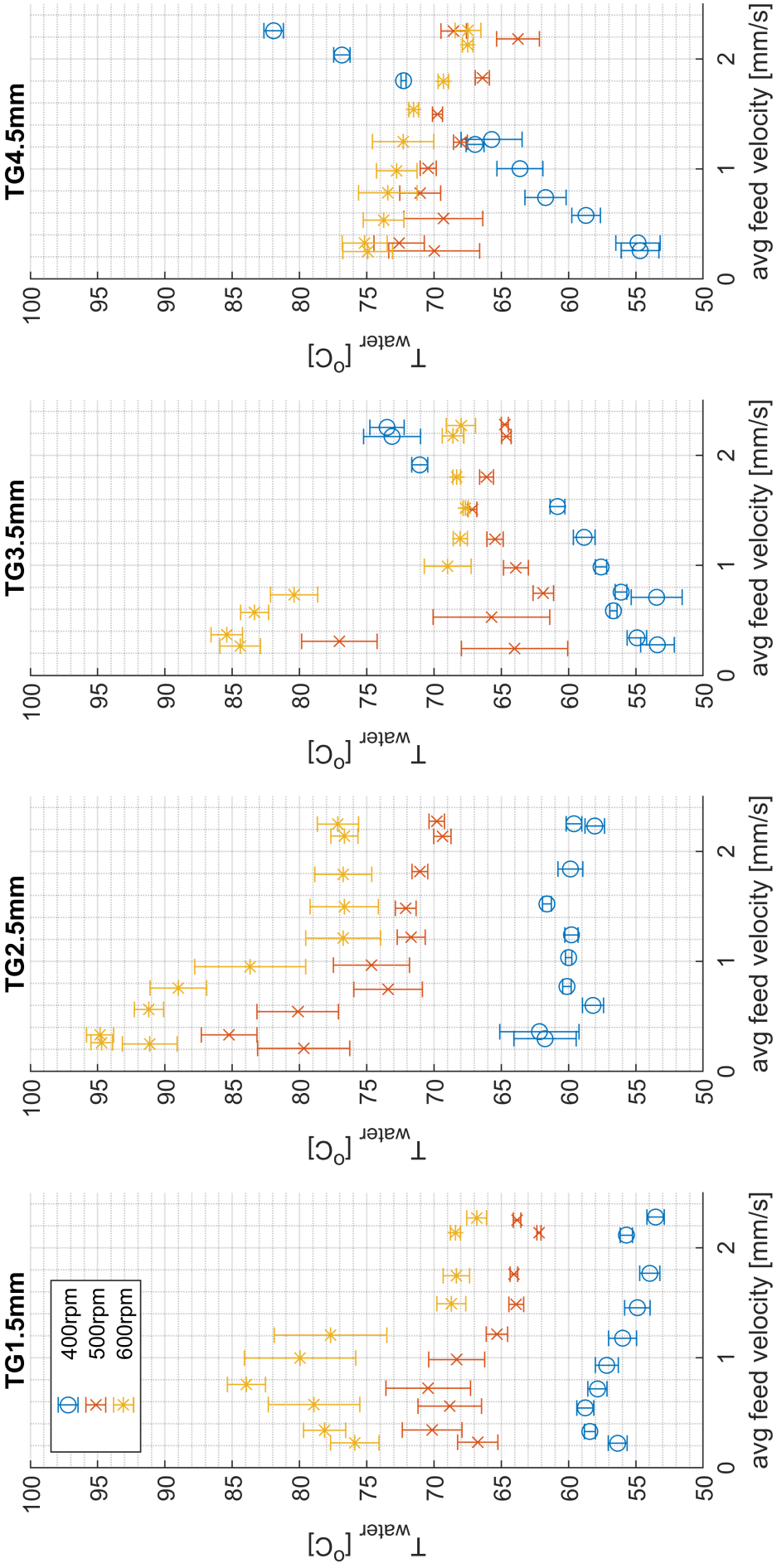

Figure 68: Average water temperature sorted per tool gap.

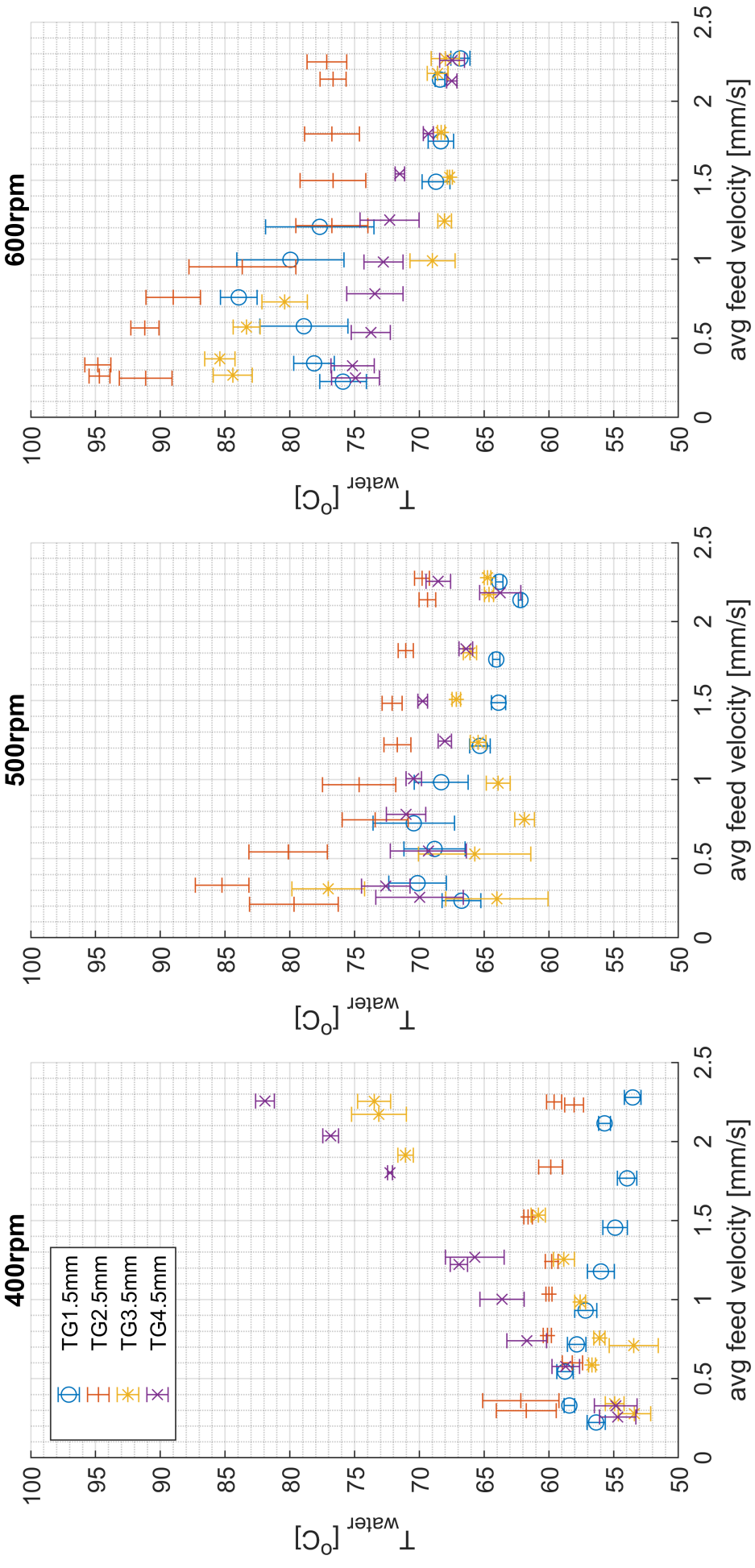

Figure 69: Average water temperature sorted per tool rotation rate.

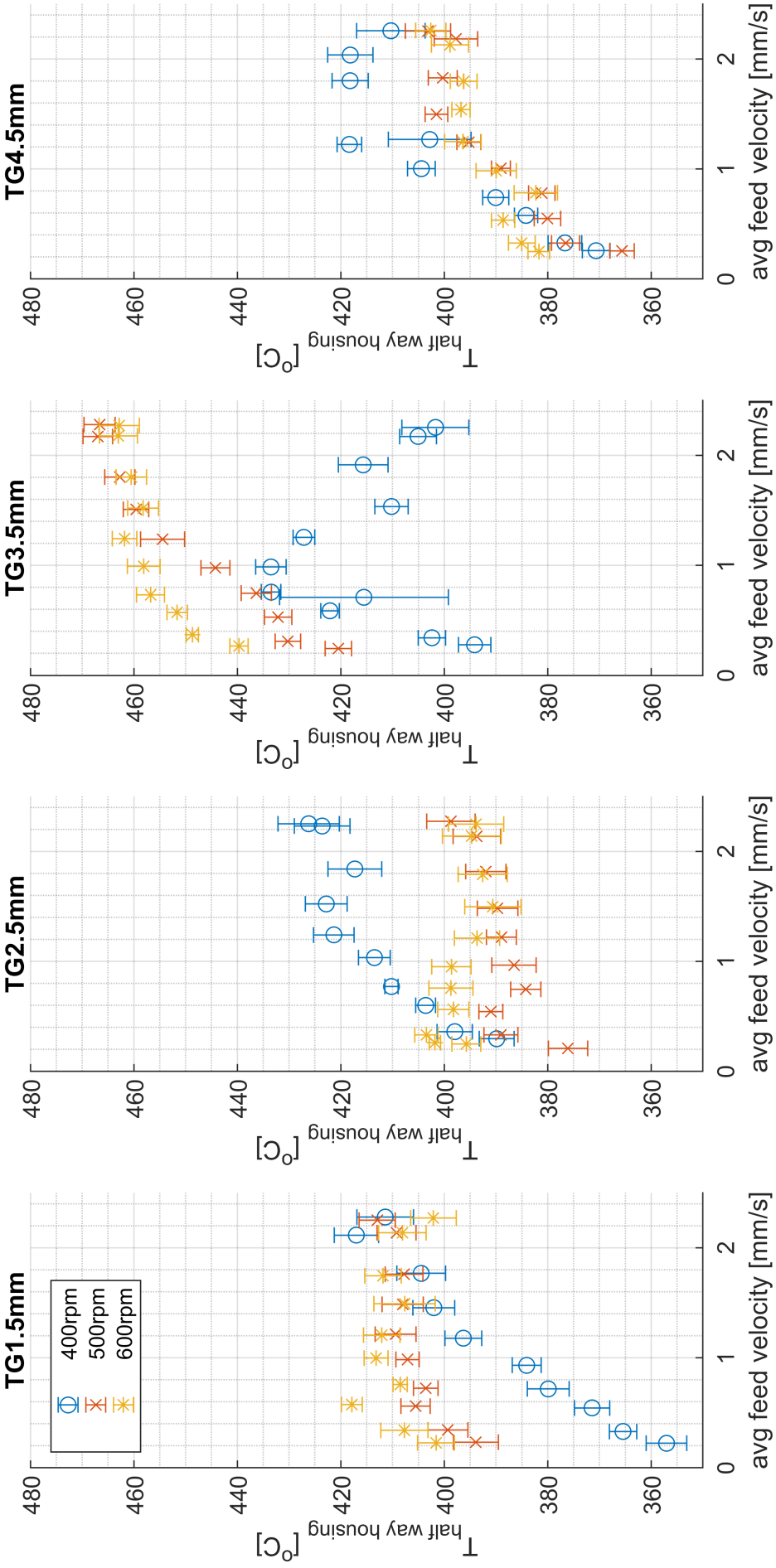

Figure 70: Average temperature half-way the housing sorted per tool gap.

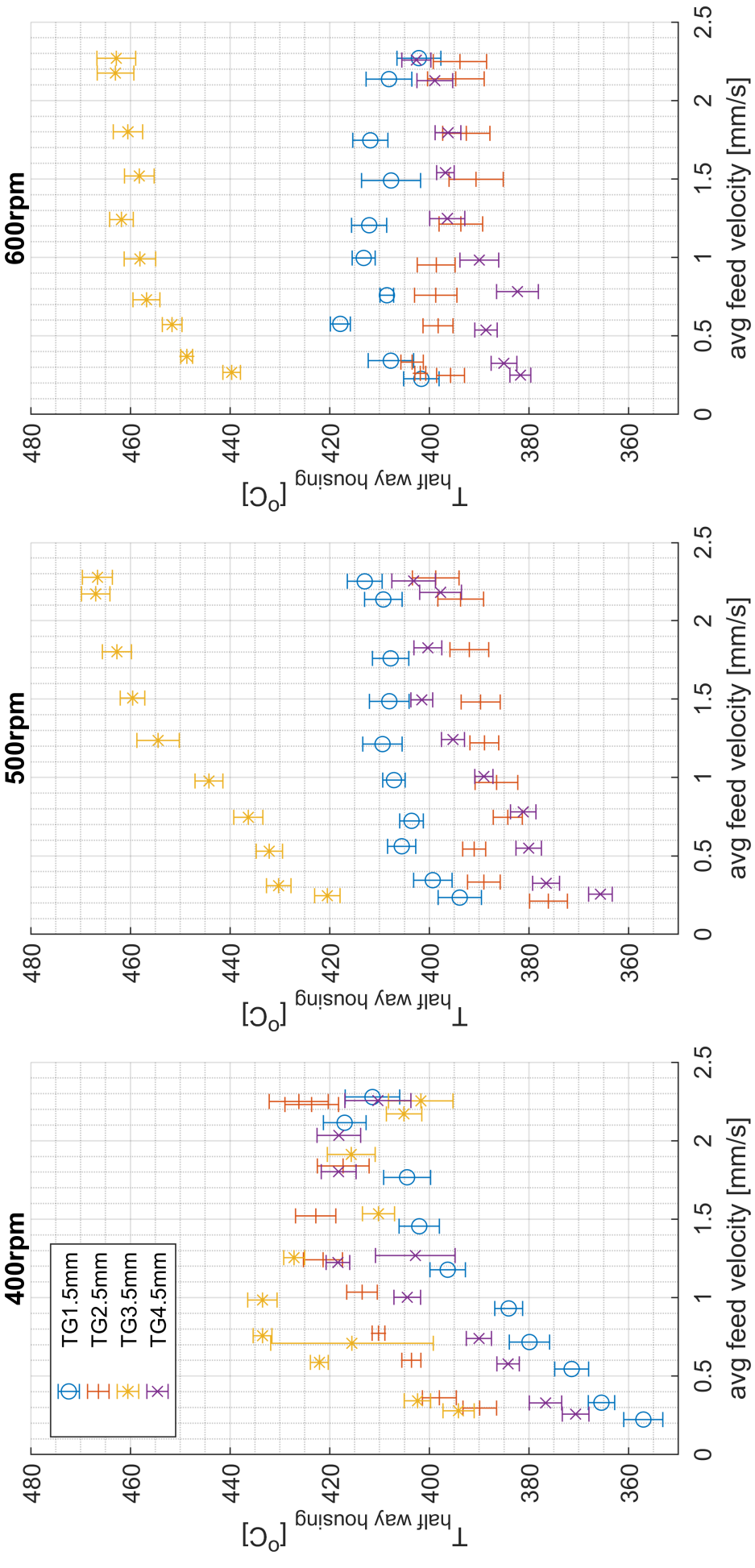

Figure 71: Average temperature half-way the housing sorted per tool rotation rate.

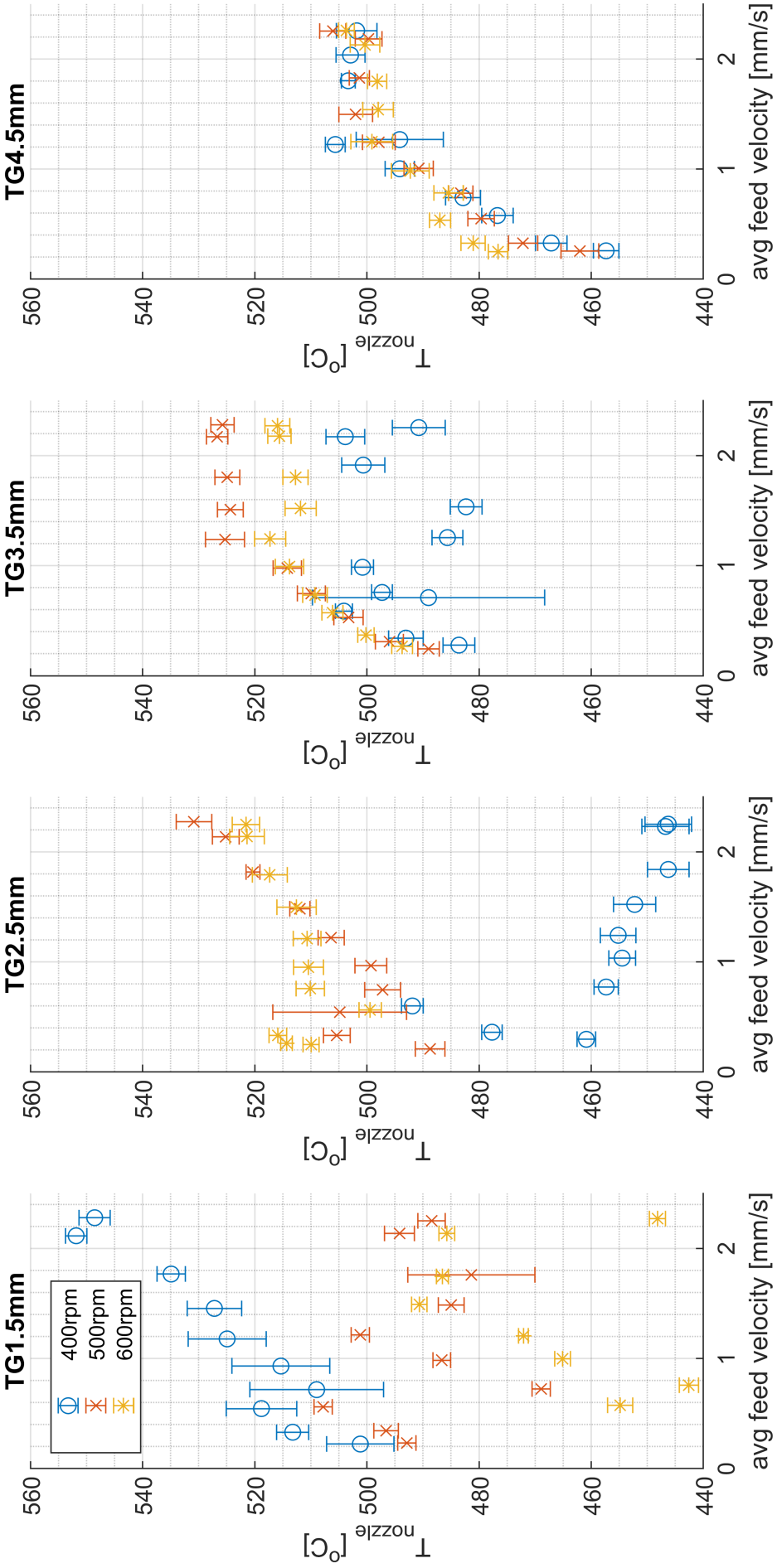

Figure 72: Average nozzle temperature sorted per tool gap.

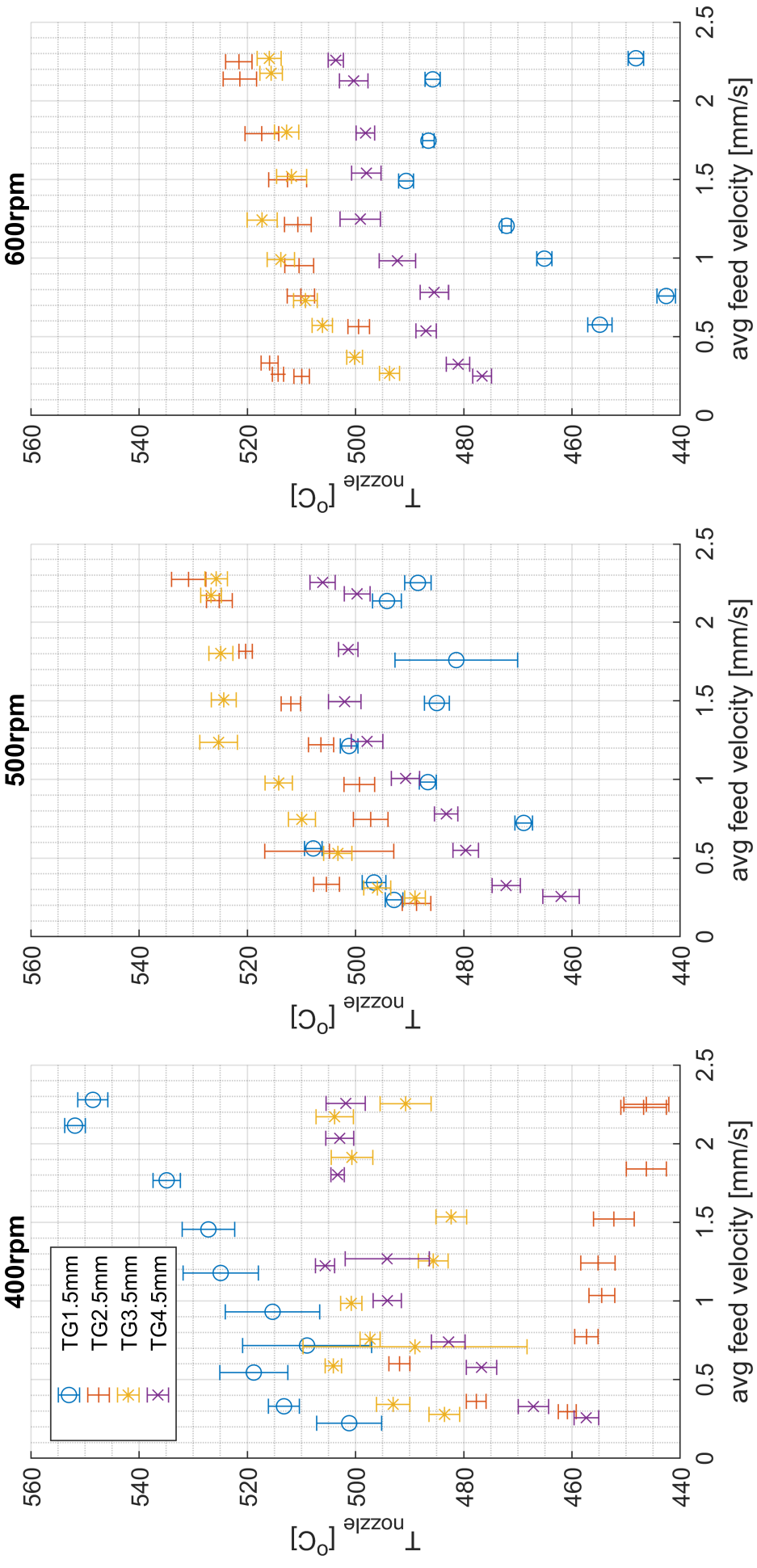

Figure 73: Average nozzle temperature sorted per tool rotation rate.

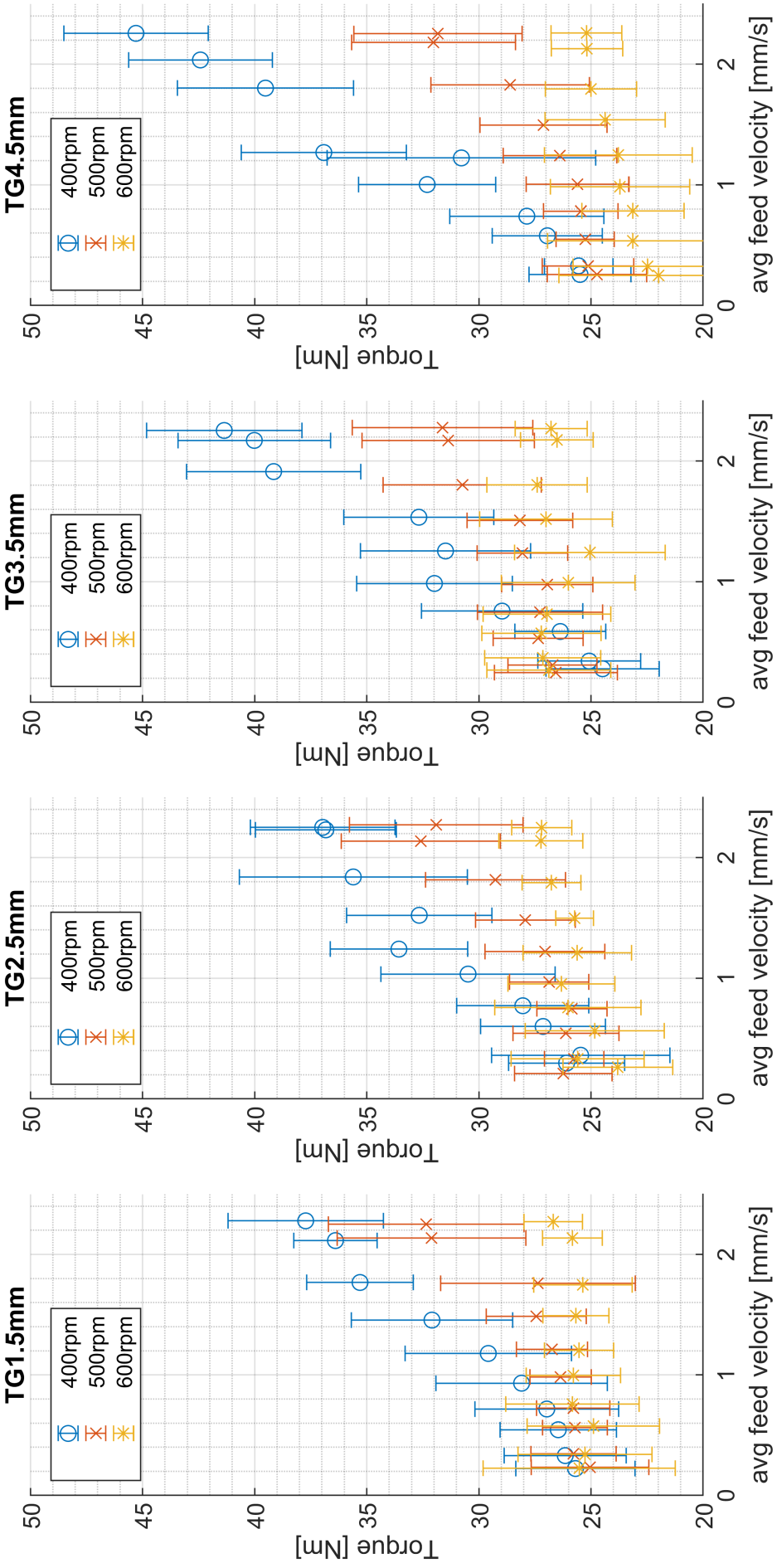

Figure 74: Average torque sorted per tool gap.

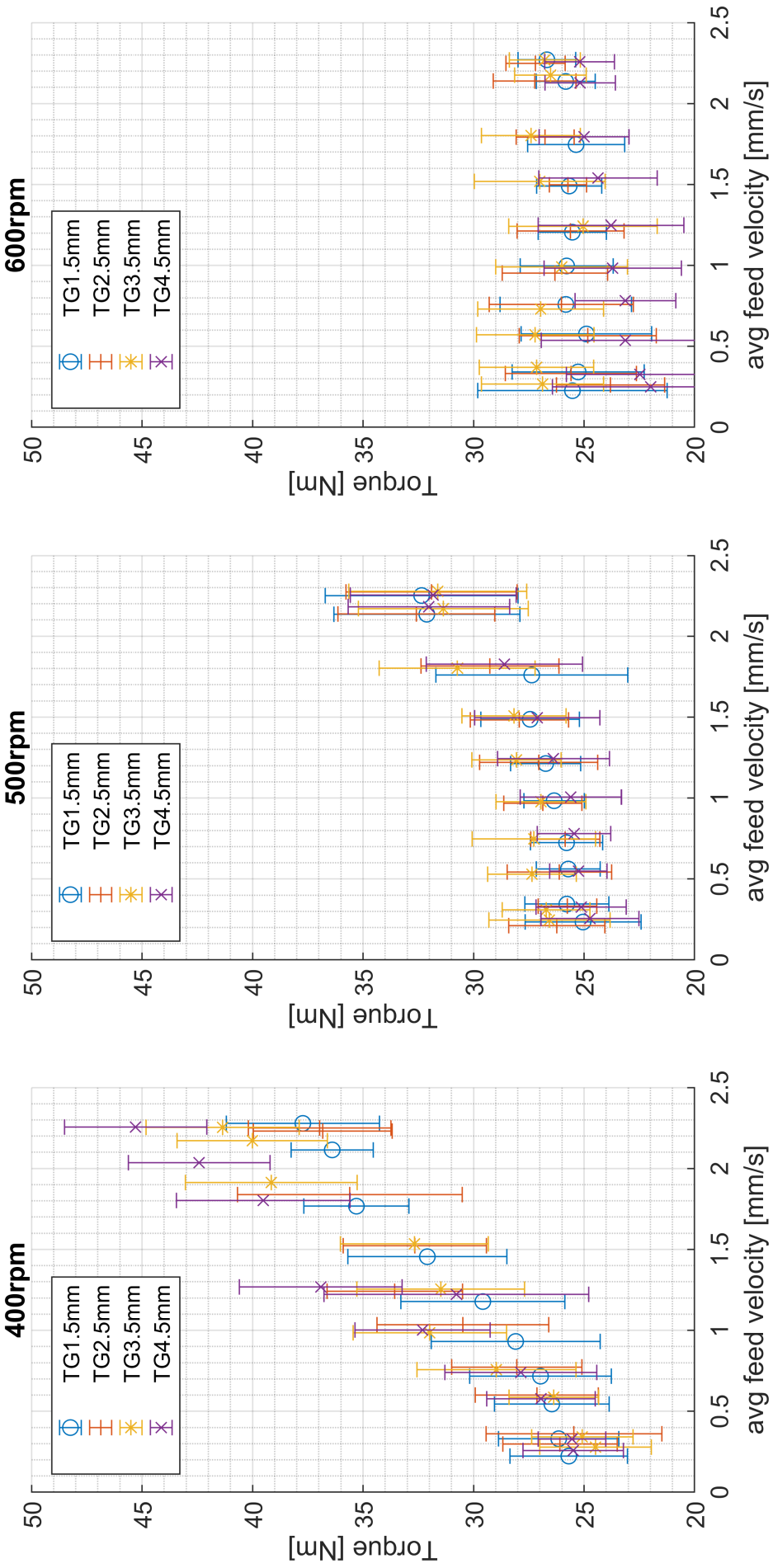

Figure 75: Average torque sorted per tool rotation rate.

E.2 Raw Data Figures per Experiment

The remaining of this page is left blank intentionally to maximise figure size on the next page.

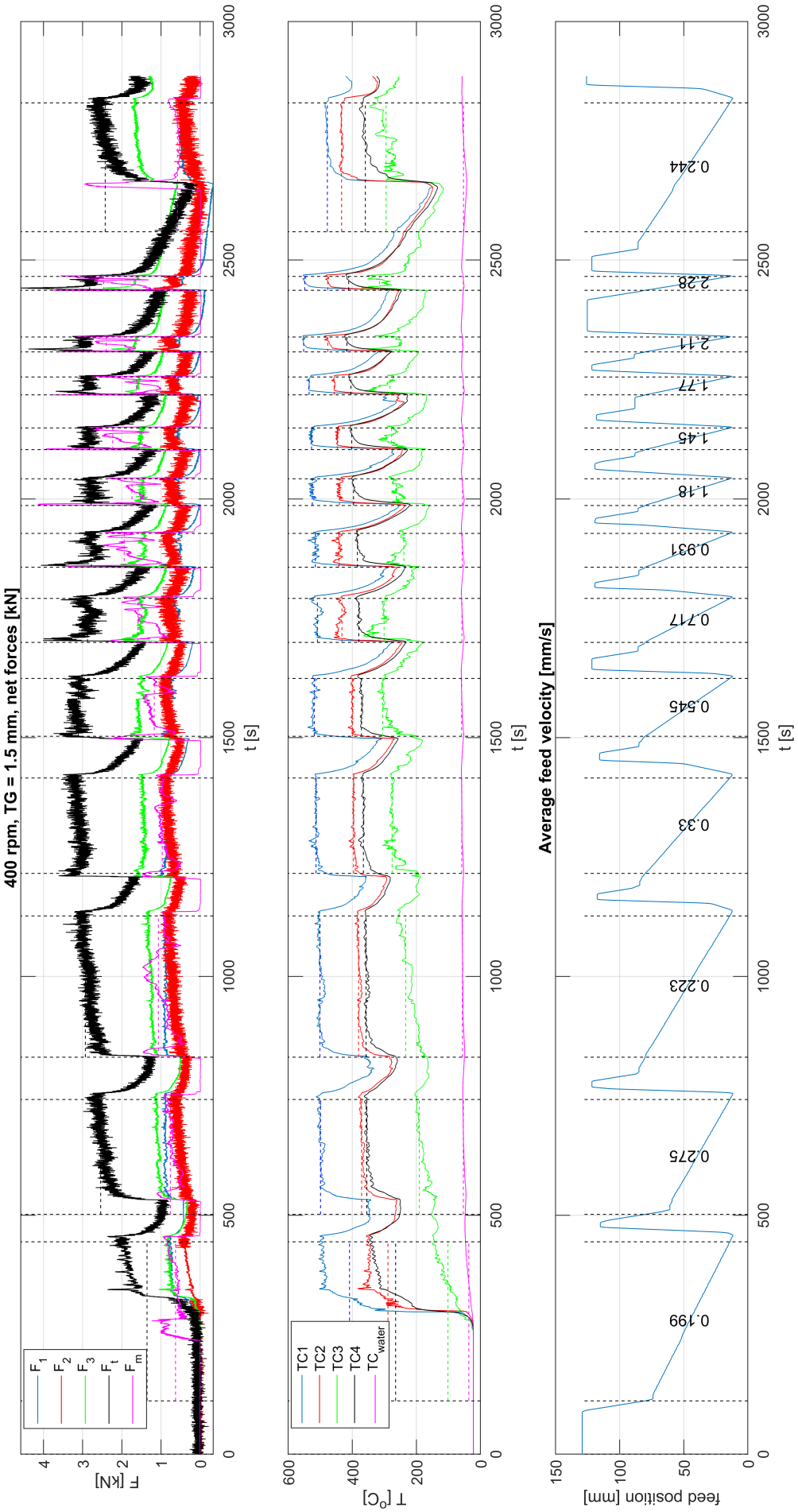

Figure 76: TG1.5_400_x: raw force, temperature and feed displacement data

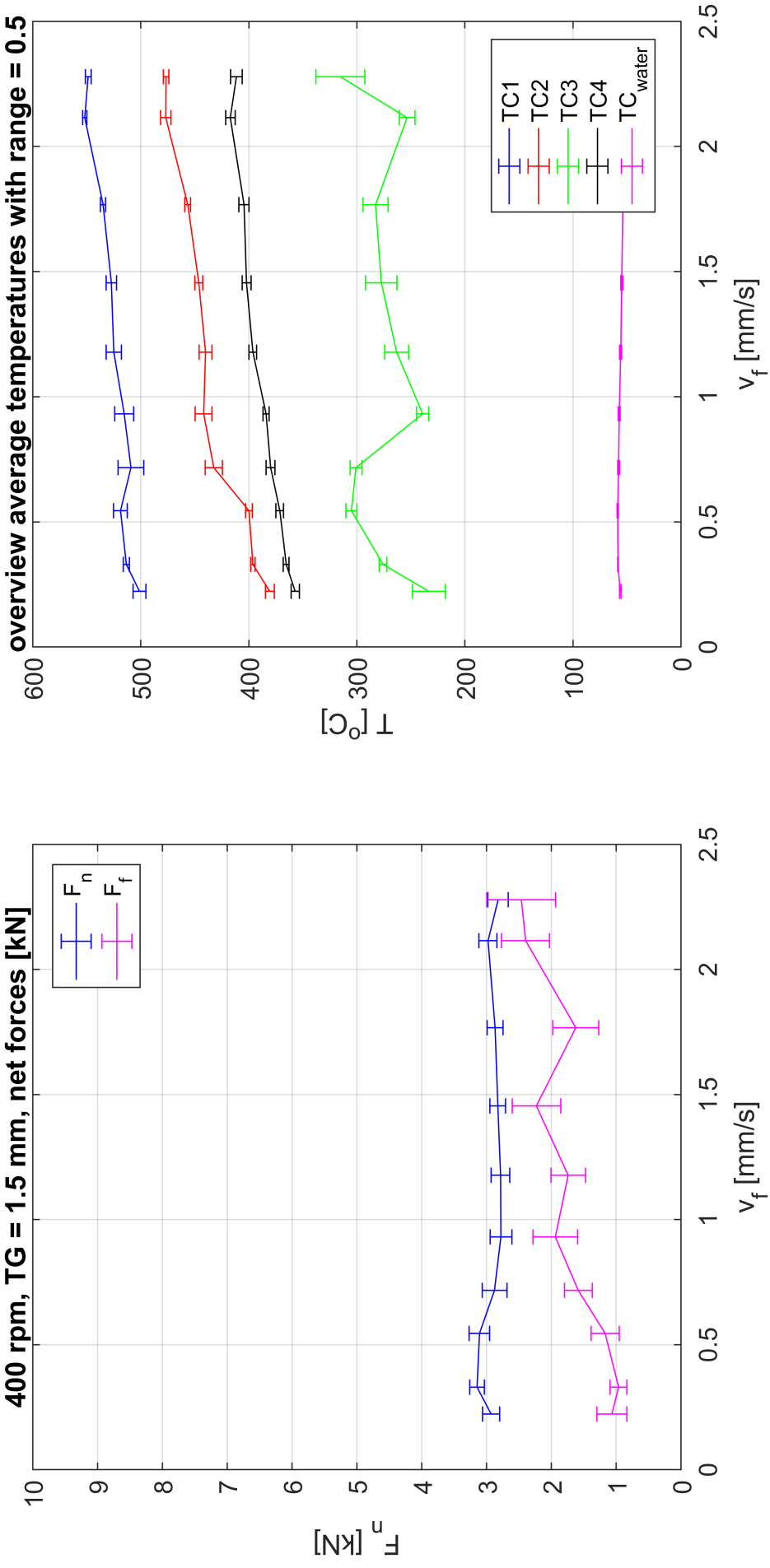

Figure 77: TG1.5_400_x: average forces and temperatures

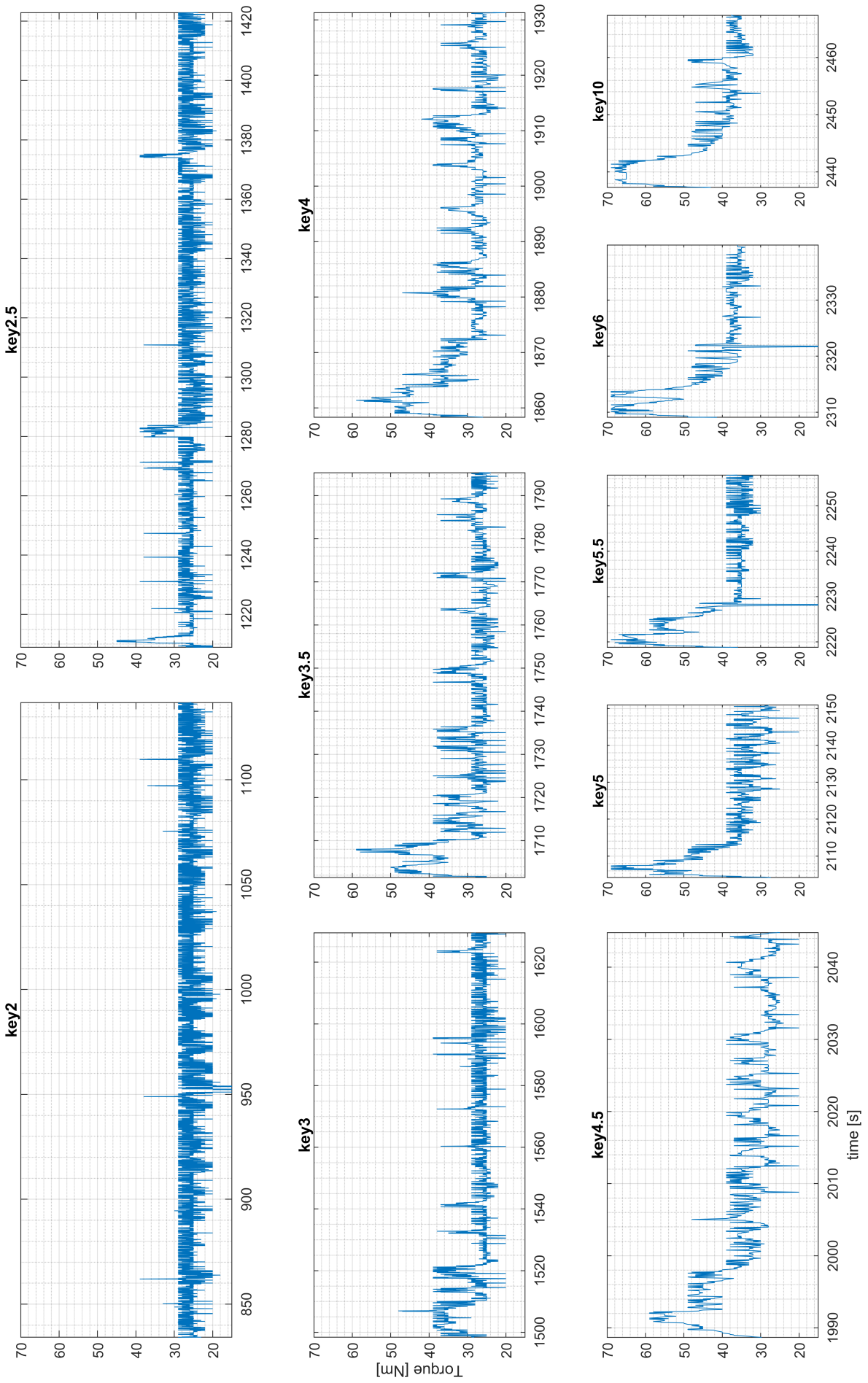

Figure 78: TG1.5_400_x: raw torque data cut per feed cylinder key velocity

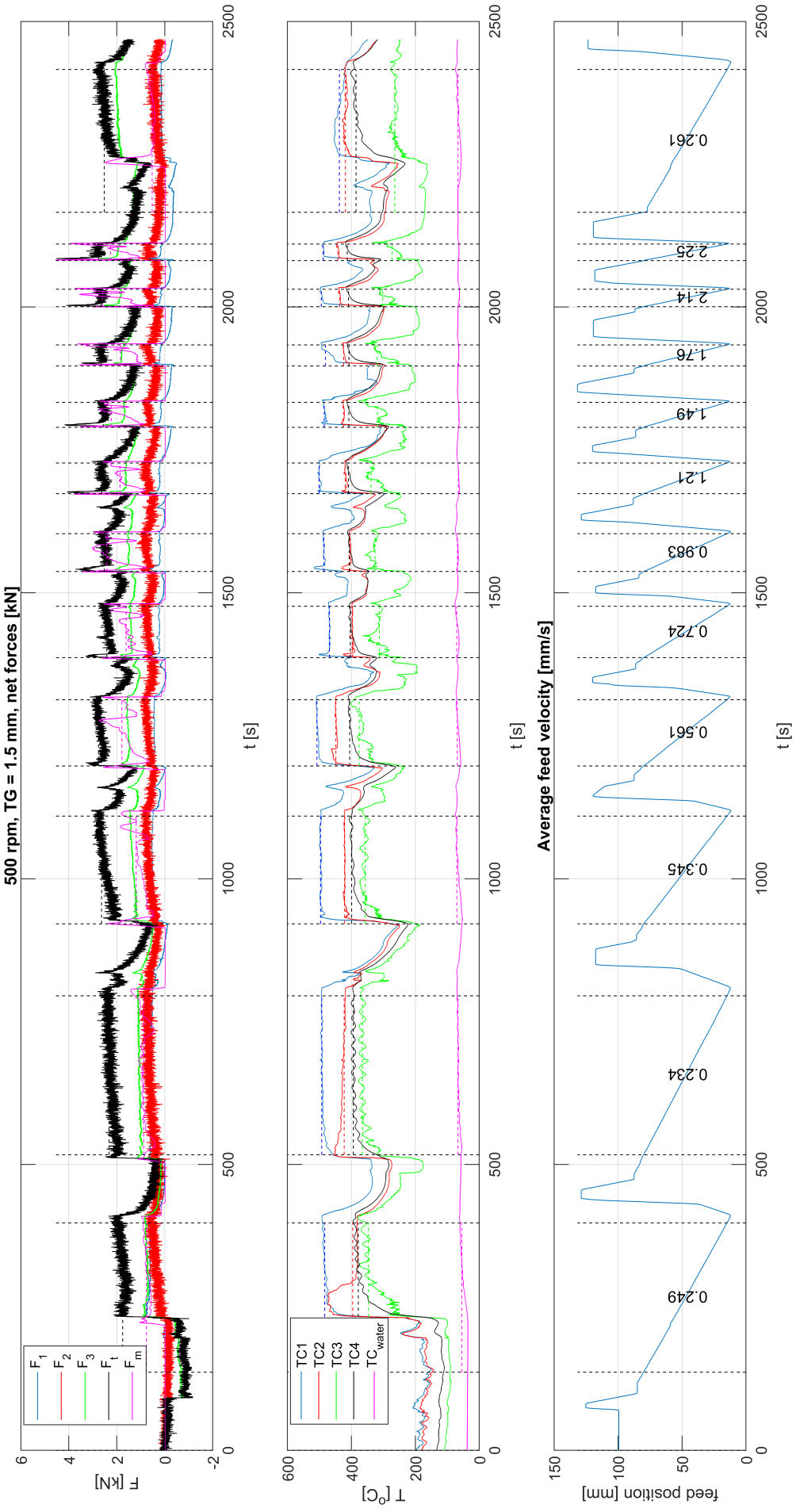

Figure 79: TG1.5_500_x: raw force, temperature and feed displacement data

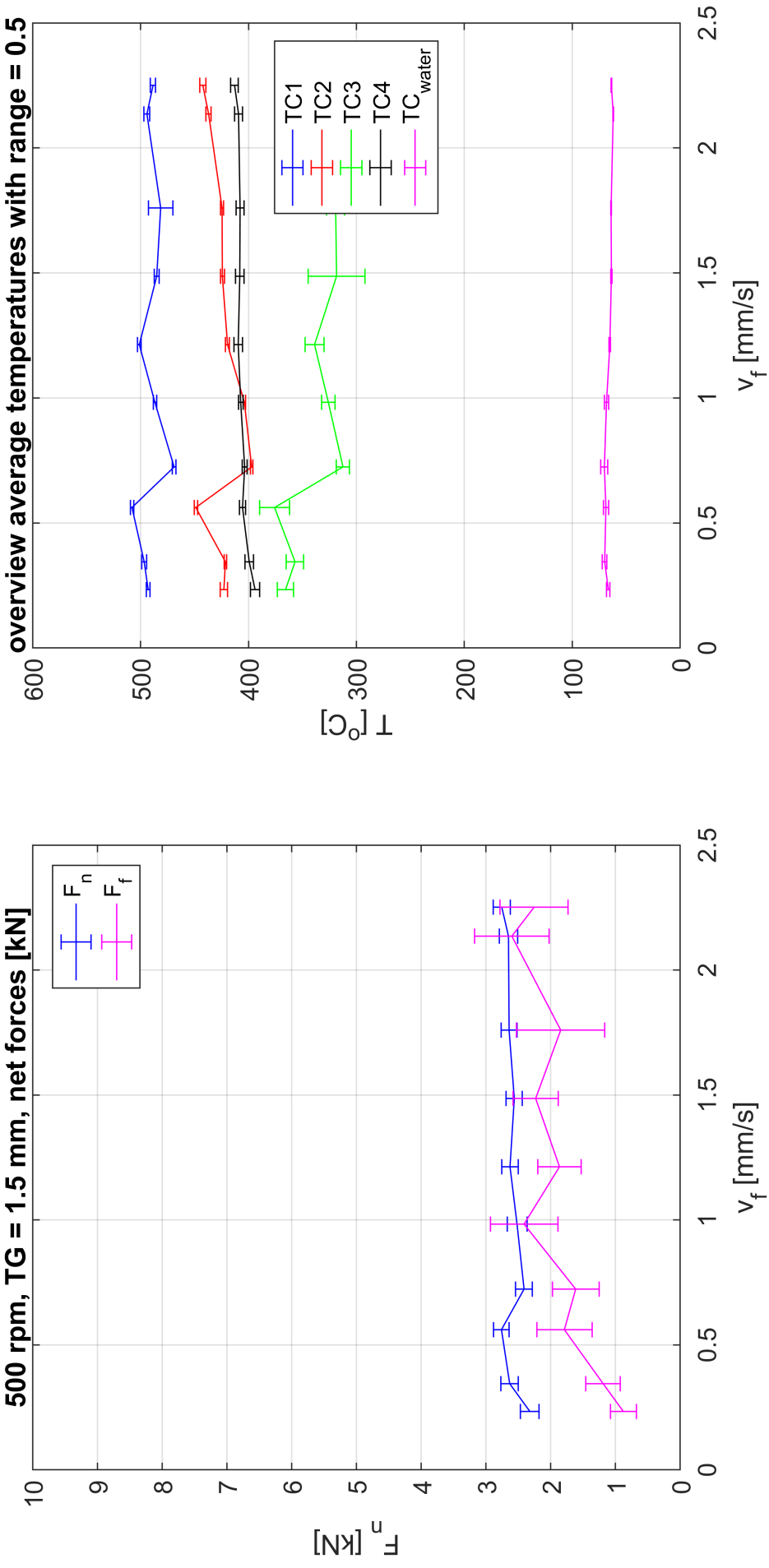

Figure 80: TG1.5_500_x: average forces and temperatures

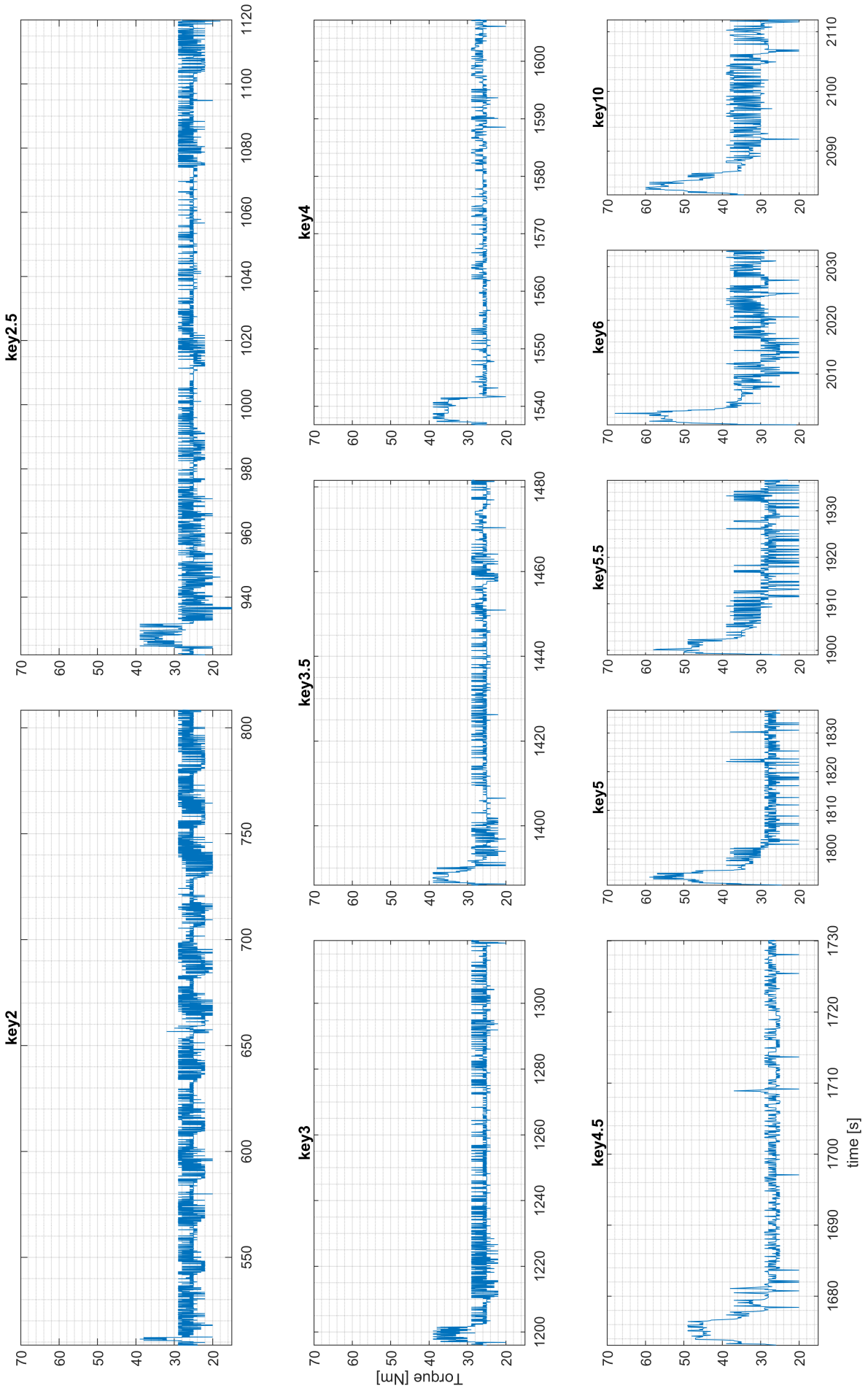

Figure 81: TG1.5_500_x: raw torque data cut per feed cylinder key velocity

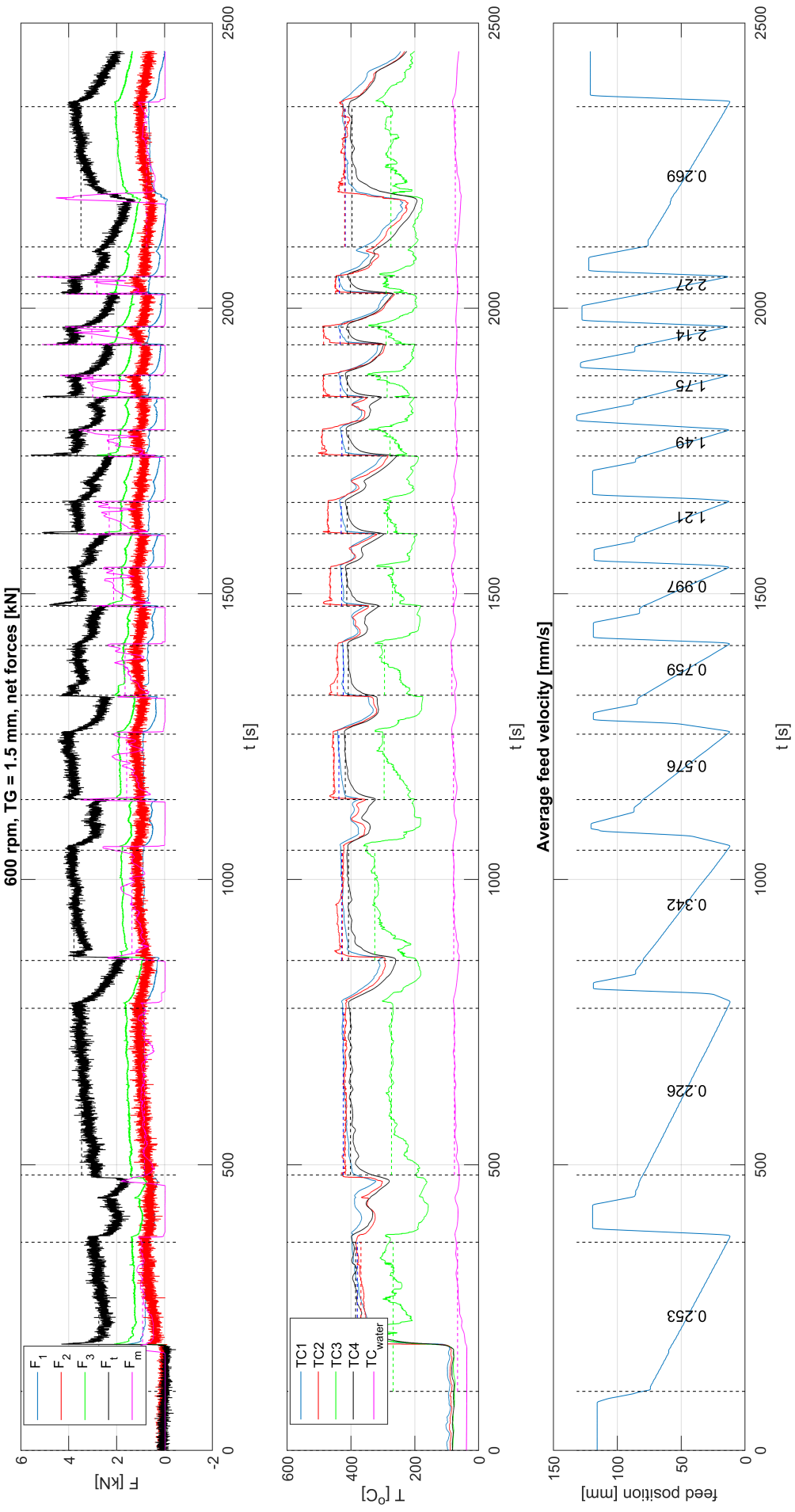

Figure 82: TG1.5_600_x: raw force, temperature and feed displacement data

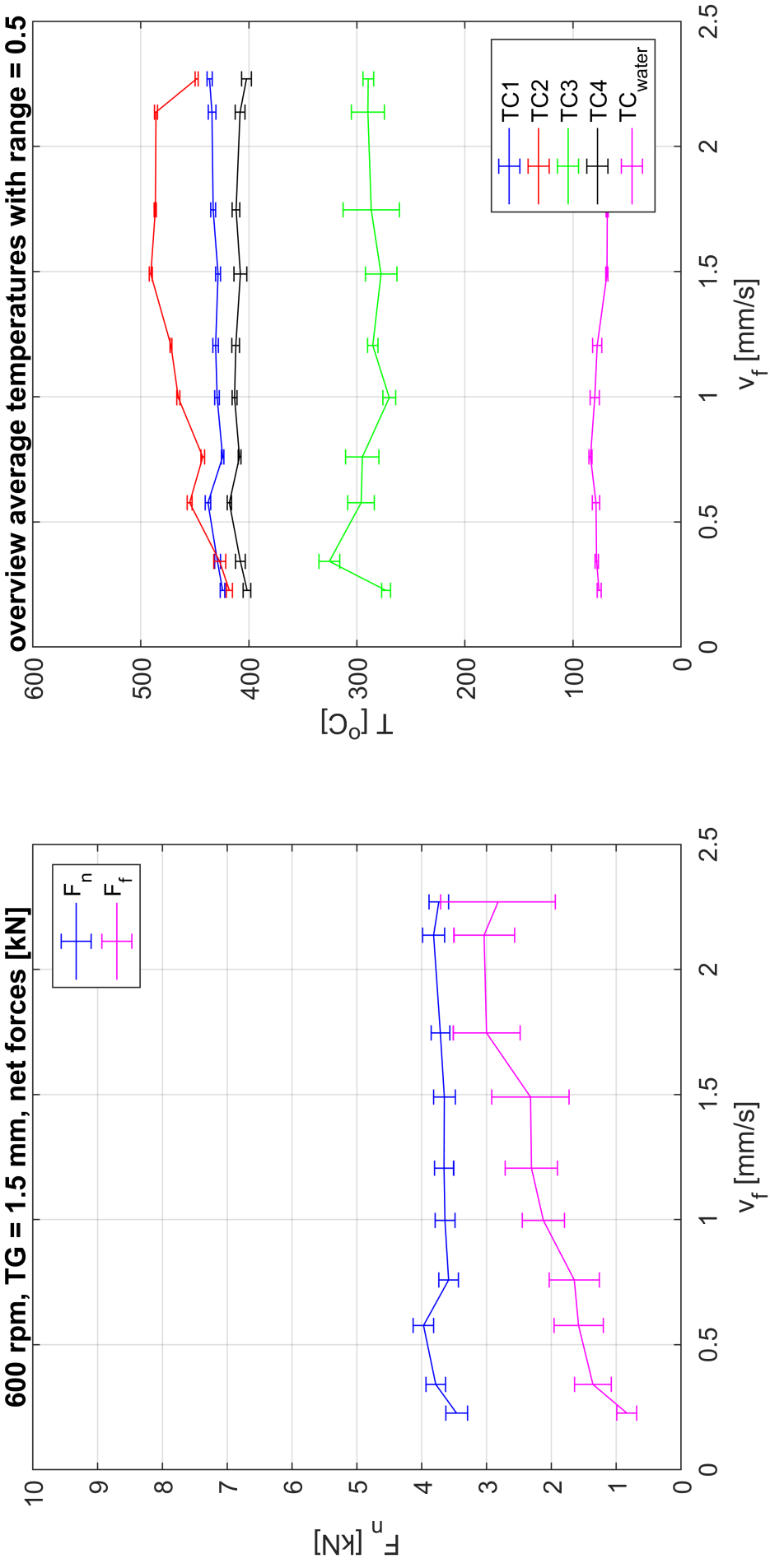

Figure 83: TG1.5_600_x: average forces and temperatures

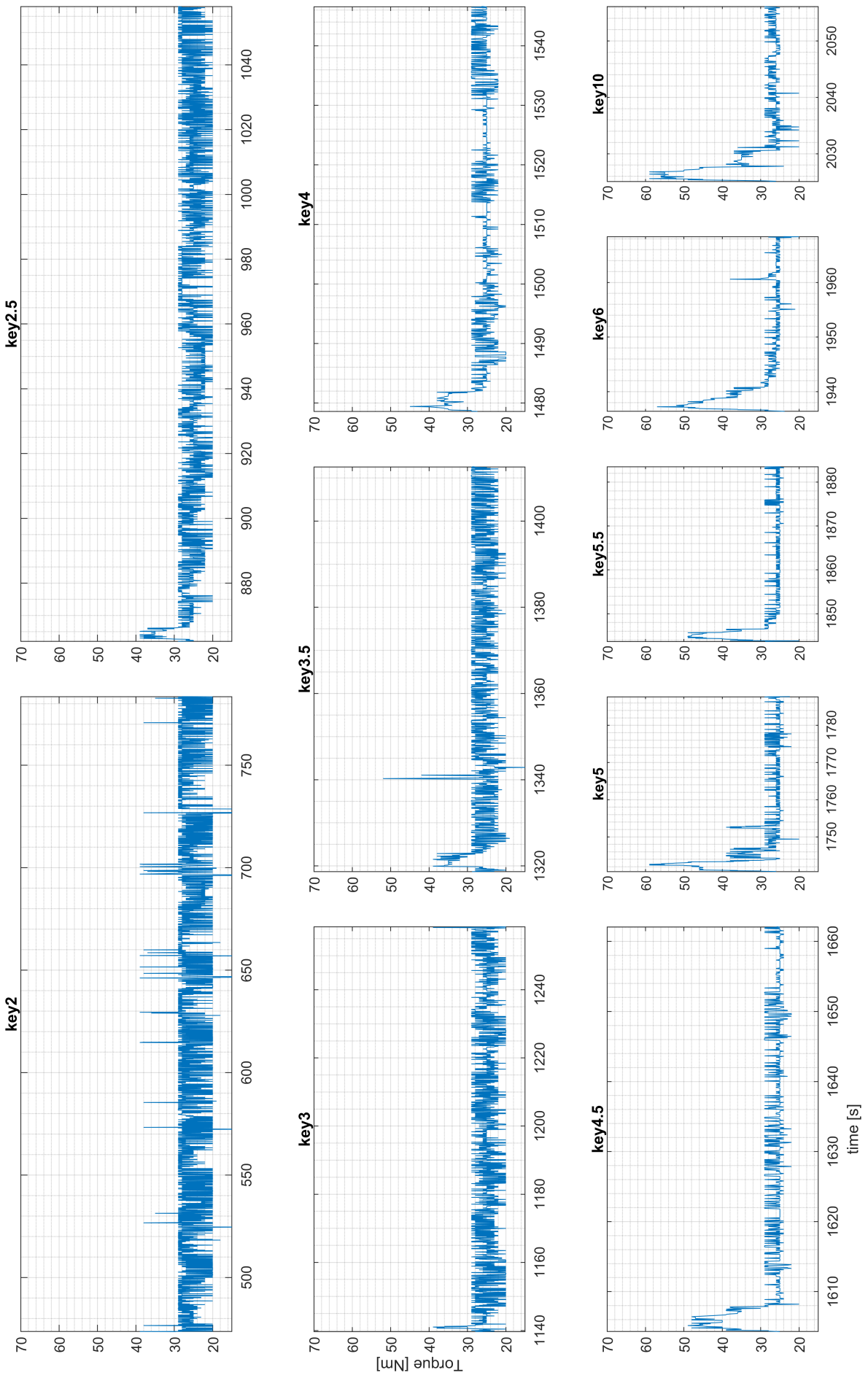

Figure 84: TG1.5_600_x: raw torque data cut per feed cylinder key velocity

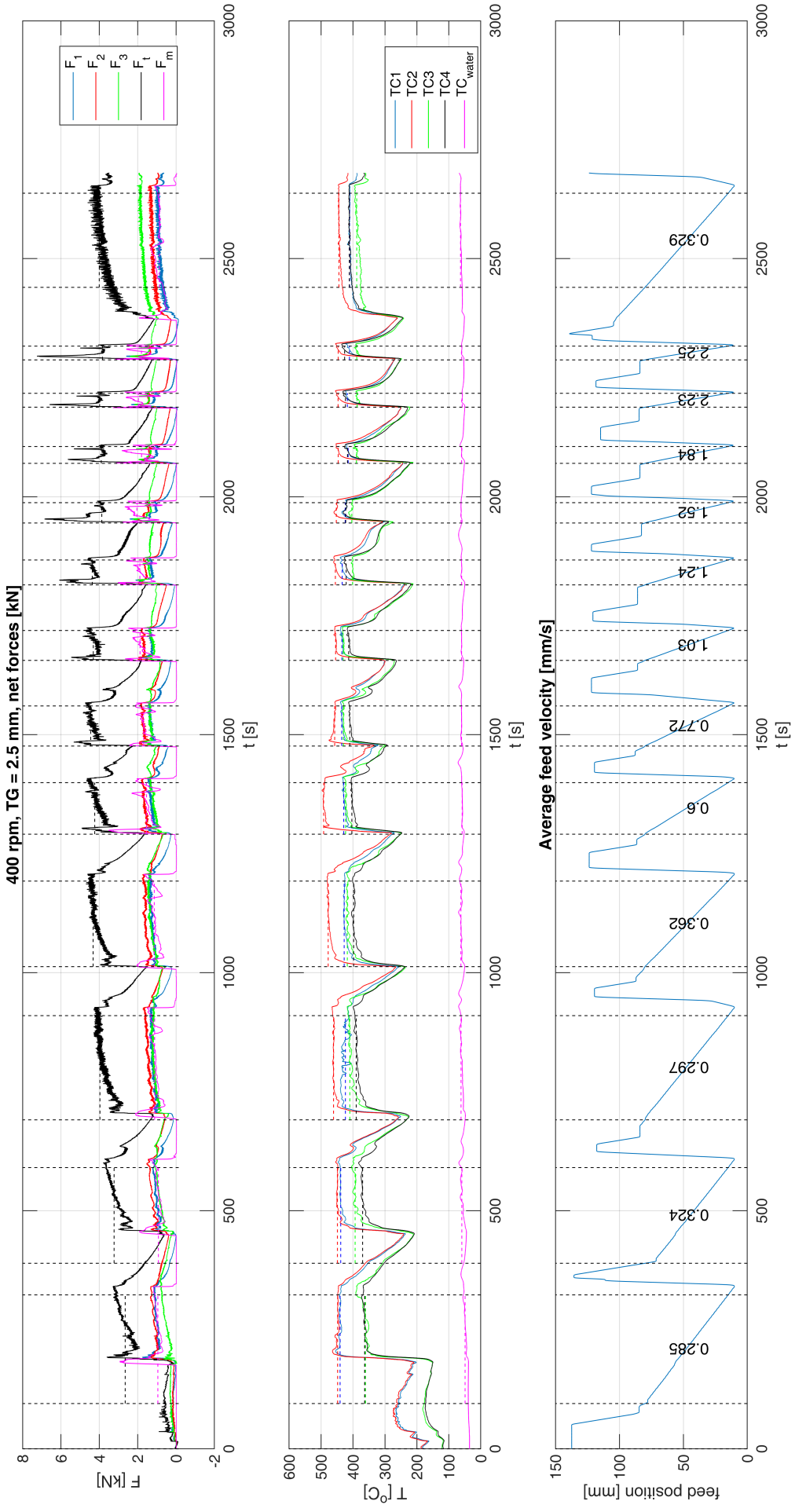

Figure 85: TG2.5_400_x: raw force, temperature and feed displacement data

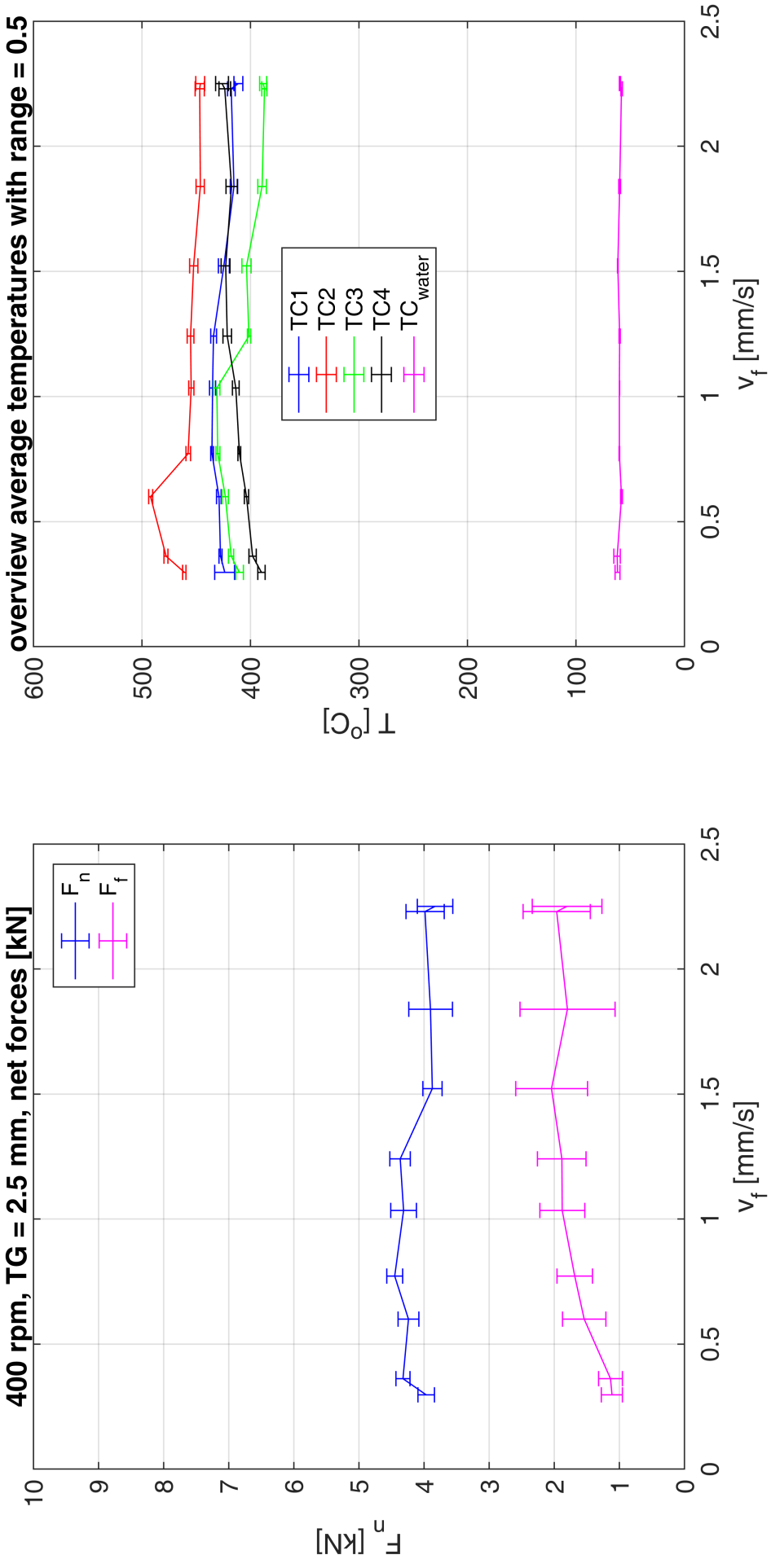

Figure 86: TG2.5_400_x: average forces and temperatures

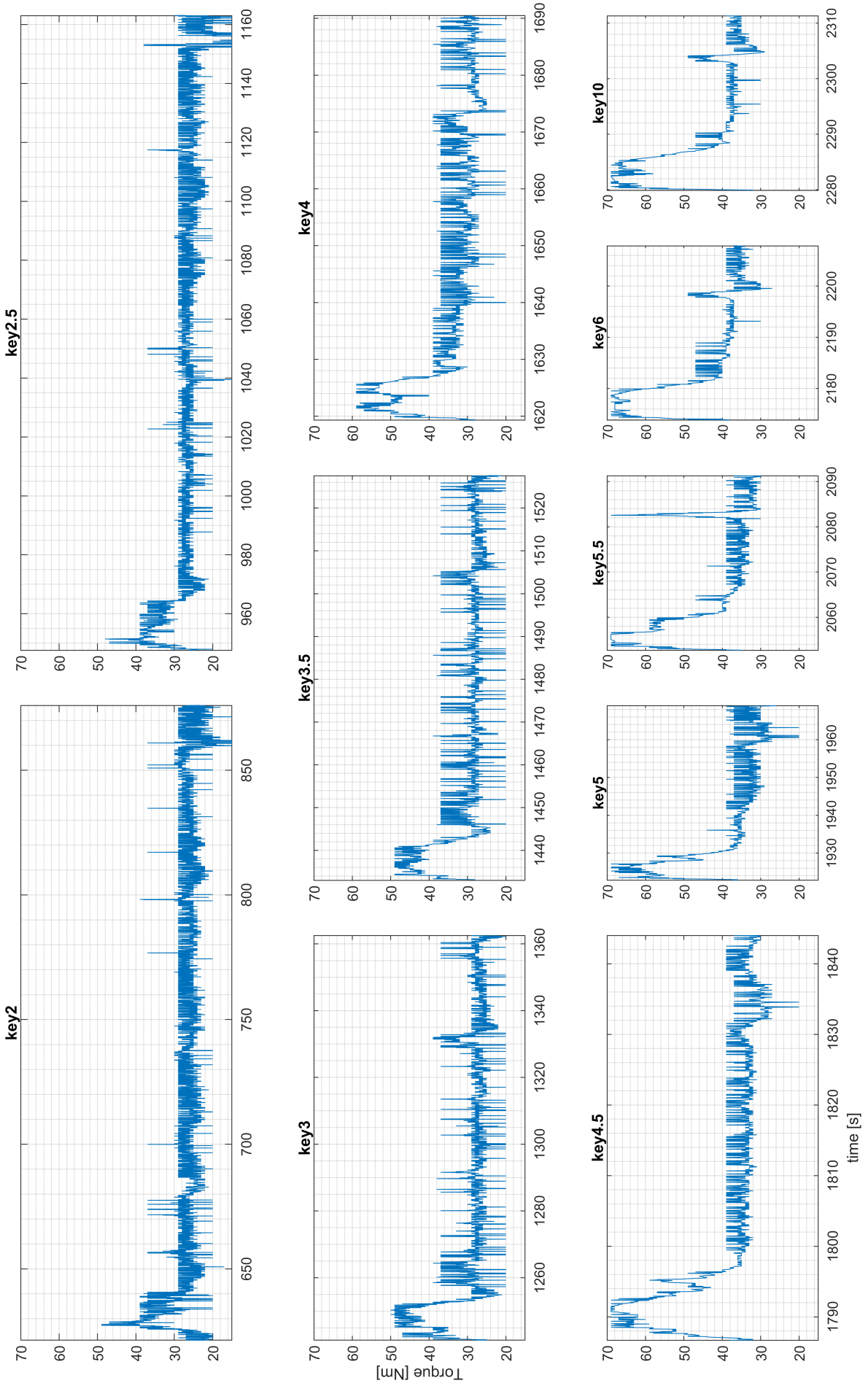

Figure 87: TG2.5_400_x: raw torque data cut per feed cylinder key velocity

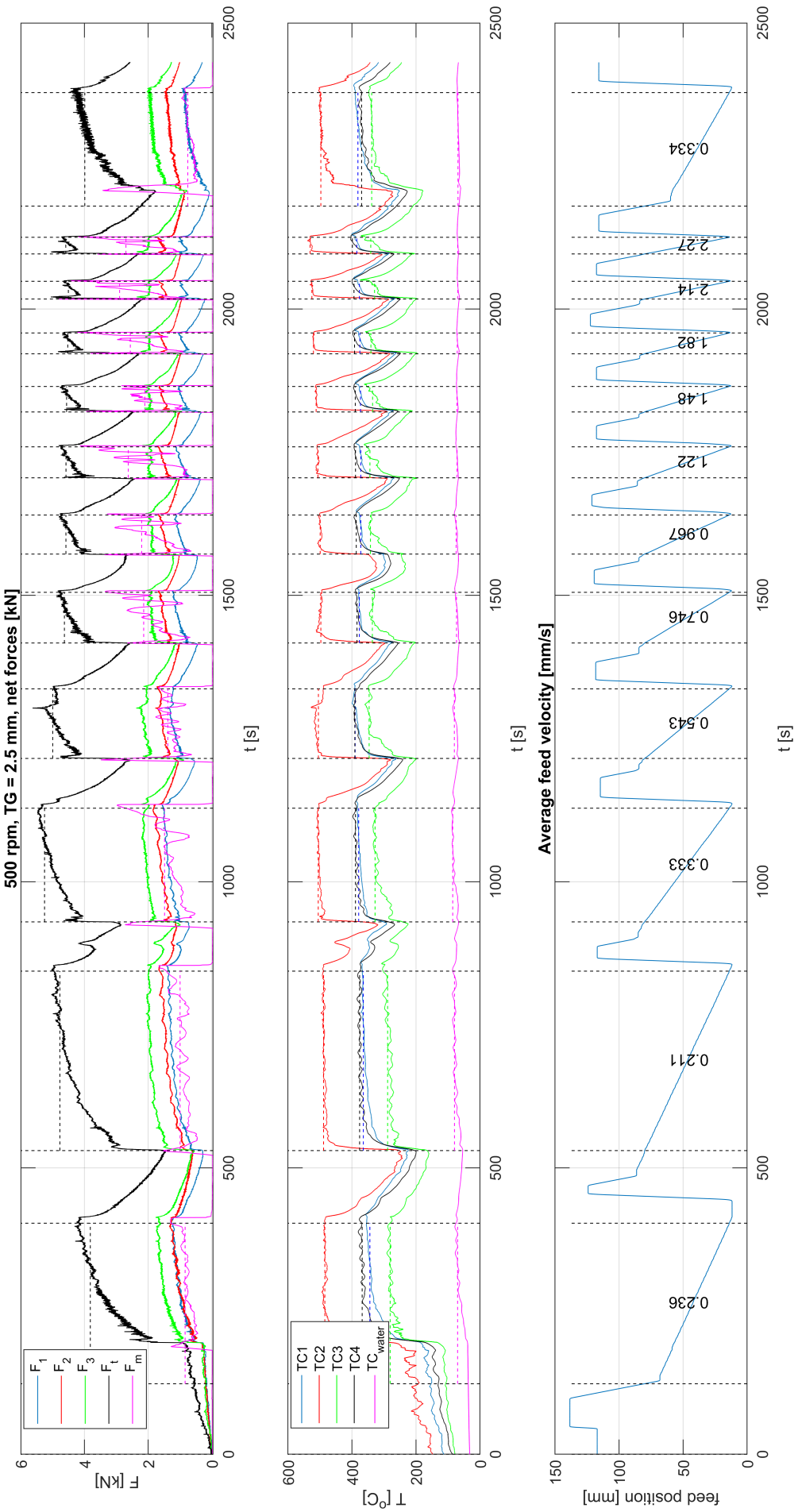

Figure 88: TG2.5_500_x: raw force, temperature and feed displacement data

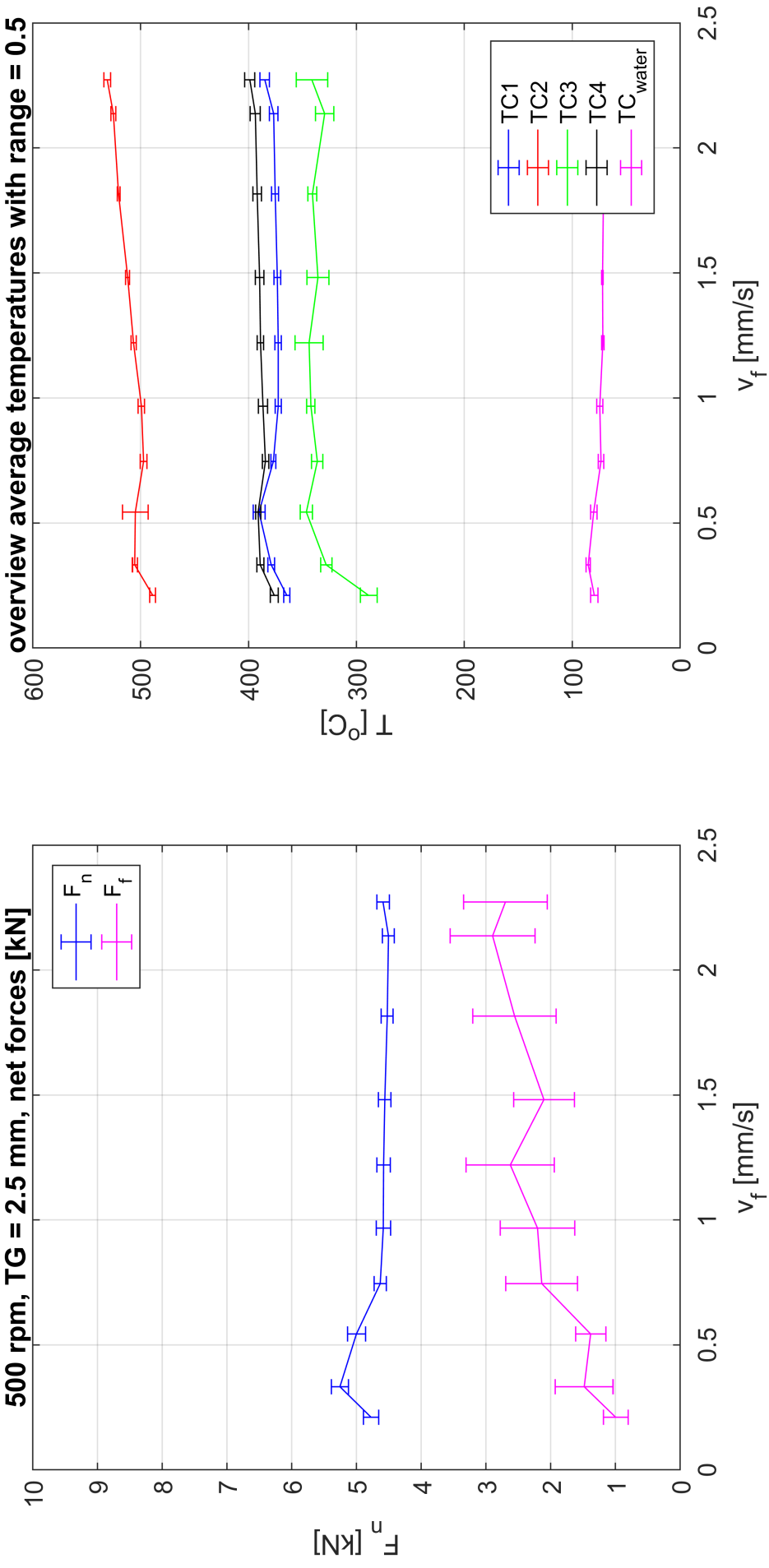

Figure 89: TG2.5_500_x: average forces and temperatures

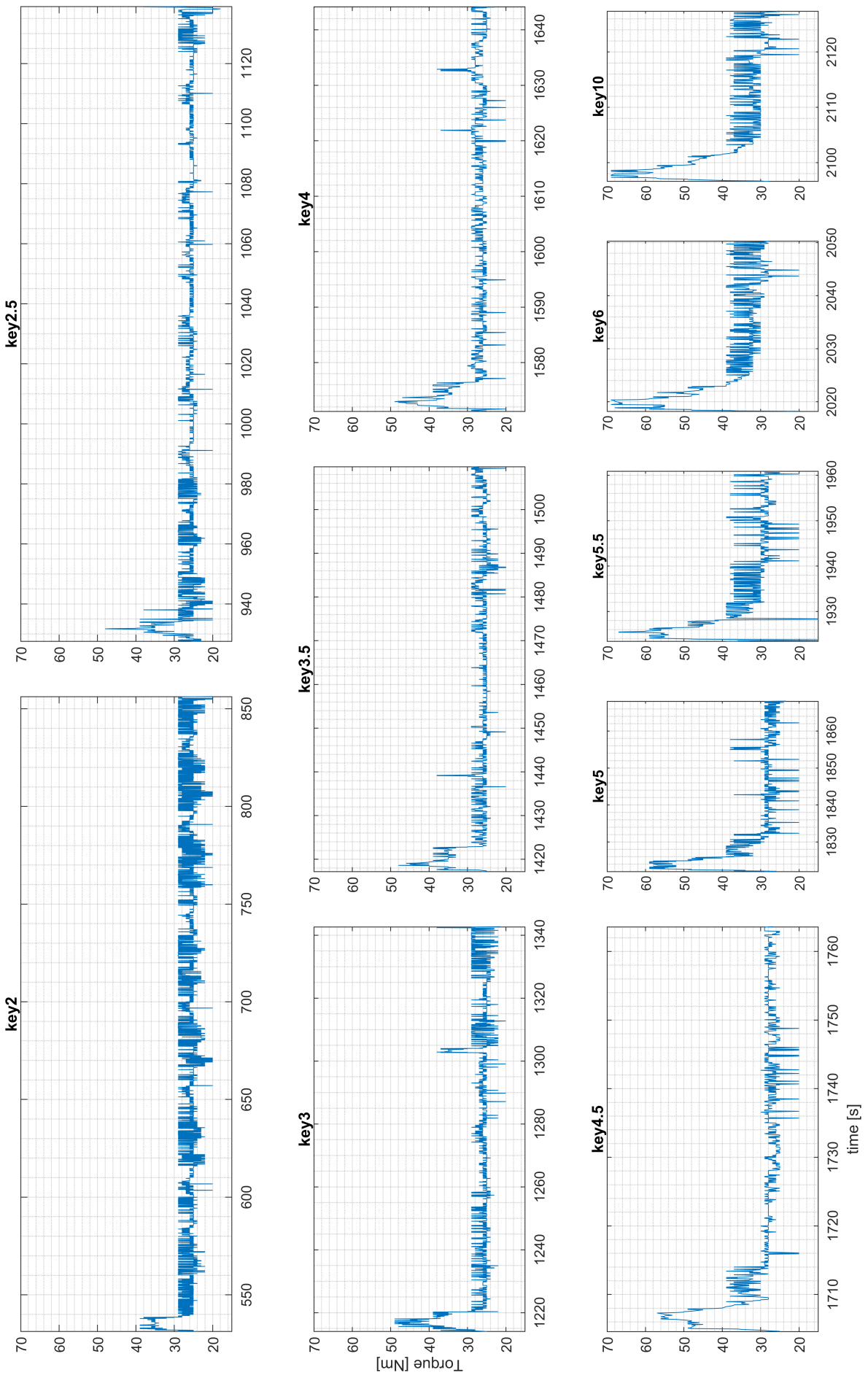

Figure 90: TG2.5_500_x: raw torque data cut per feed cylinder key velocity

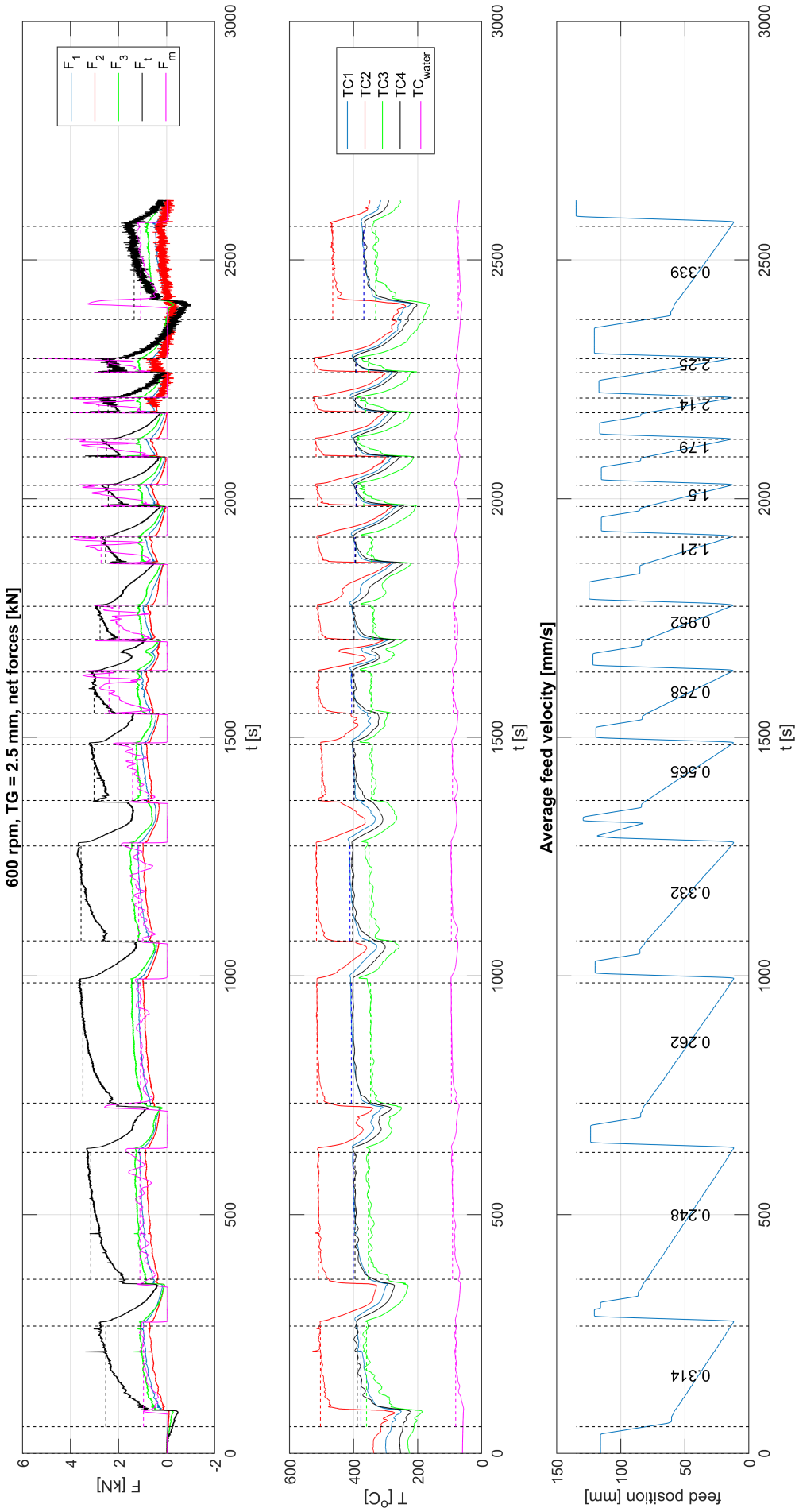

Figure 91: TG2.5_600_x: raw force, temperature and feed displacement data

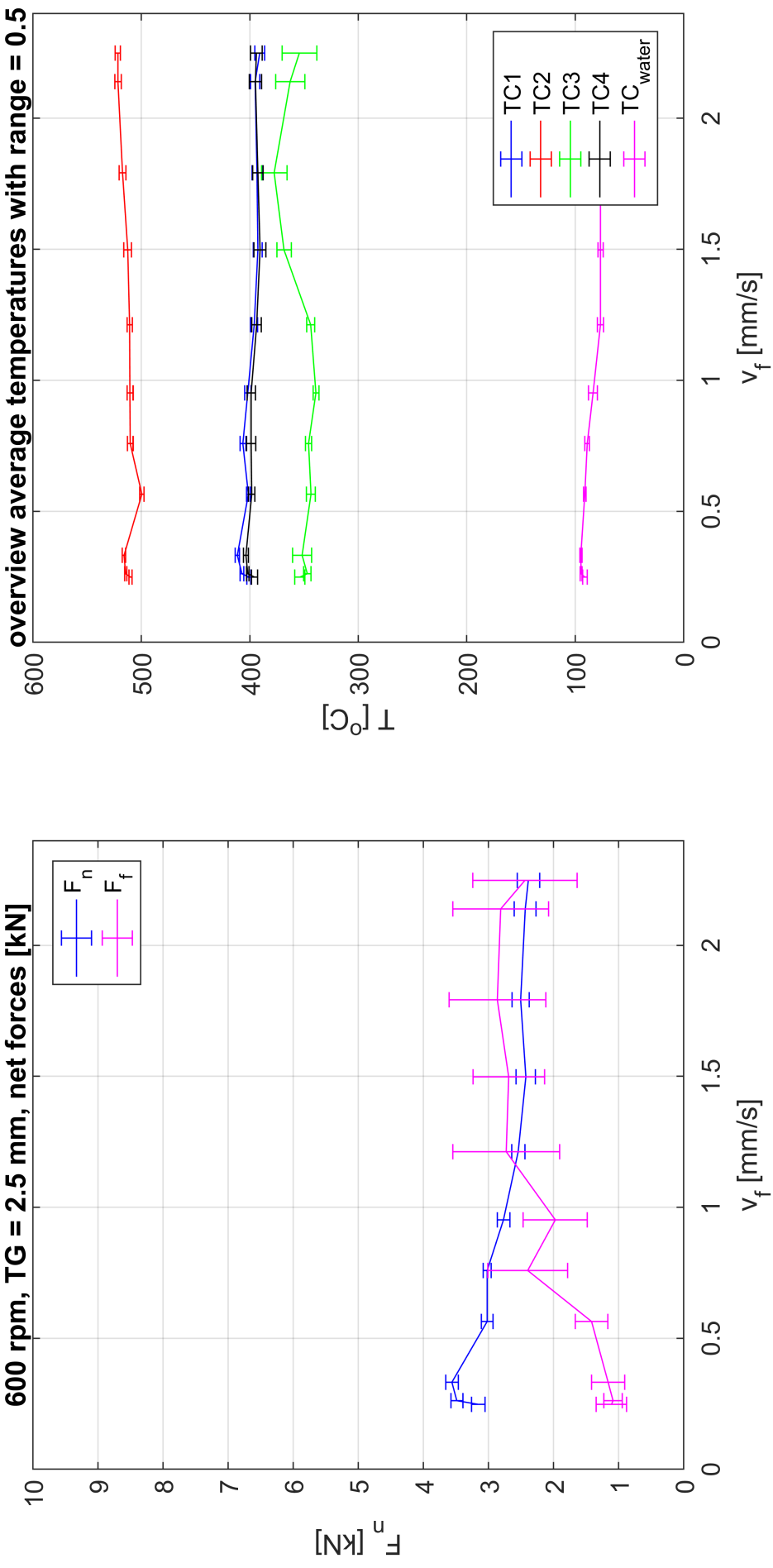

Figure 92: TG2.5_600_x: average forces and temperatures

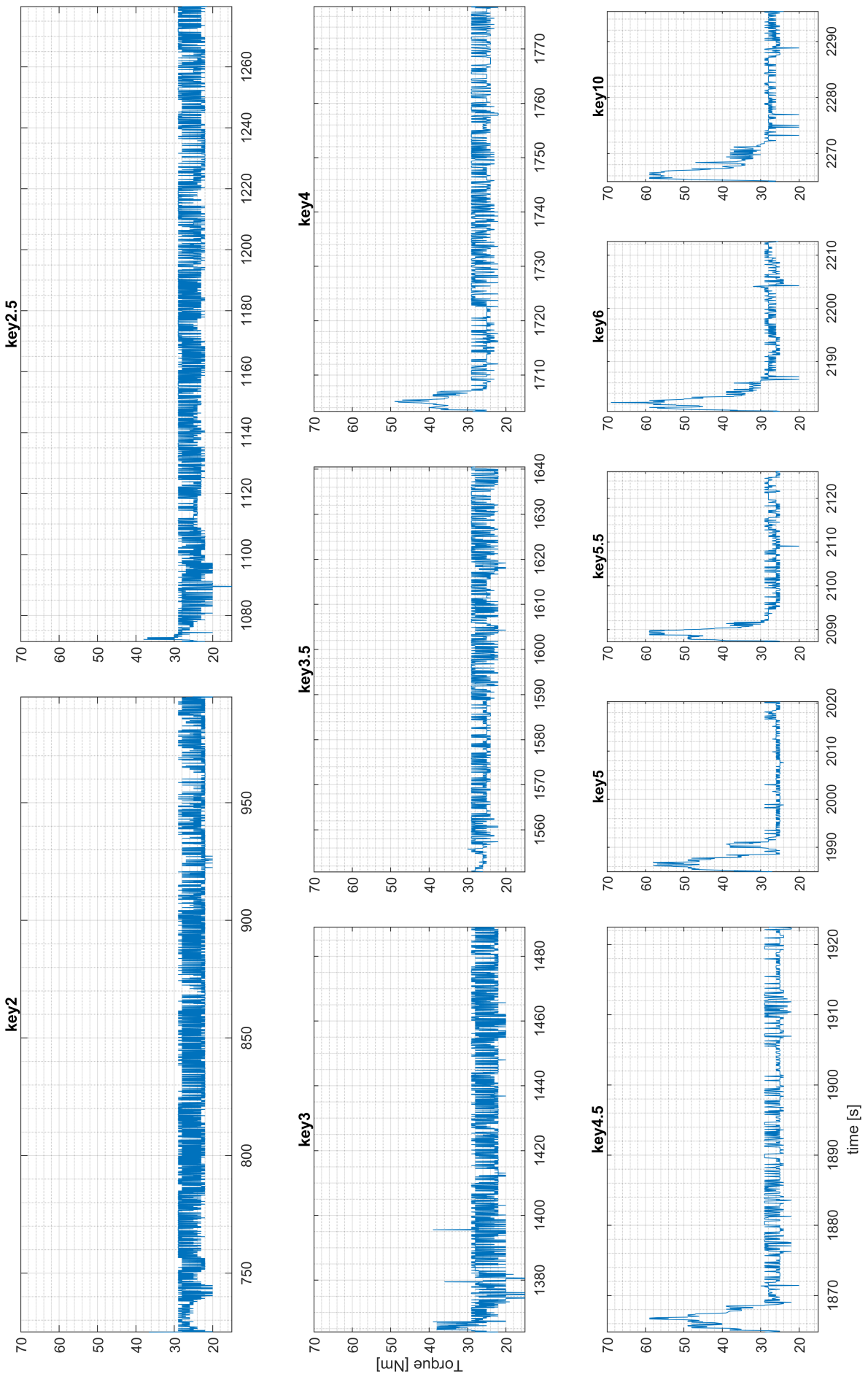

Figure 93: TG2.5_600_x: raw torque data cut per feed cylinder key velocity

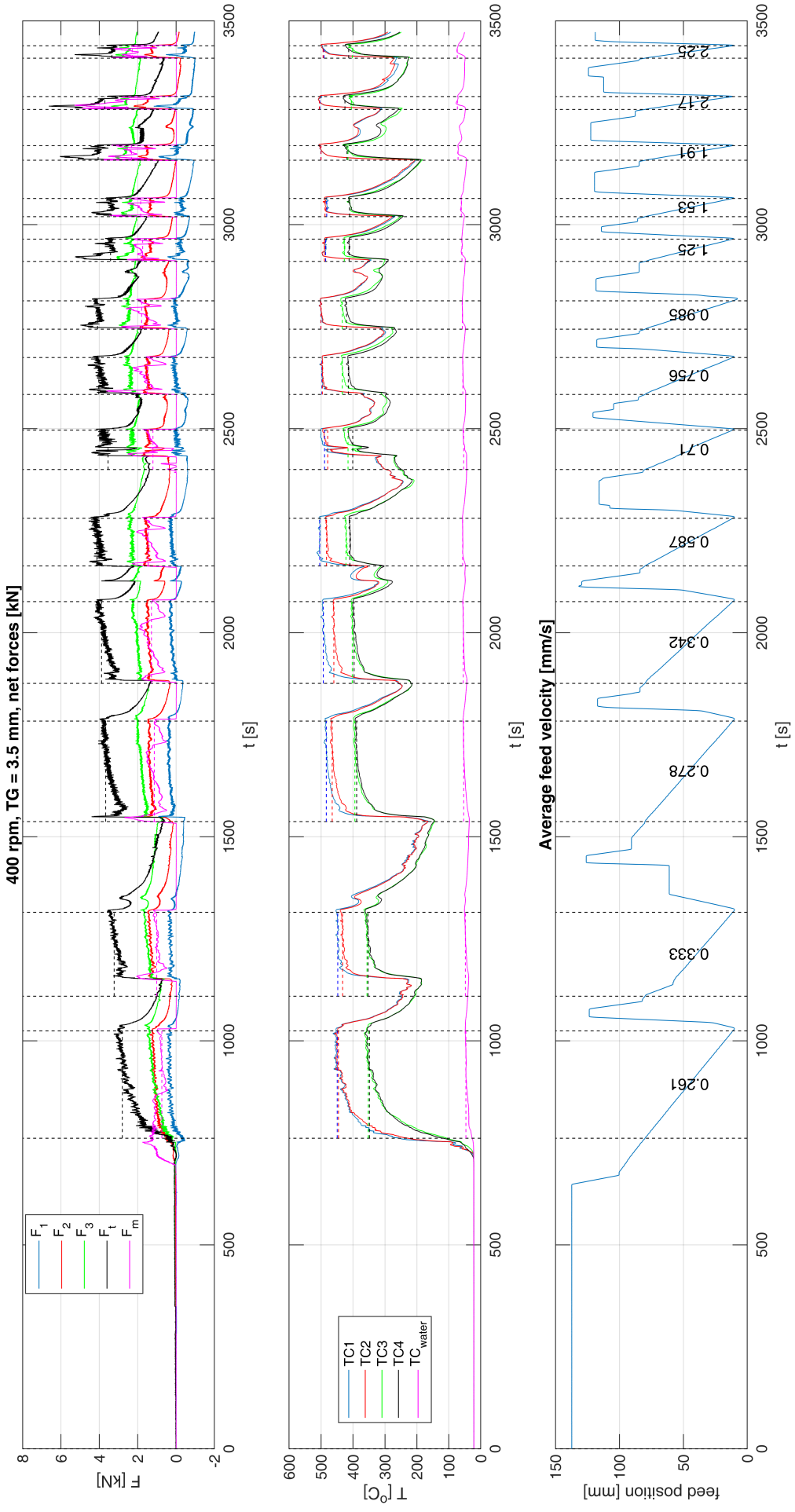

Figure 94: TG3.5_400_x: raw force, temperature and feed displacement data

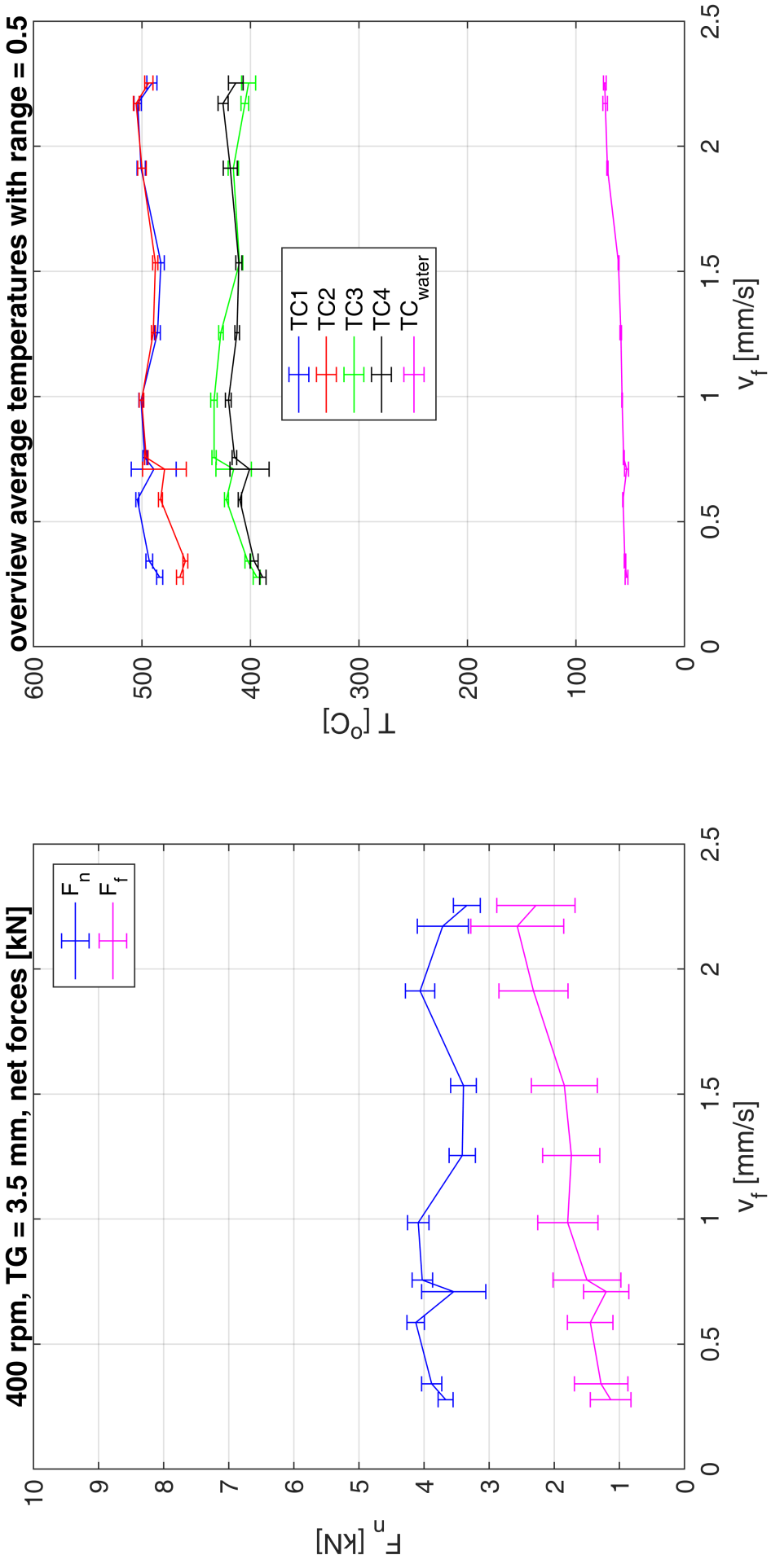

Figure 95: TG3.5_400_x: average forces and temperatures

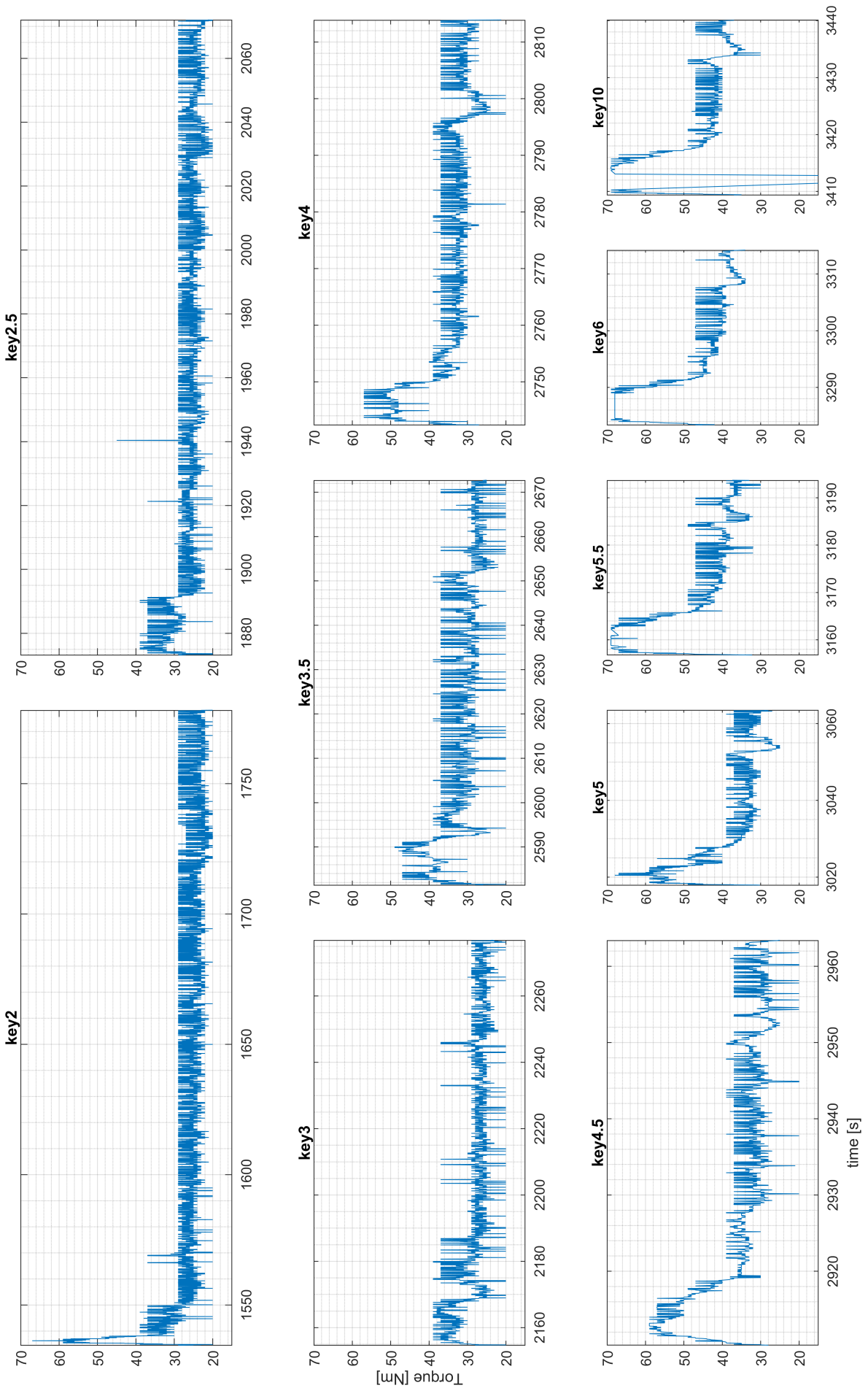

Figure 96: TG3.5_400_x: raw torque data cut per feed cylinder key velocity

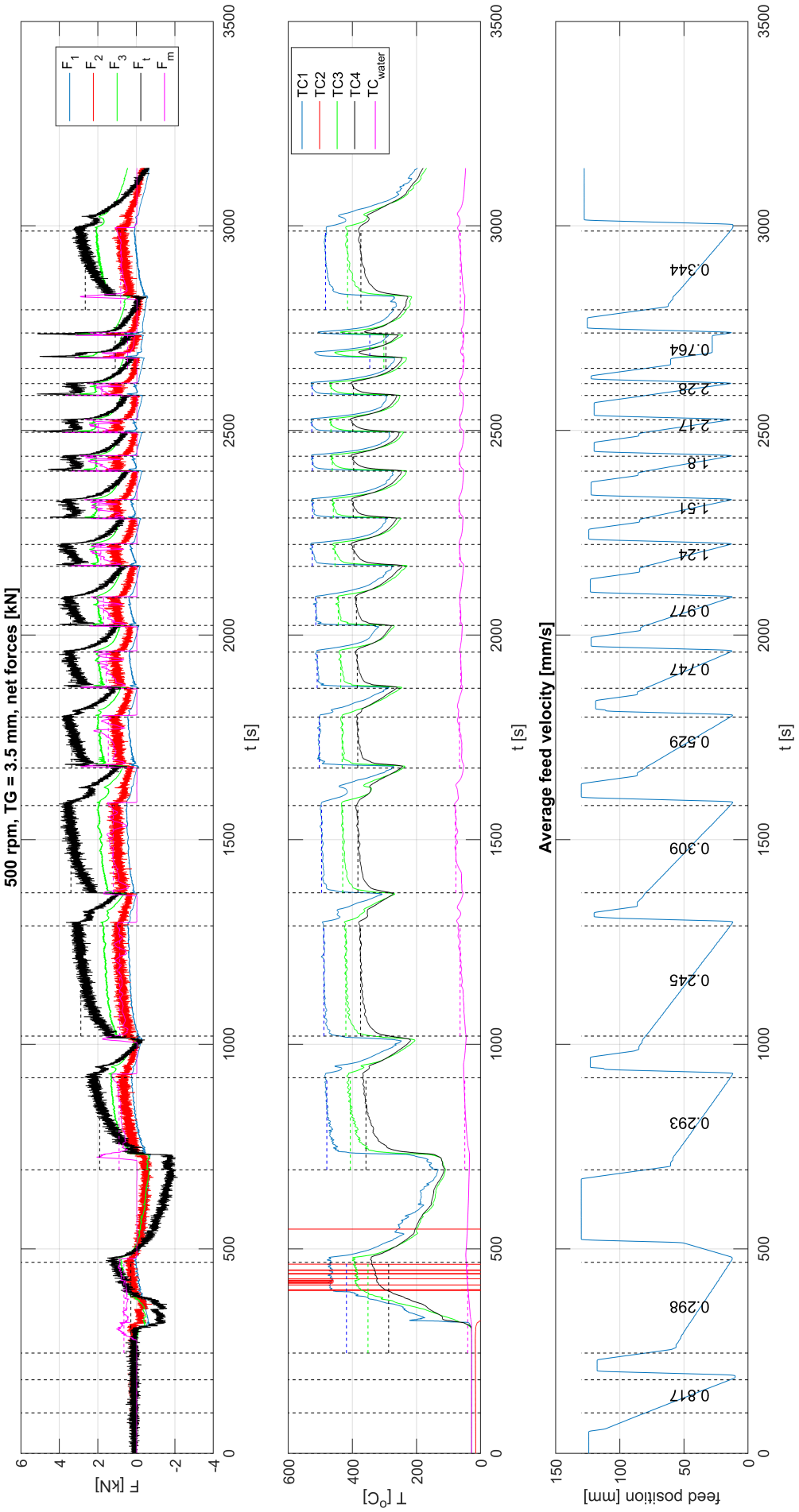

Figure 97: TG3.5_500_x: raw force, temperature and feed displacement data

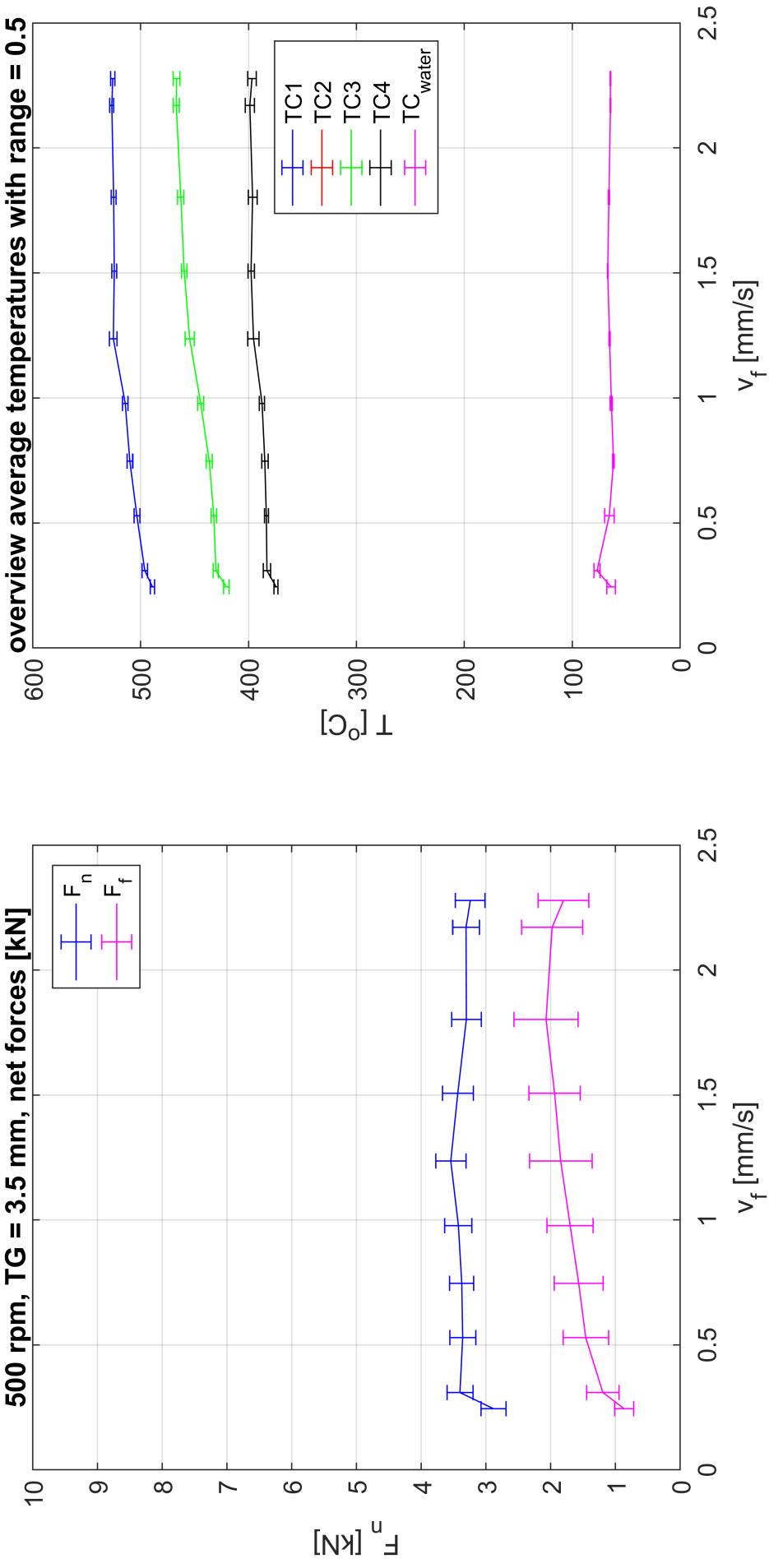

Figure 98: TG3.5_500_x: average forces and temperatures

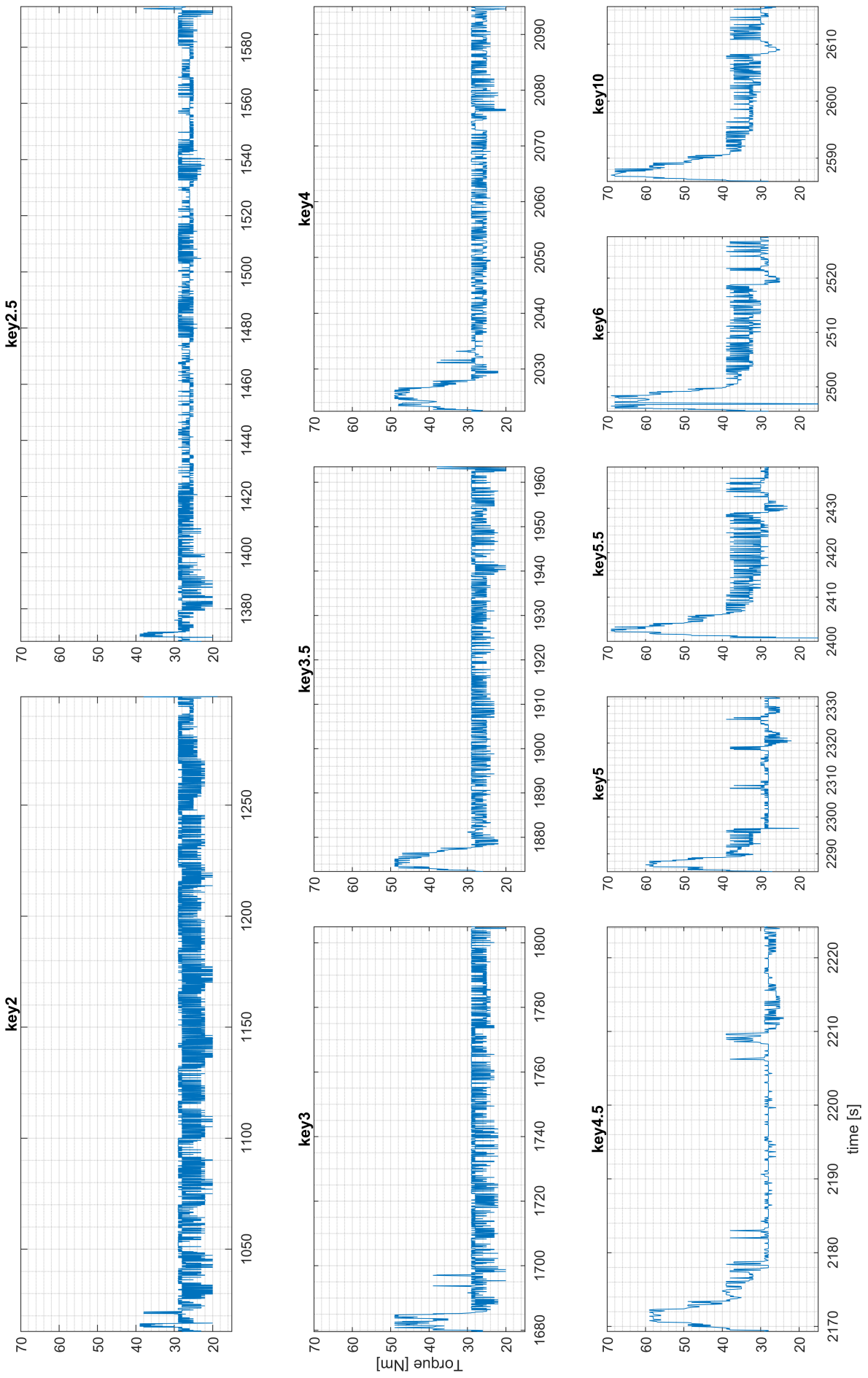

Figure 99: TG3.5_500_x: raw torque data cut per feed cylinder key velocity

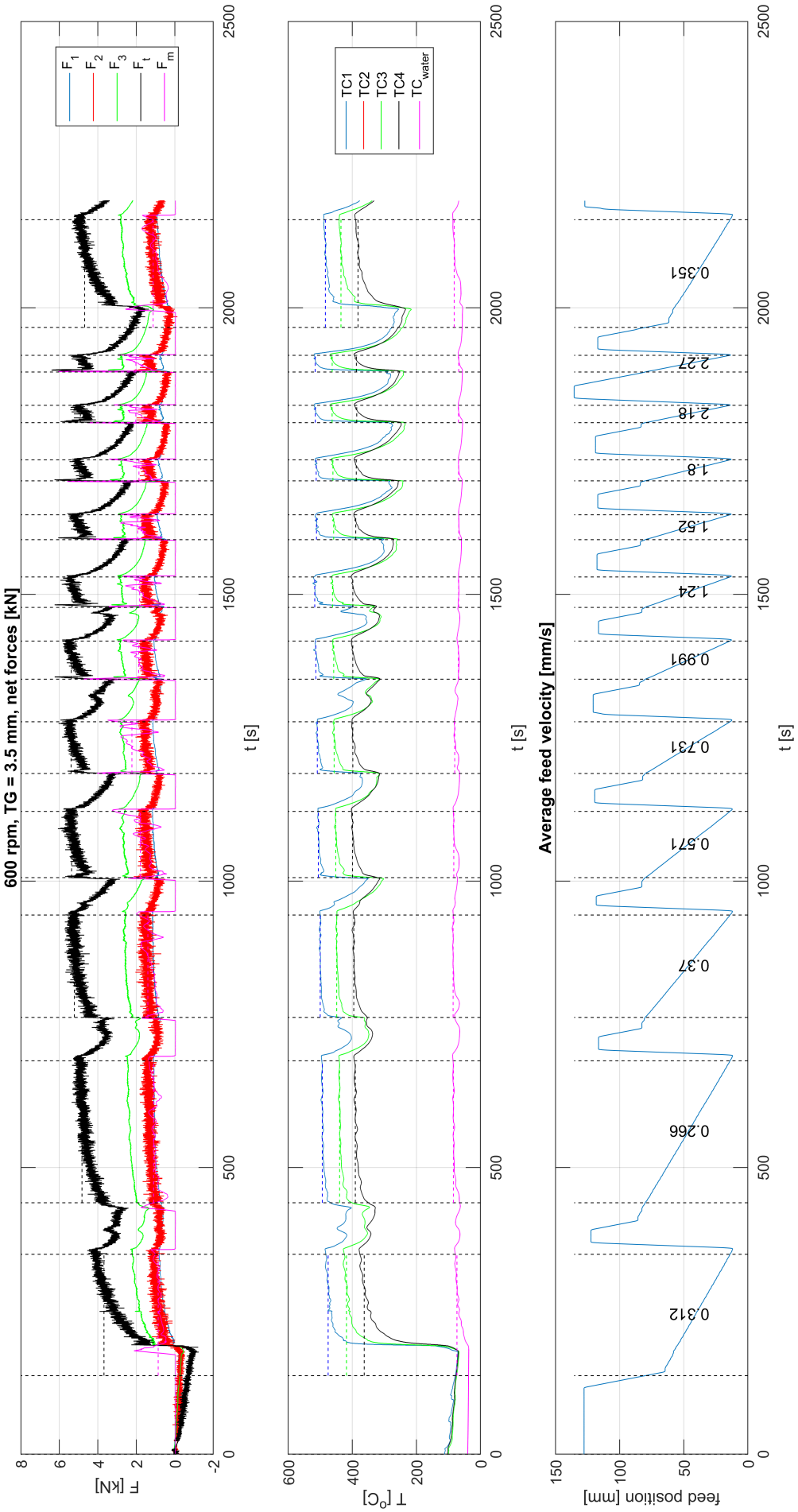

Figure 100: TG3.5_600_x: raw force, temperature and feed displacement data

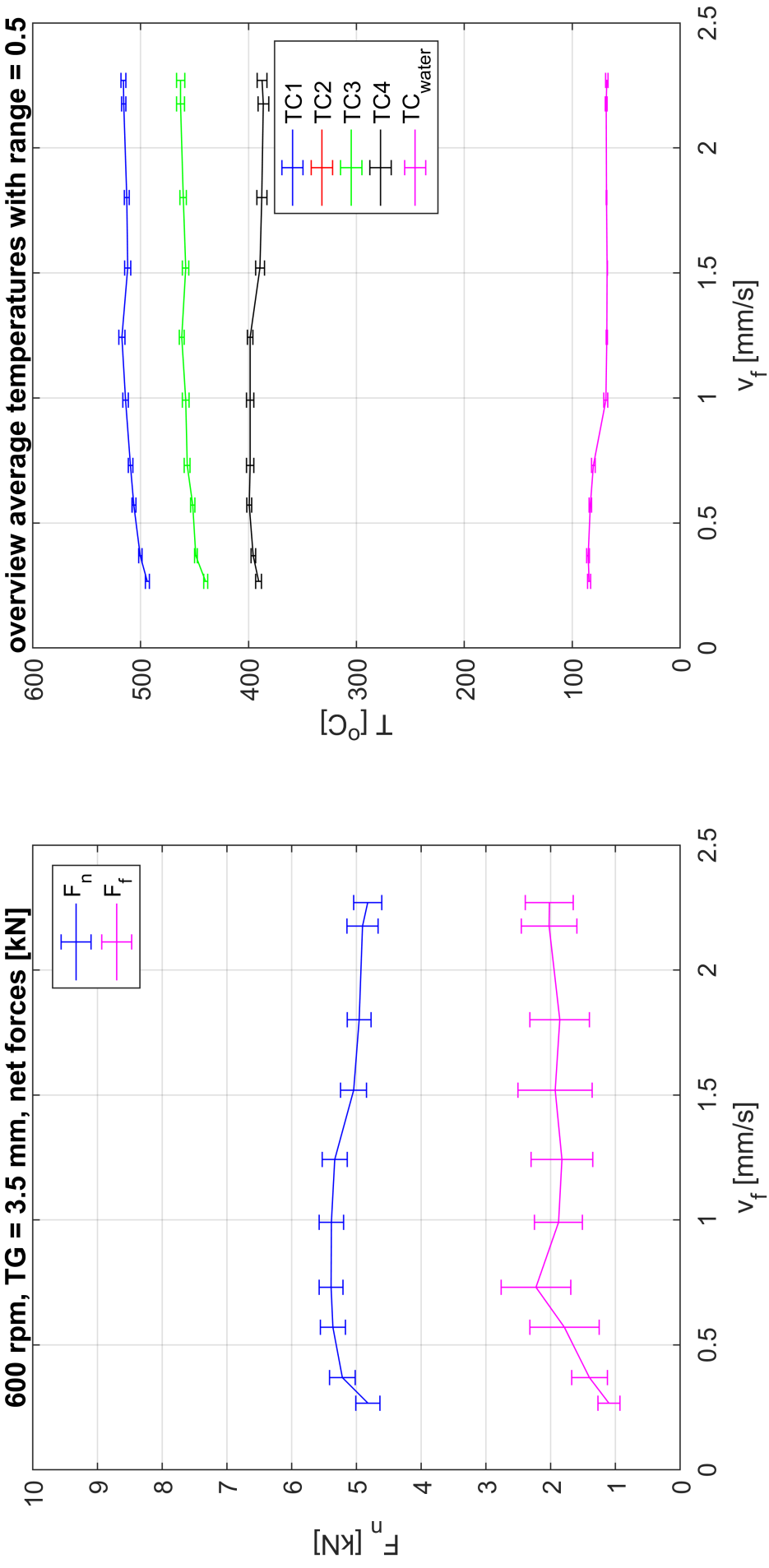

Figure 101: TG3.5_600_x: average forces and temperatures

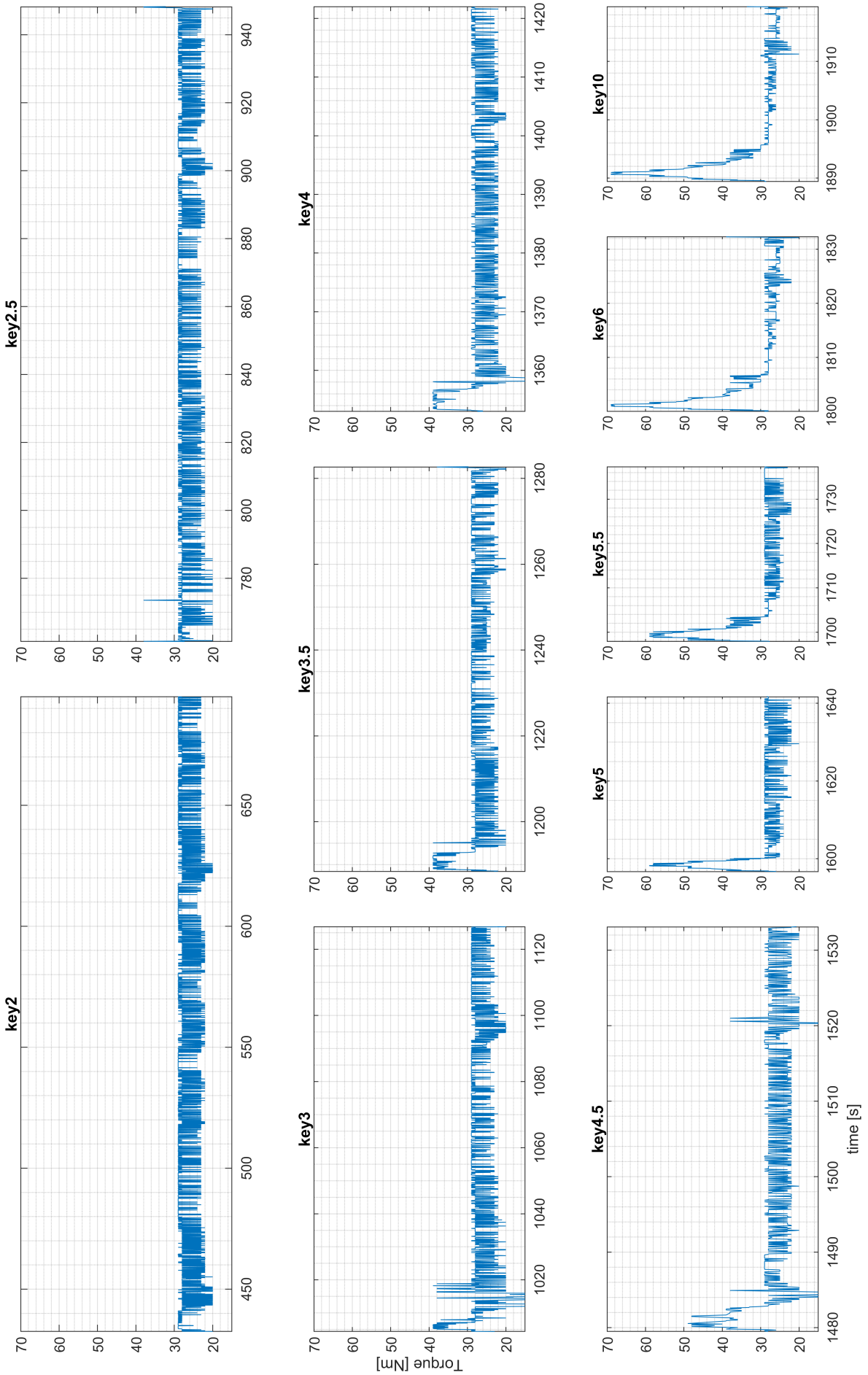

Figure 102: TG3.5_600_x: raw torque data cut per feed cylinder key velocity

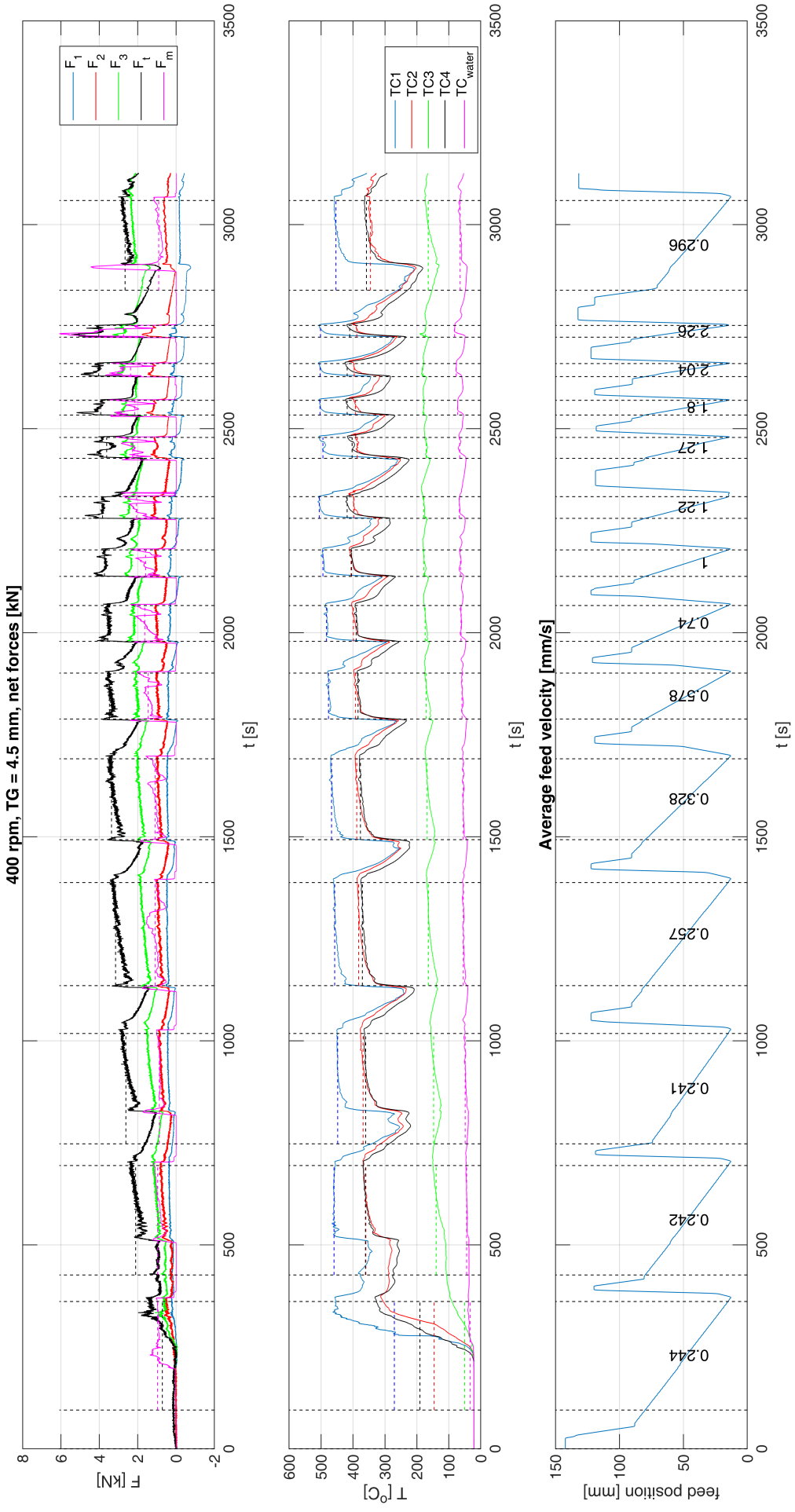

Figure 103: TG4.5_400_x: raw force, temperature and feed displacement data

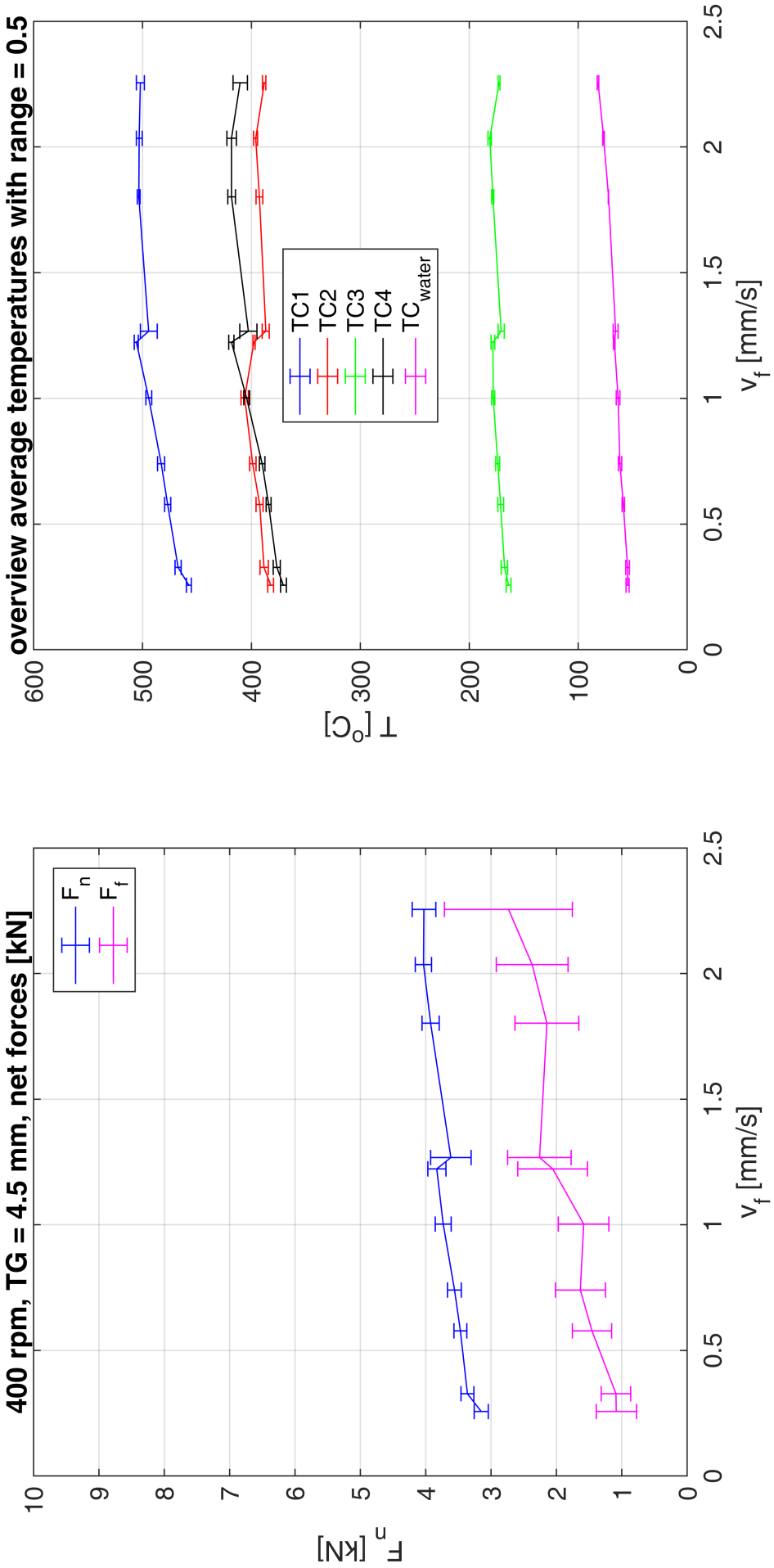

Figure 104: TG4.5_400_x: average forces and temperatures

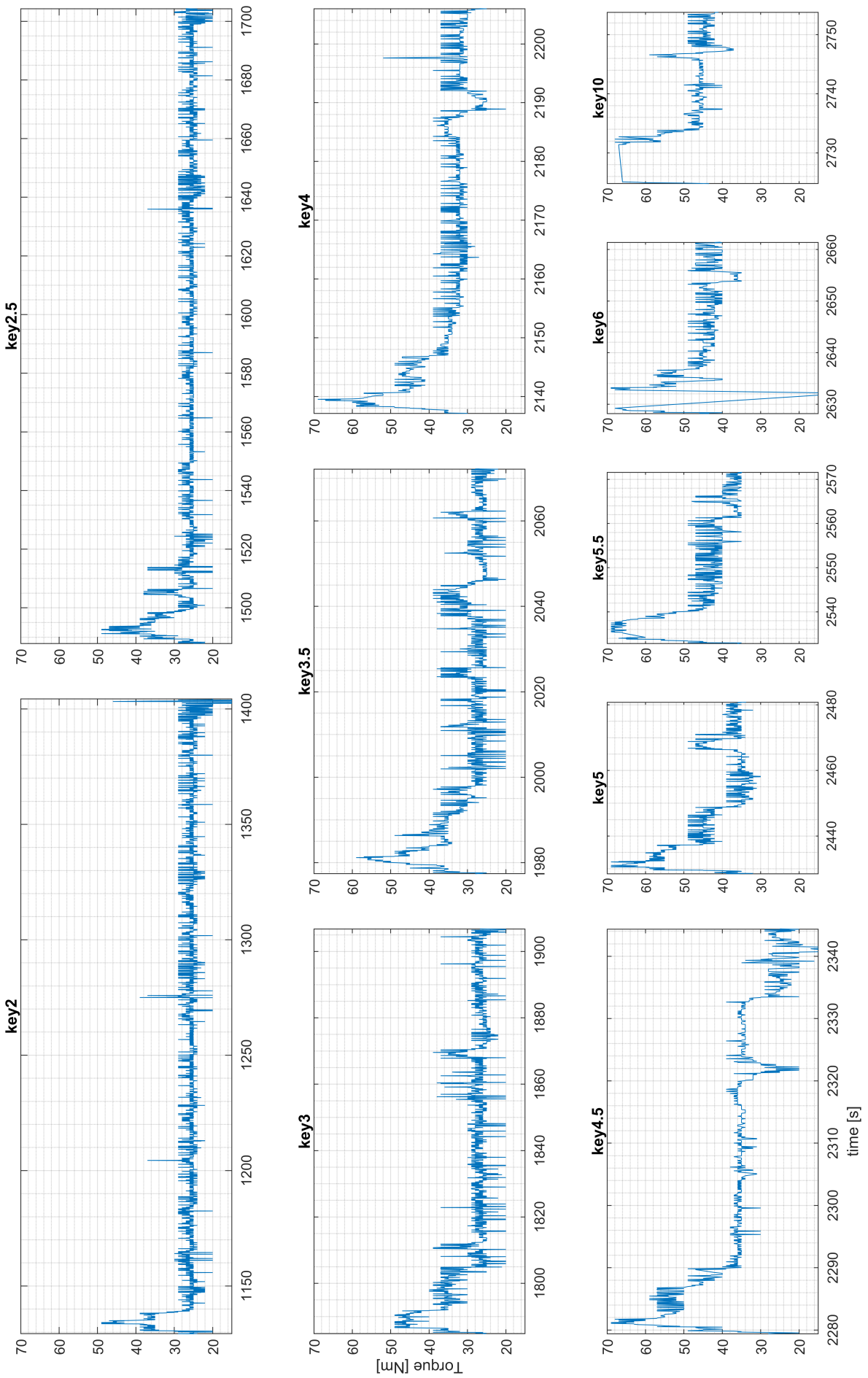

Figure 105: TG4.5_400_x: raw torque data cut per feed cylinder key velocity

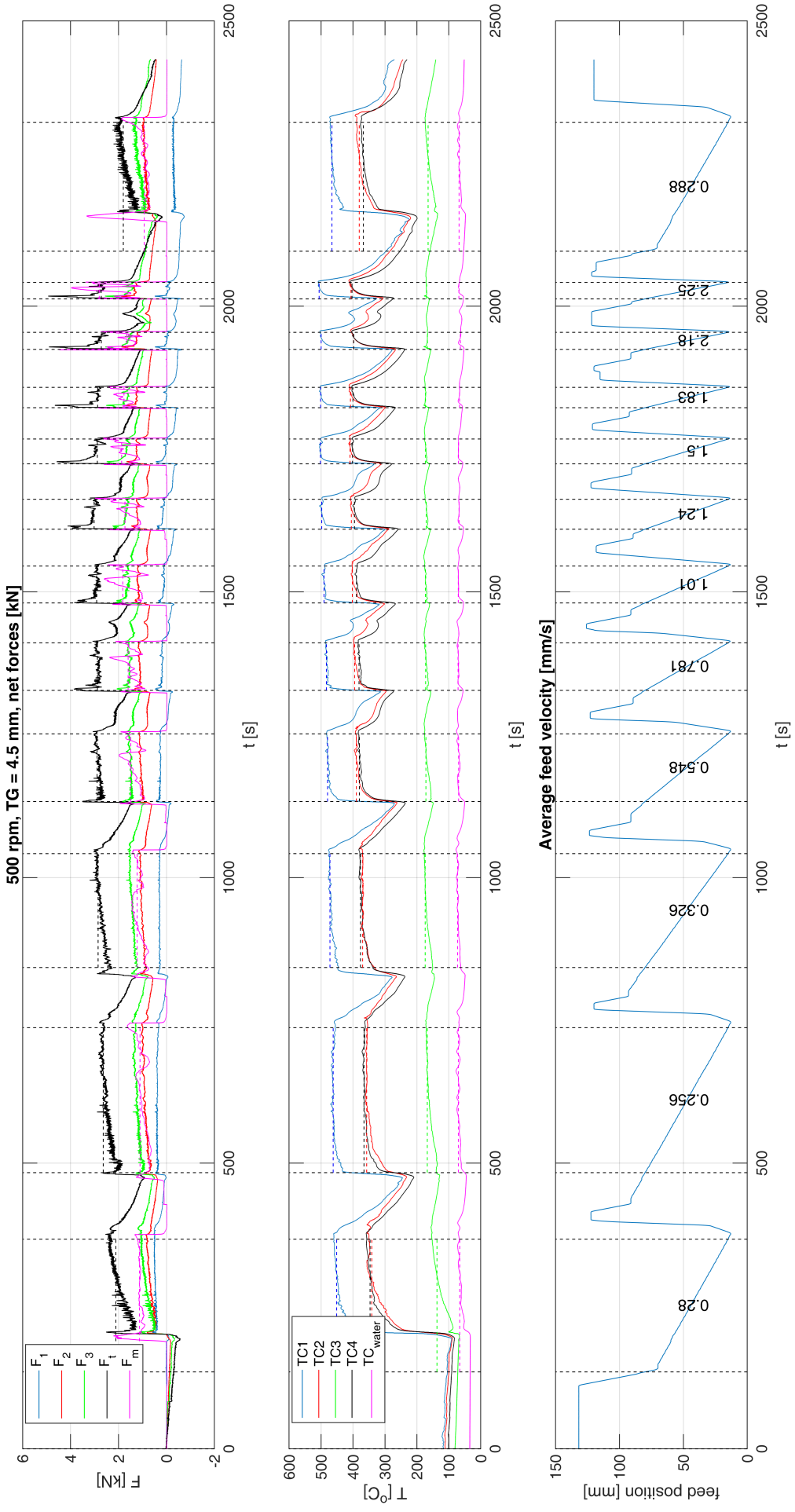

Figure 106: TG4.5_500_x: raw force, temperature and feed displacement data

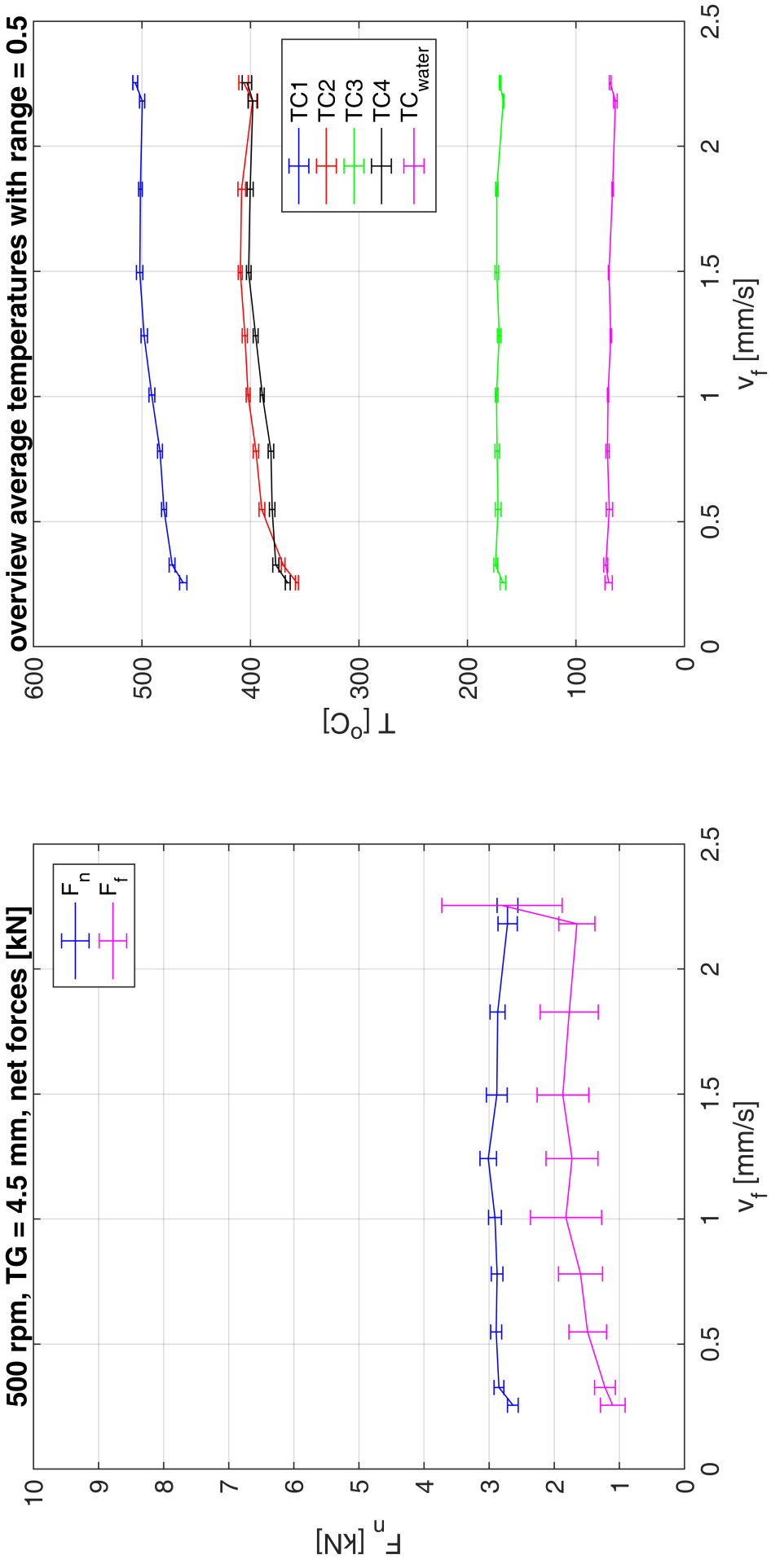

Figure 107: TG4.5_500_x: average forces and temperatures

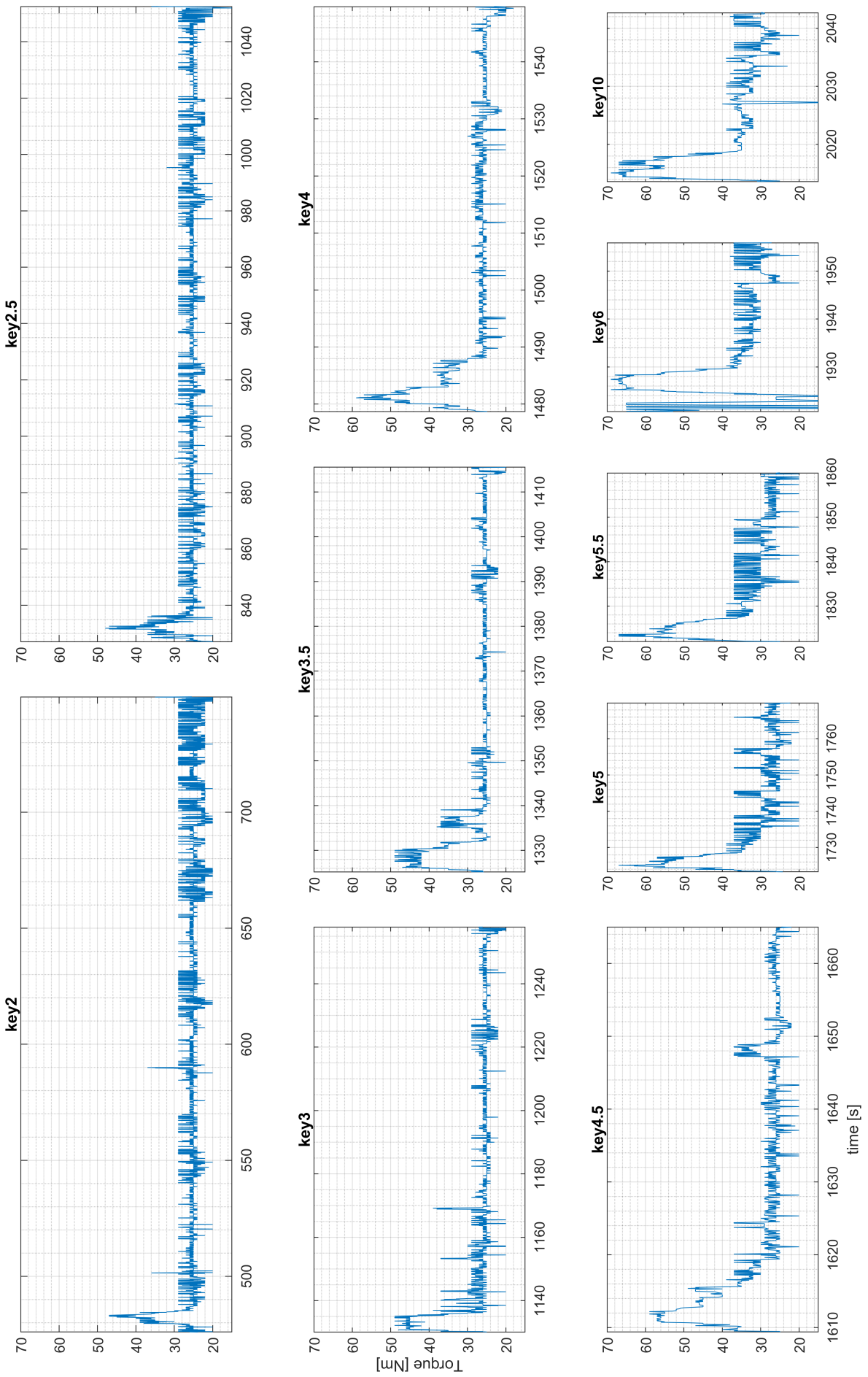

Figure 108: TG4.5_500_x: raw torque data cut per feed cylinder key velocity

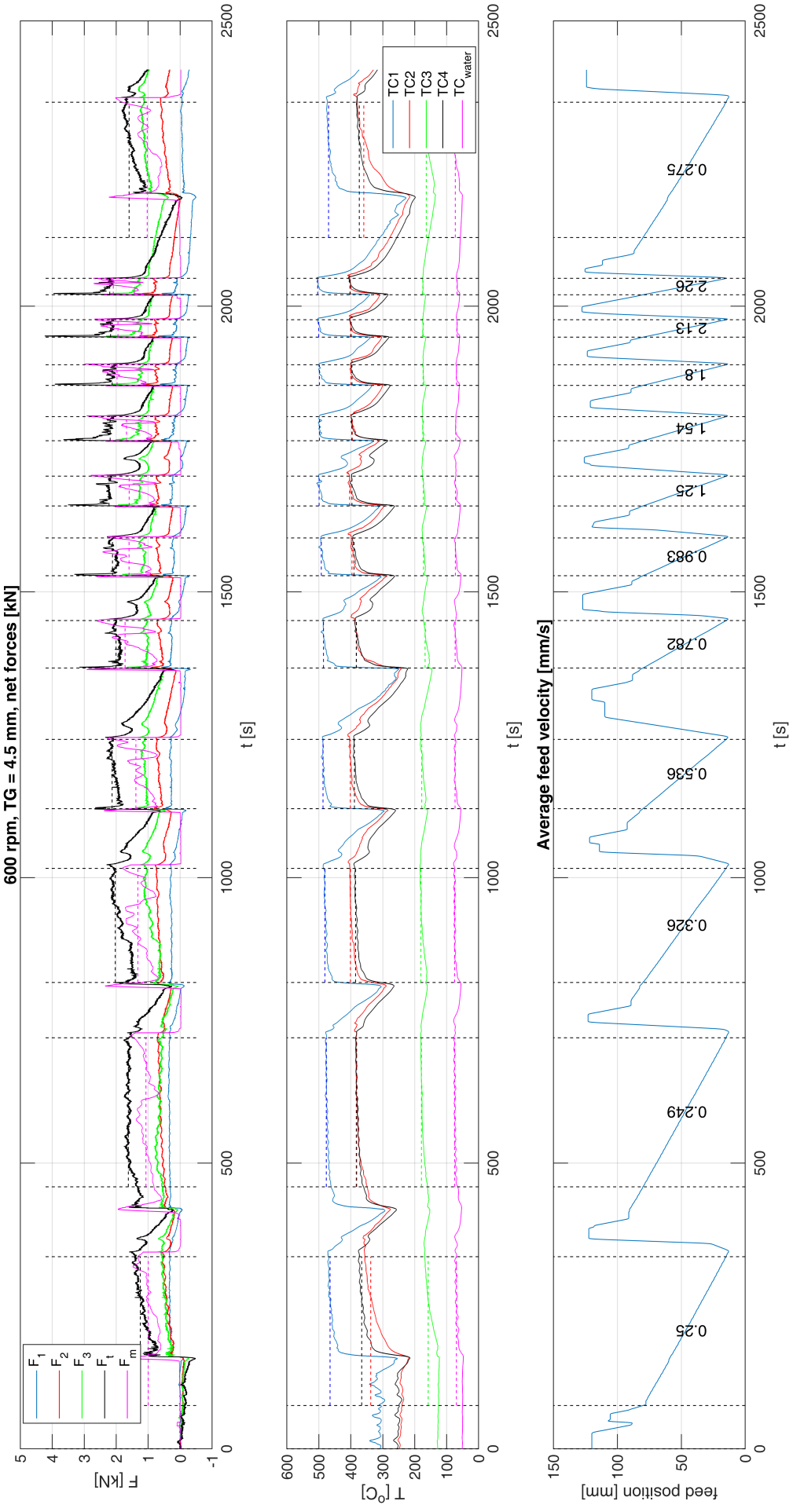

Figure 109: TG4.5_600_x: raw force, temperature and feed displacement data

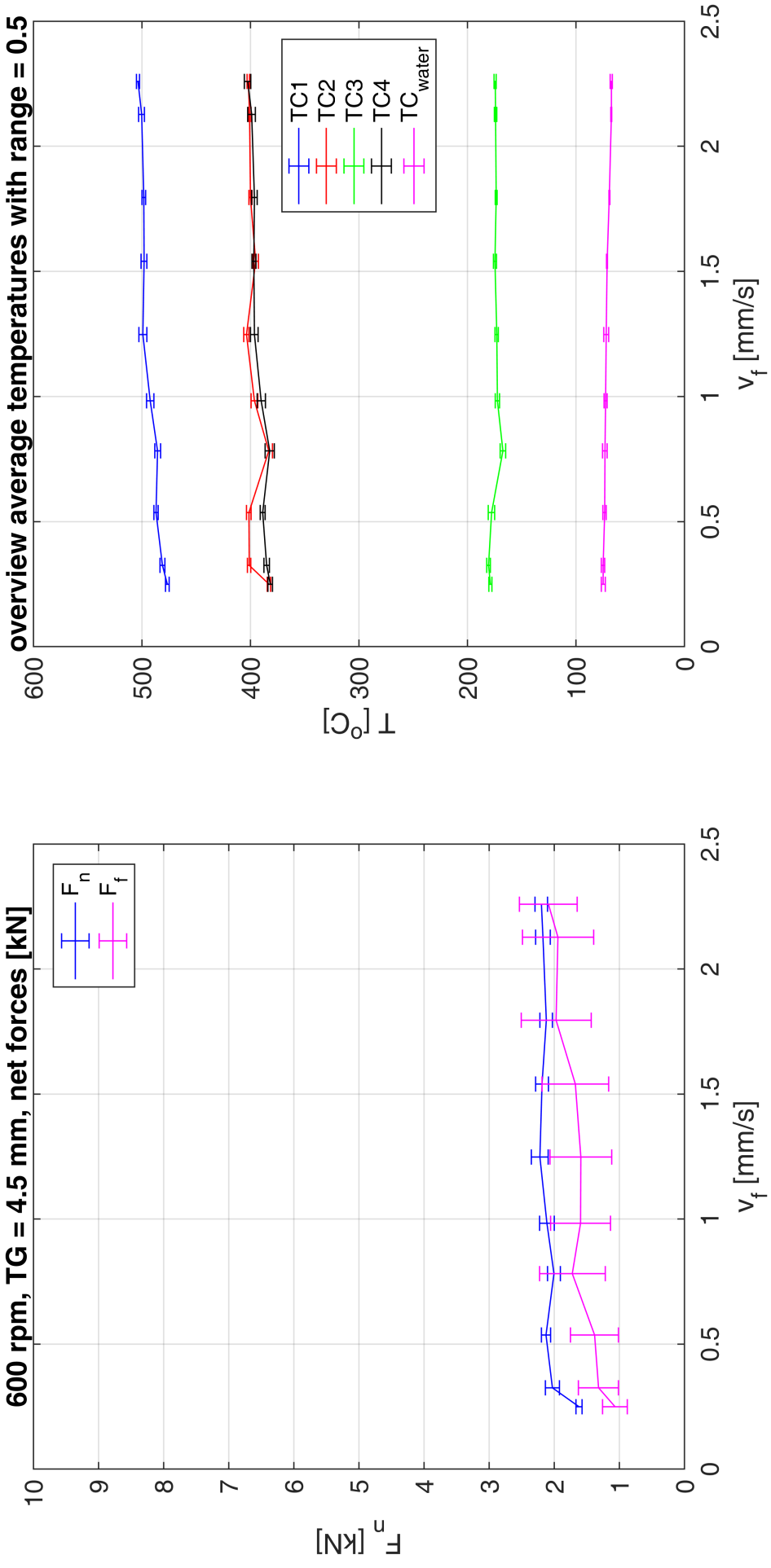

Figure 110: TG4.5_600_x: average forces and temperatures

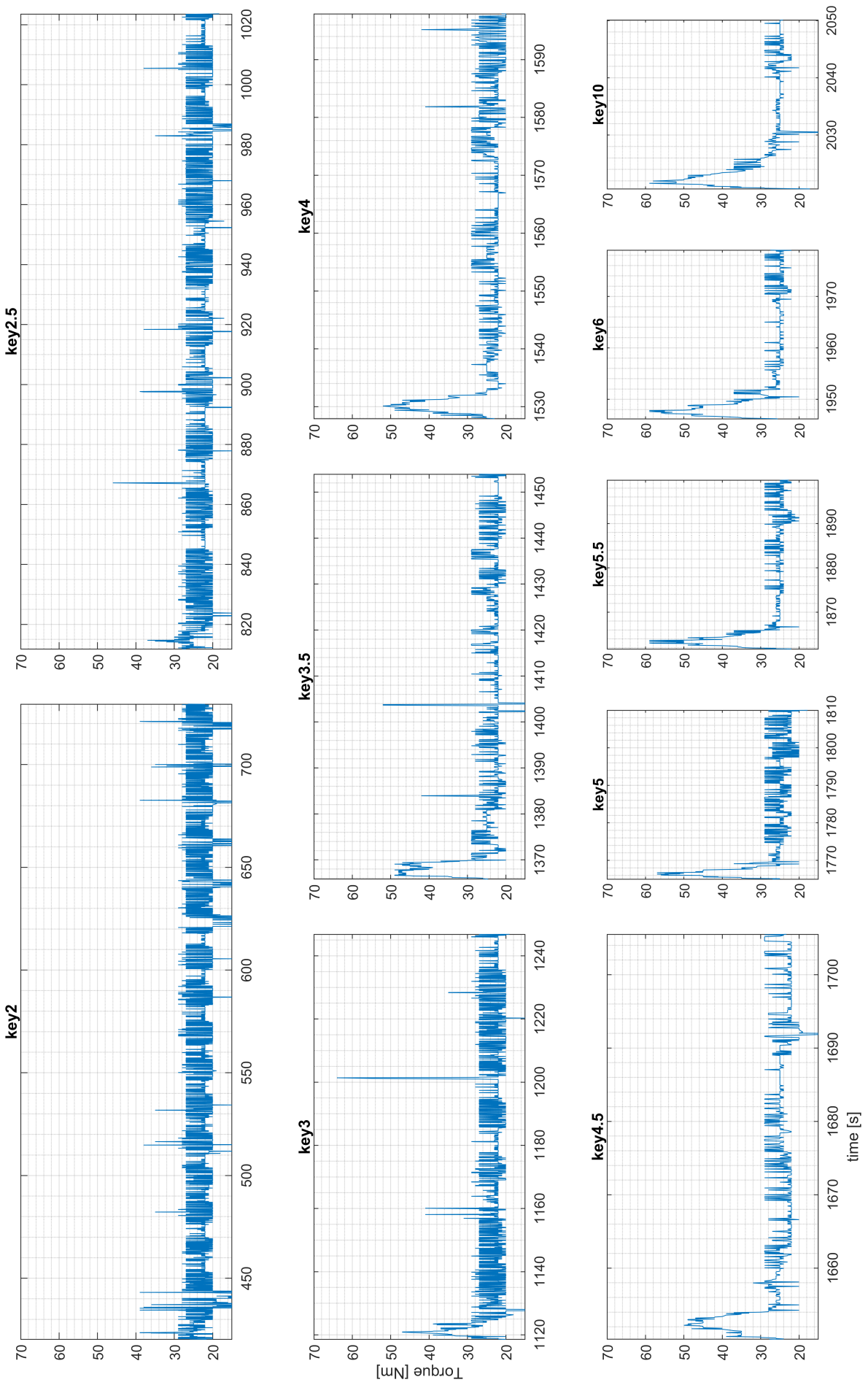

Figure 111: TG4.5_600_x: raw torque data cut per feed cylinder key velocity

F Experiment Data Figures: Series 2

On the next pages, additional data figures are presented from the tool gap experiments series 2 of which the results are presented and discussed in Chapter 4. This in order to give a complete and comprehensive overview of the experimental data for future reference.

The experiments are performed in the working order as presented in Table 3.

At first, the overview graphs of average forces, temperatures or torque are presented sorted per tool gap or tool rotation rate with and also without standard deviation for clearer possible trend indication. Next, the raw data per experiment is presented in three figures per experiment;

1. The raw data straight from the mentioned Labview programme. This includes normal forces, feed force, thermocouple data and hydraulic cylinder travel with average velocity.
2. The averaged forces and thermocouple data per key. Averages taken from the last halve of an extrusion run.
3. The raw torque data cut per key section.

F.1 Overview Figures

The remaining of this page is left blank intentionally to maximise figure size on the next page.

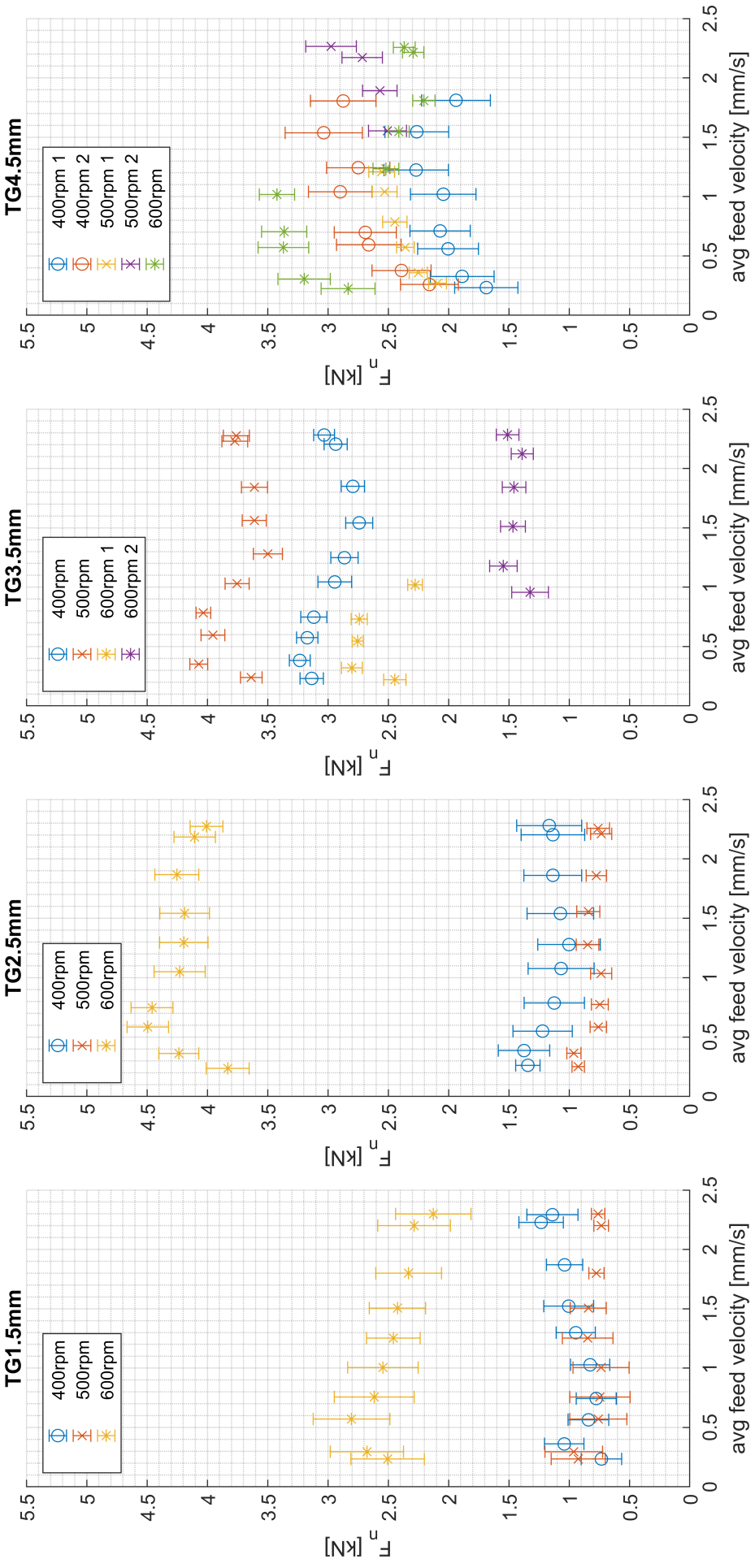

Figure 112: Average normal force sorted per tool gap

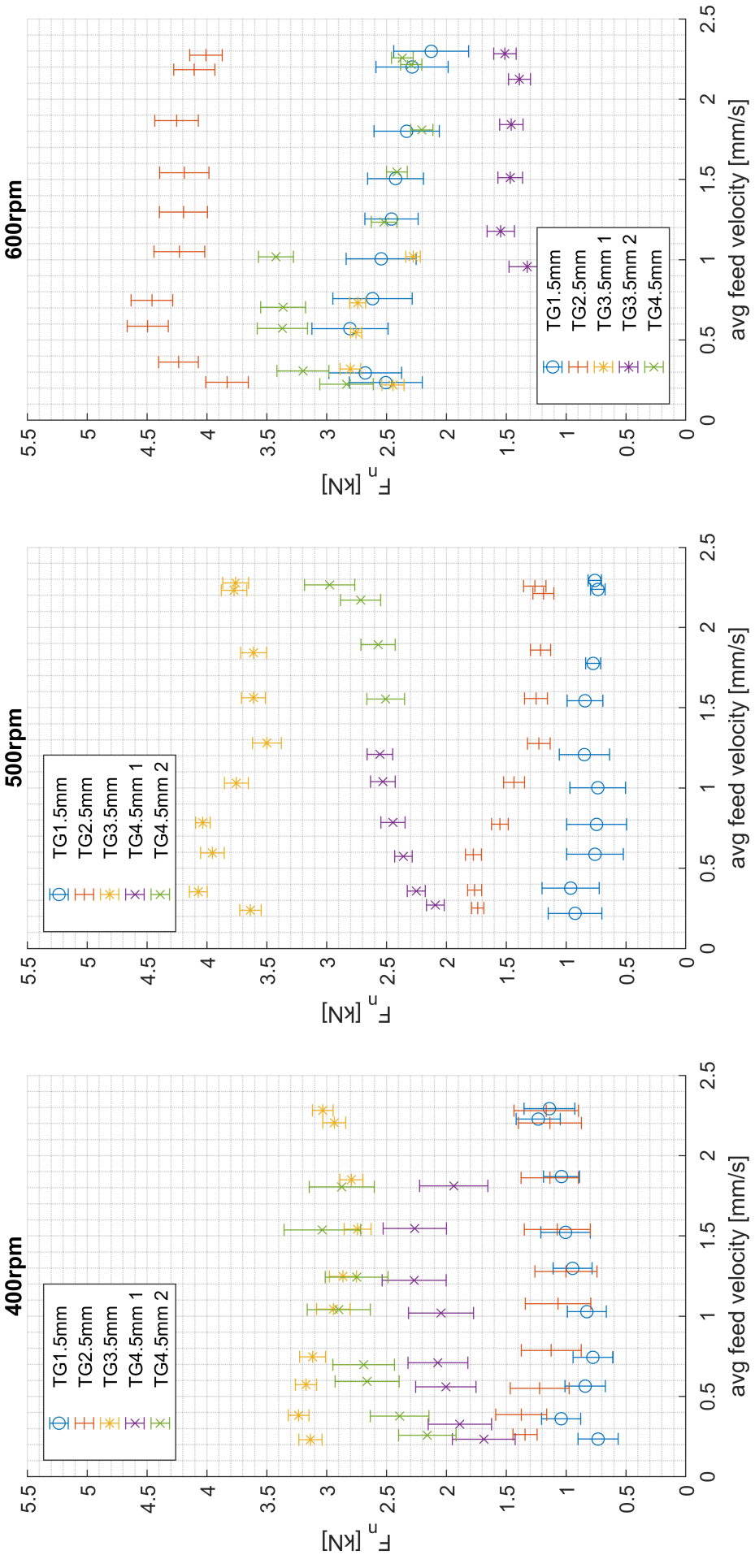

Figure 113: Average normal force sorted per tool rotation rate

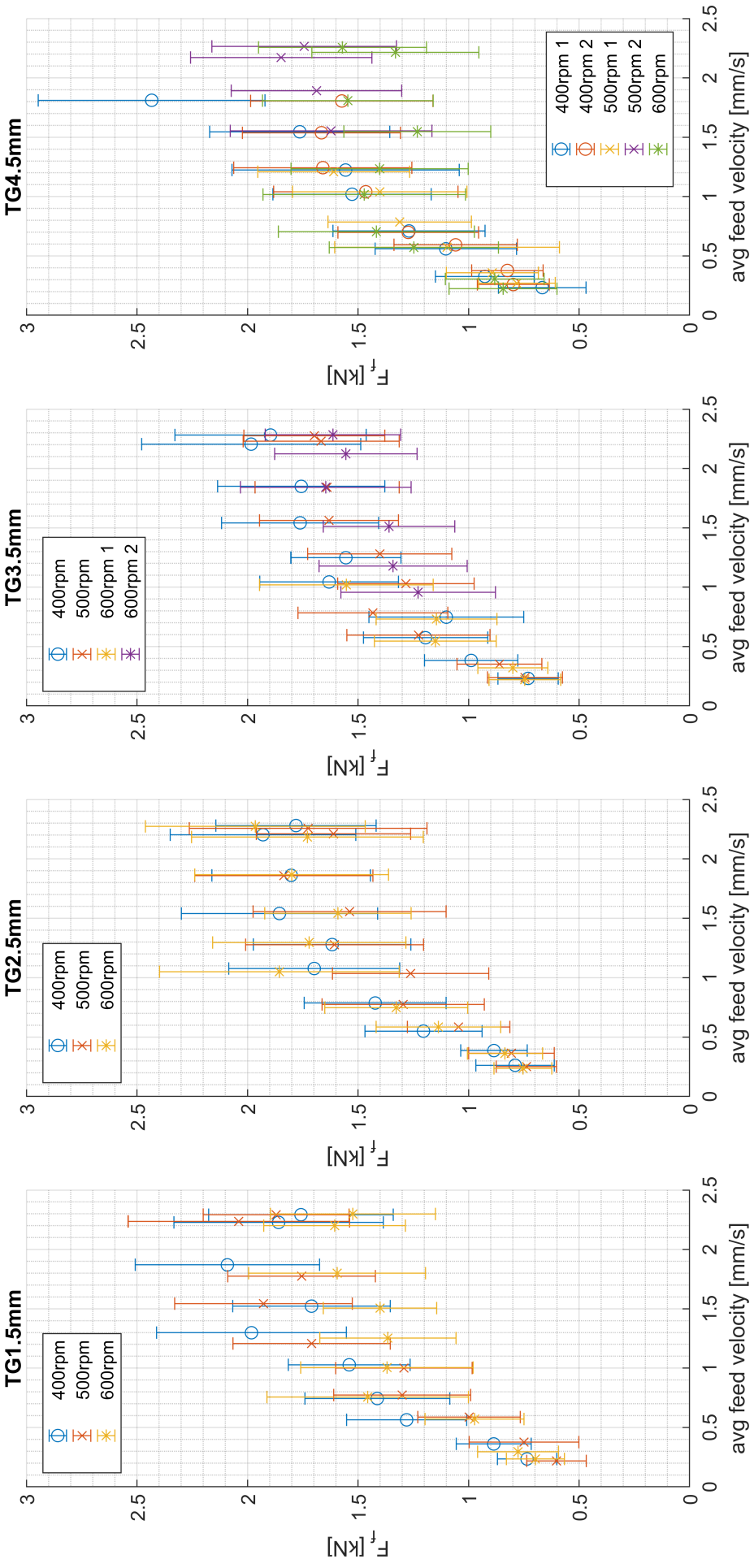

Figure 114: Average feed force sorted per tool gap

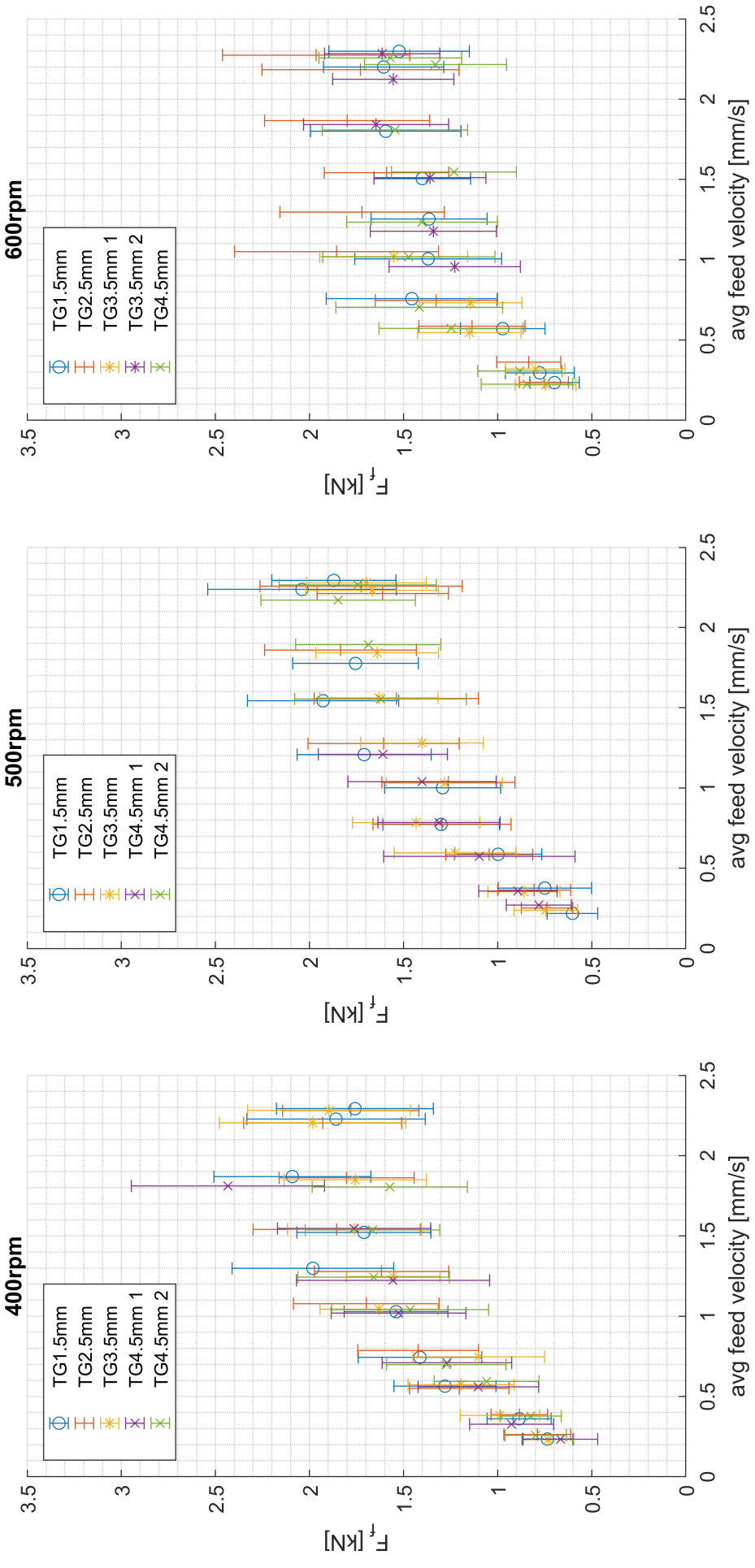

Figure 115: Average feed force sorted per tool rotation rate

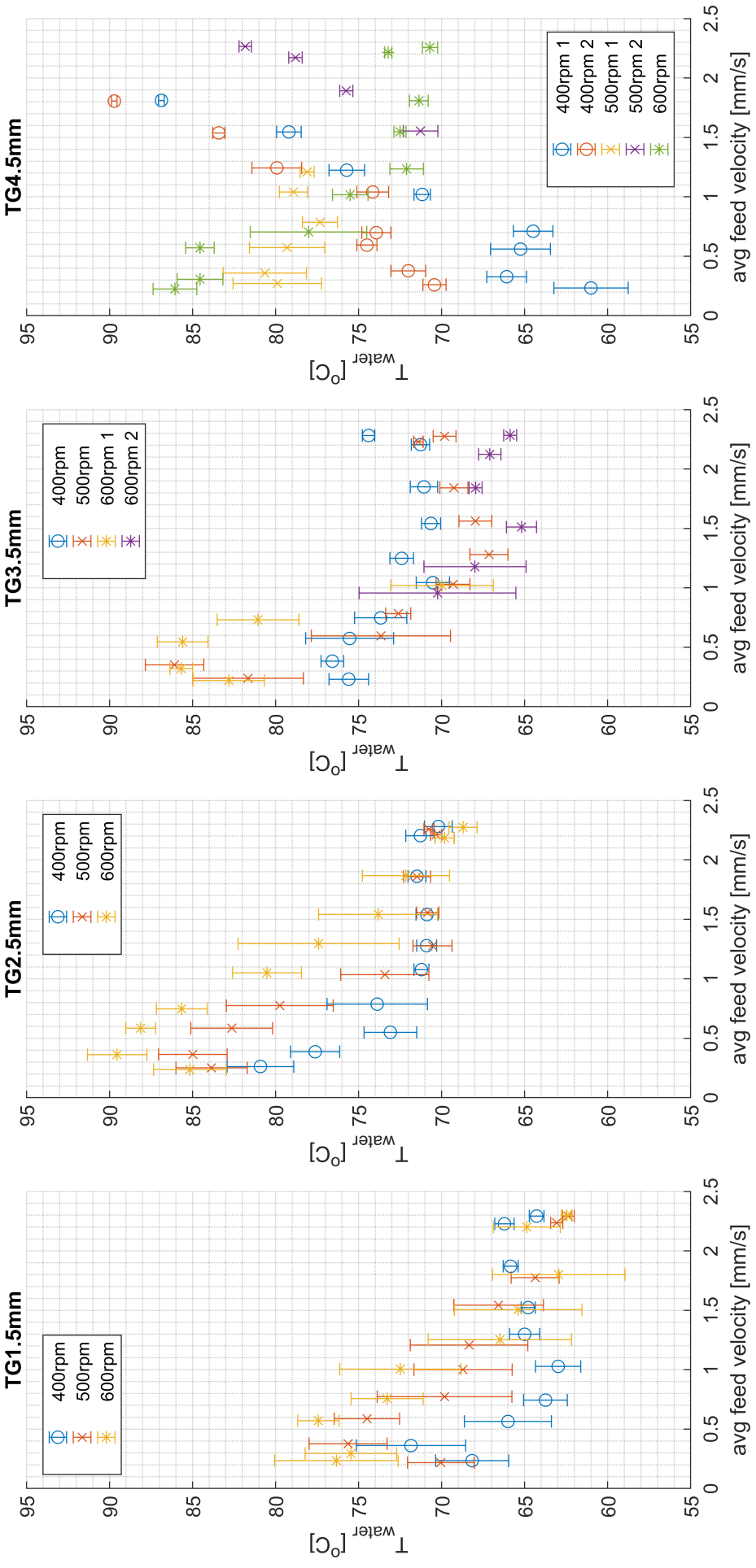

Figure 116: Average water temperature sorted per tool gap

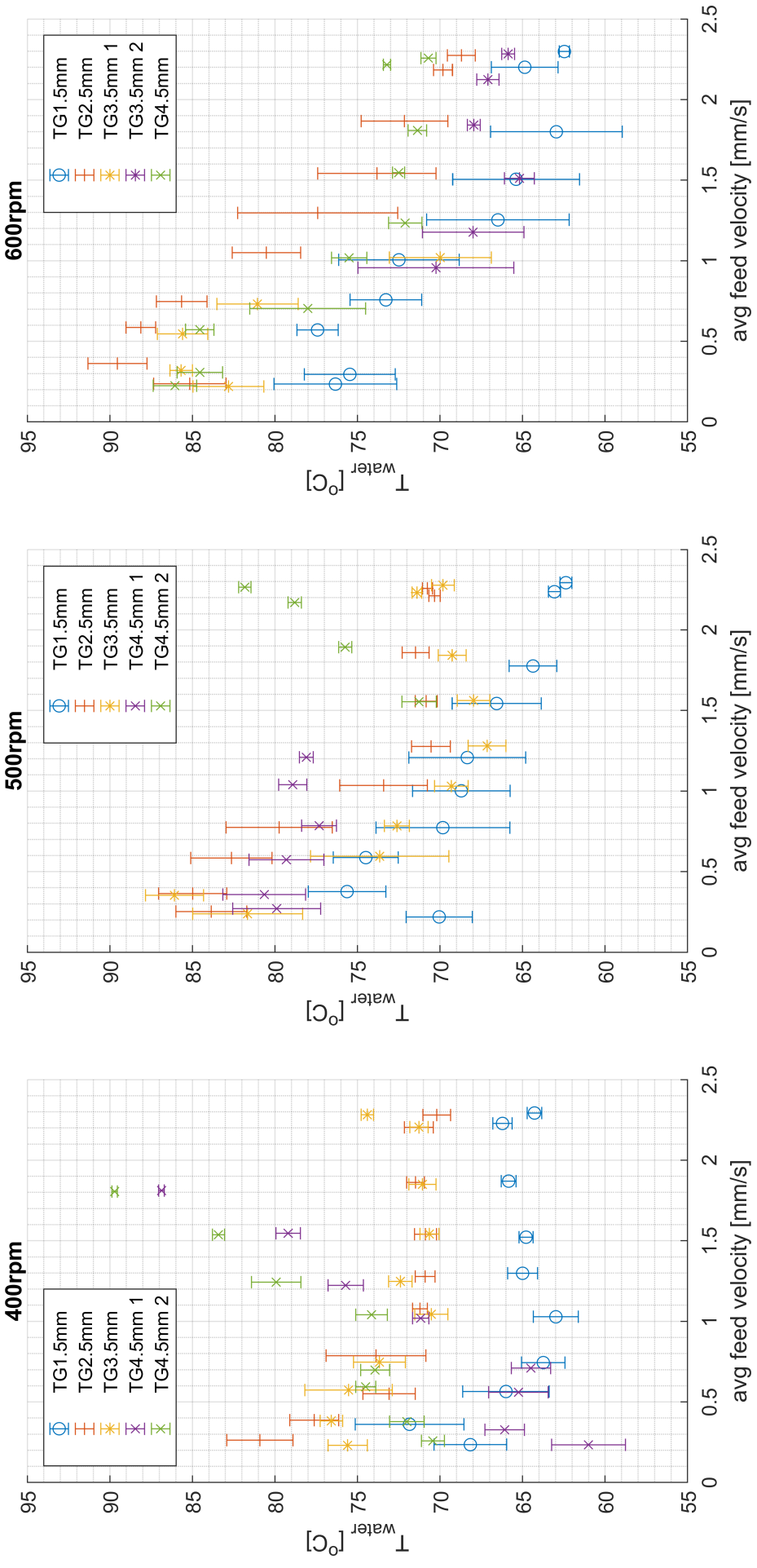

Figure 117: Average water temperature sorted per tool rotation rate

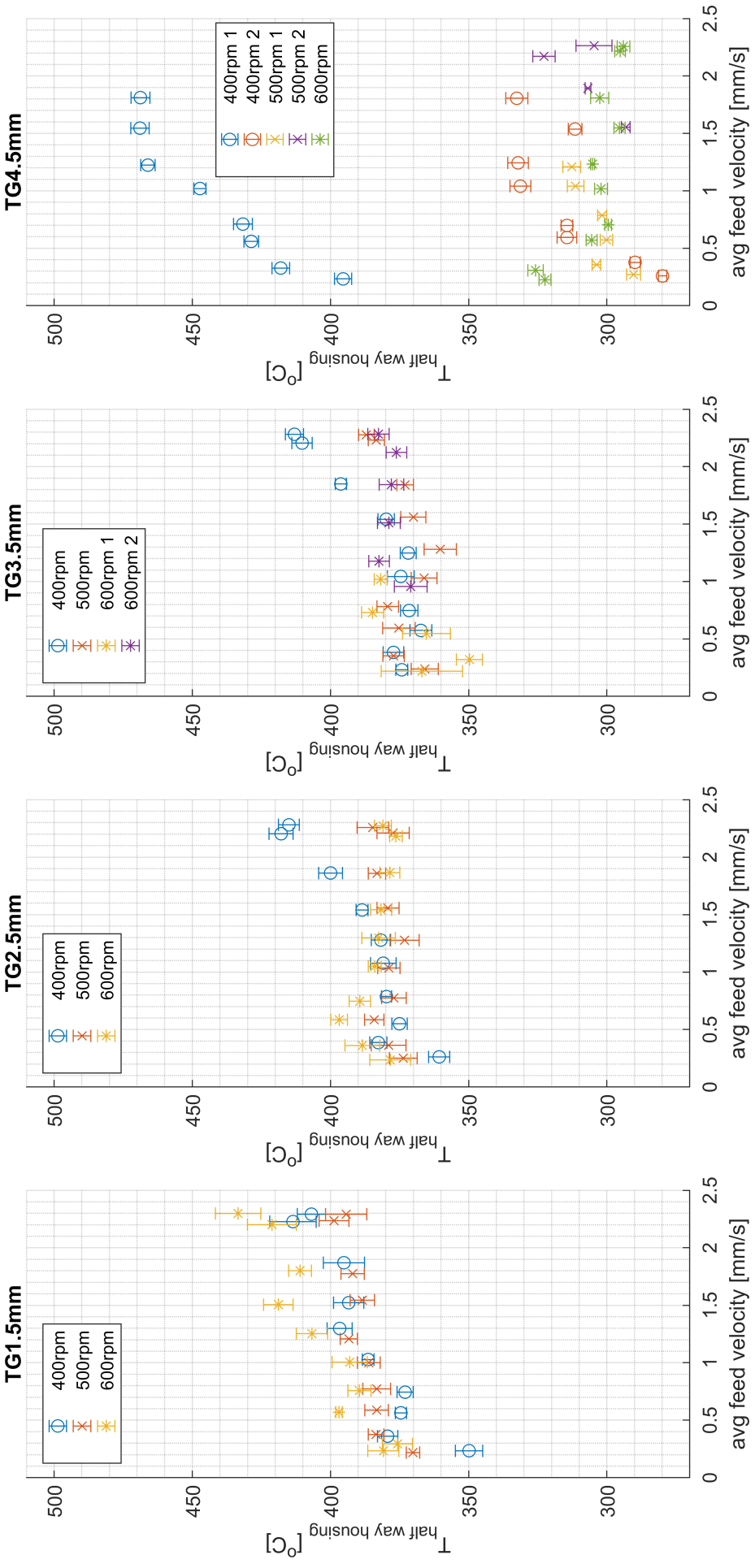

Figure 118: Average temperature half-way the housing sorted per tool gap

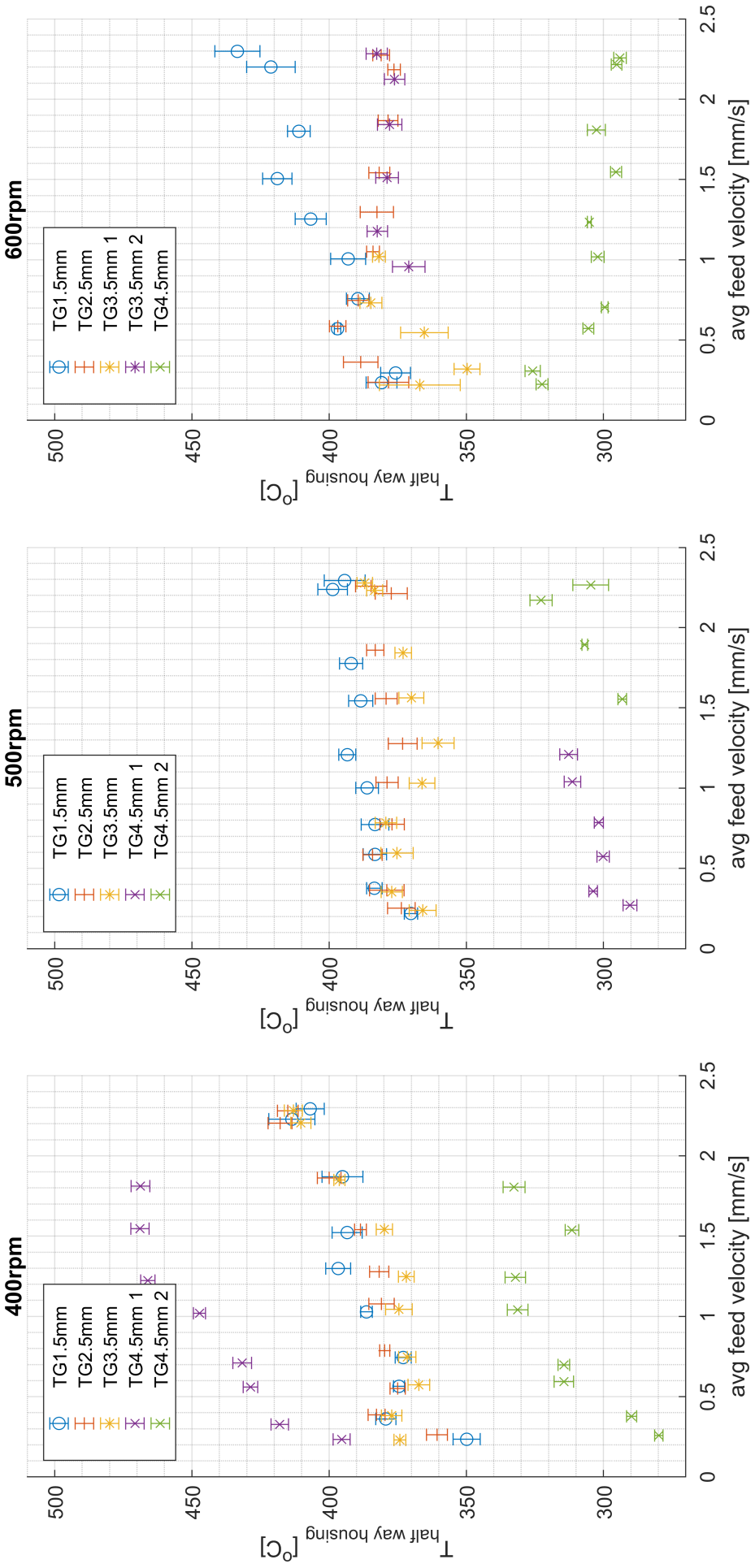

Figure 119: Average temperature half-way the housing sorted per tool rotation rate

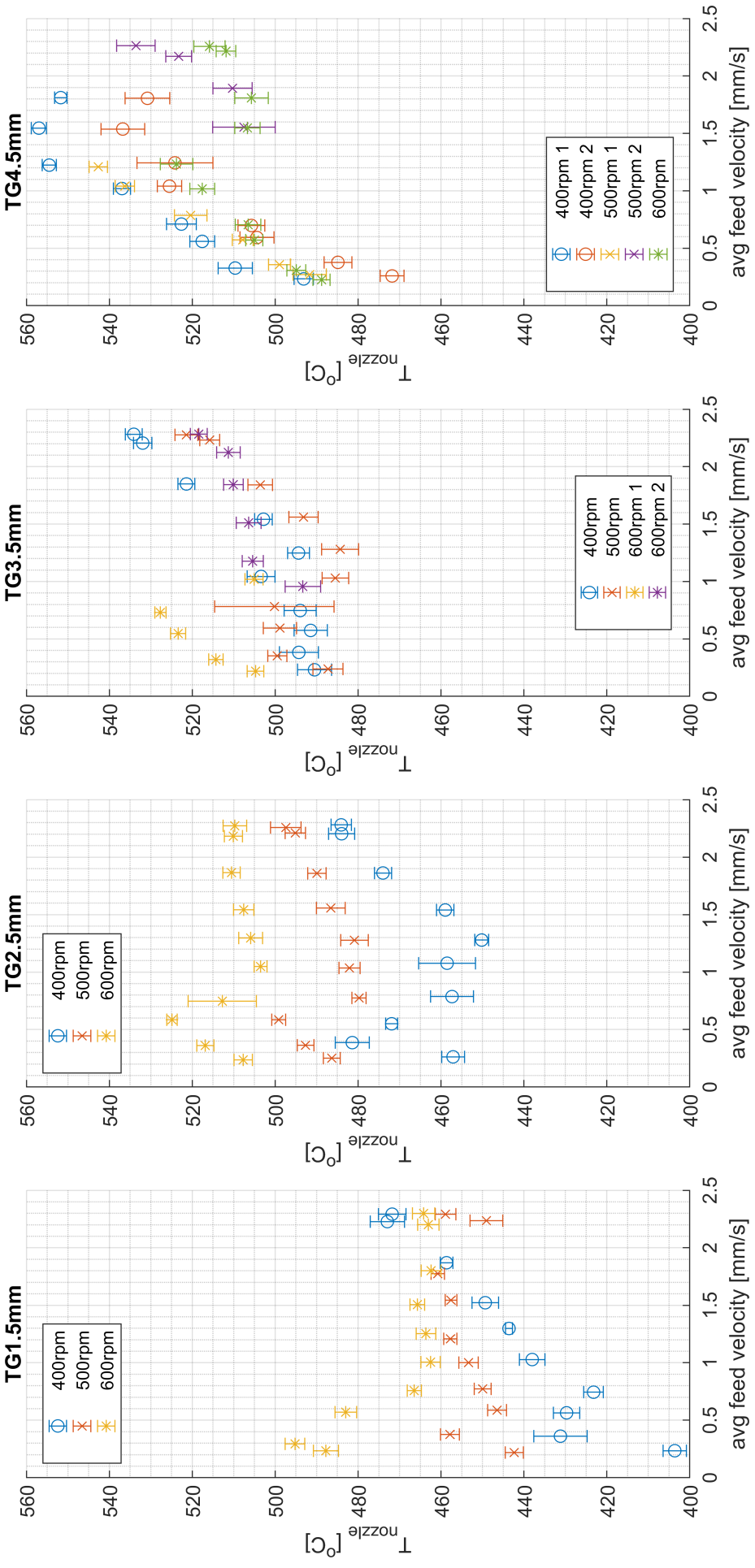

Figure 120: Average nozzle temperature sorted per tool gap

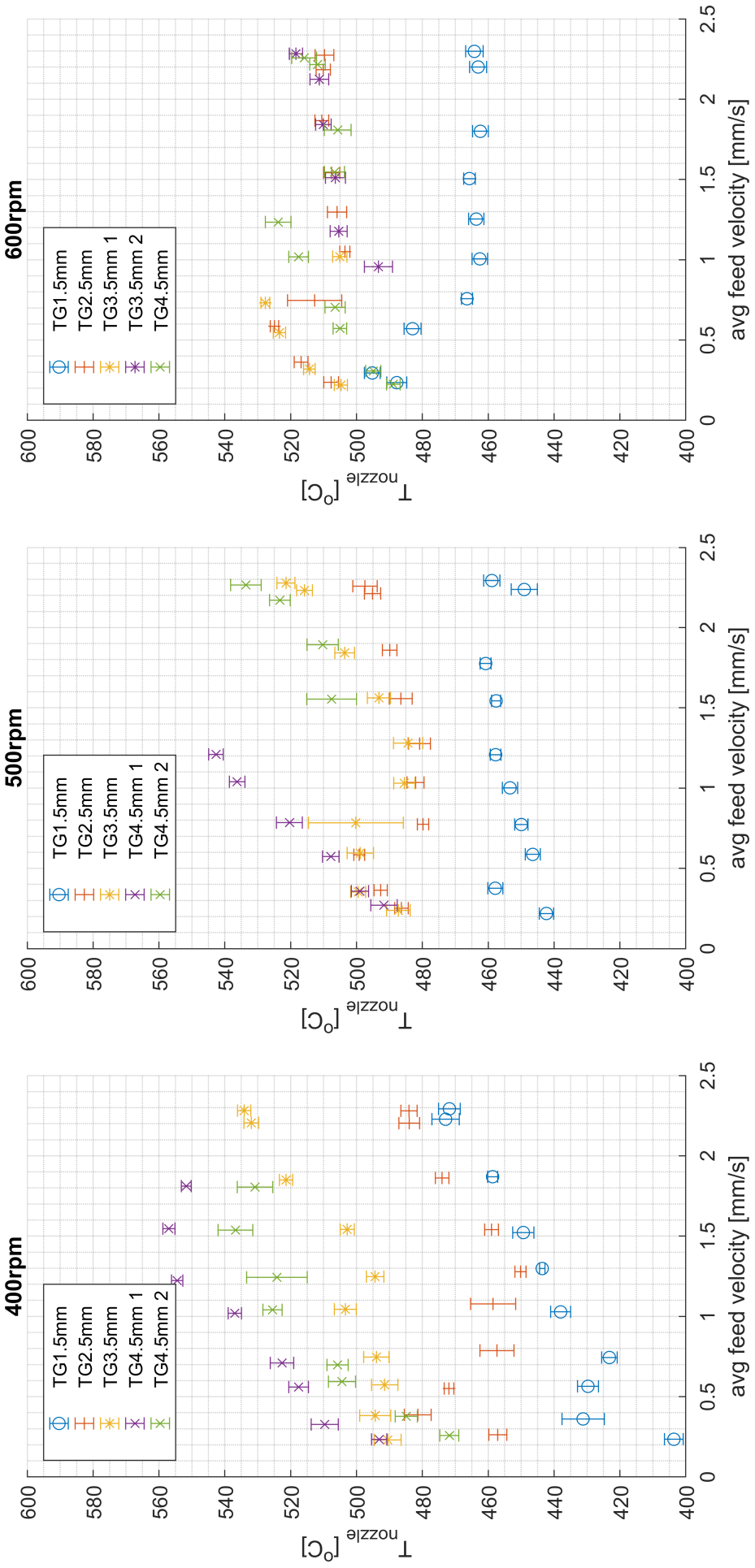

Figure 121: Average nozzle temperature sorted per tool rotation rate

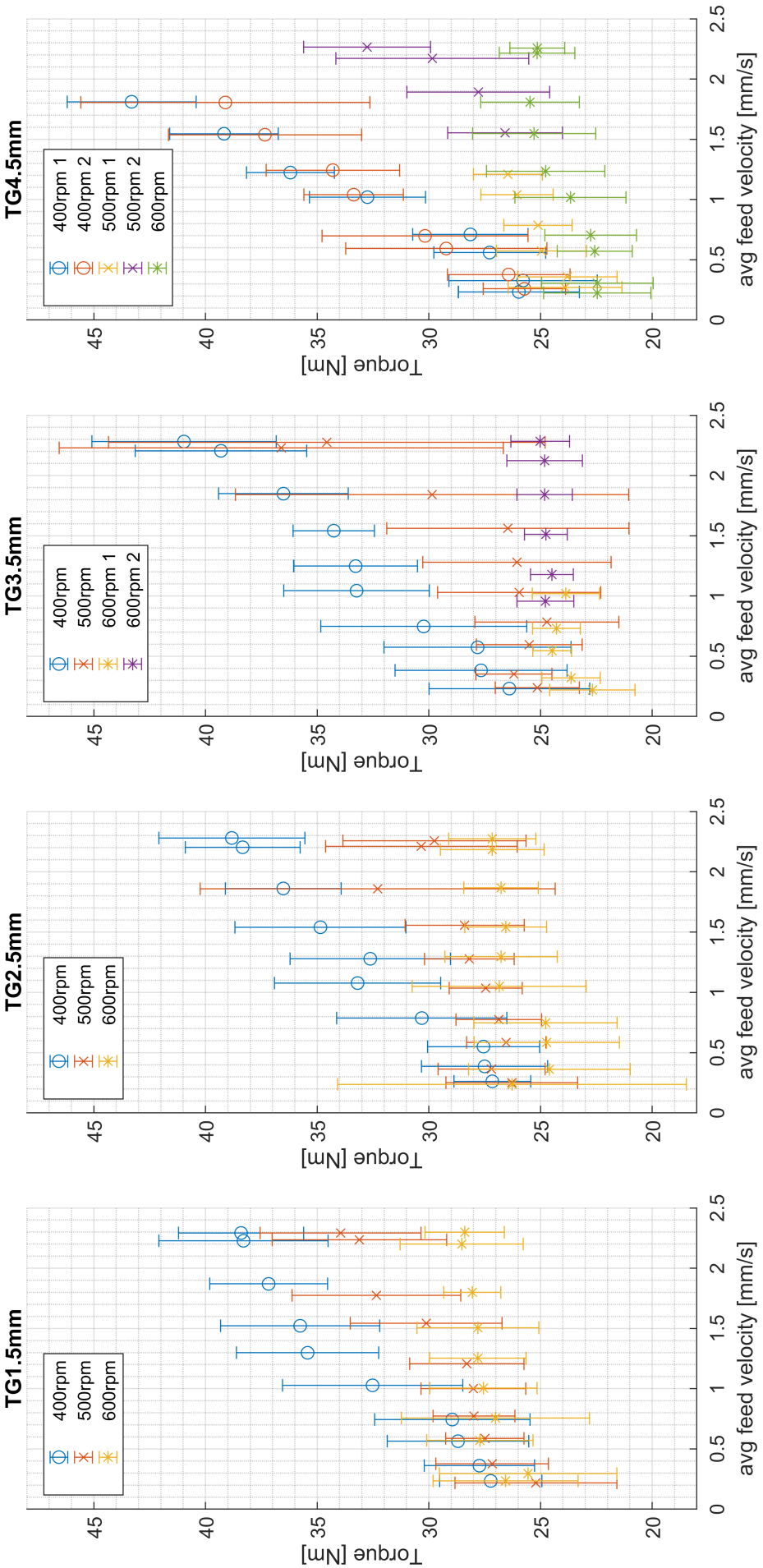

Figure 122: Average torque sorted per tool gap

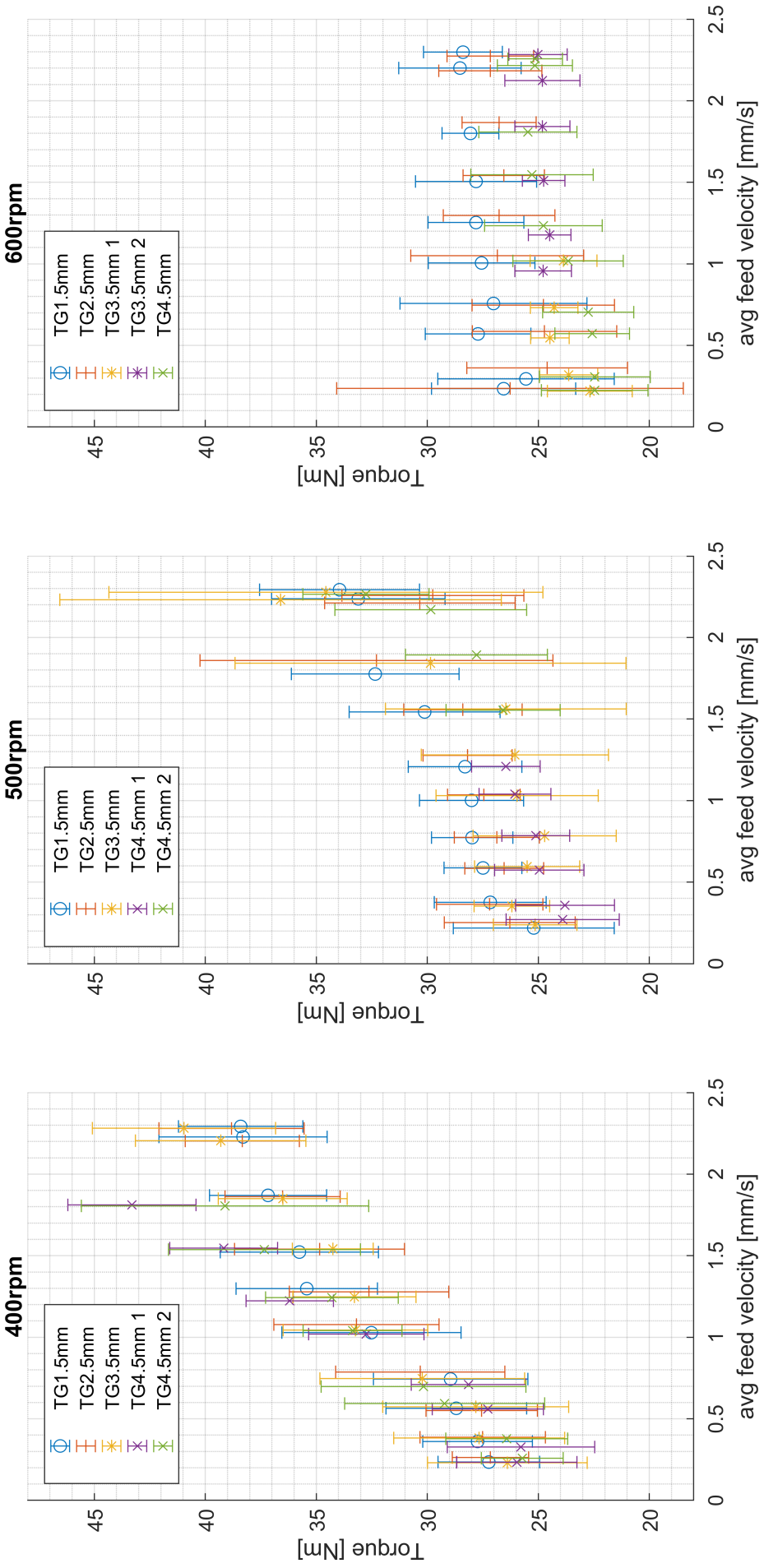

Figure 123: Average torque sorted per tool rotation rate

F.2 Raw Data Figures per Experiment

The remaining of this page is left blank intentionally to maximise figure size on the next page.

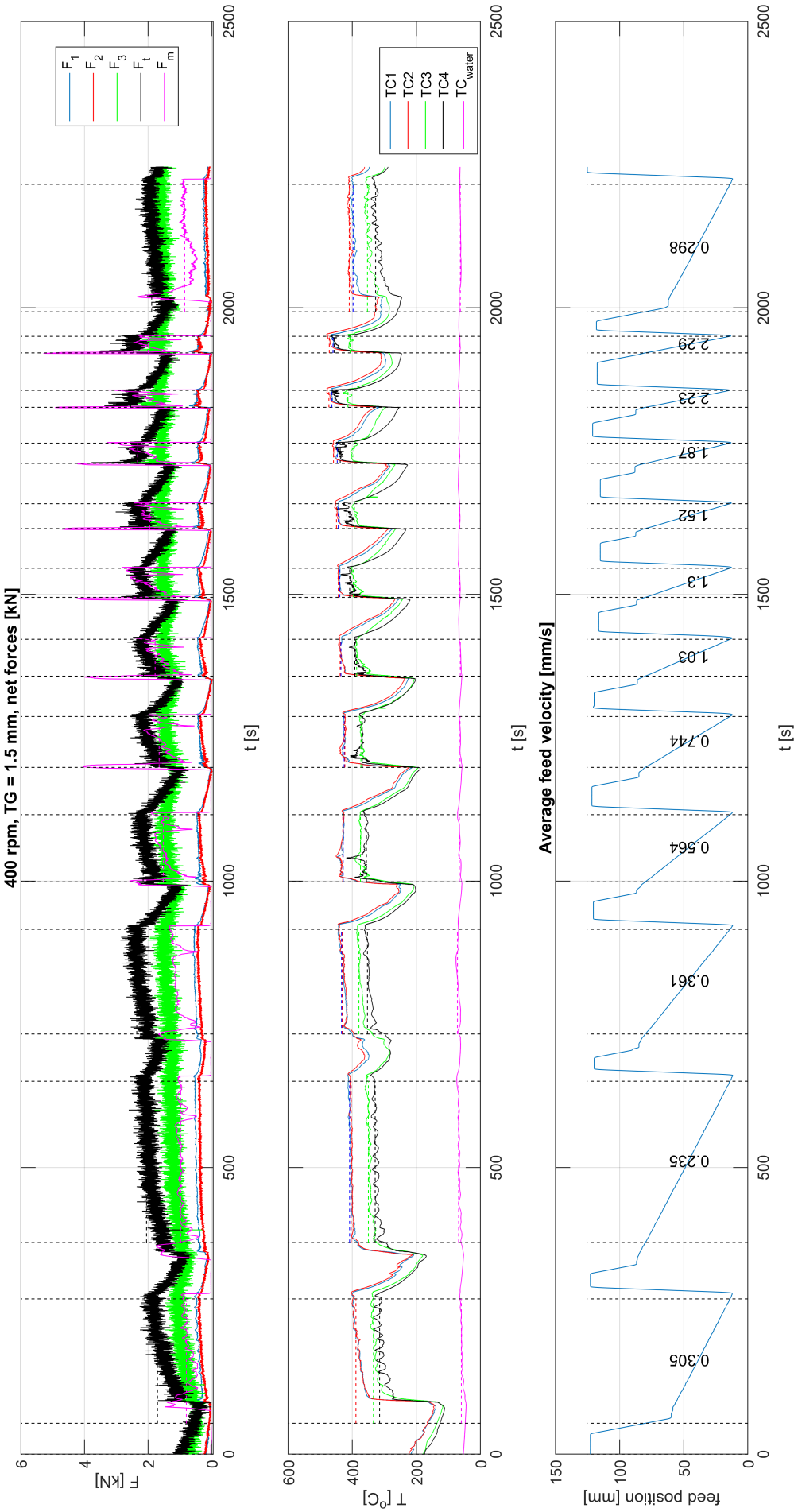

Figure 124: 2TG1.5_400_x: raw force, temperature and feed displacement data

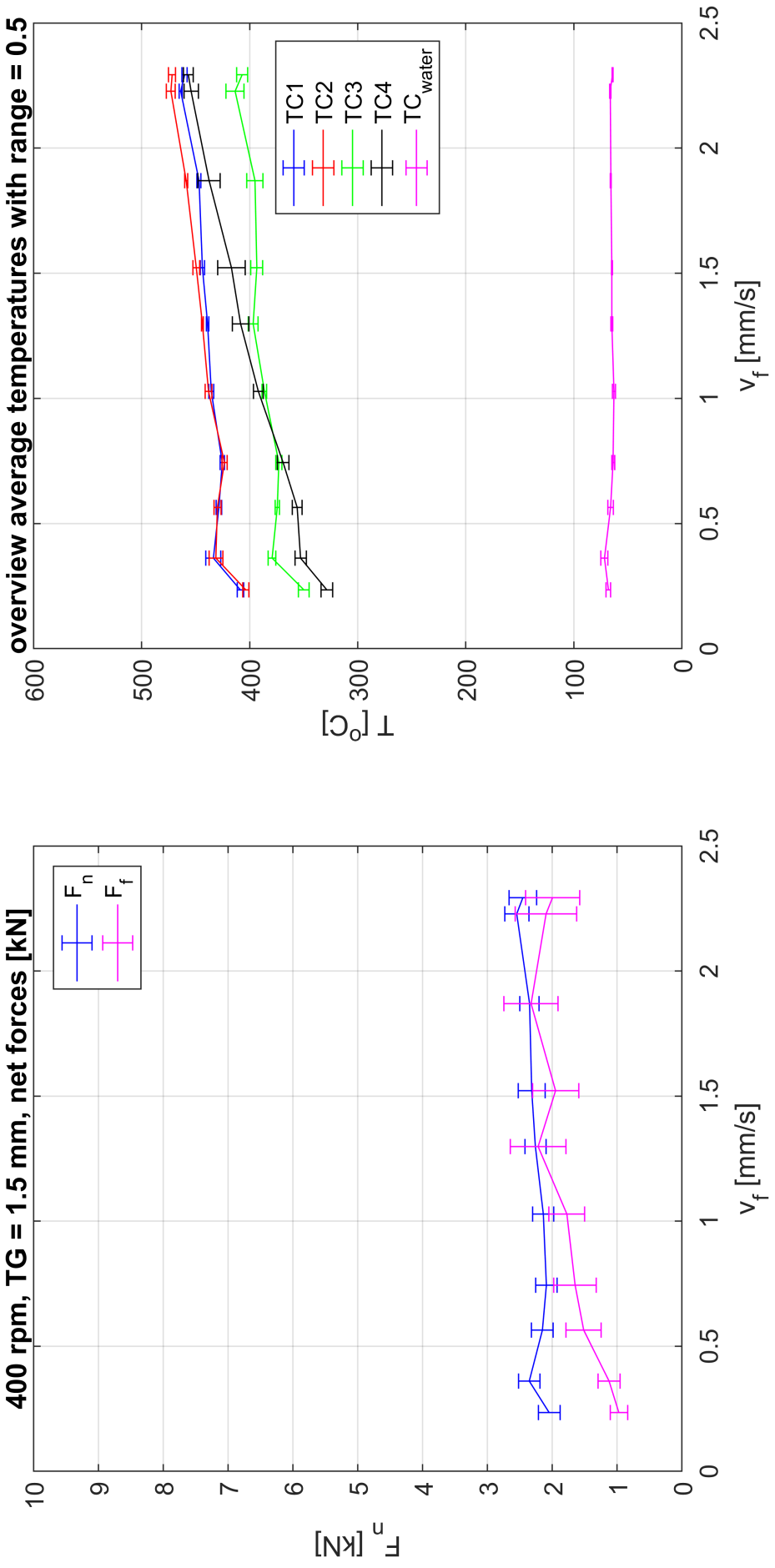

Figure 125: 2TG1.5_400_x: average forces and temperatures

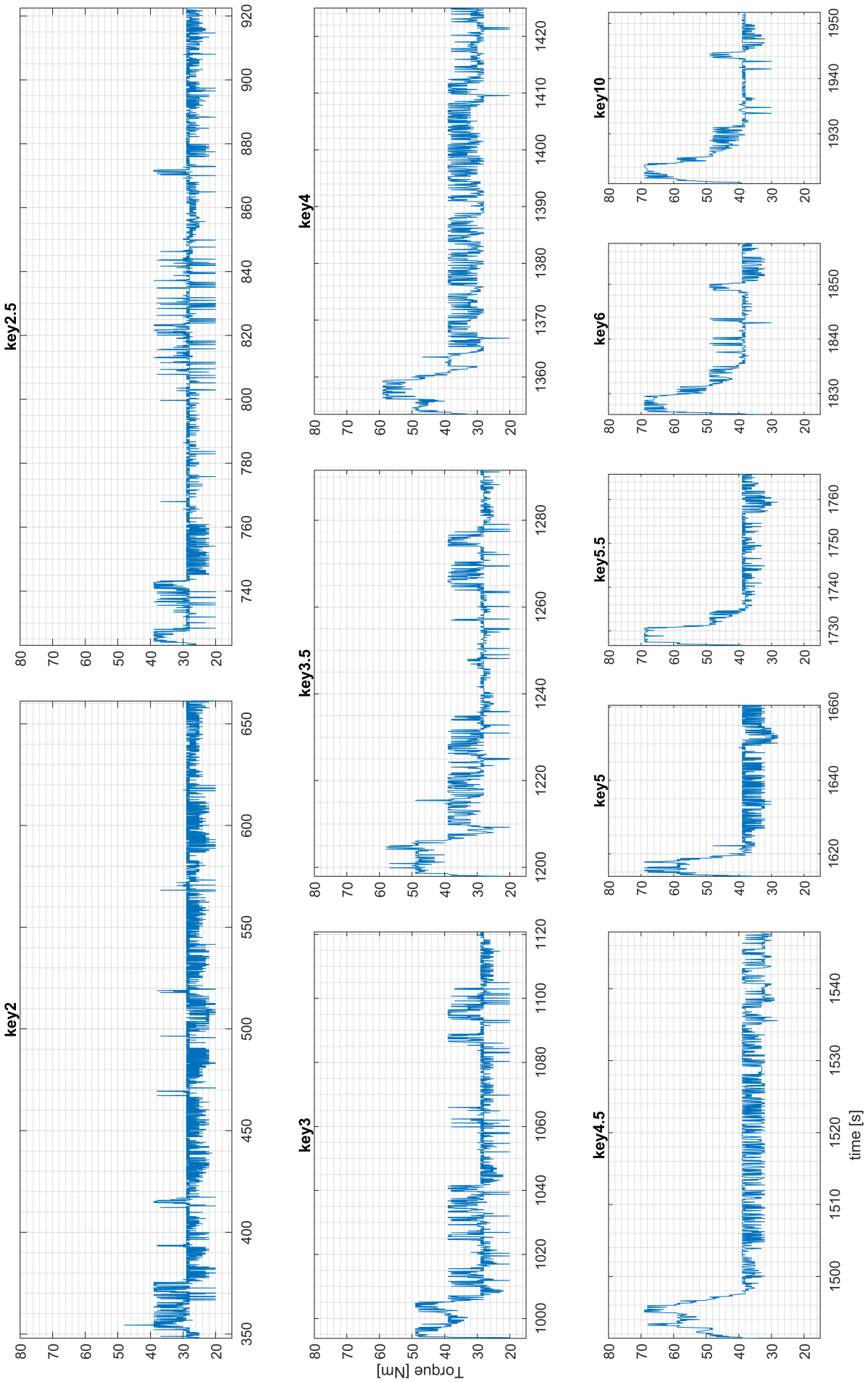

Figure 126: 2TG1.5_400_x: raw torque data cut per feed cylinder key velocity

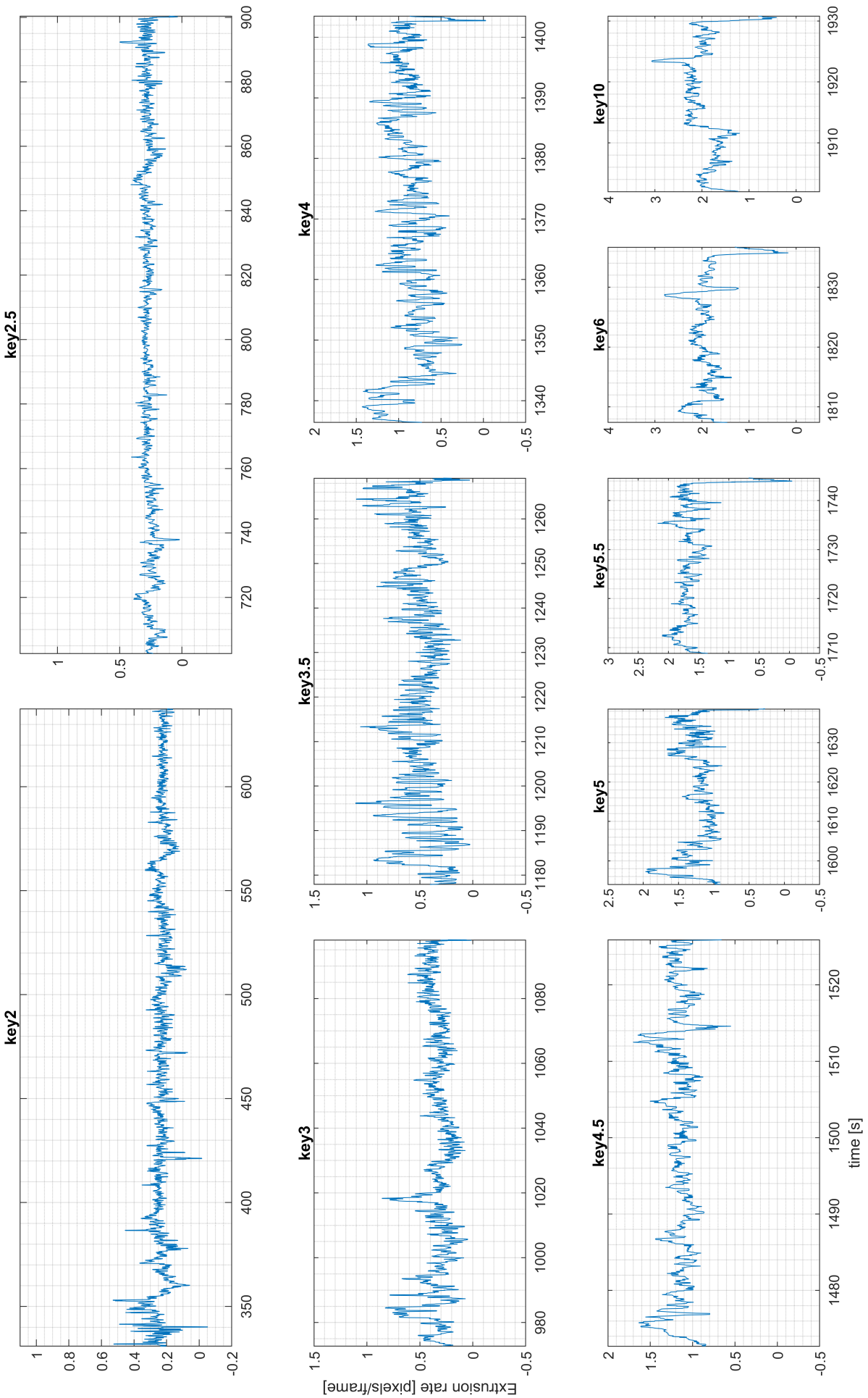

Figure 127: 2TG1.5_400_x: raw smoothed V_y data cut per feed cylinder key velocity

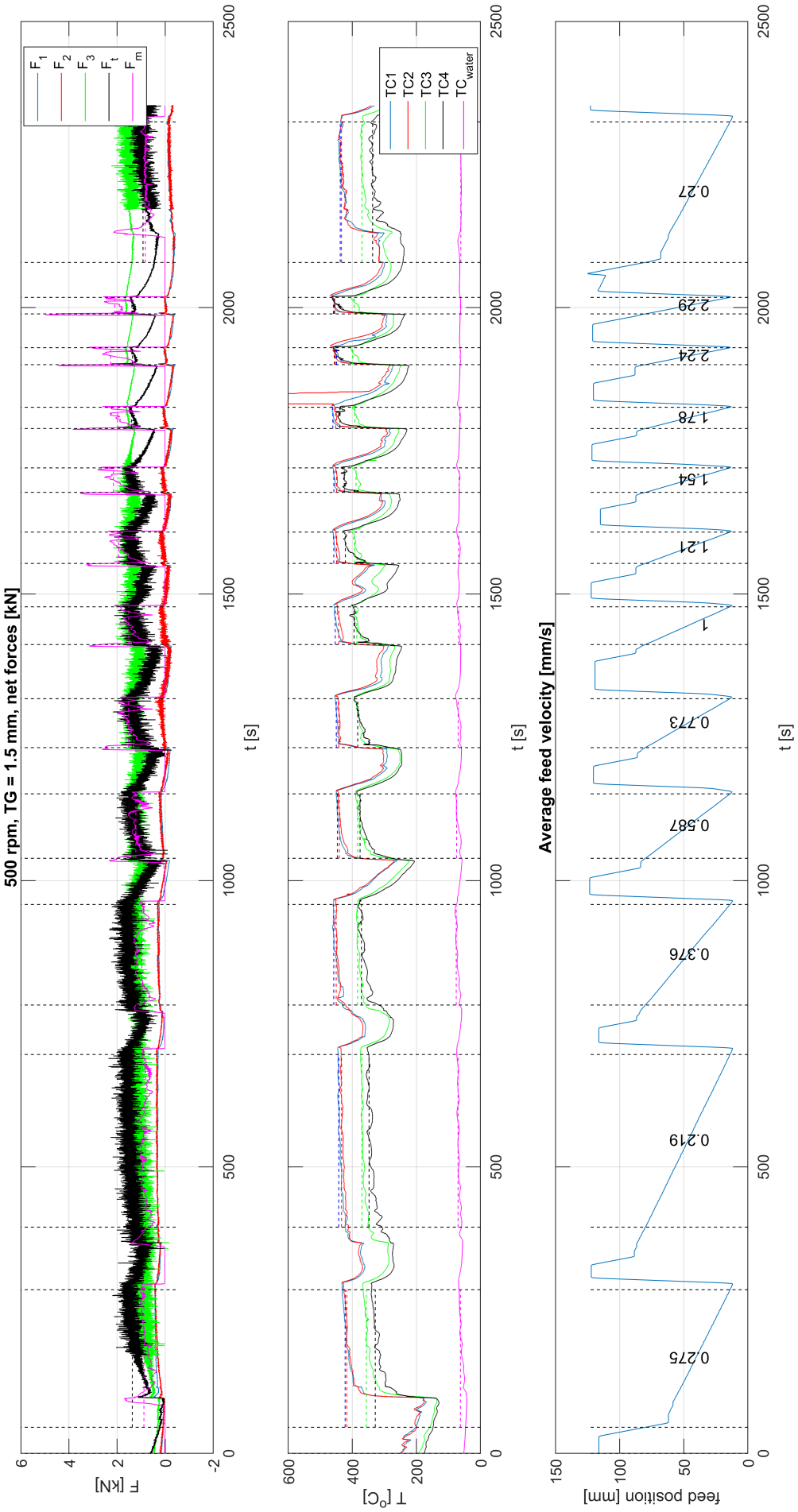

Figure 128: 2TG1.5_500_x: raw force, temperature and feed displacement data

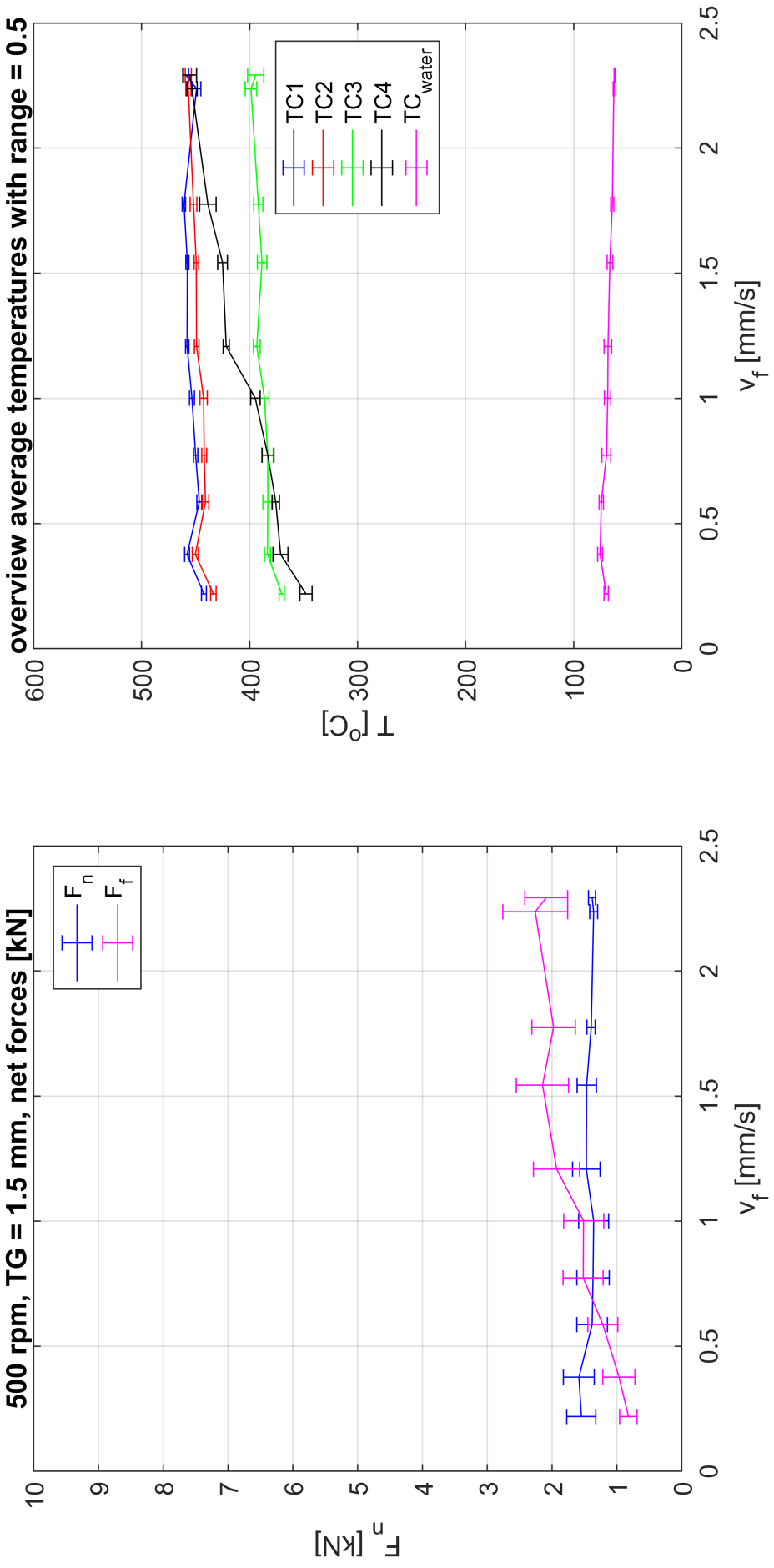

Figure 129: 2TG1.5_500_x: average forces and temperatures

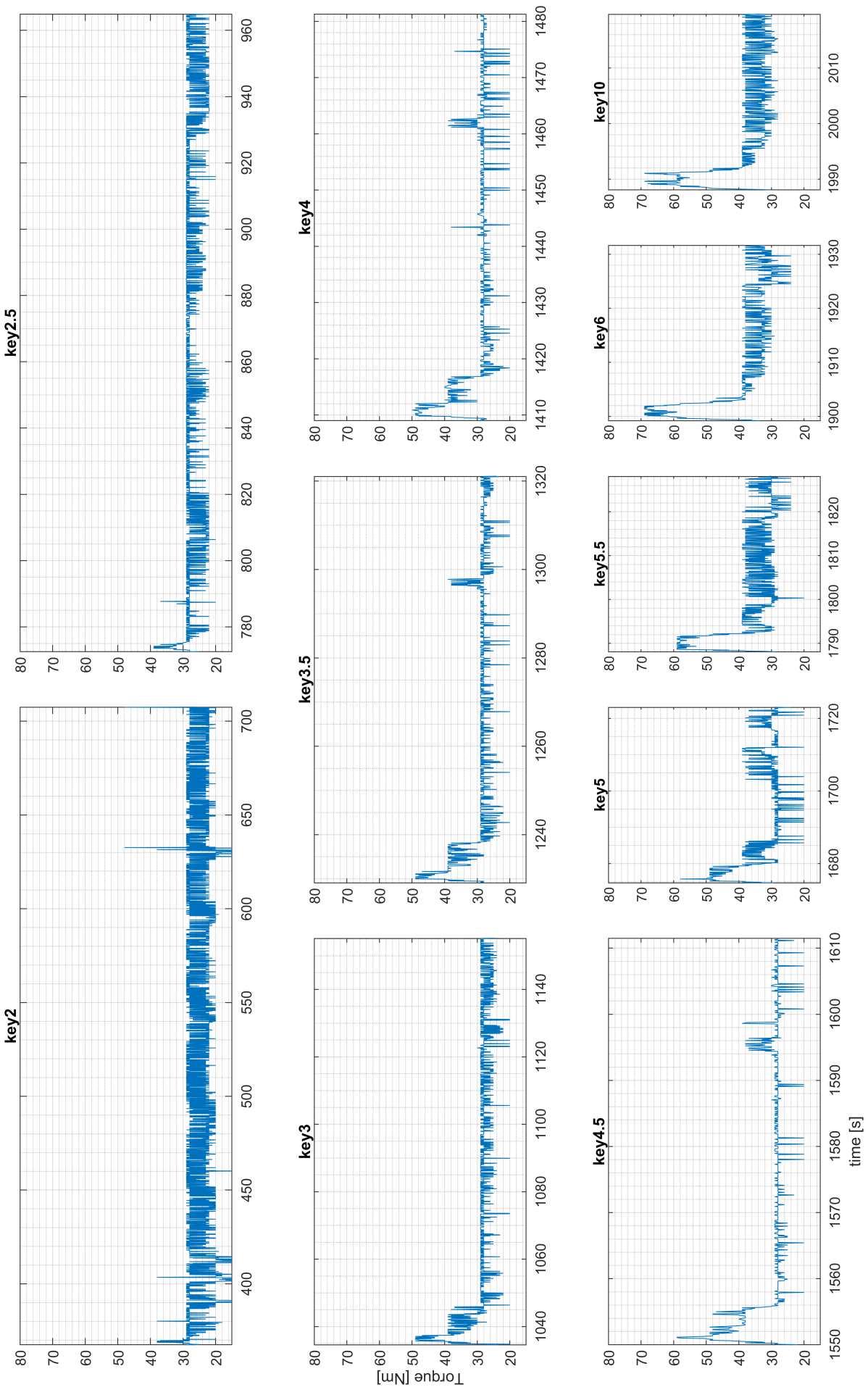

Figure 130: 2TG1.5_500_x: raw torque data cut per feed cylinder key velocity

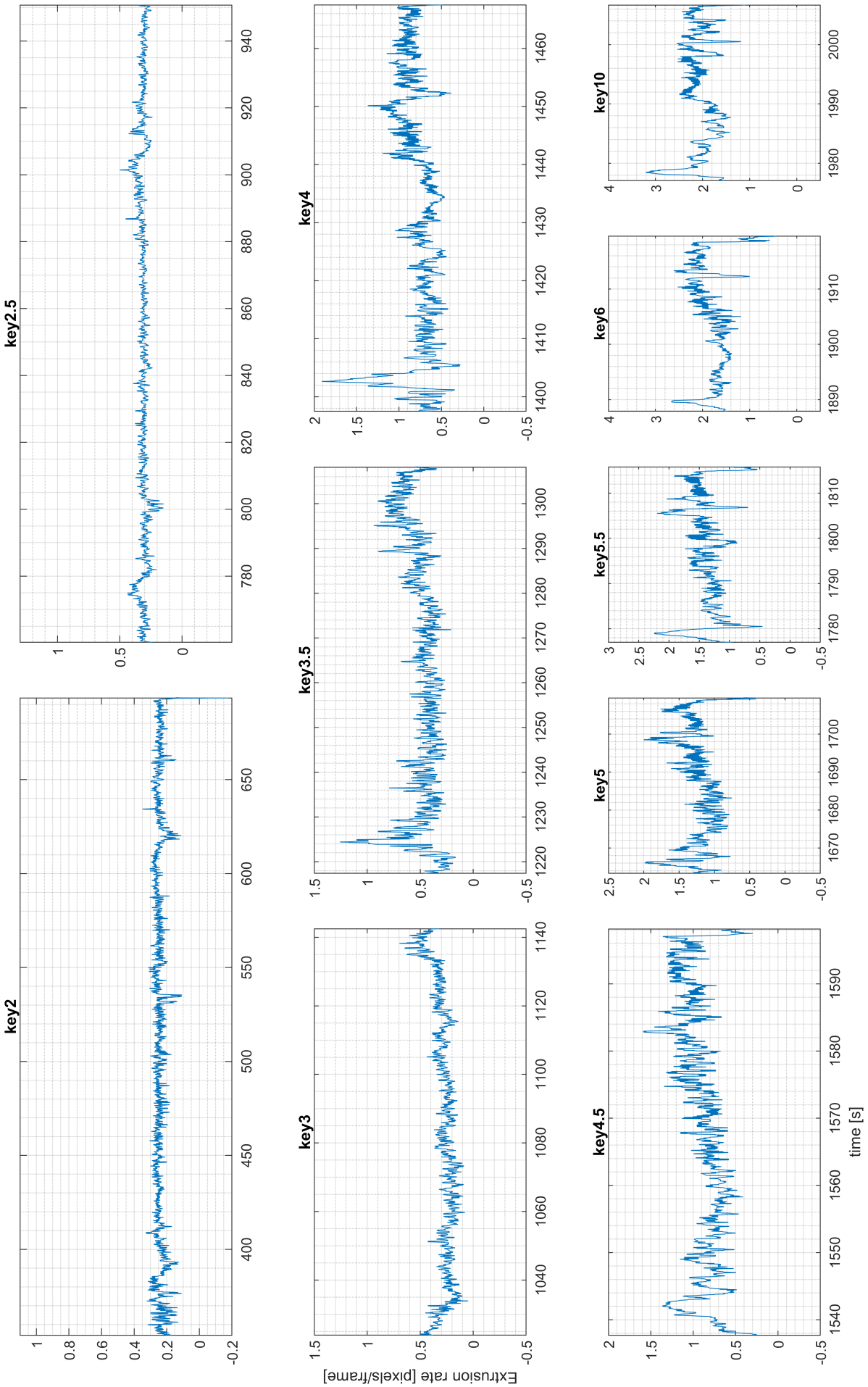

Figure 131: 2TG1.5_500_x: raw smoothed V_y data cut per feed cylinder key velocity

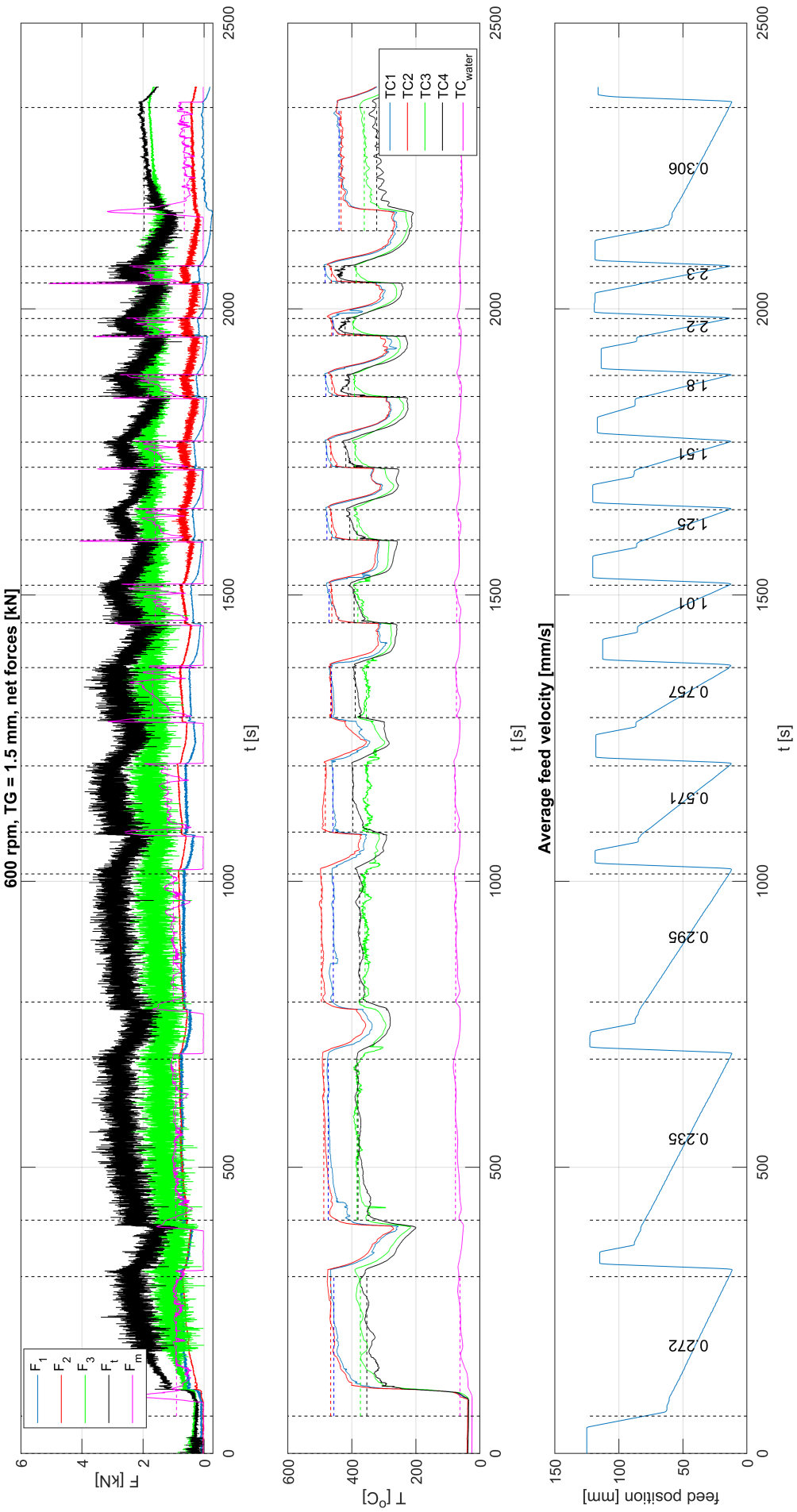

Figure 132: 2TG1.5_600_x: raw force, temperature and feed displacement data

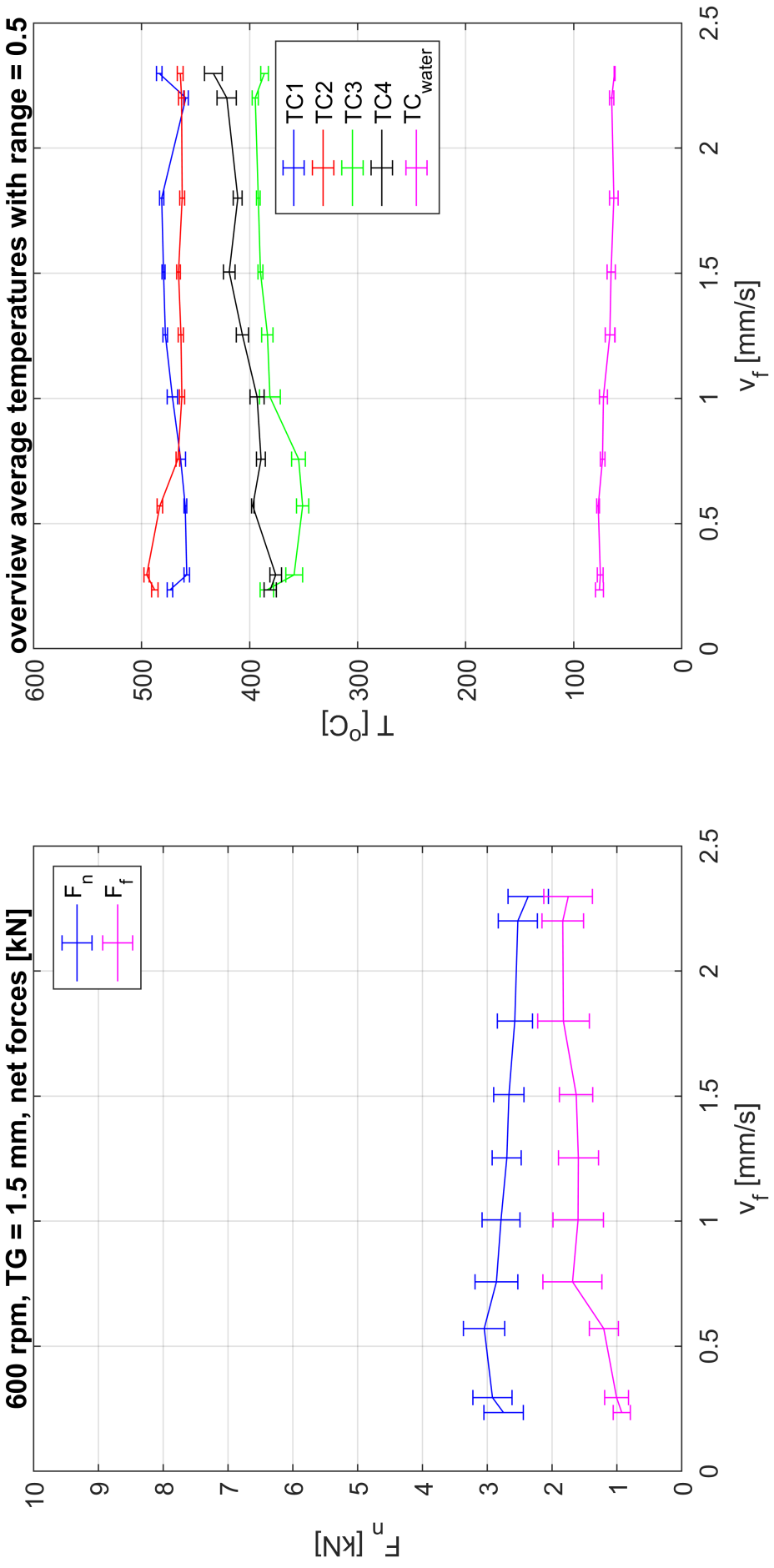

Figure 133: 2TG1.5_600_x: average forces and temperatures

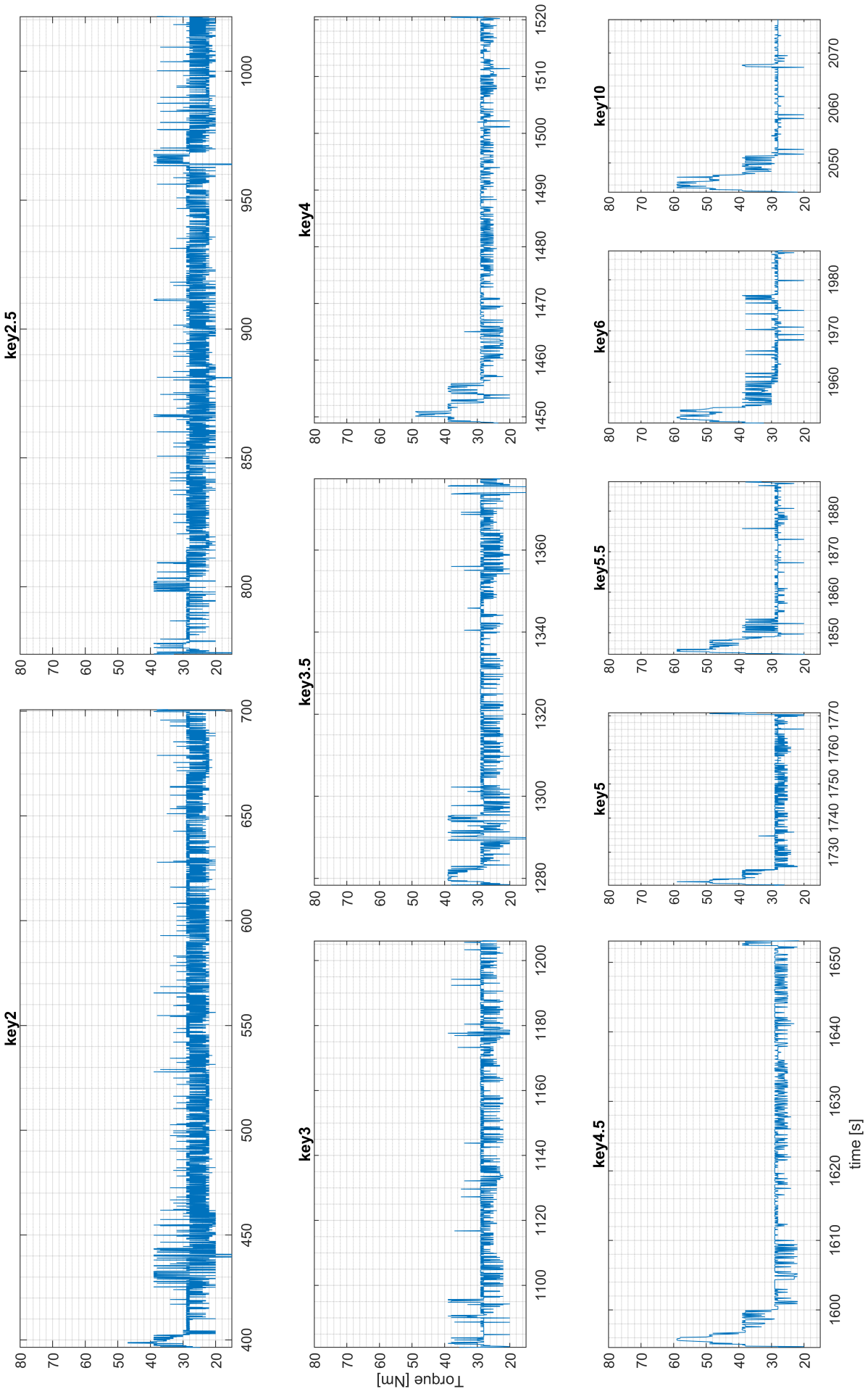

Figure 134: 2TG1.5_600_x: raw torque data cut per feed cylinder key velocity

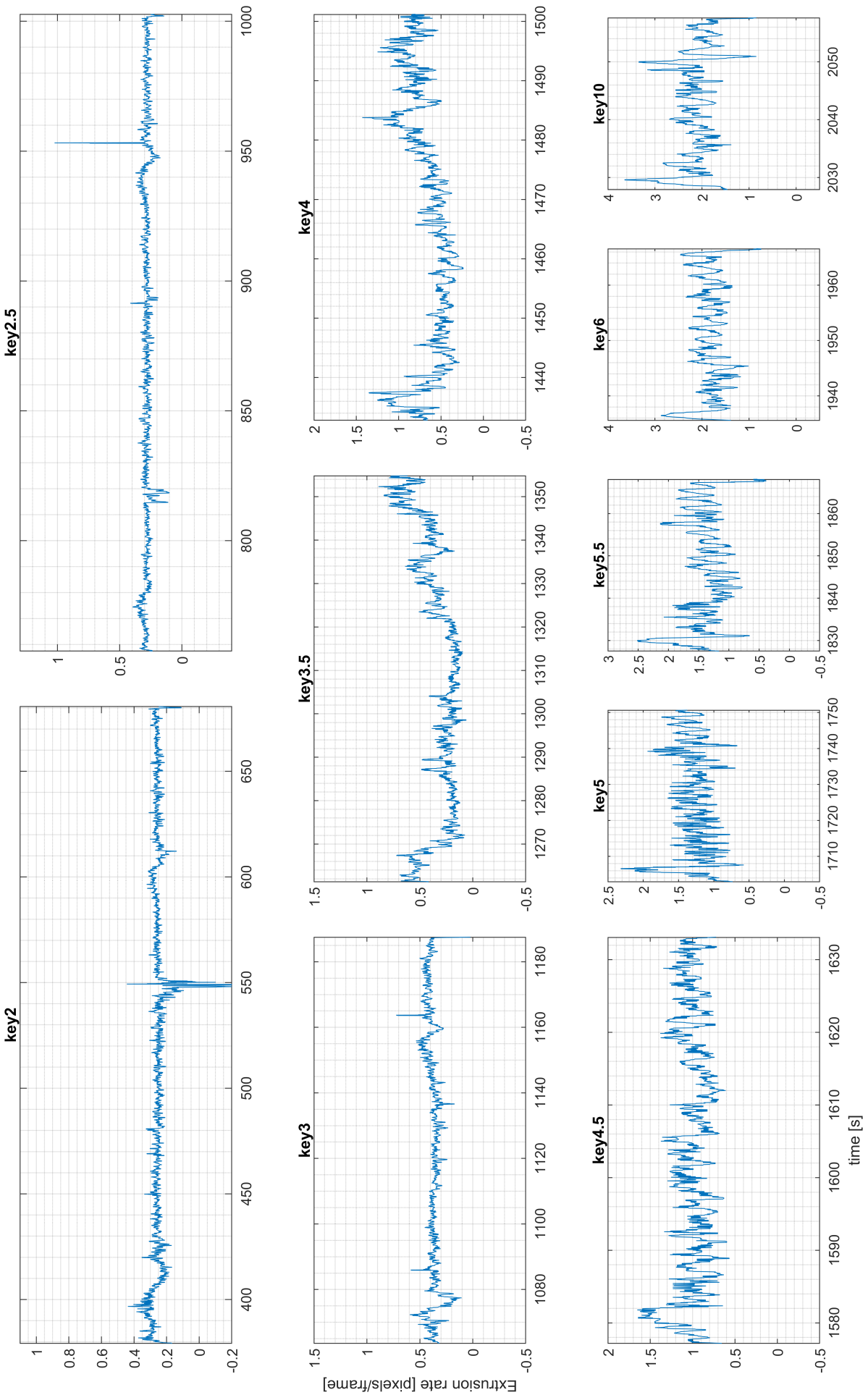

Figure 135: 2TG1.5_600_x: raw smoothed V_y data cut per feed cylinder key velocity

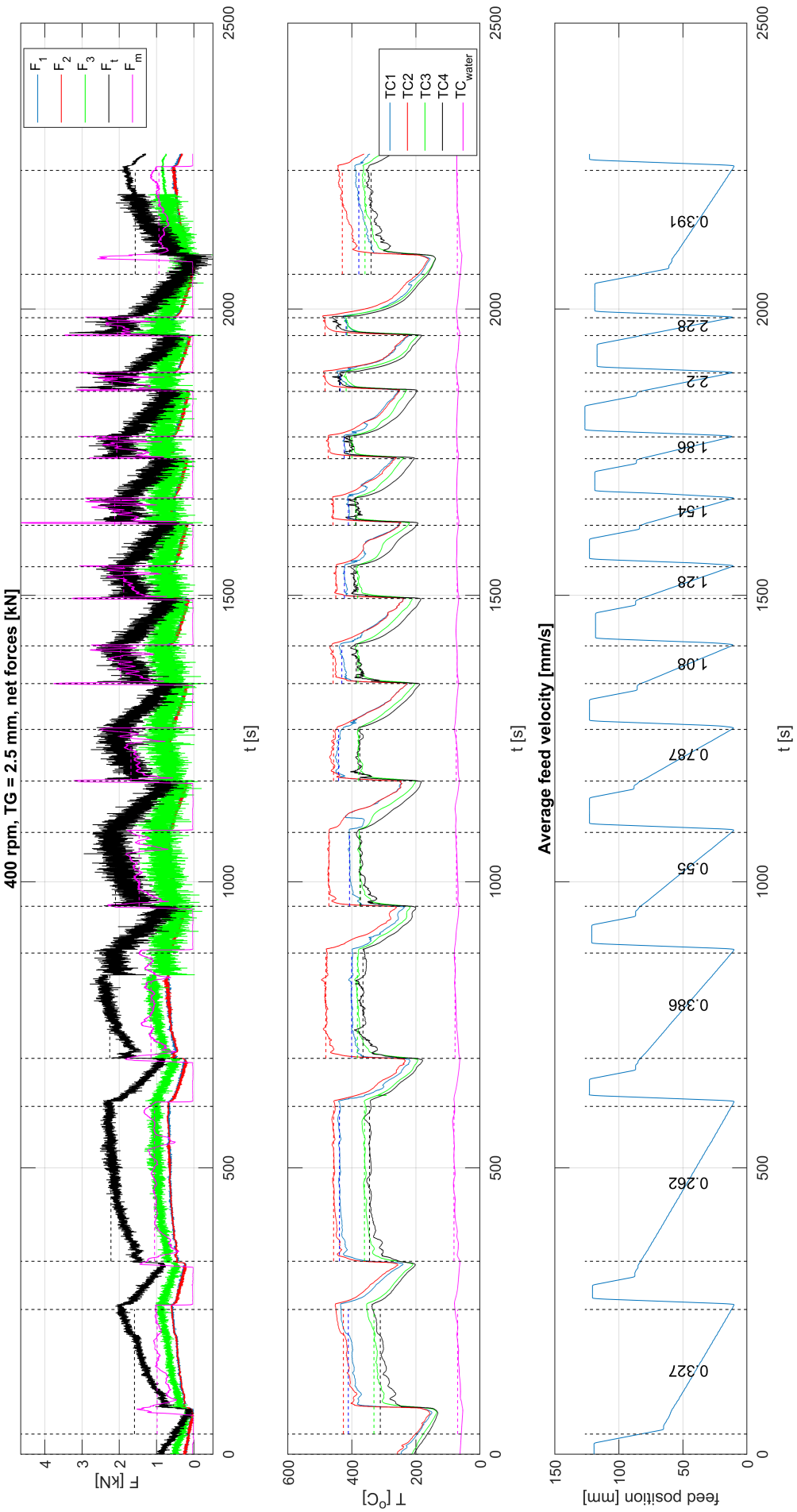

Figure 136: 2TG2.5_400_x: raw force, temperature and feed displacement data

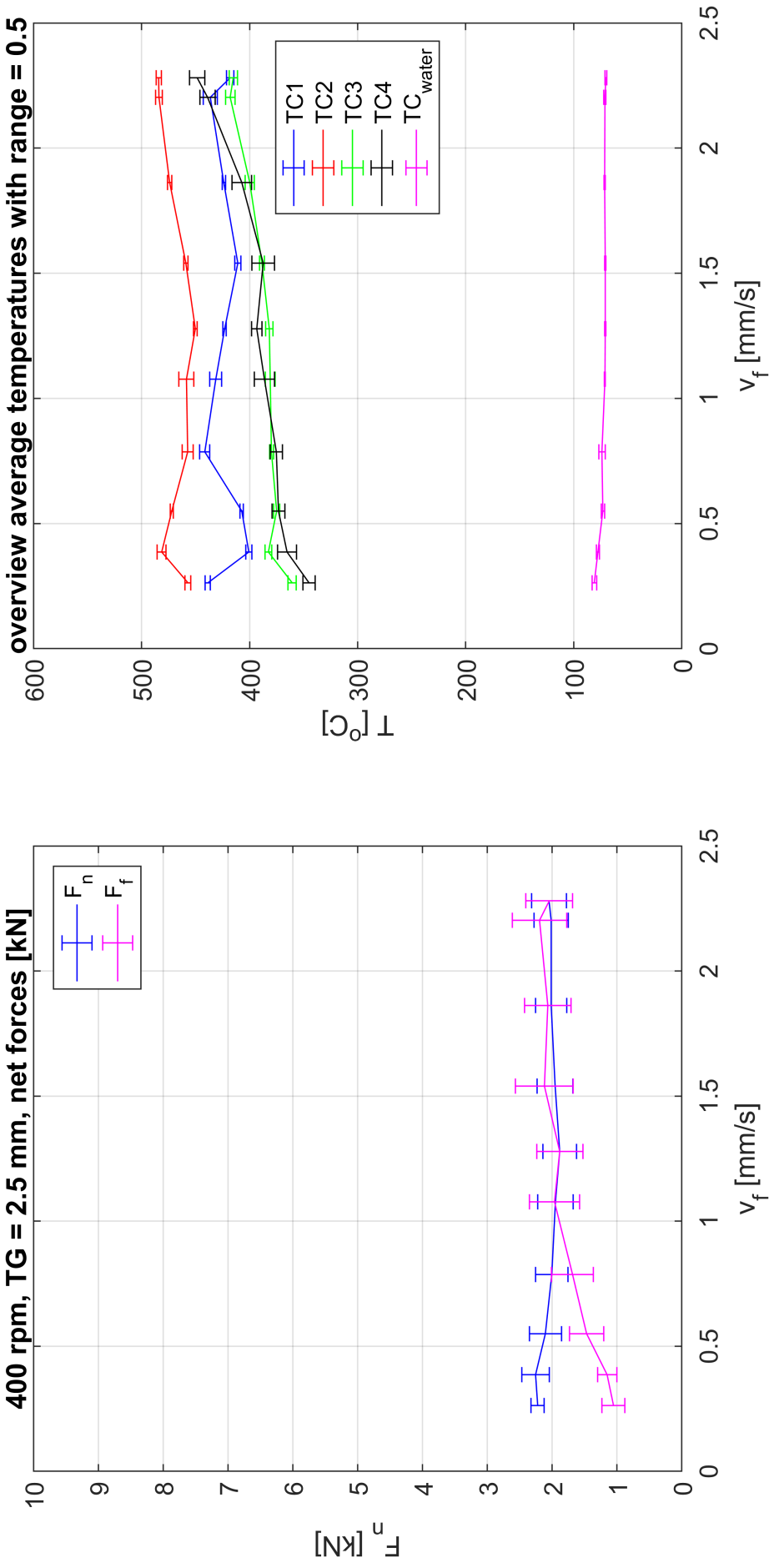

Figure 137: 2TG2.5_400_x: average forces and temperatures

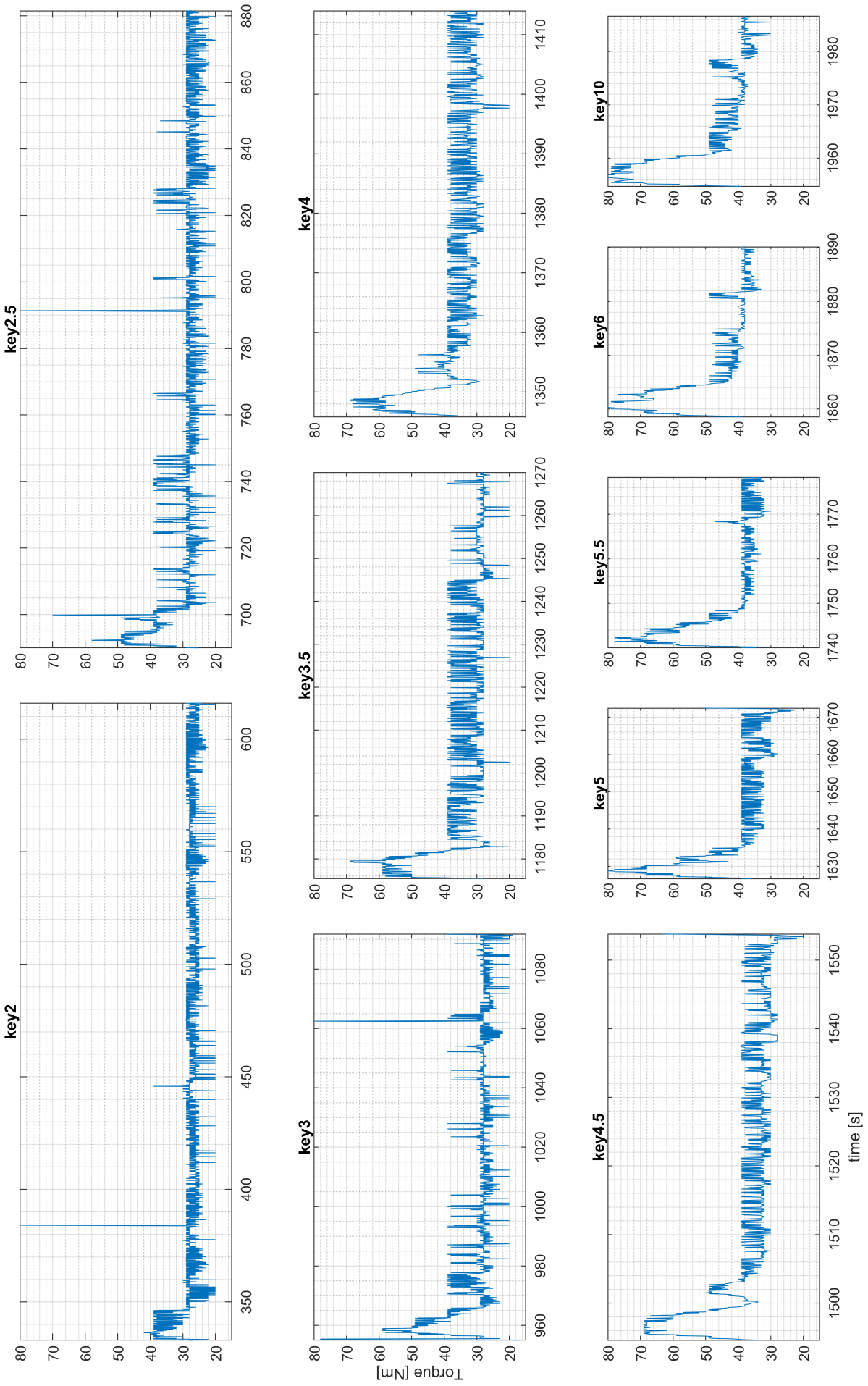

Figure 138: 2TG2.5_400_x: raw torque data cut per feed cylinder key velocity

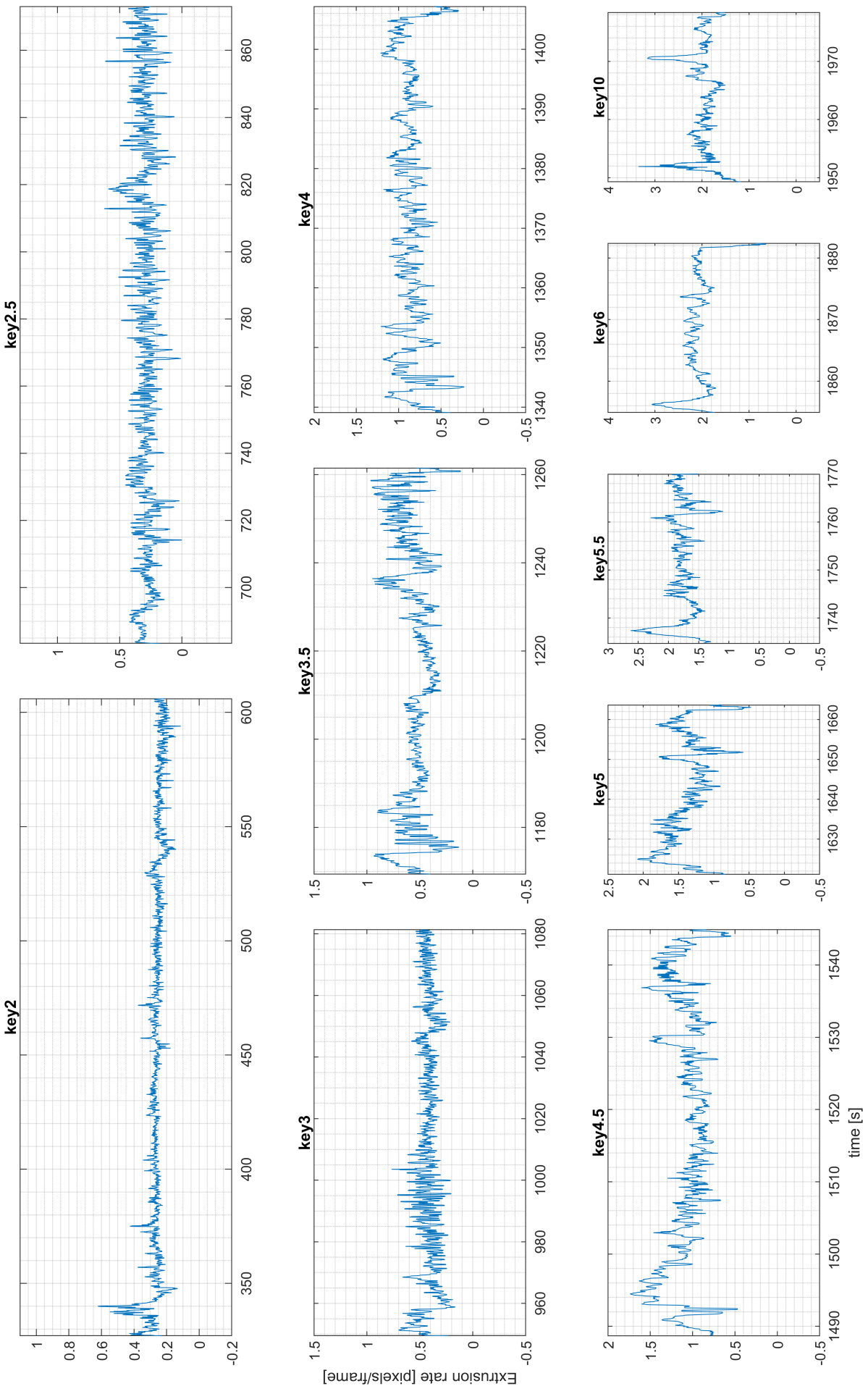

Figure 139: 2TG2.5_400_x: raw smoothed V_y data cut per feed cylinder key velocity

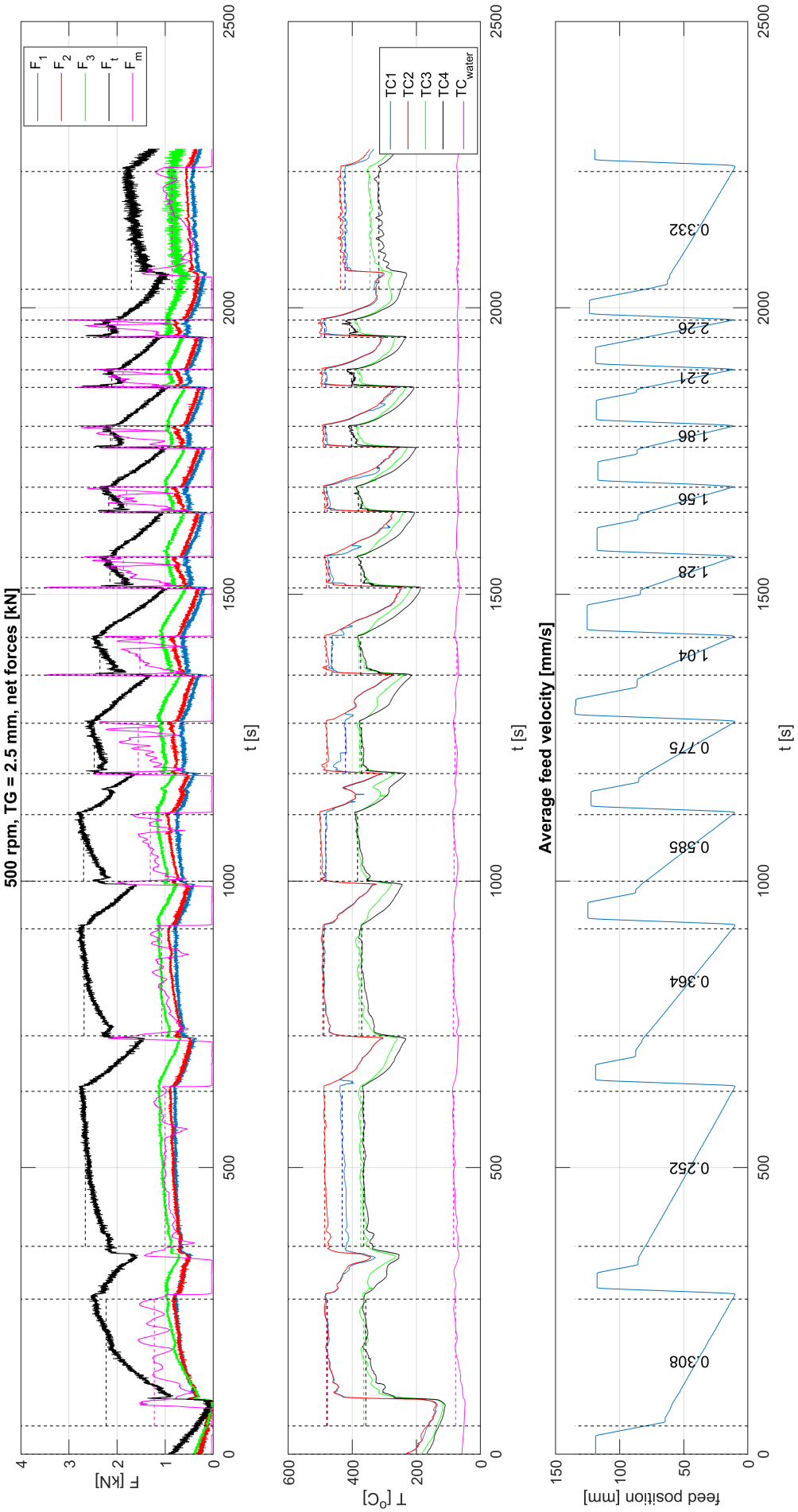

Figure 140: 2TG2.5_500_x: raw force, temperature and feed displacement data

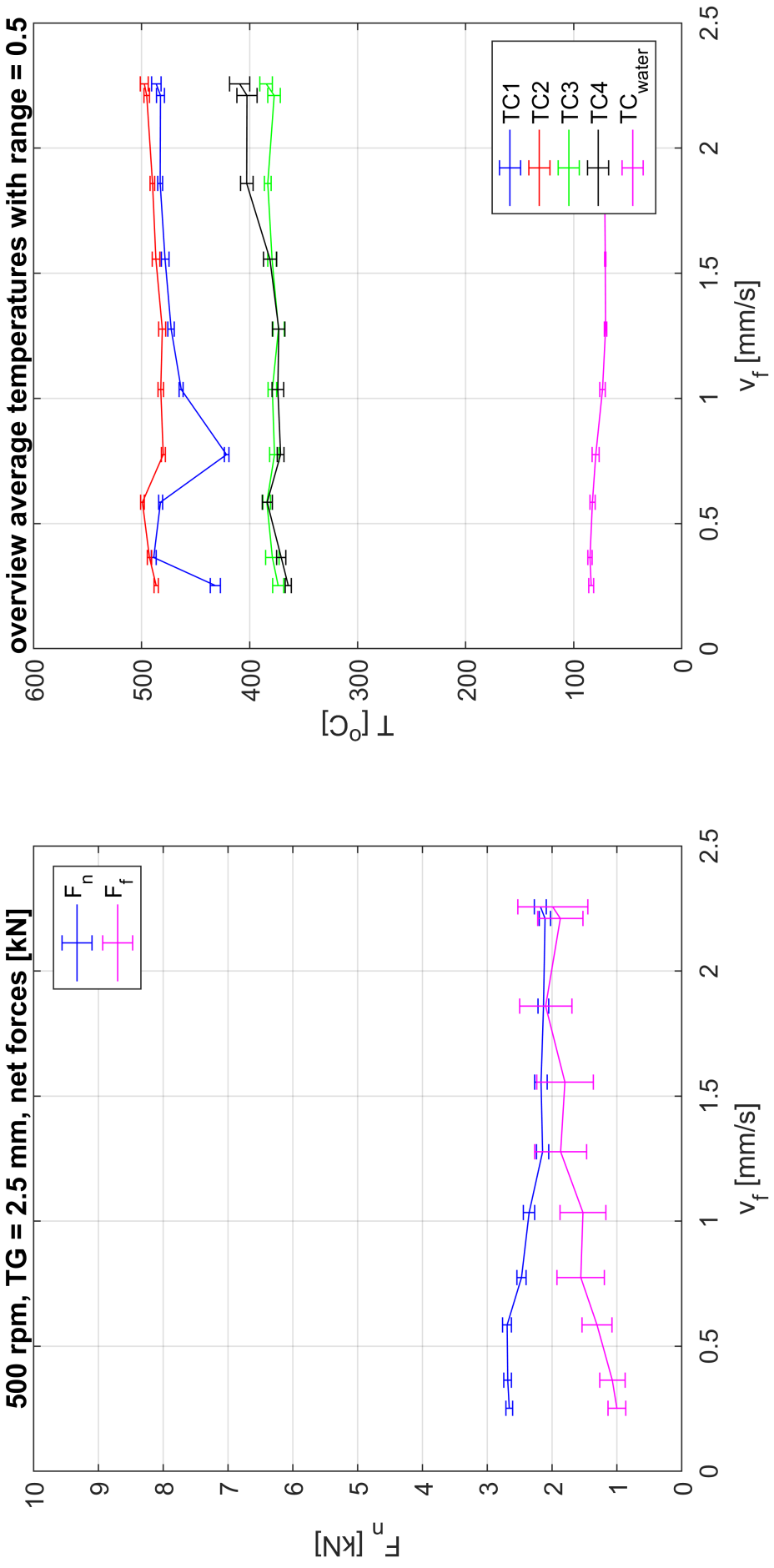

Figure 141: 2TG2.5_500_x: average forces and temperatures

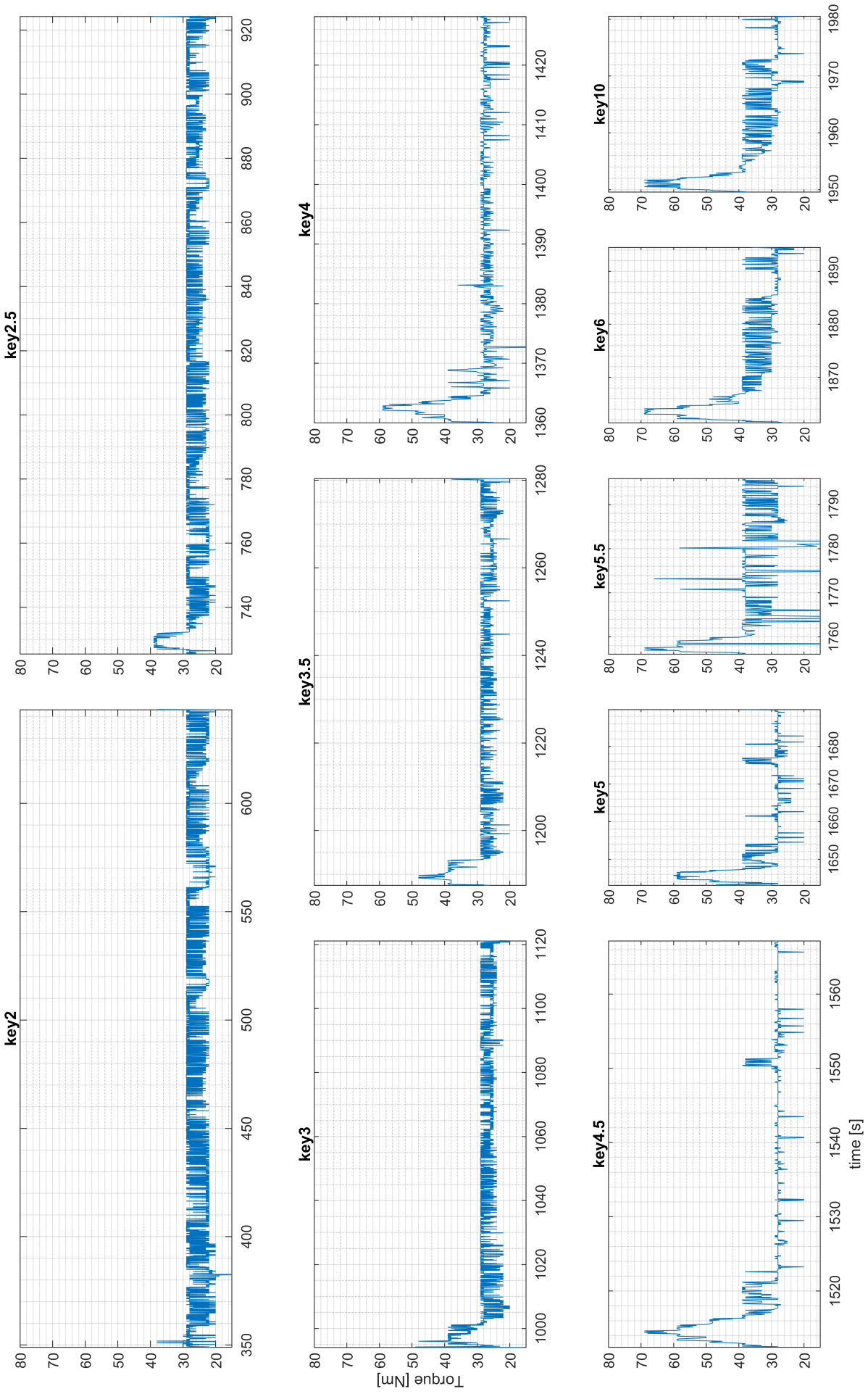

Figure 142: 2TG2.5_500_x: raw torque data cut per feed cylinder key velocity

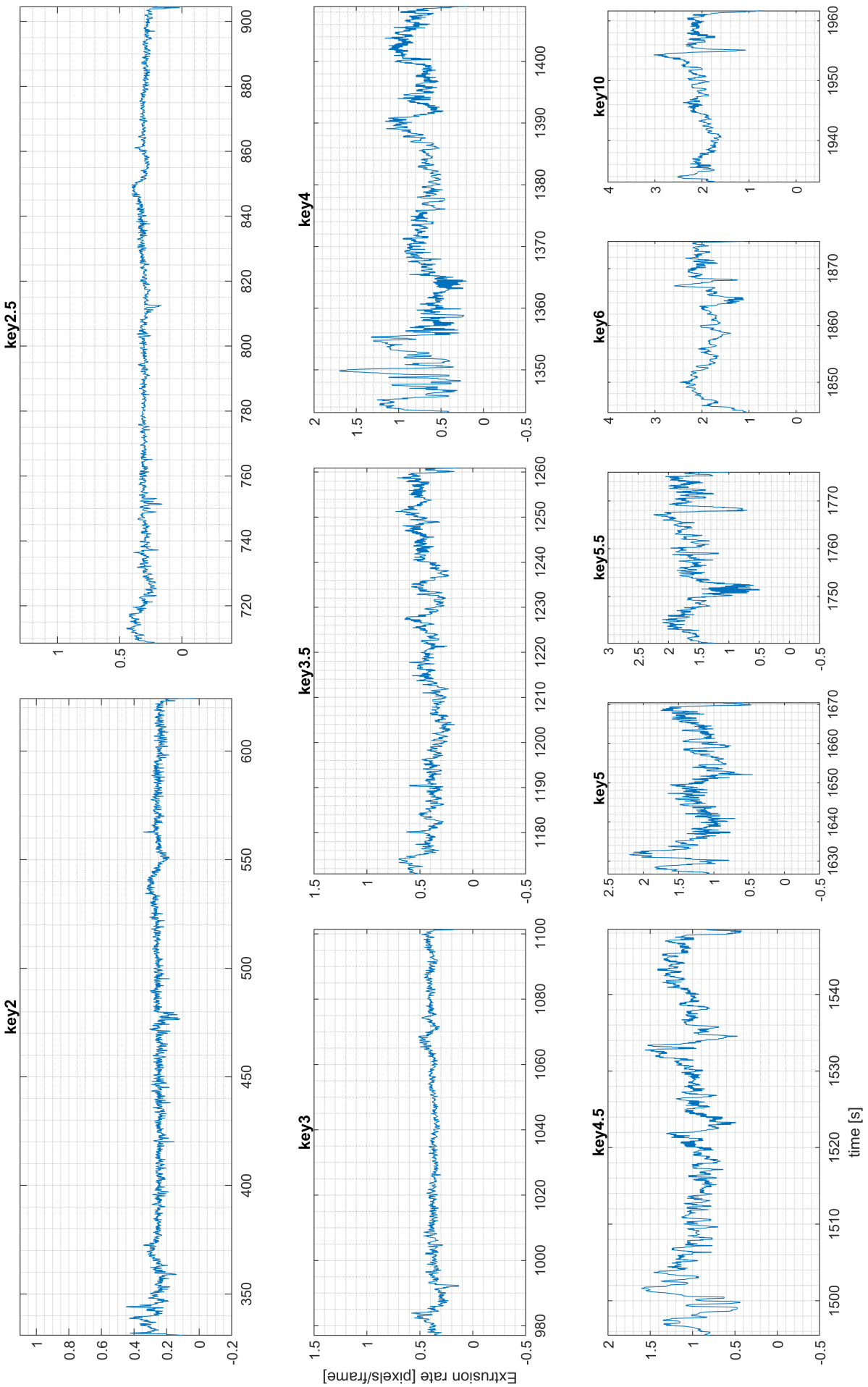

Figure 143: 2TG2.5_500_x: raw smoothed V_y data cut per feed cylinder key velocity

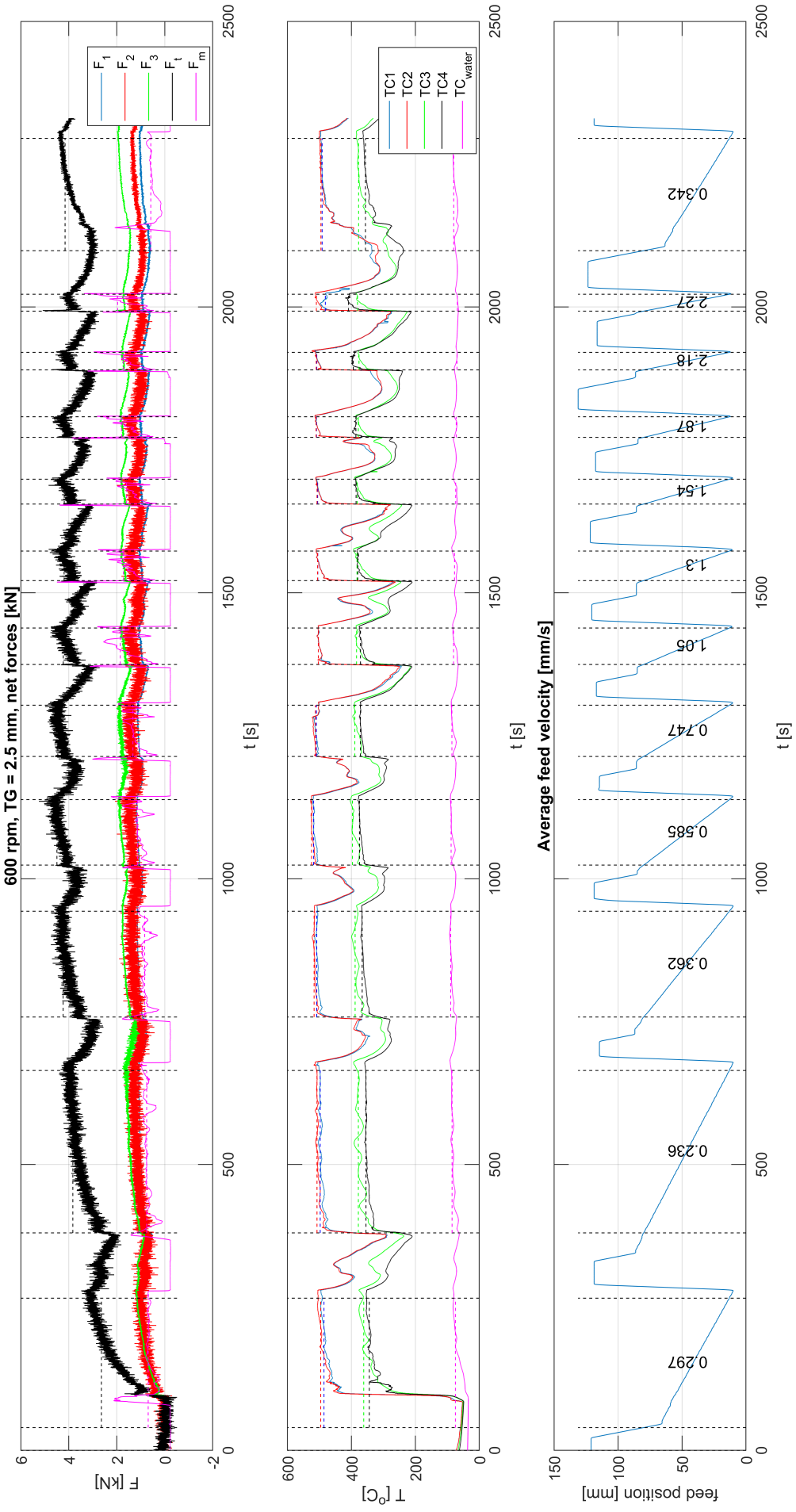

Figure 144: 2TG2.5_600_x: raw force, temperature and feed displacement data

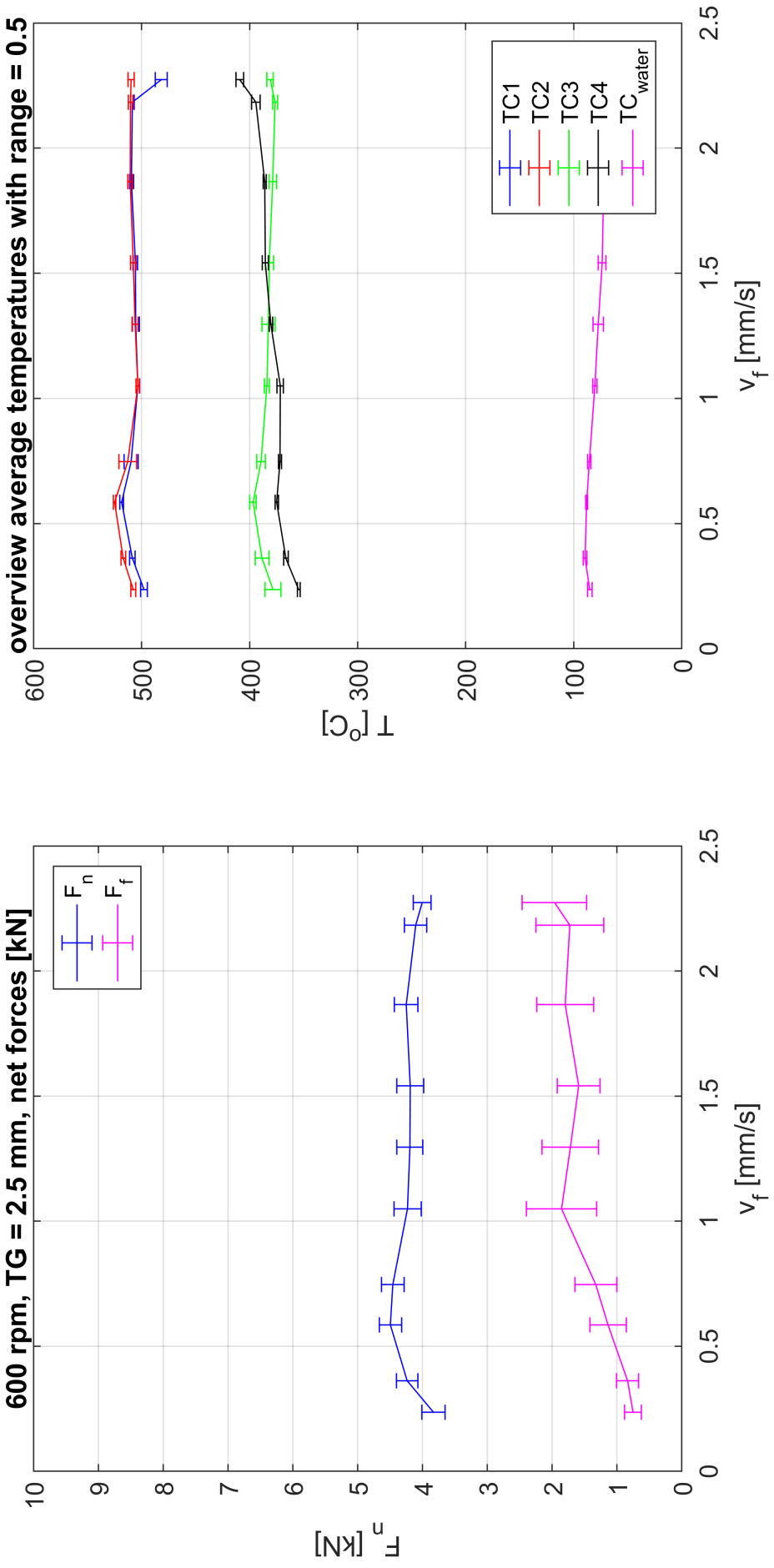

Figure 145: 2TG2.5_600_x: average forces and temperatures

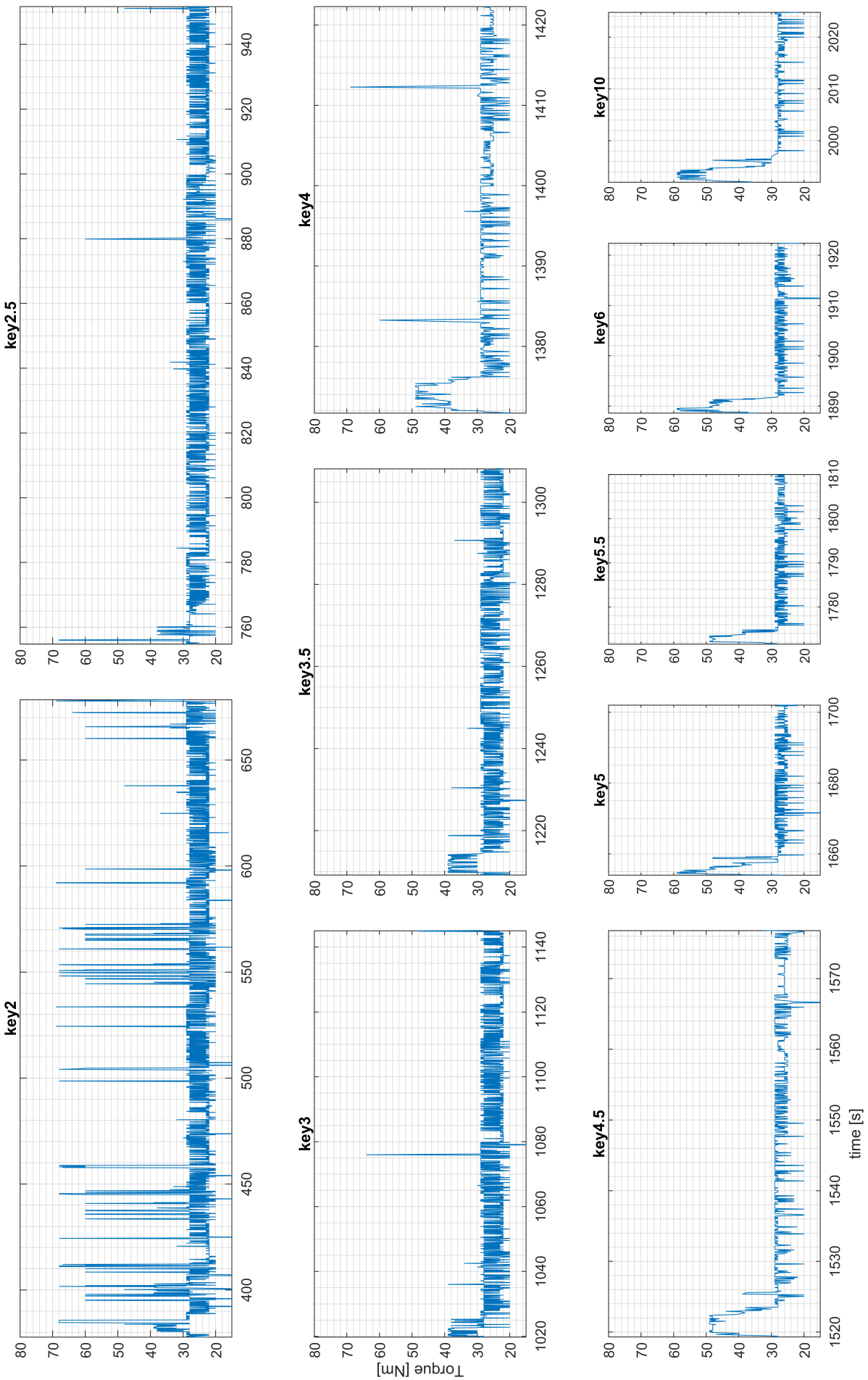

Figure 146: 2TG2.5_600_x: raw torque data cut per feed cylinder key velocity

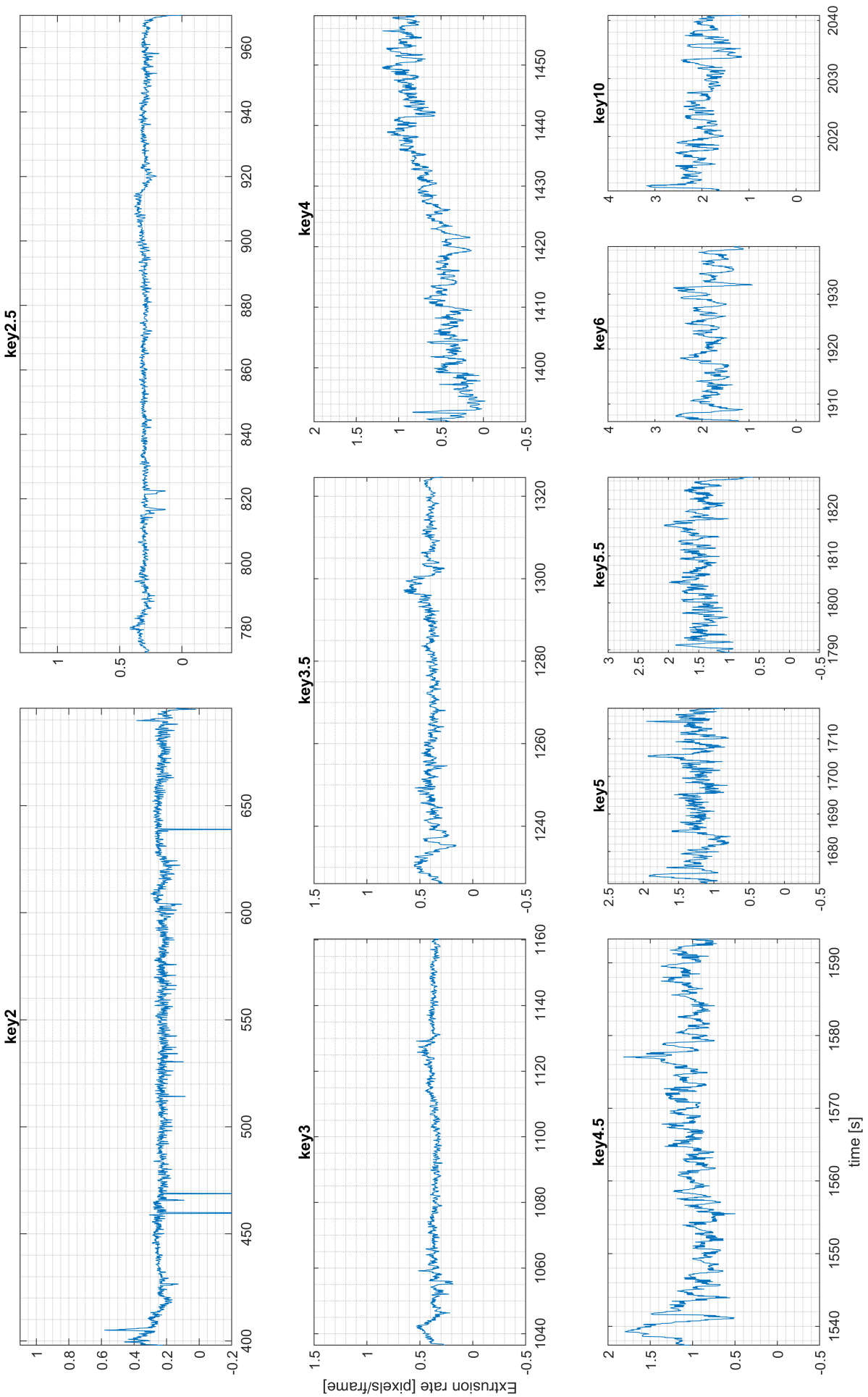

Figure 147: 2TG2.5_600_x: raw smoothed V_y data cut per feed cylinder key velocity

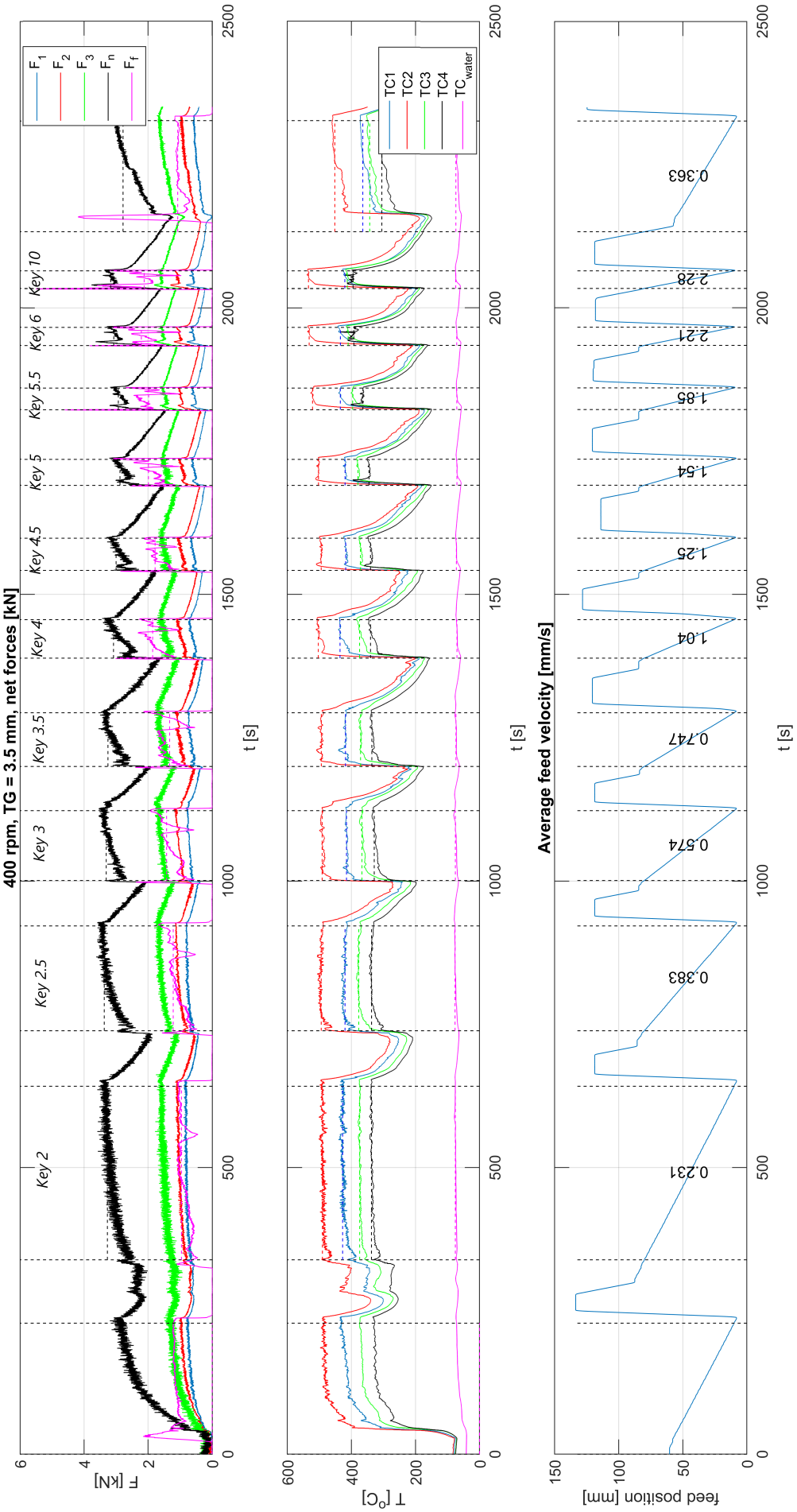

Figure 148: 2TG3.5_400_x: raw force, temperature and feed displacement data

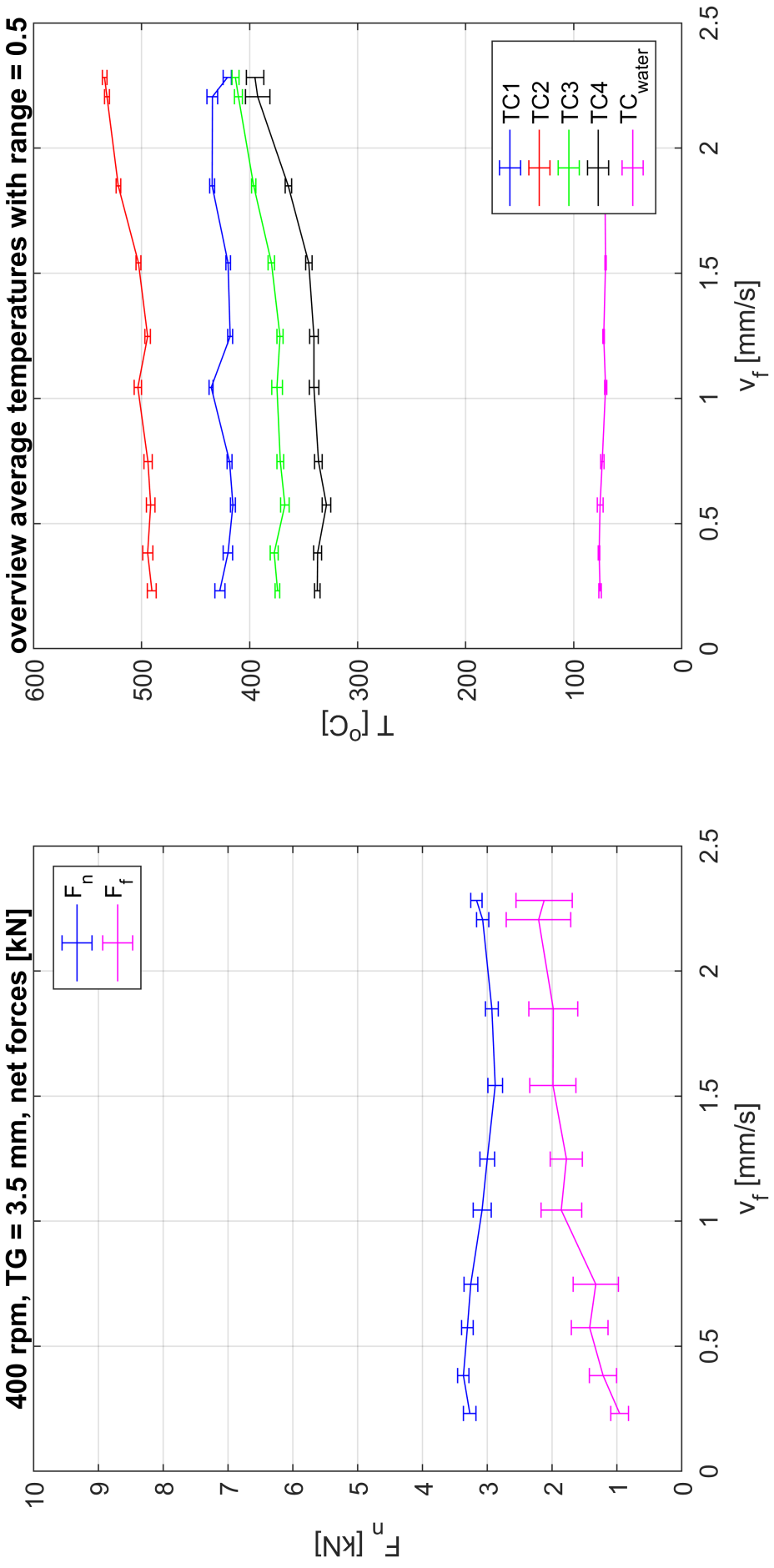

Figure 149: 2TG3.5_400_x: average forces and temperatures

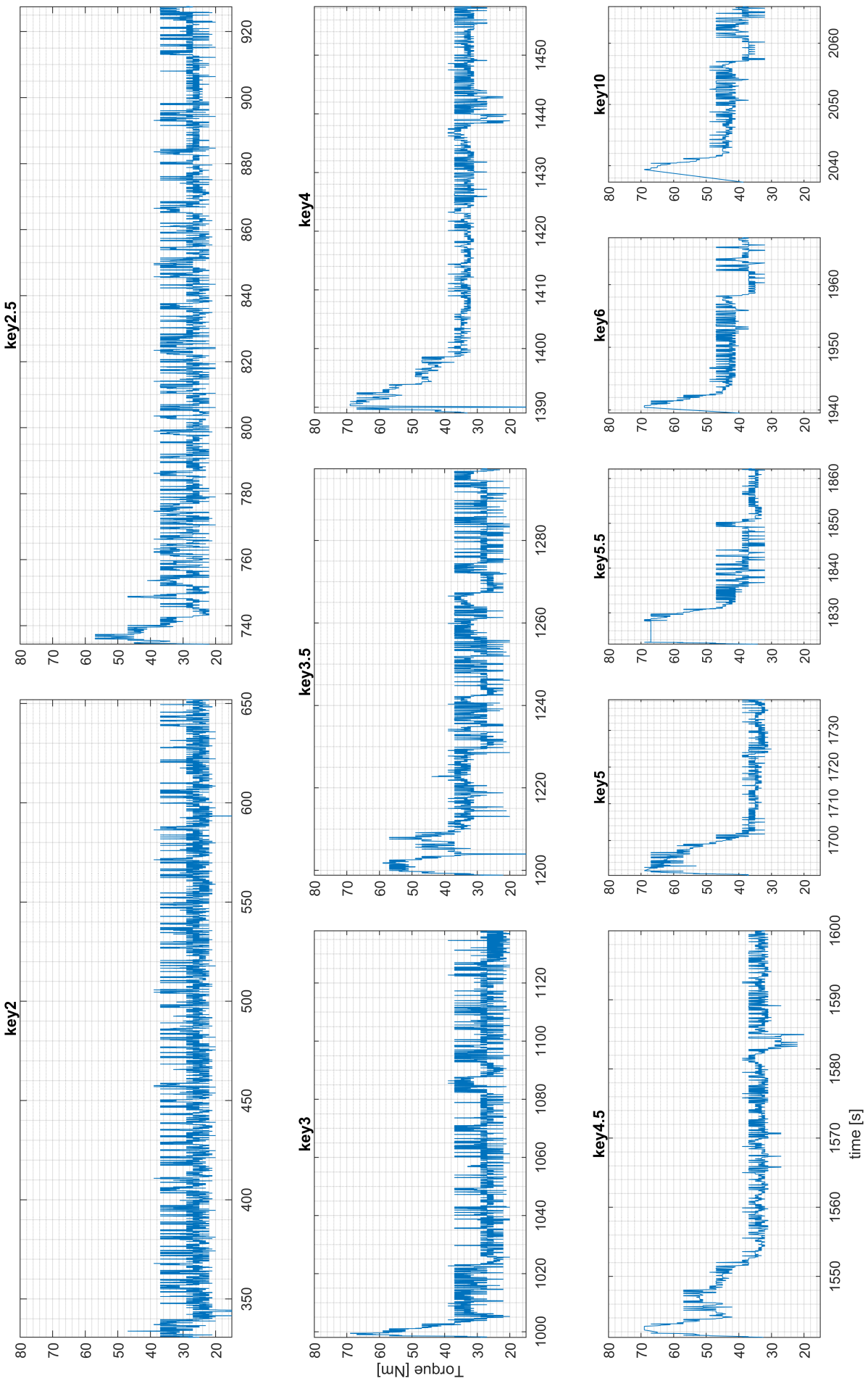

Figure 150: 2TG3.5_400_x: raw torque data cut per feed cylinder key velocity

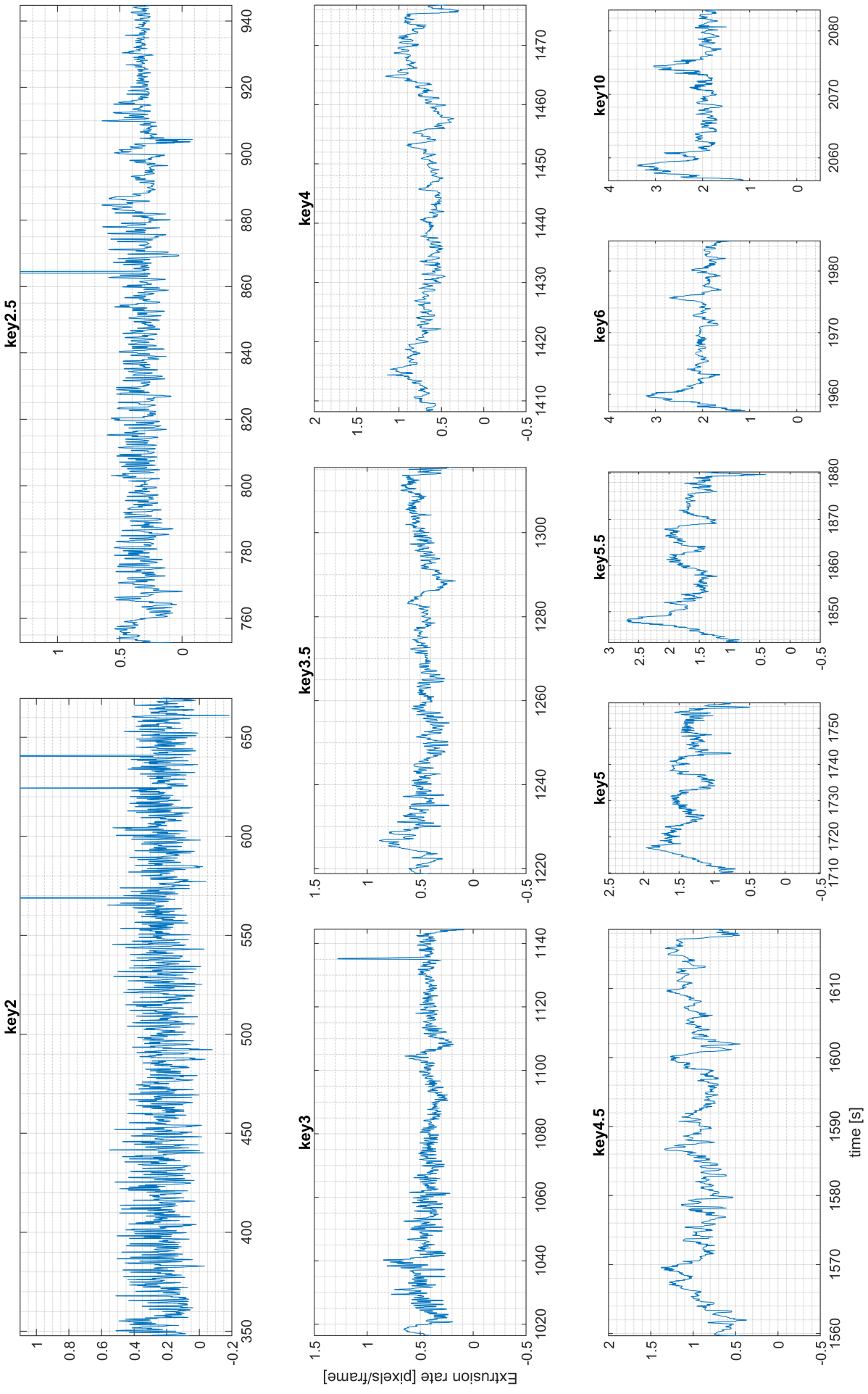

Figure 151: 2TG3.5_400_x: raw smoothed V_y data cut per feed cylinder key velocity

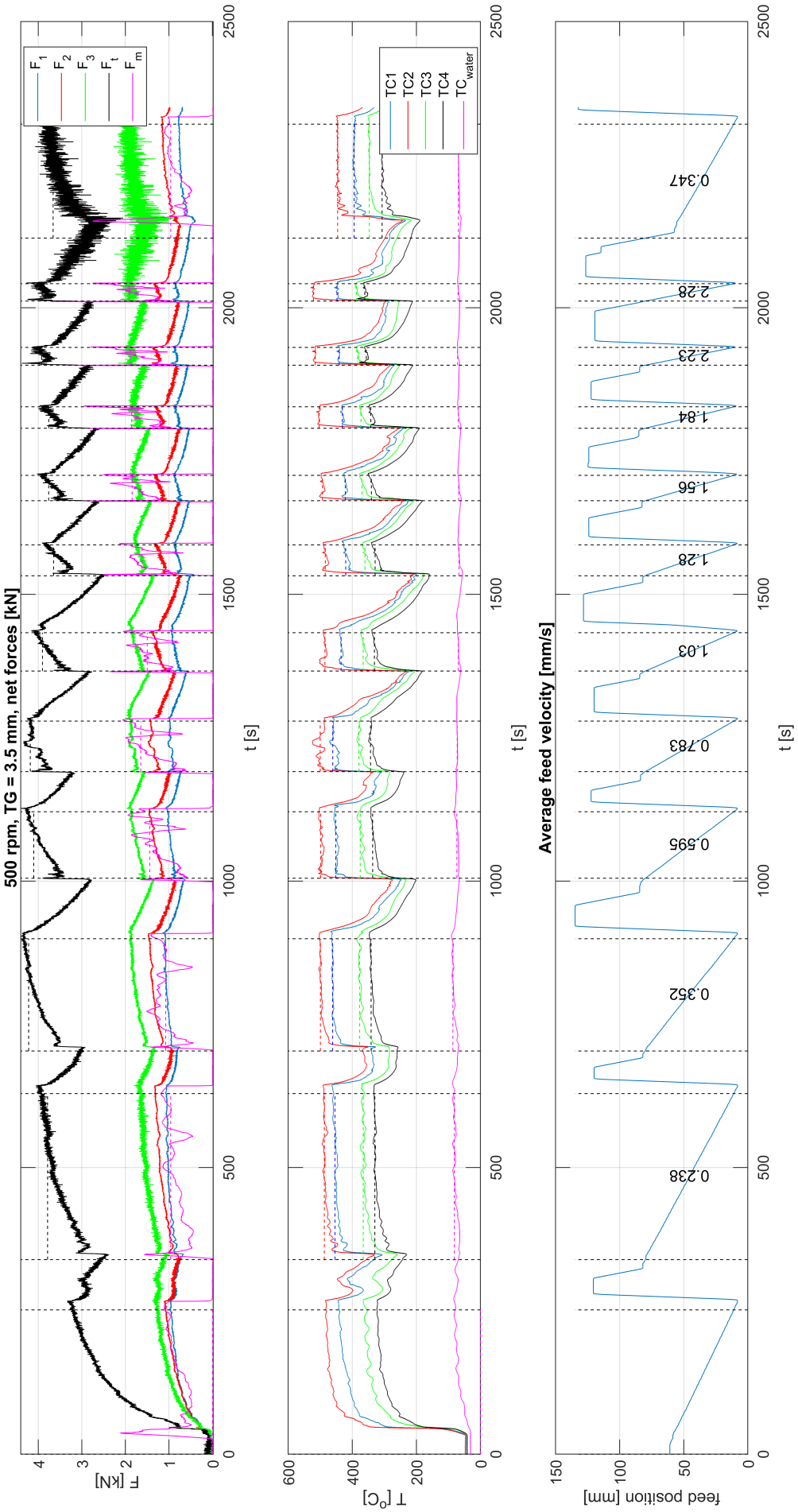

Figure 152: 2TG3.5_500_x: raw force, temperature and feed displacement data

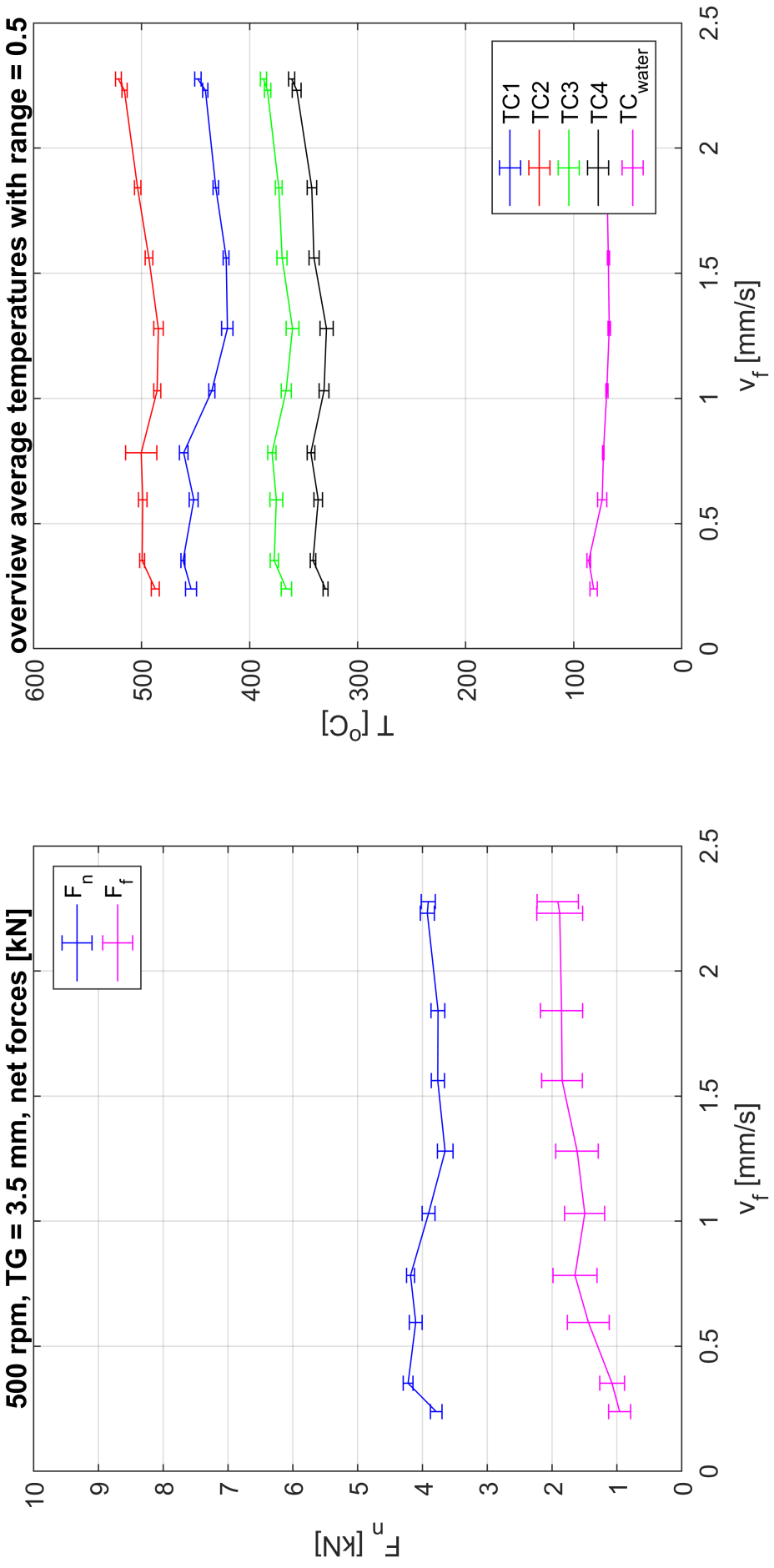

Figure 153: 2TG3.5_500_x: average forces and temperatures

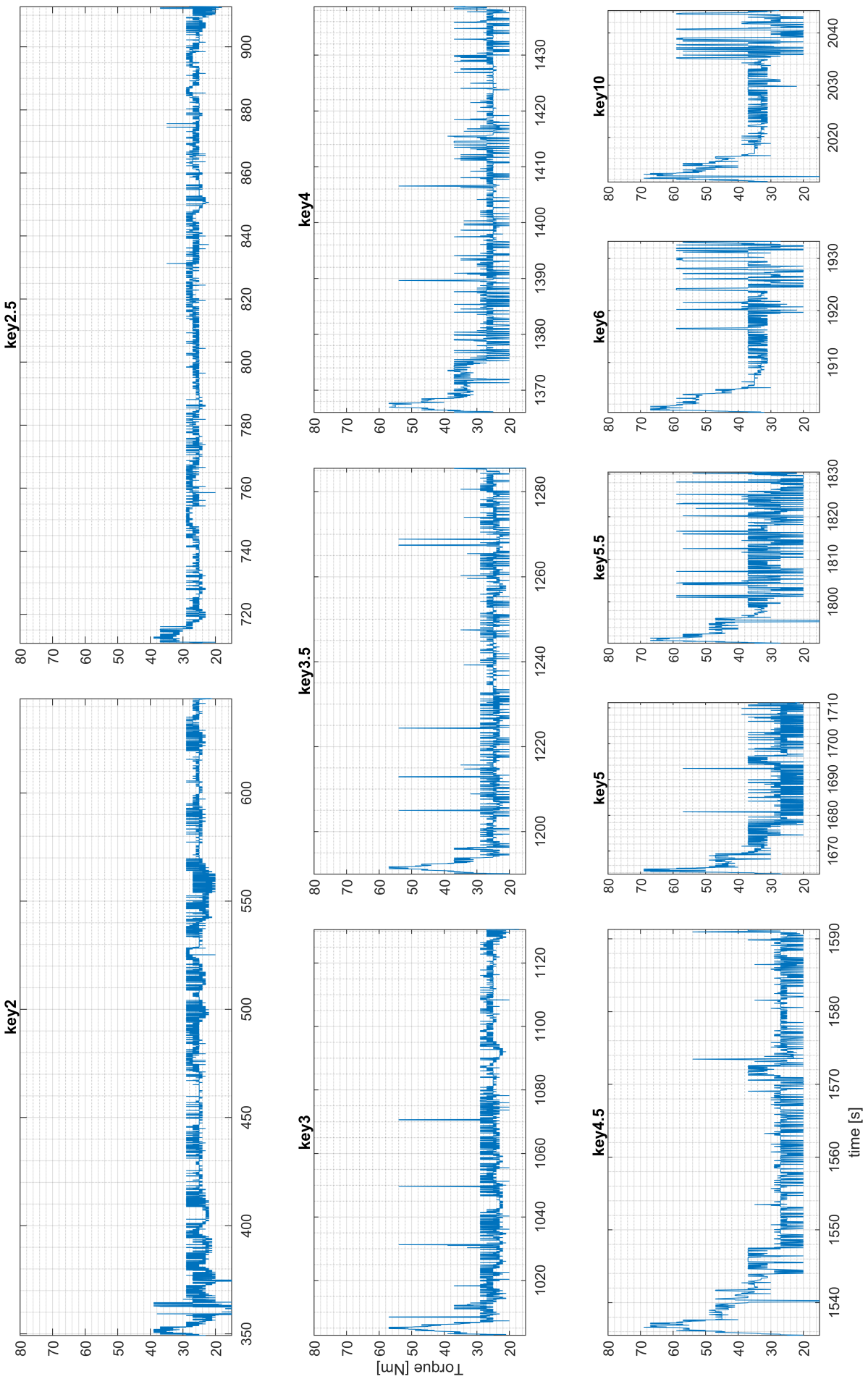

Figure 154: 2TG3.5_500_x: raw torque data cut per feed cylinder key velocity

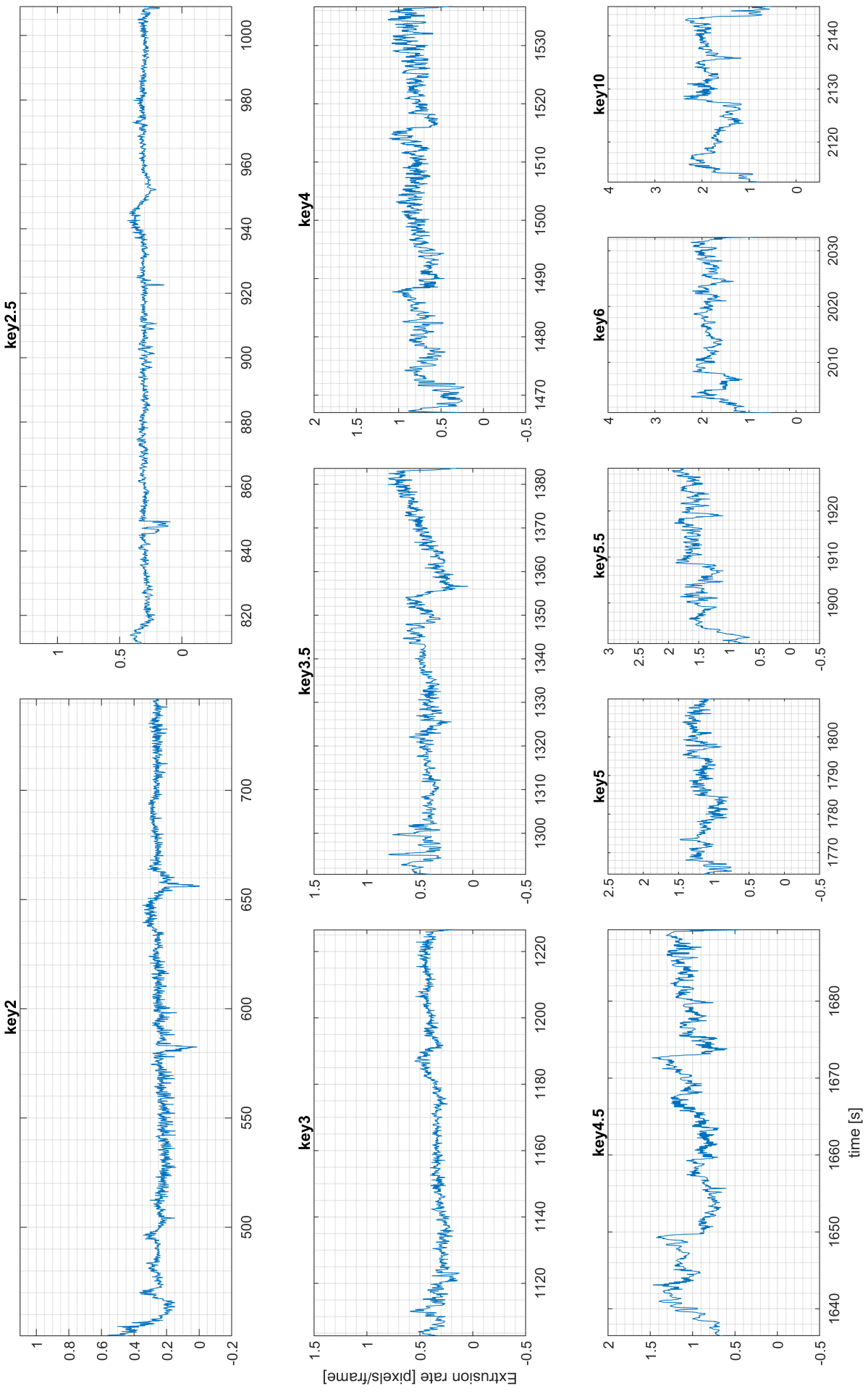

Figure 155: 2TG3.5_500_x: raw smoothed V_y data cut per feed cylinder key velocity

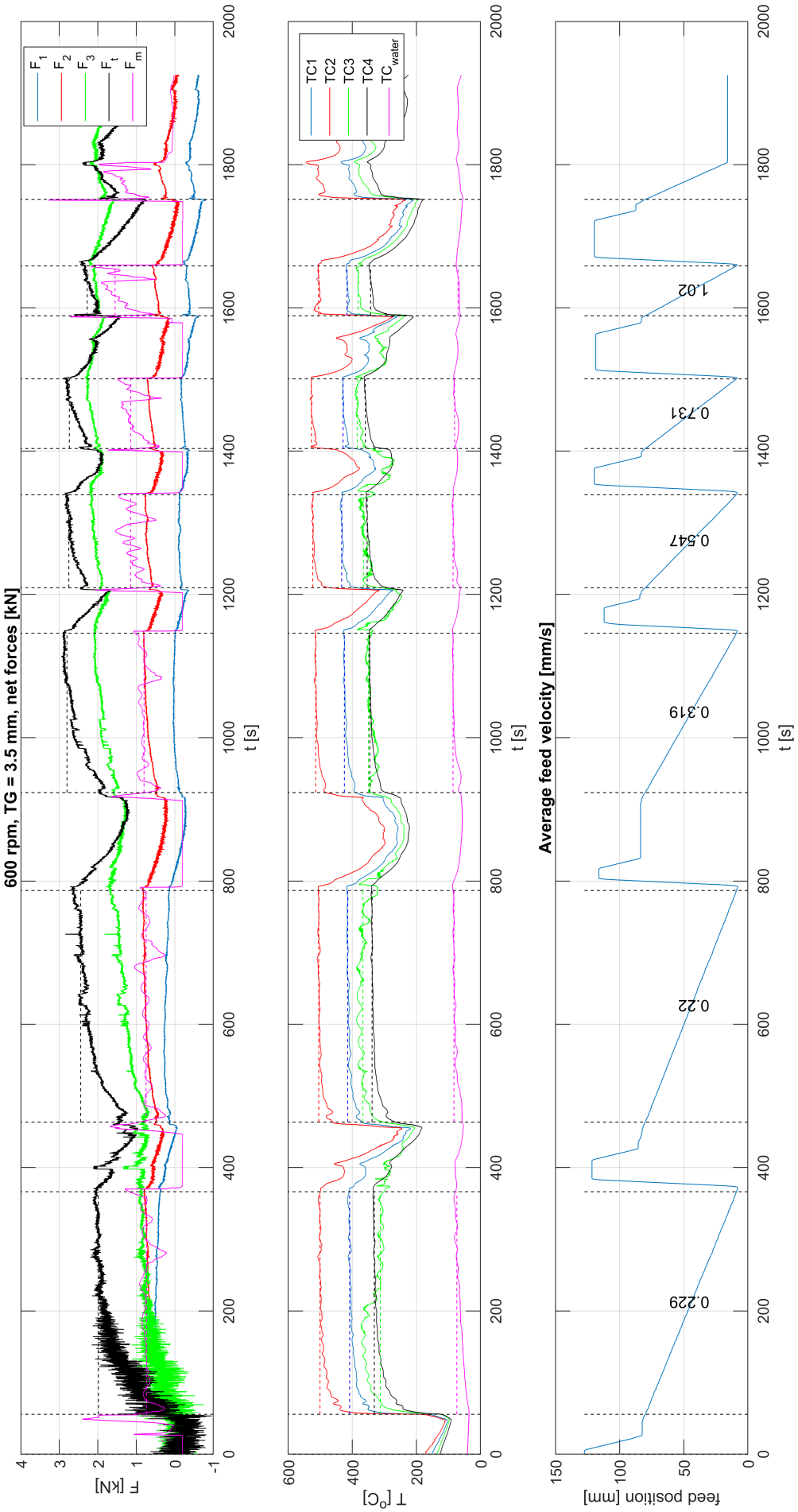

Figure 156: 2TG3.5_600_x_1: raw force, temperature and feed displacement data

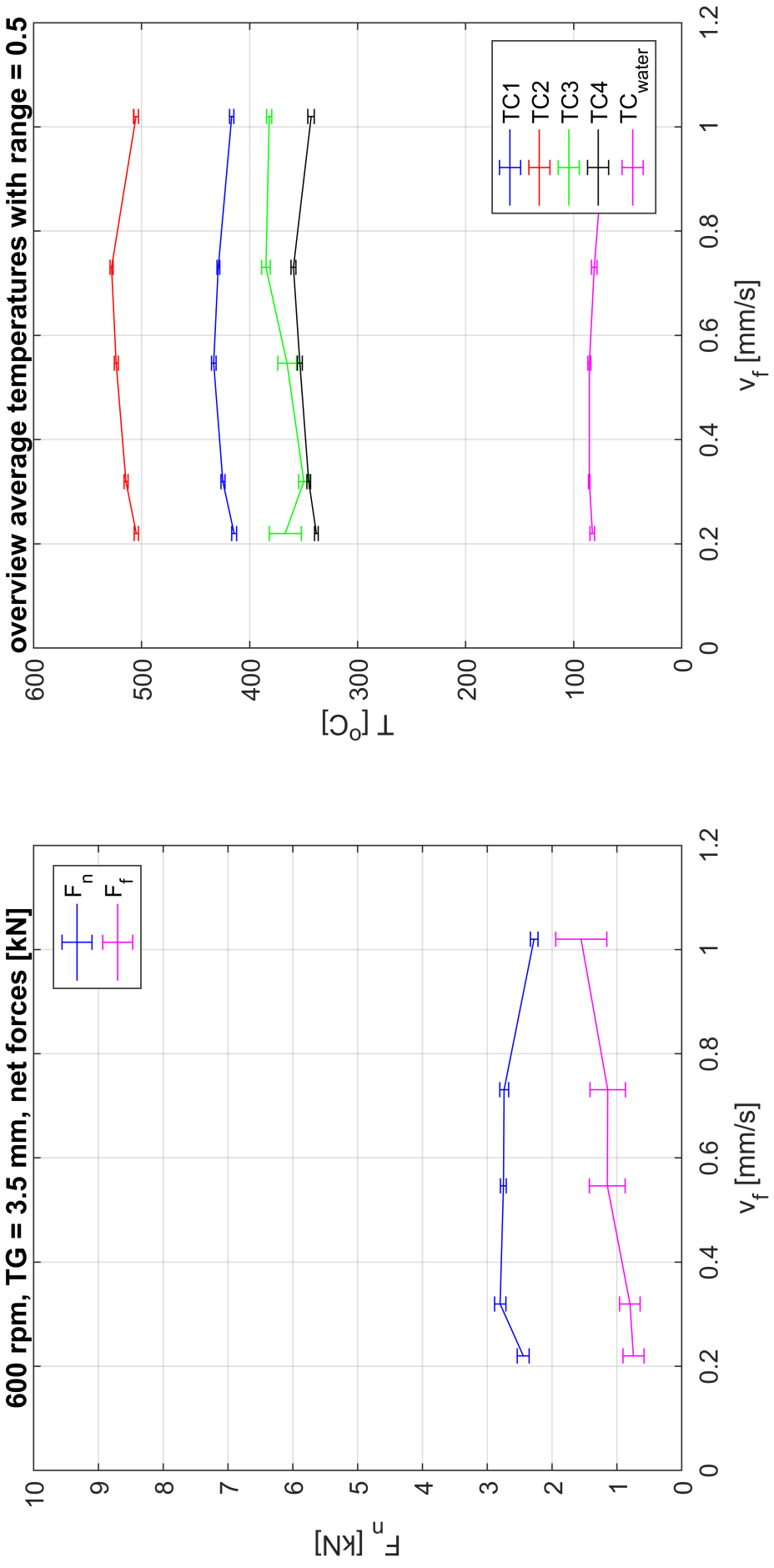

Figure 157: 2TG3.5_600_x_1: average forces and temperatures

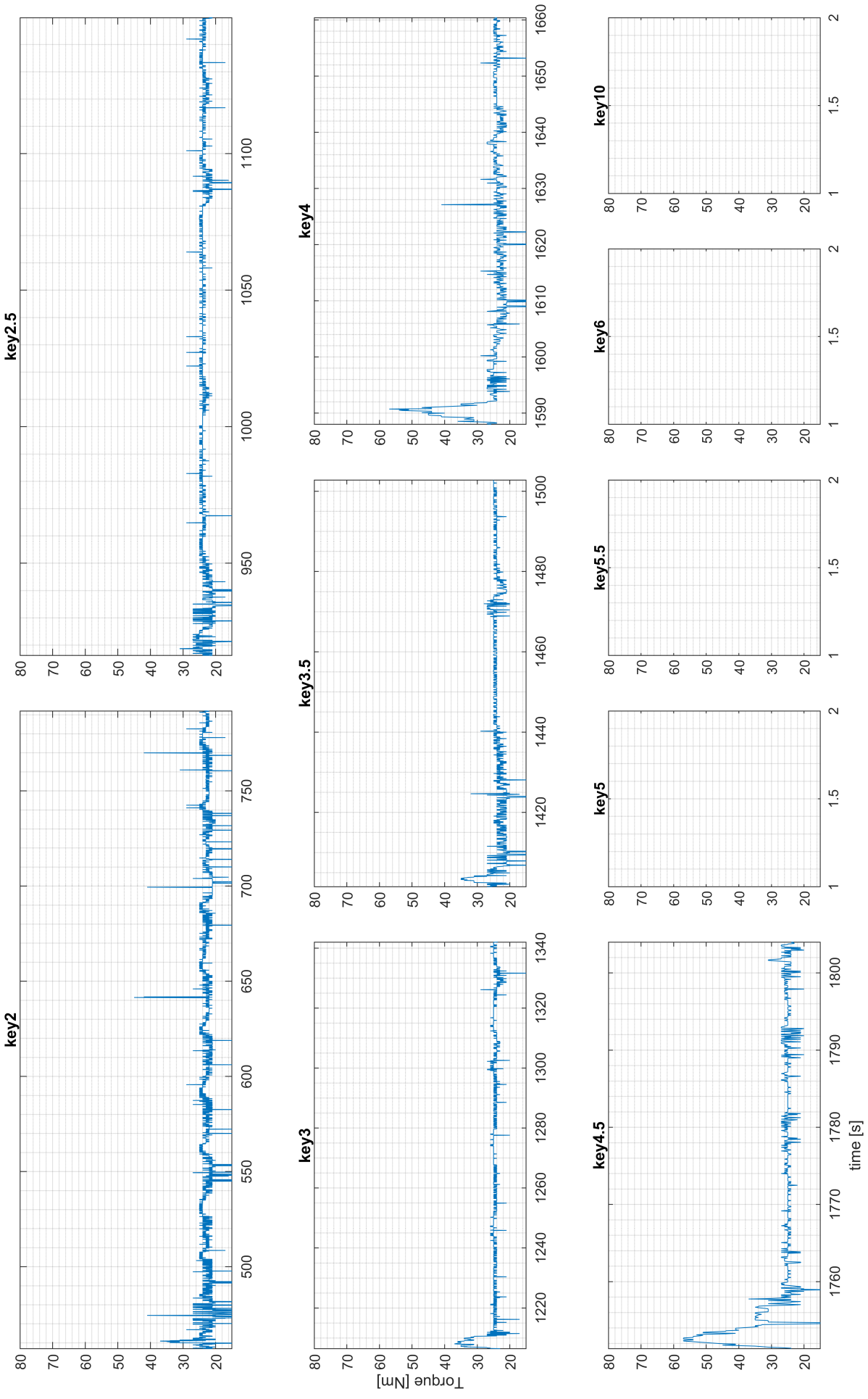

Figure 158: 2TG3.5_600_x_1: raw torque data cut per feed cylinder key velocity

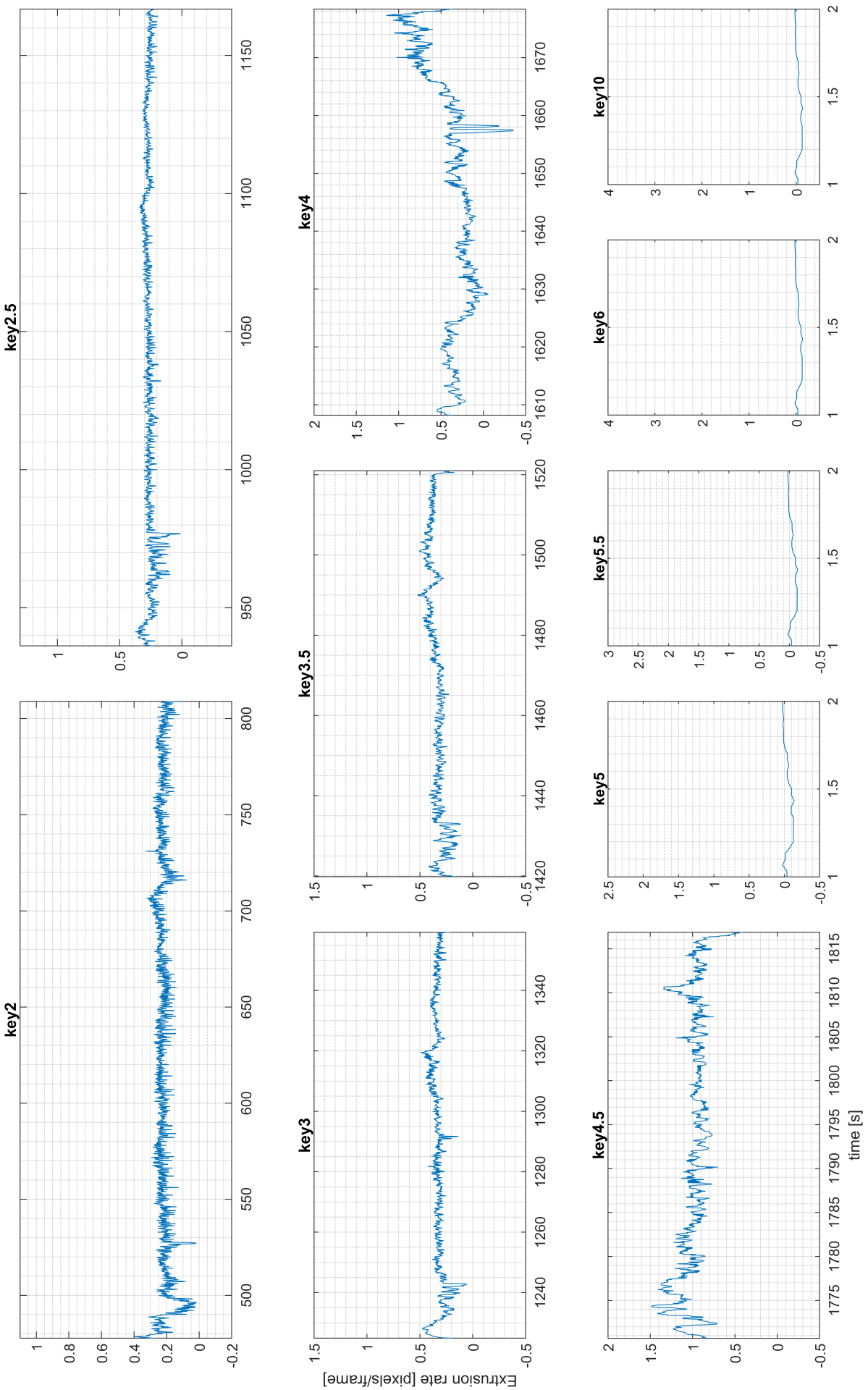

Figure 159: 2TG3.5_600_x_1: raw smoothed V_y data cut per feed cylinder key velocity

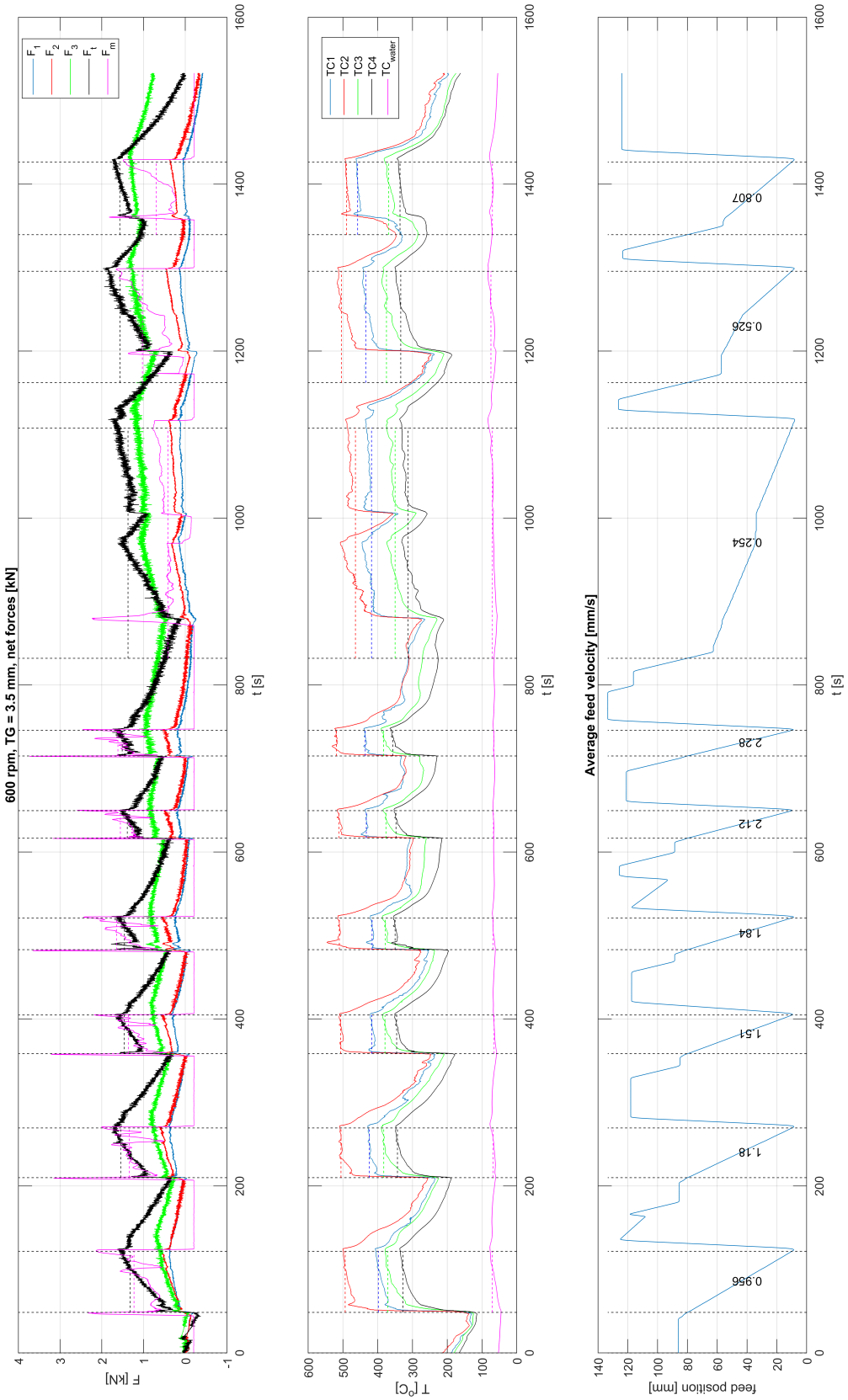

Figure 160: 2TG3.5_600_x_2: raw force, temperature and feed displacement data

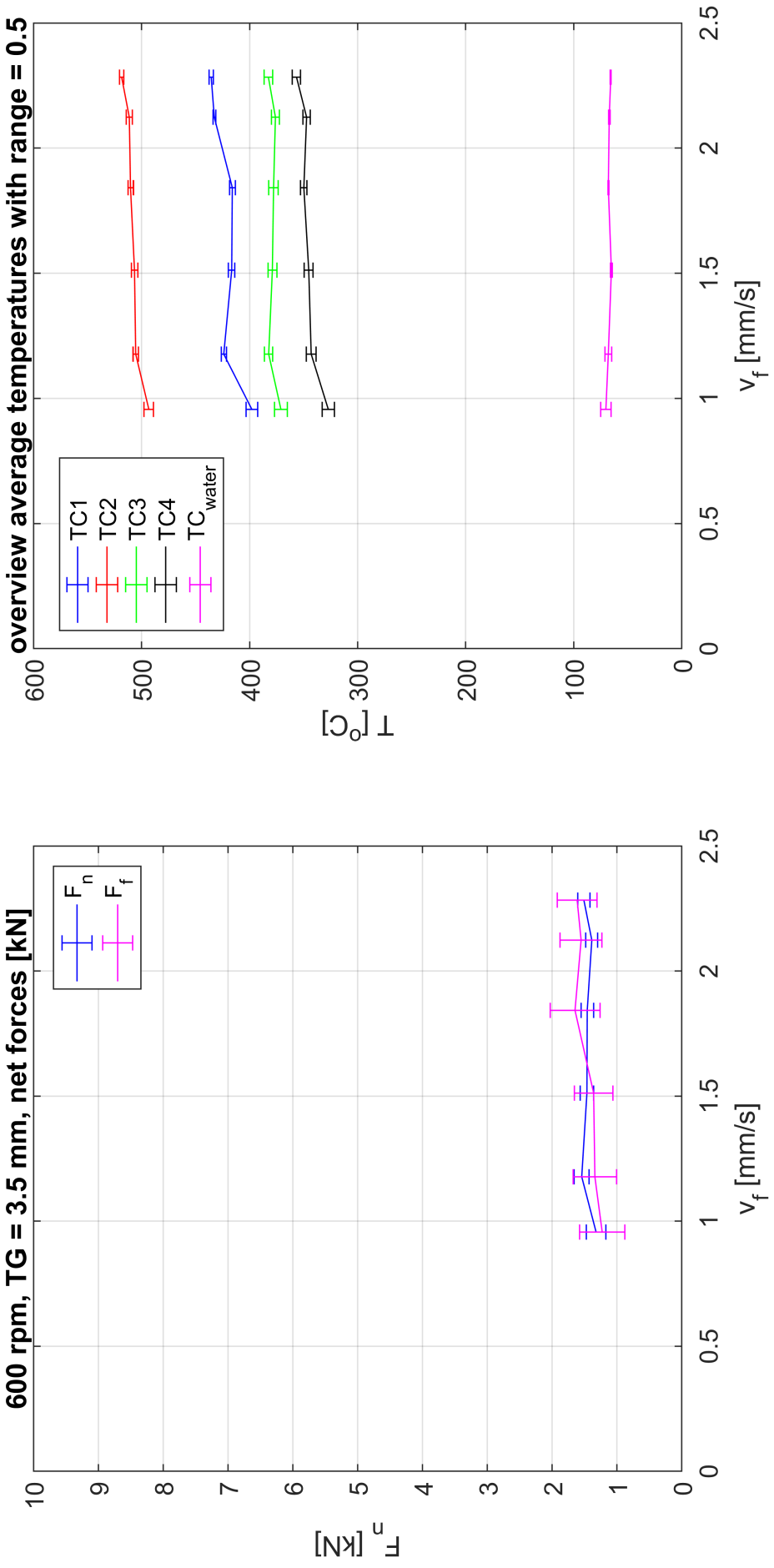

Figure 161: 2TG3.5_600_x_2: average forces and temperatures

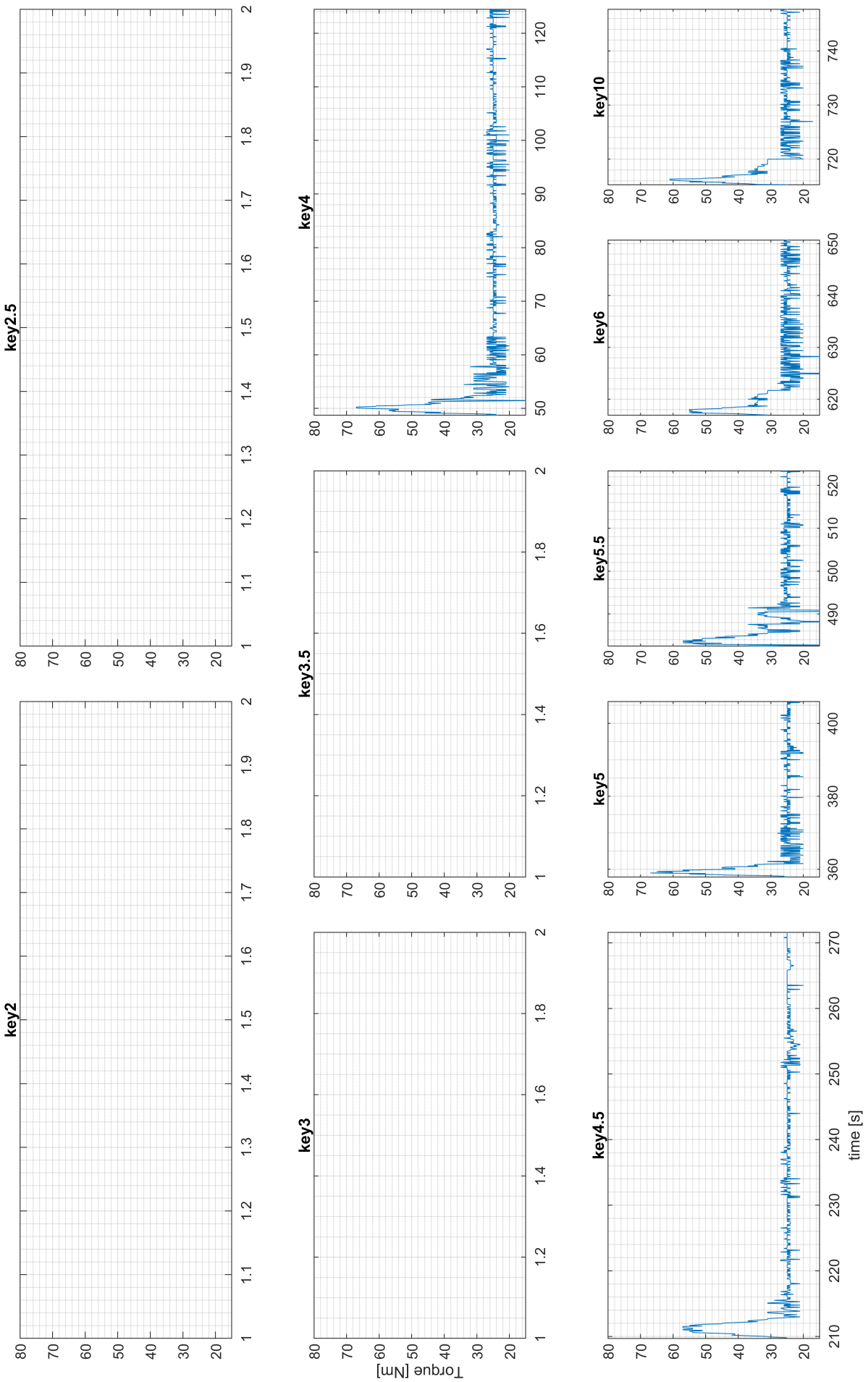

Figure 162: 2TG3.5_600_x_2: raw torque data cut per feed cylinder key velocity

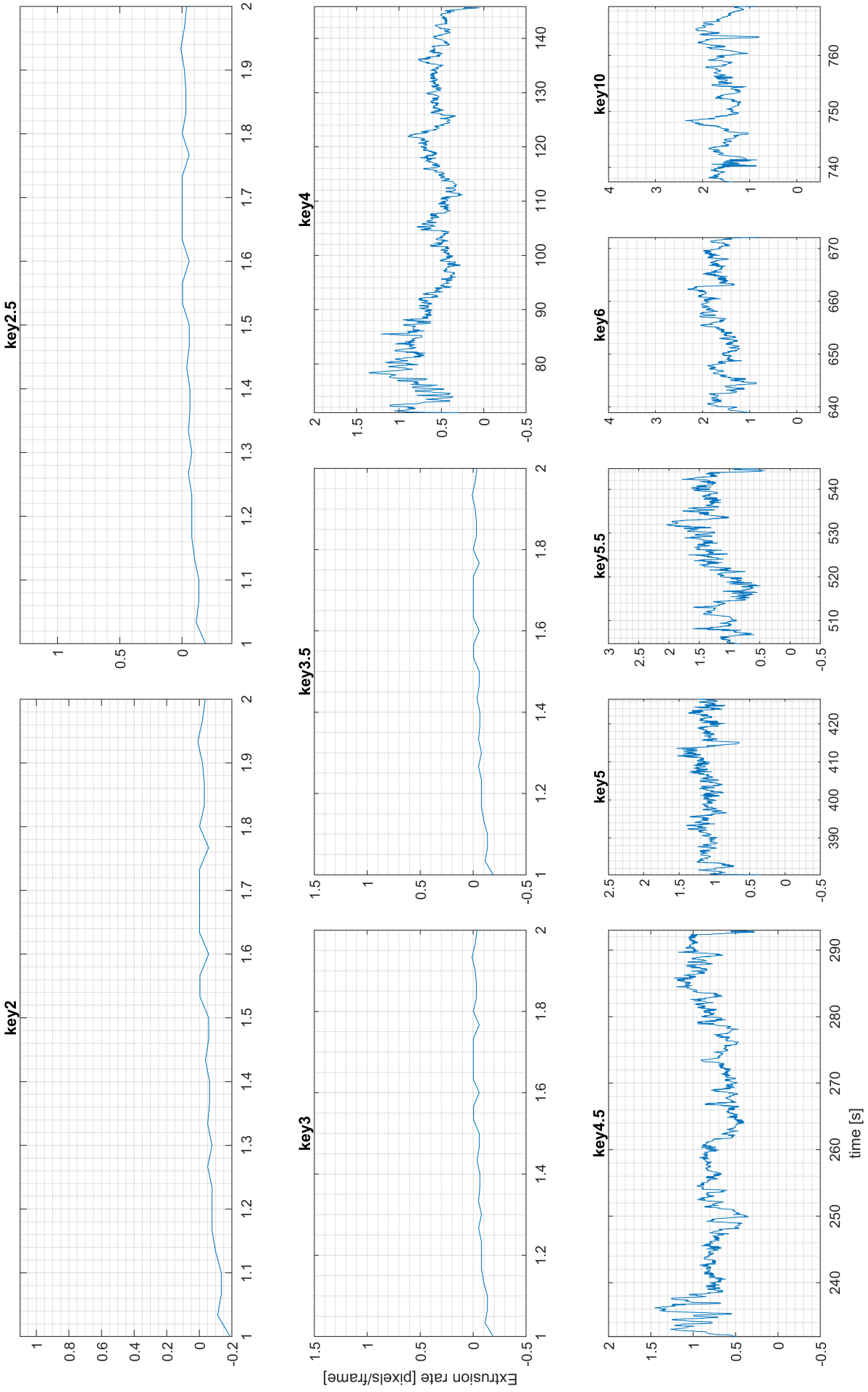

Figure 163: 2TG3.5_600_x_2: raw smoothed V_y data cut per feed cylinder key velocity

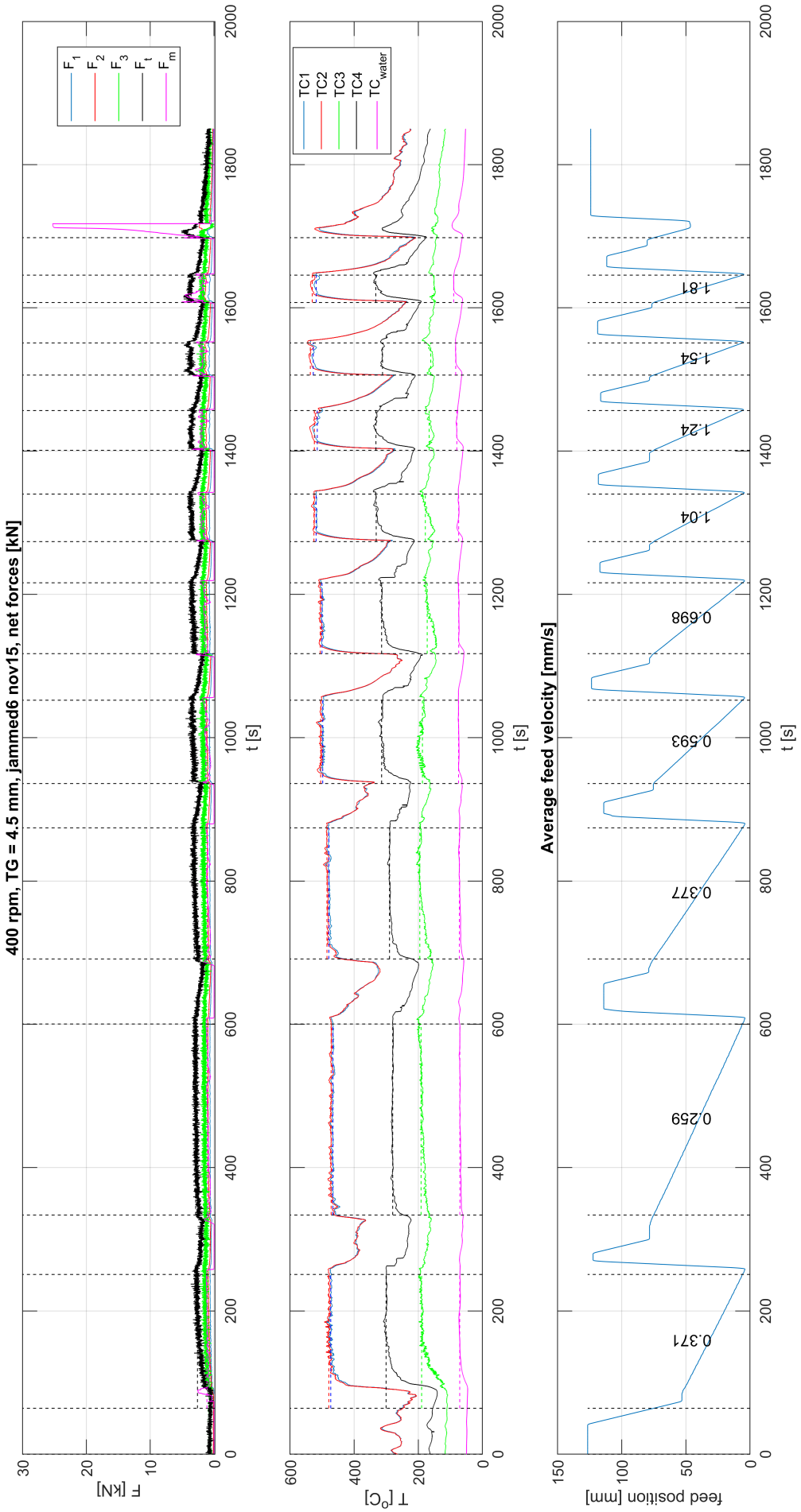

Figure 164: 2TG4.5_400_2_x: raw force, temperature and feed displacement data

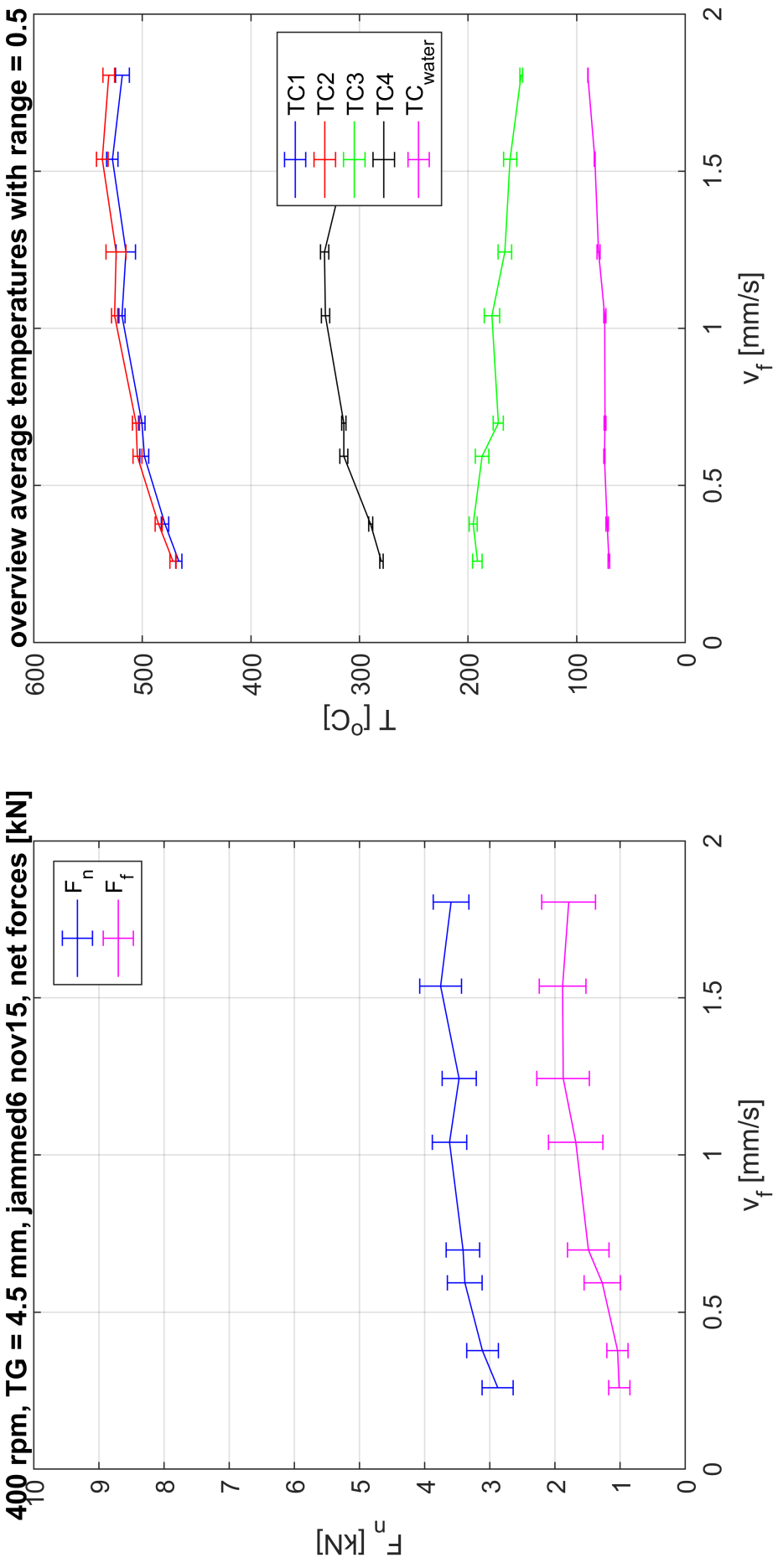

Figure 165: 2TG4.5_400_2_x: average forces and temperatures

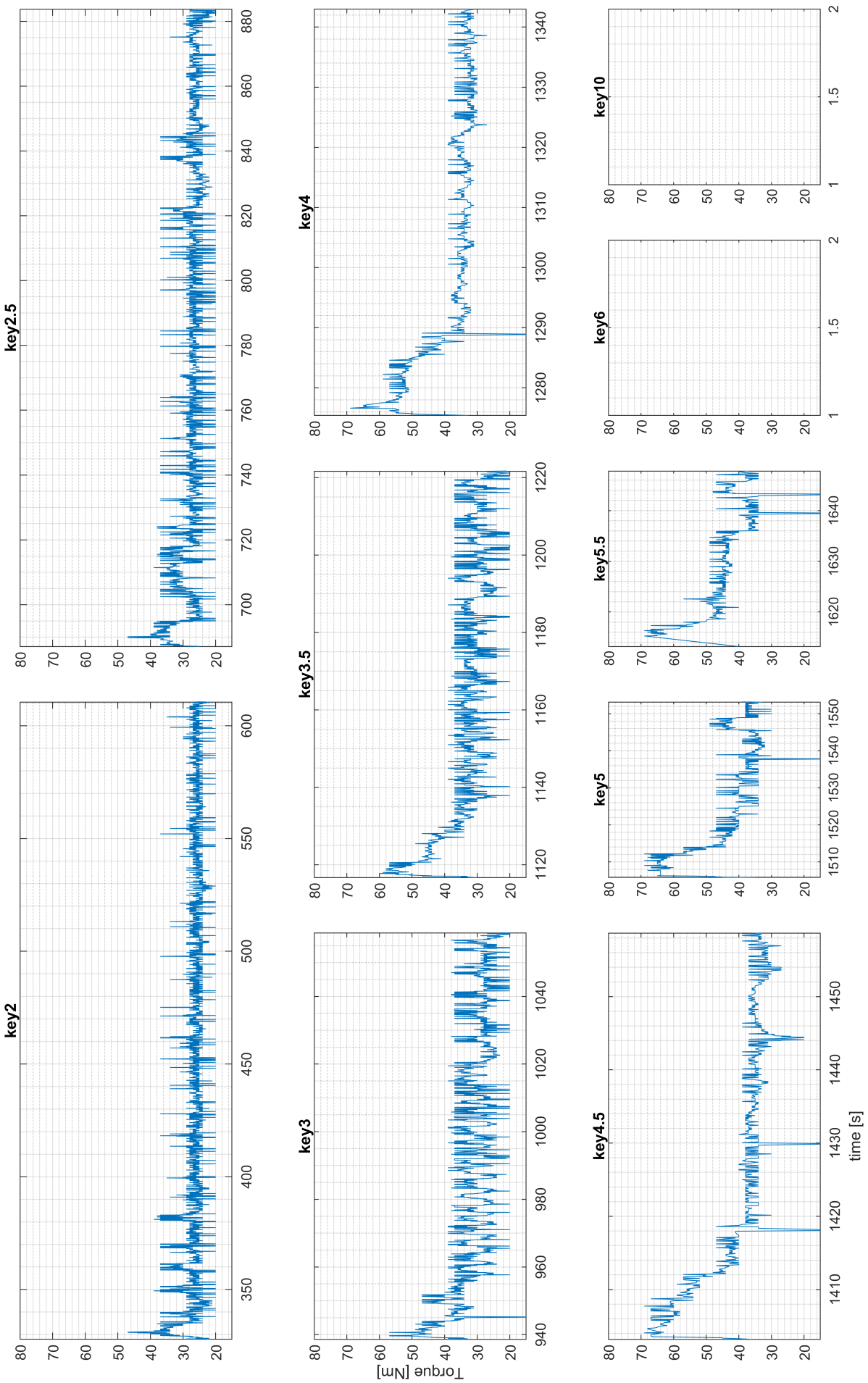

Figure 166: 2TG4.5_400_2_x: raw torque data cut per feed cylinder key velocity

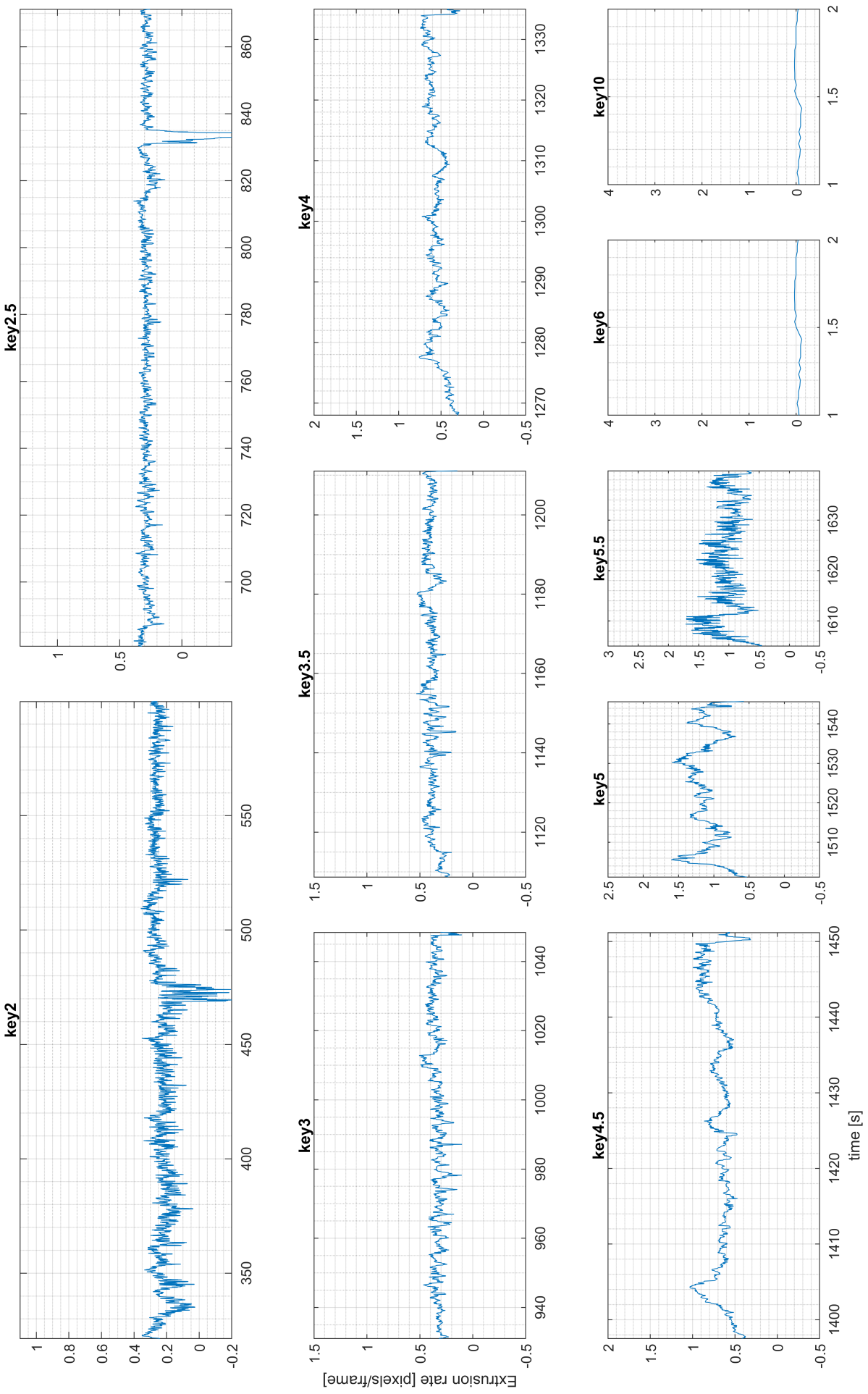

Figure 167: 2TG4.5_400_2_x: raw smoothed V_y data cut per feed cylinder key velocity

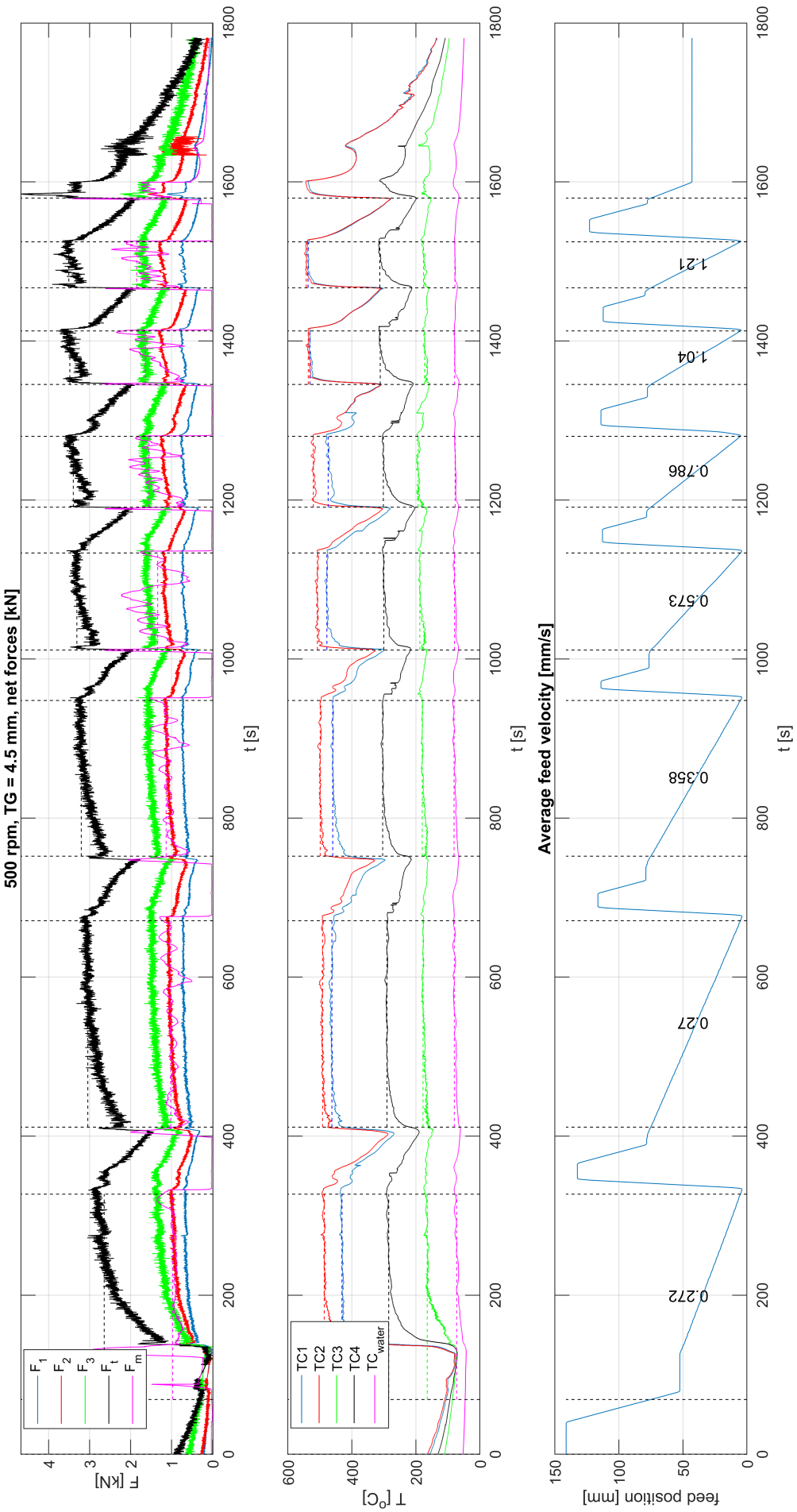

Figure 168: 2TG4.5_500_x_1: raw force, temperature and feed displacement data

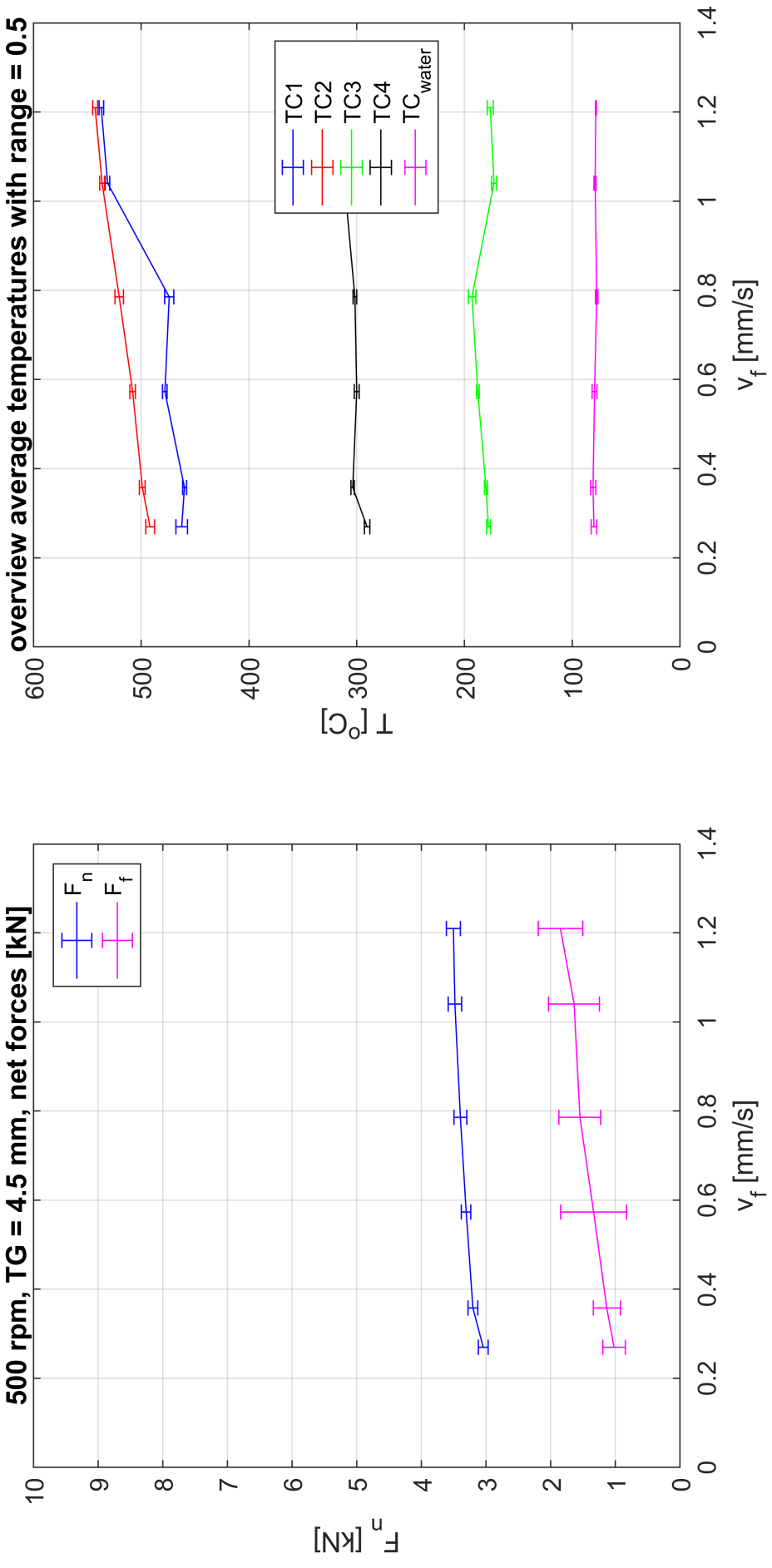

Figure 169: 2TG4.5_500_x_1: average forces and temperatures

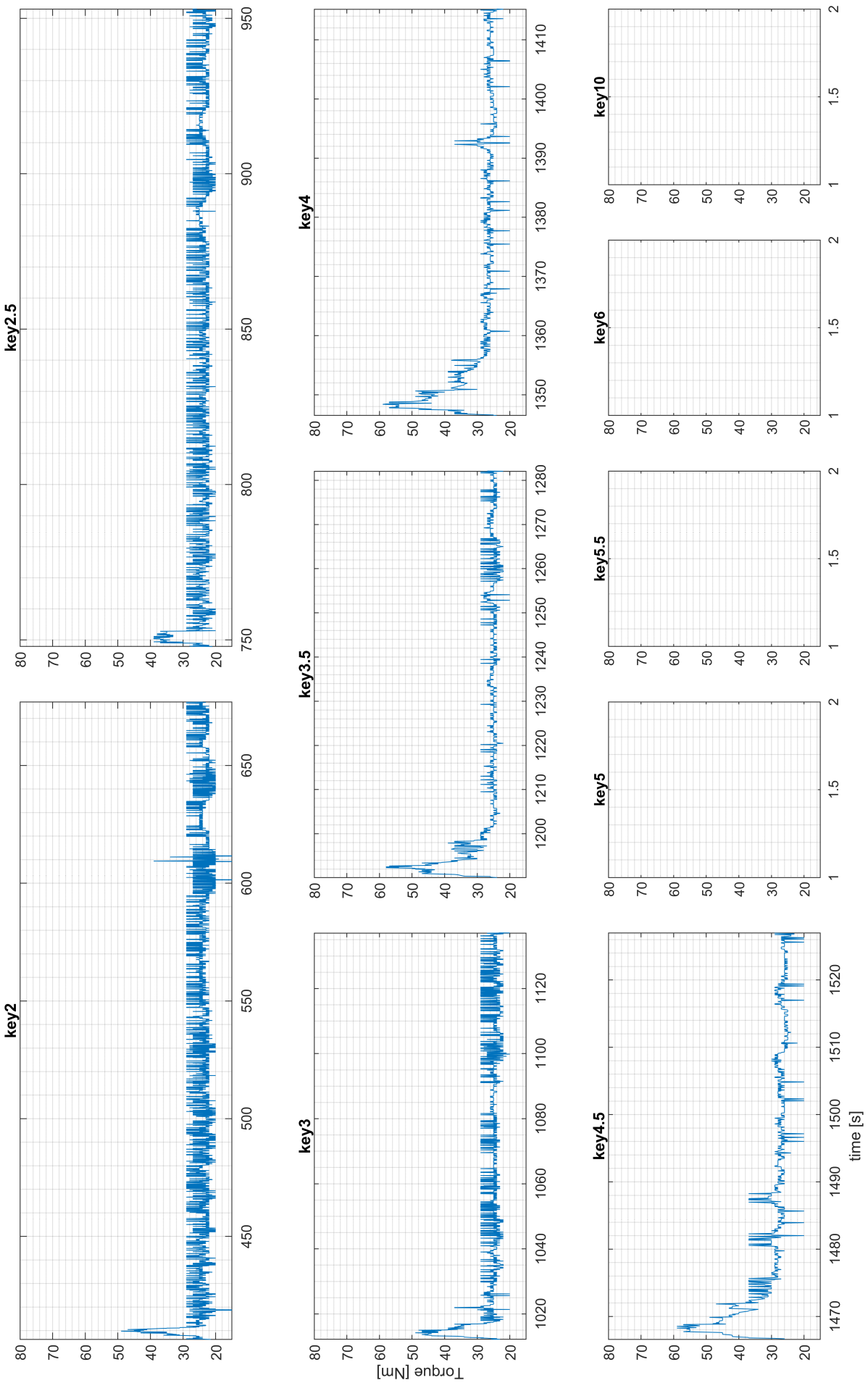

Figure 170: 2TG4.5_500_x_1: raw torque data cut per feed cylinder key velocity

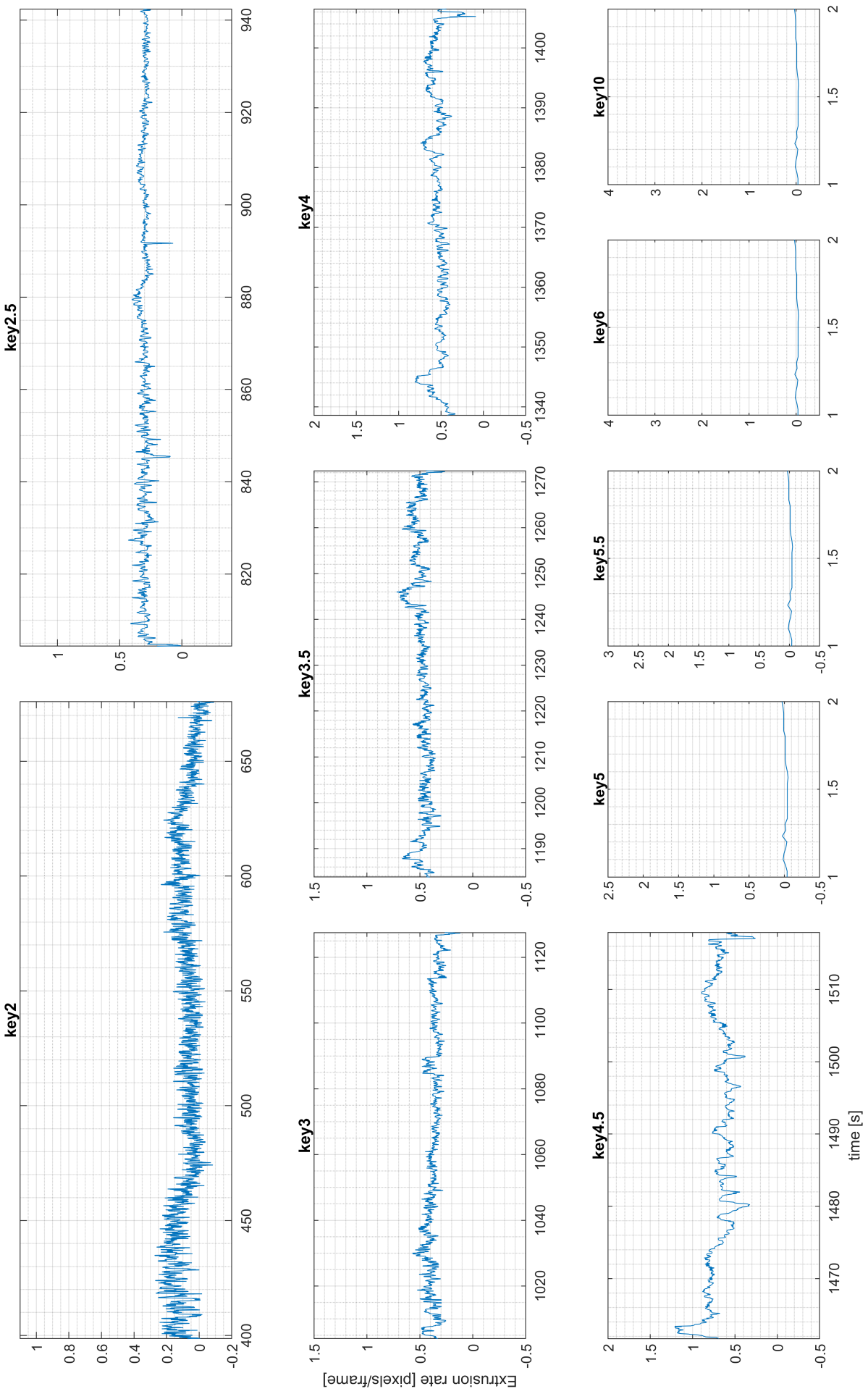

Figure 171: 2TG4.5_500_x_1: raw smoothed V_y data cut per feed cylinder key velocity

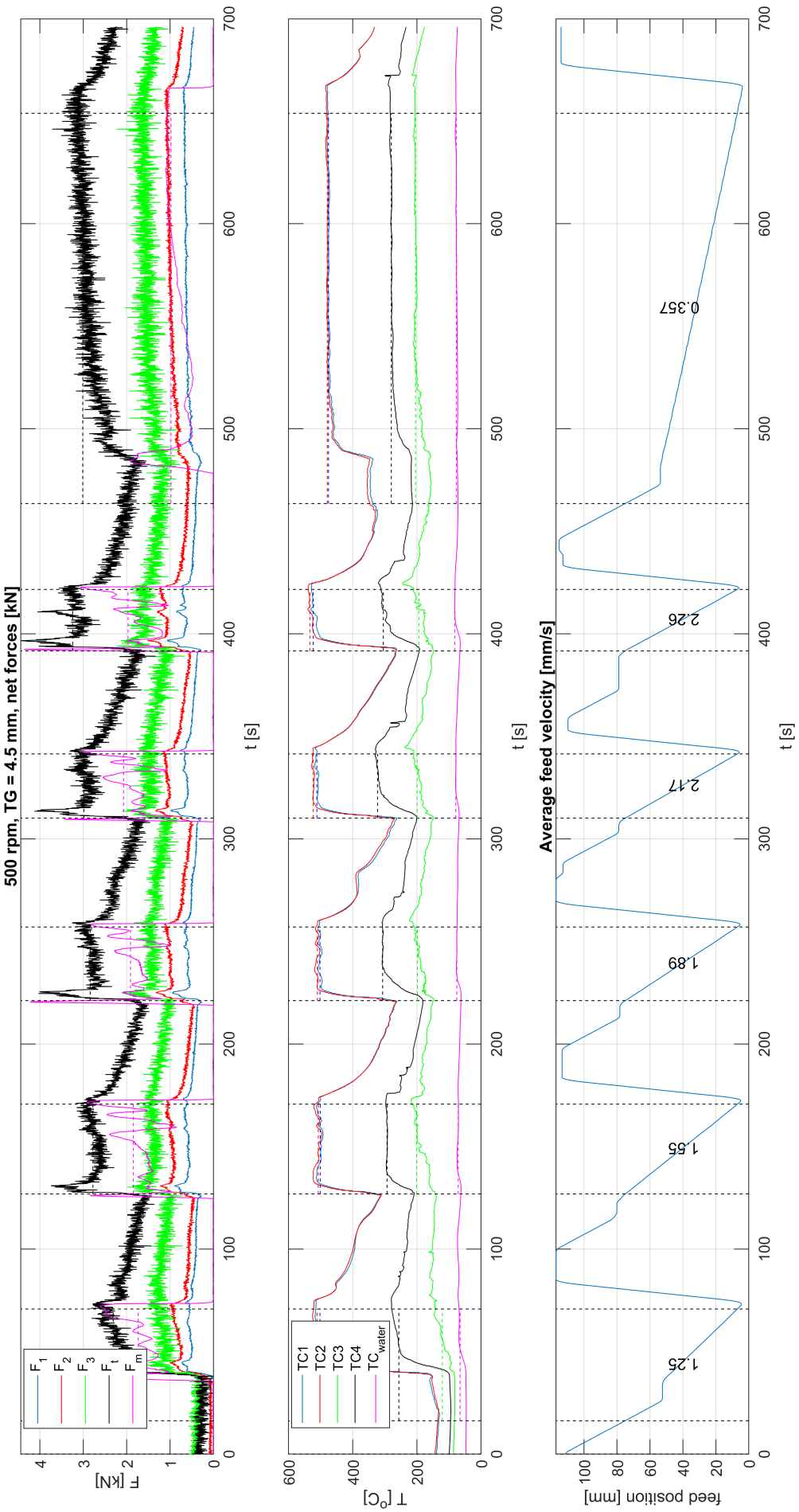

Figure 172: 2TG4.5_500_x_2: raw force, temperature and feed displacement data

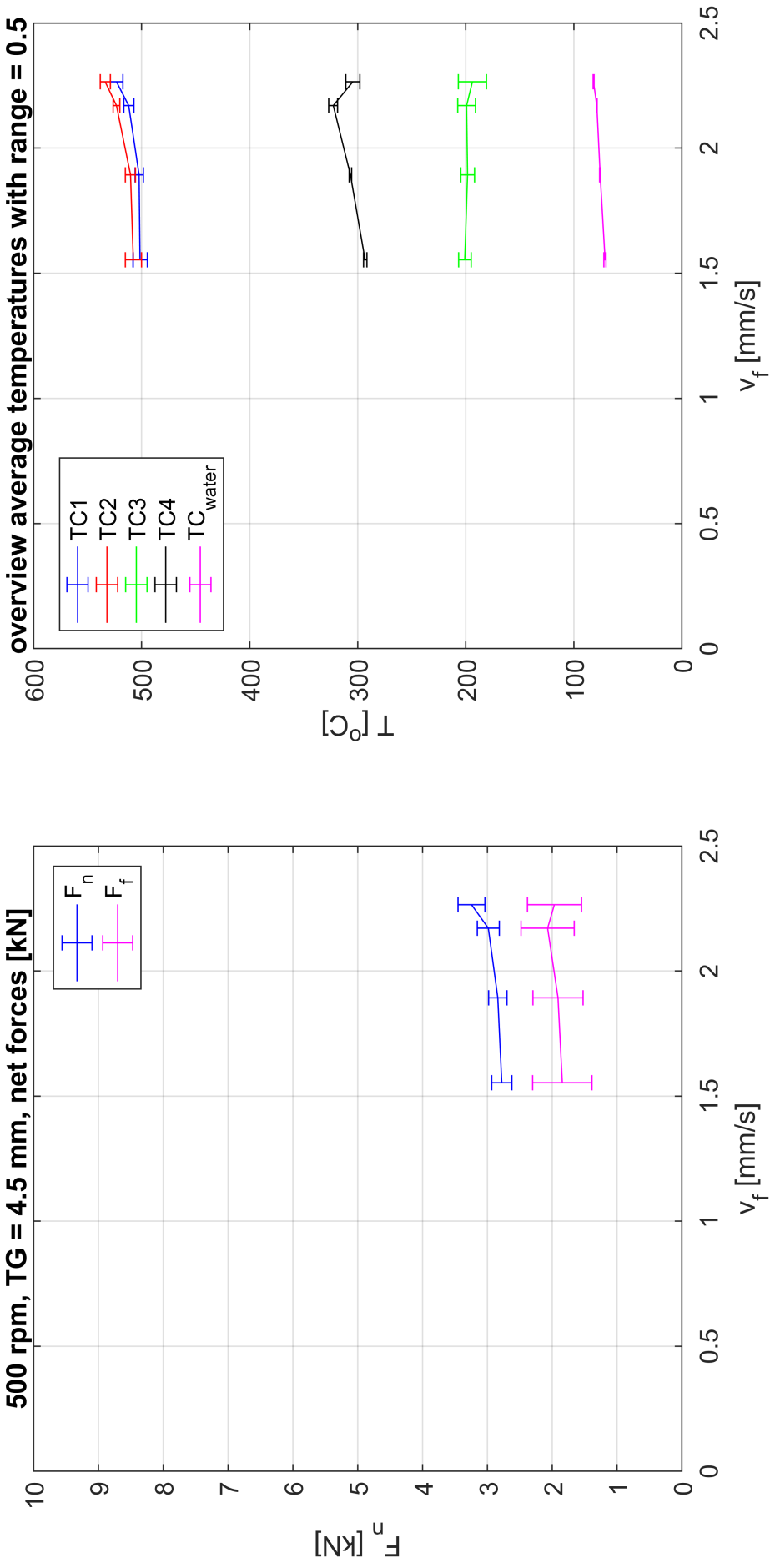

Figure 173: 2TG4.5_500_x_2: average forces and temperatures

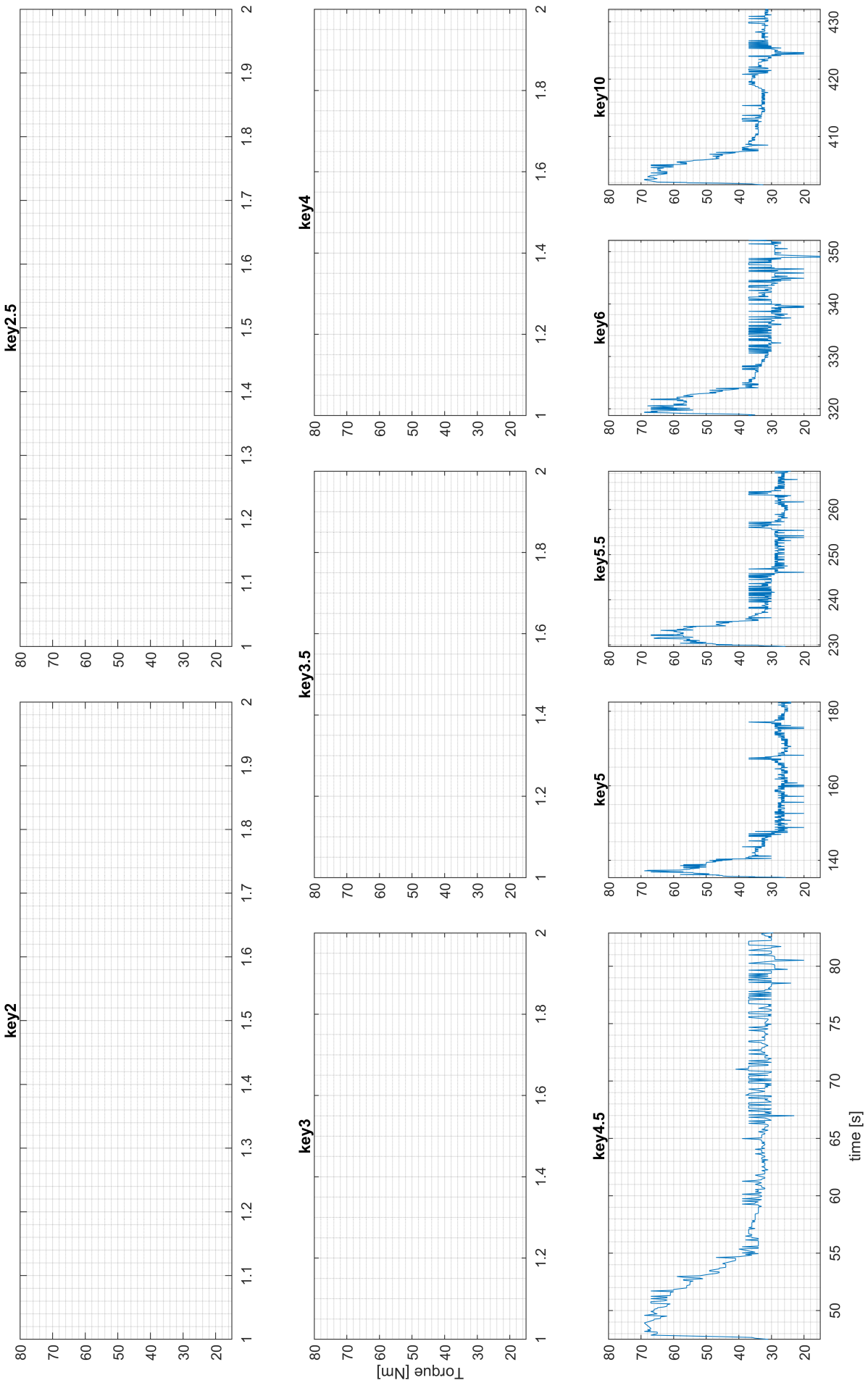

Figure 174: 2TG4.5_500_x_2: raw torque data cut per feed cylinder key velocity

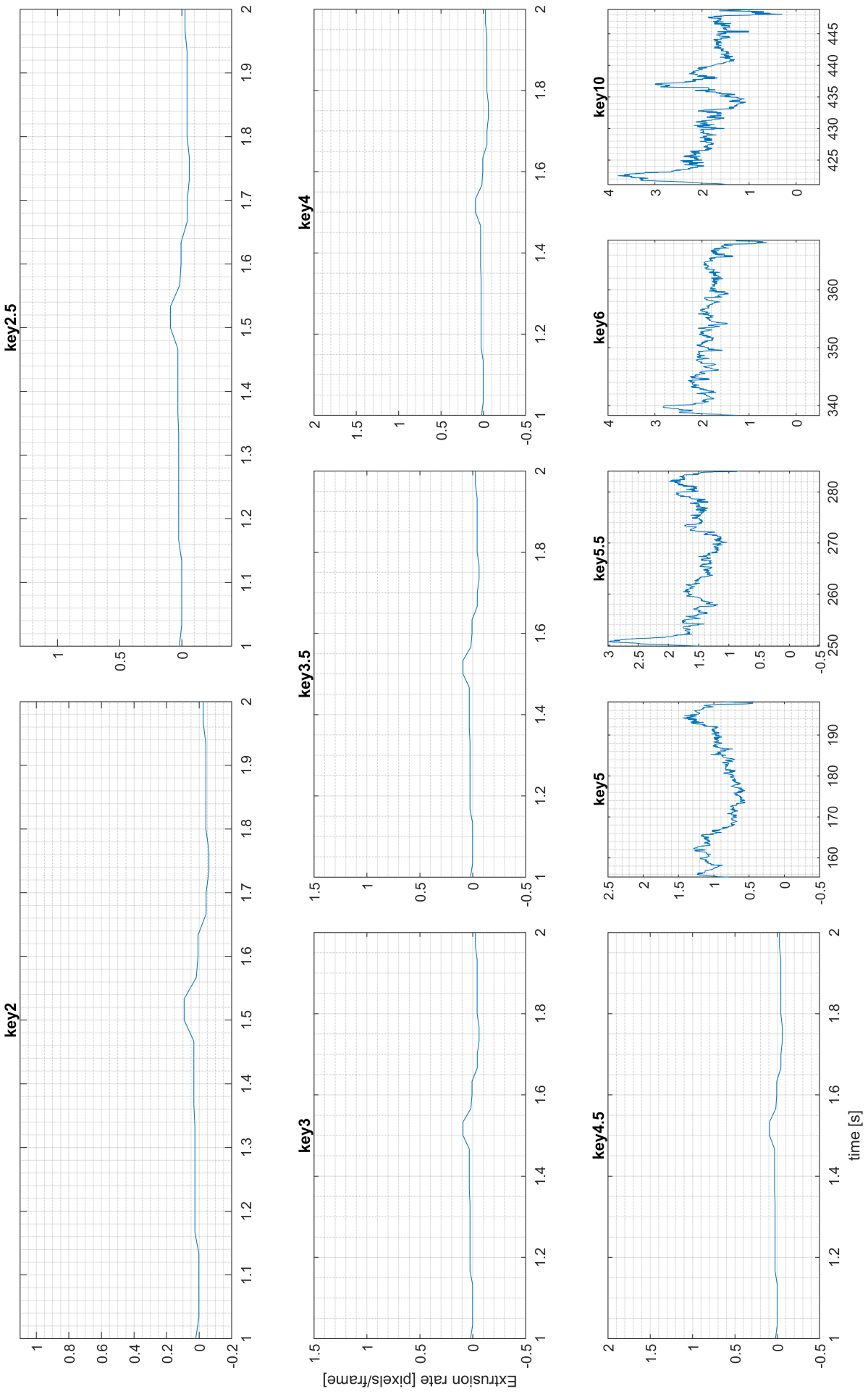

Figure 175: 2TG4.5_500_x_2: raw smoothed V_y data cut per feed cylinder key velocity

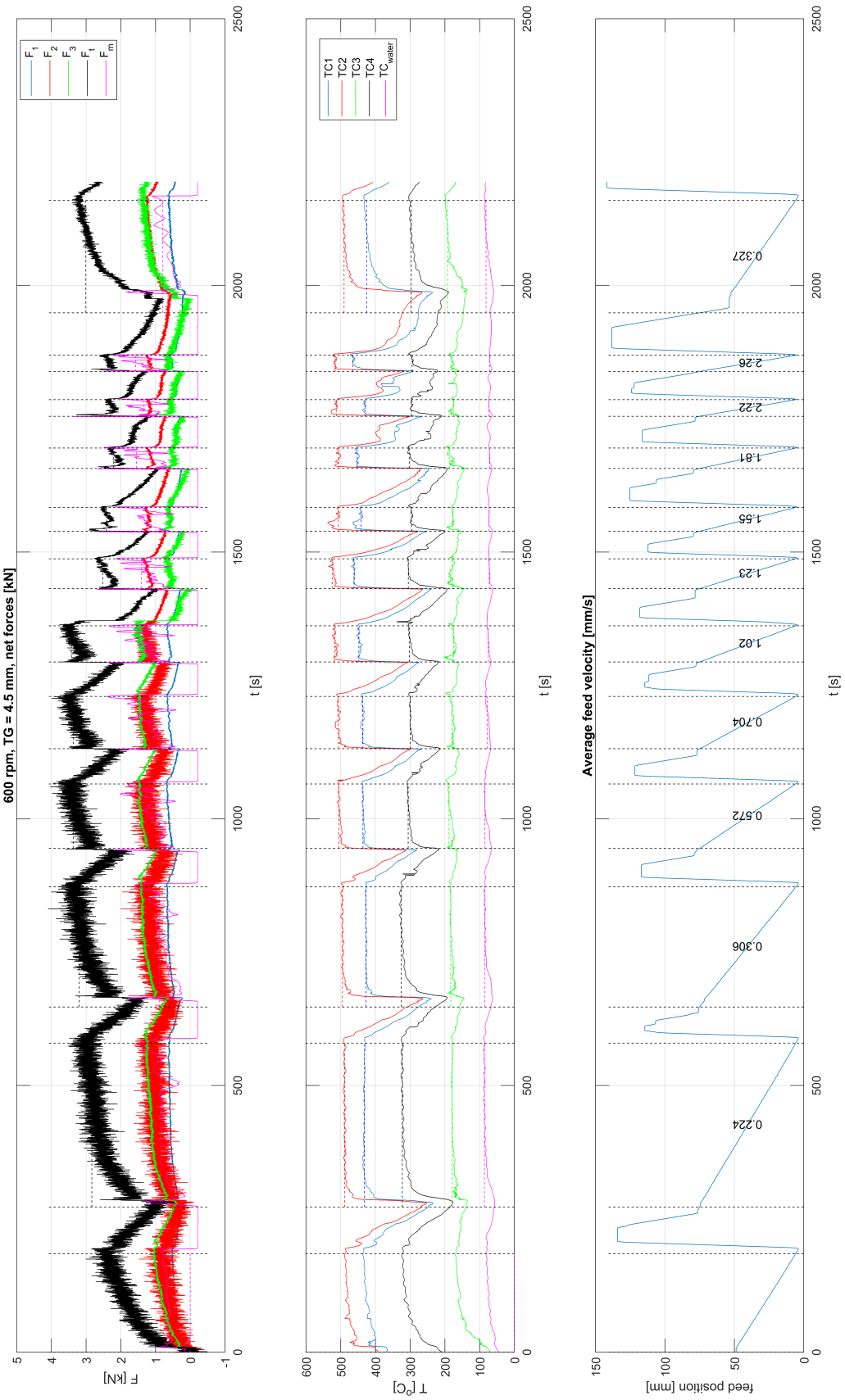

Figure 176: 2TG4.5_600_x: raw force, temperature and feed displacement data

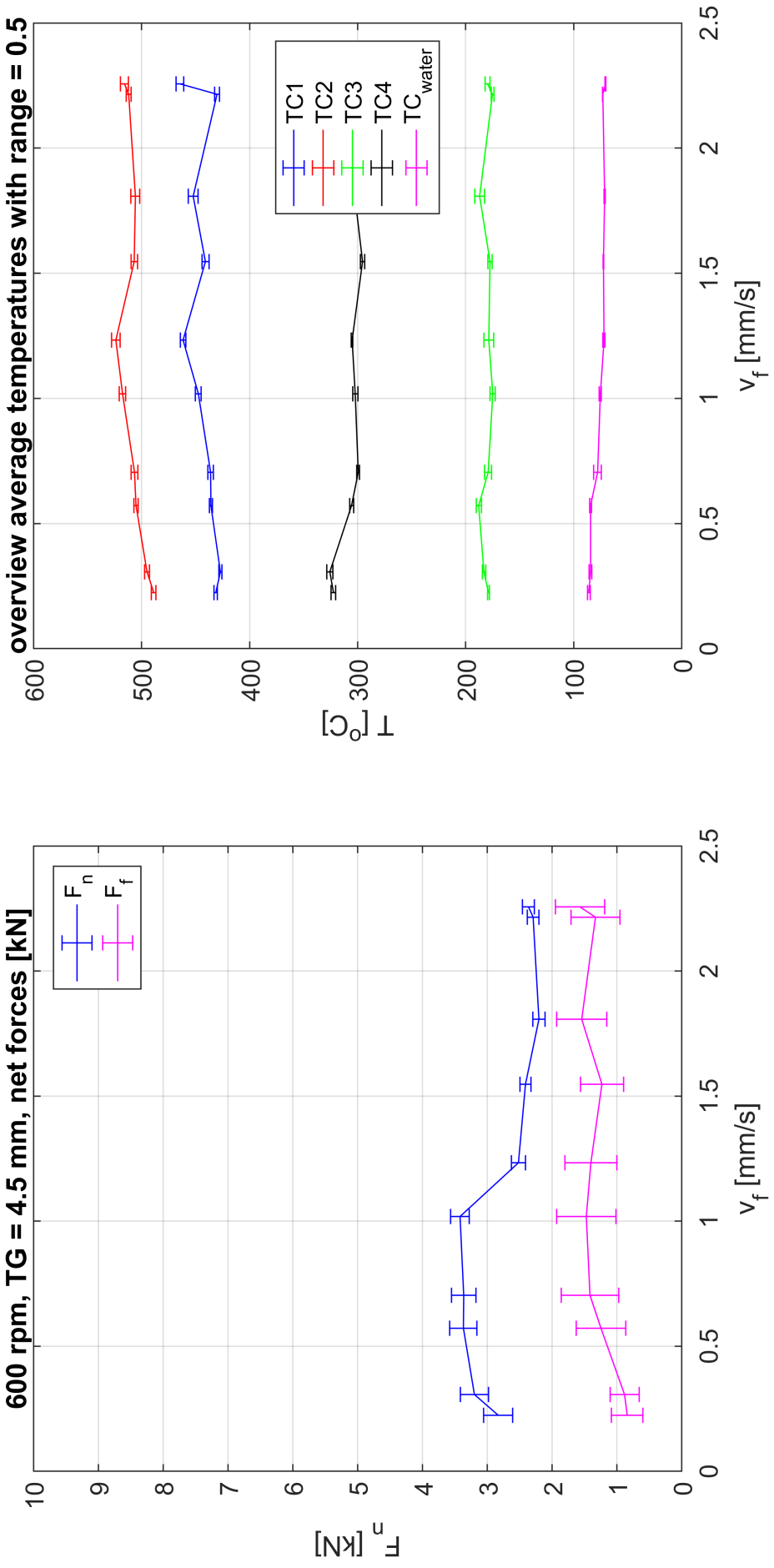

Figure 177: 2TG4.5_600_x: average forces and temperatures

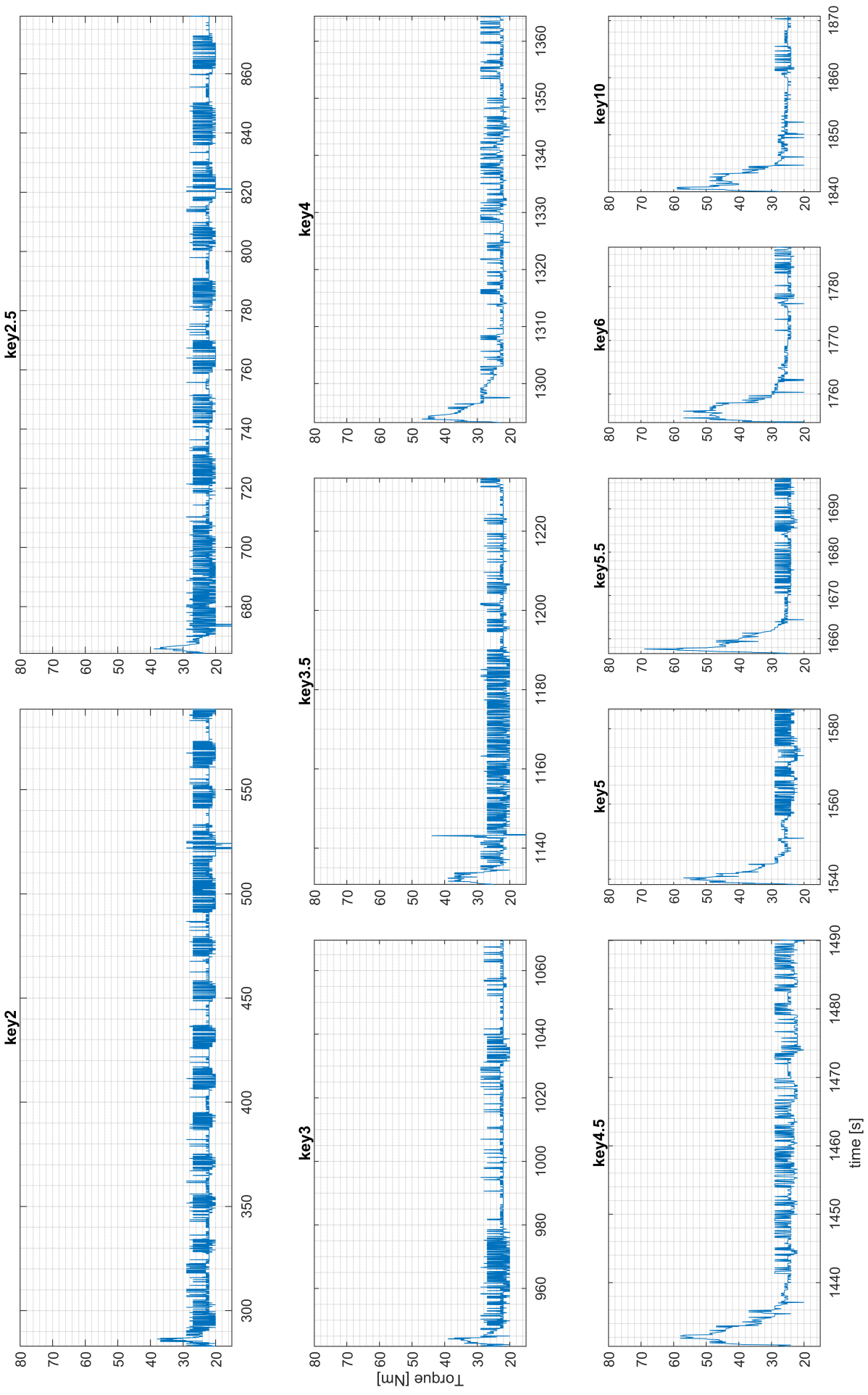

Figure 178: 2TG4.5_600_x: raw torque data cut per feed cylinder key velocity

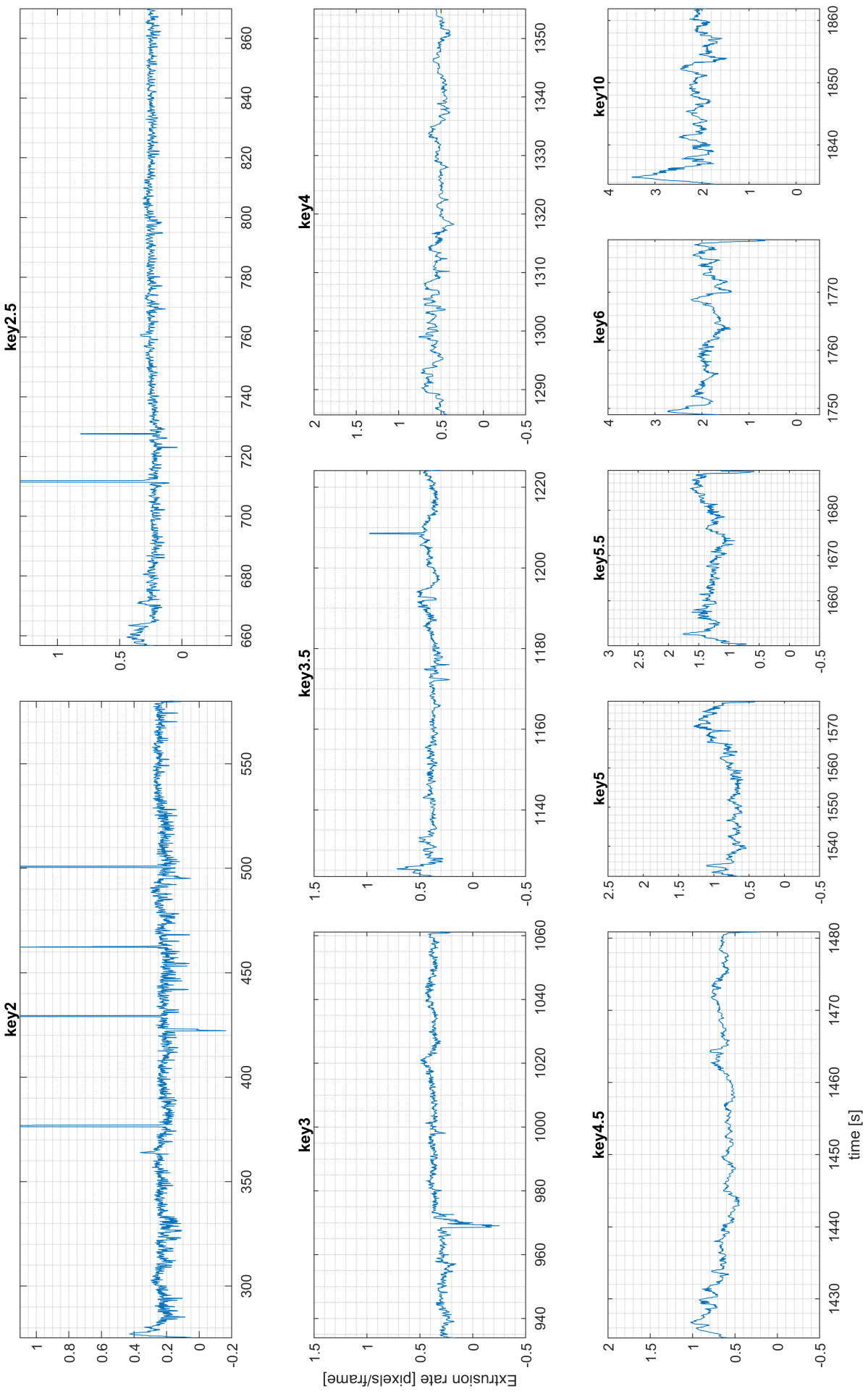

Figure 179: 2TG4.5_600_x: raw smoothed V_y data cut per feed cylinder key velocity

G Correlation & Severity Analysis graphs

Below, a complete overview of additional contour map graphs is presented for future reference. Graphs are included for r_{med}, n_{std} , n_{cv} and σ_{F2} for all available tool rotation rates.

The remaining of this page is left blank for improving figure layout on the next pages.

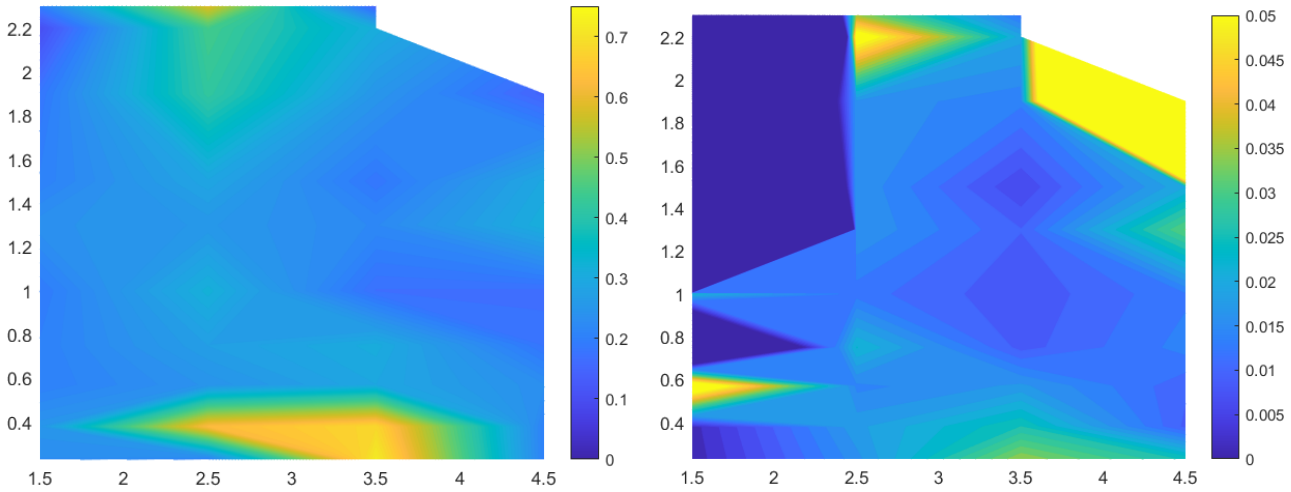

180.a. Correlation coefficient r_{med} **180.b.** Severity ratio n_{cv}

Figure 180: $\omega = 400$ $[rpm]$. x-axis: TG in $[mm]$. y-axis: v_f in $[mm/s]$

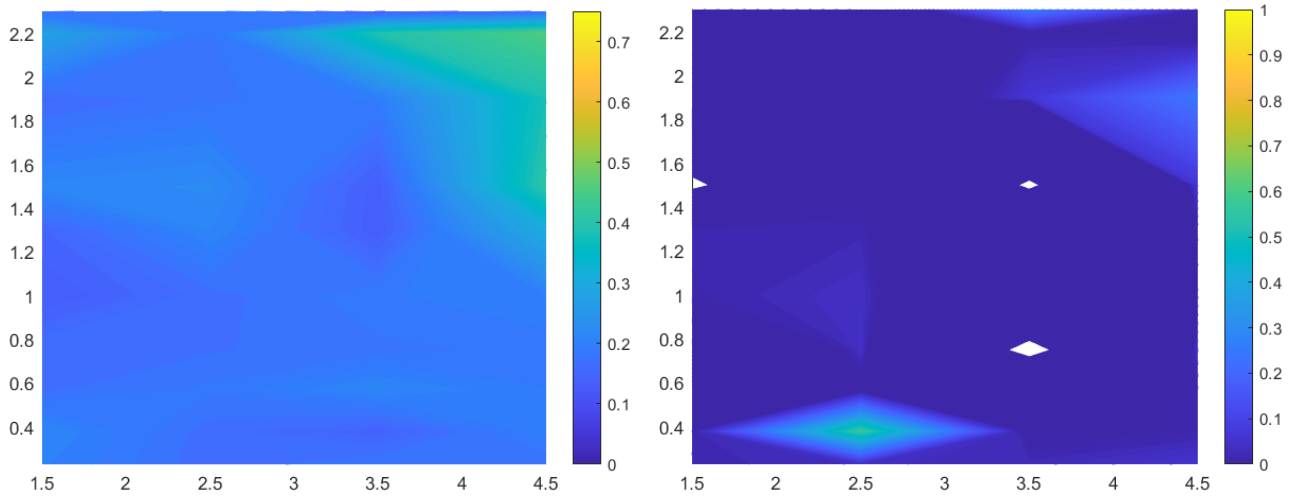

181.a. Correlation coefficient r_{med} **181.b.** Severity ratio n_{cv}

Figure 181: $\omega = 500$ $[rpm]$. x-axis: TG in $[mm]$. y-axis: v_f in $[mm/s]$

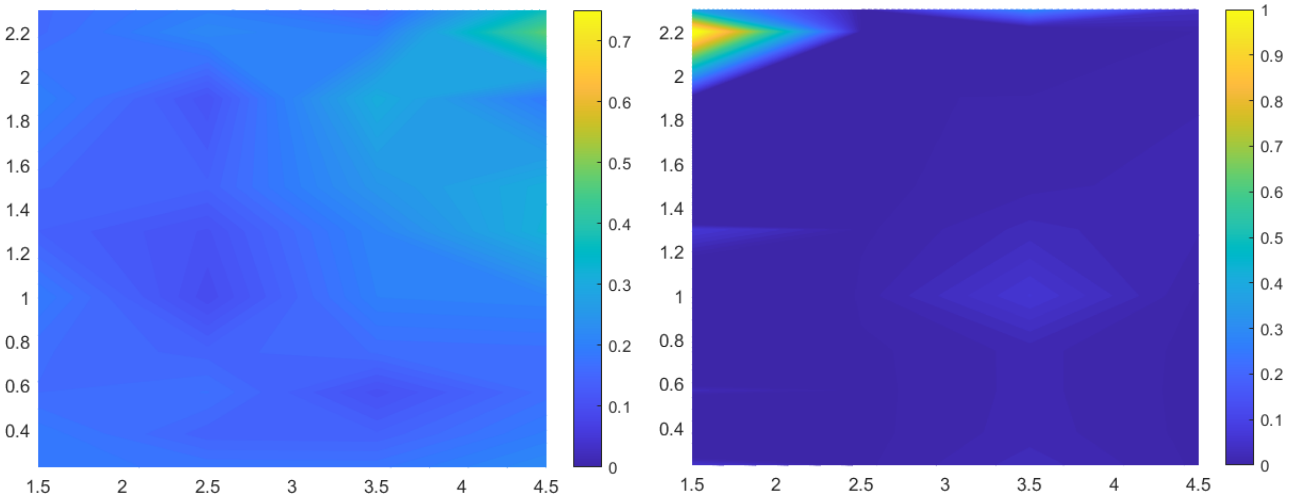

182.a. Correlation coefficient r_{med} **182.b.** Severity ratio n_{cv}

Figure 182: $\omega = 600$ $[rpm]$. x-axis: TG in $[mm]$. y-axis: v_f in $[mm/s]$

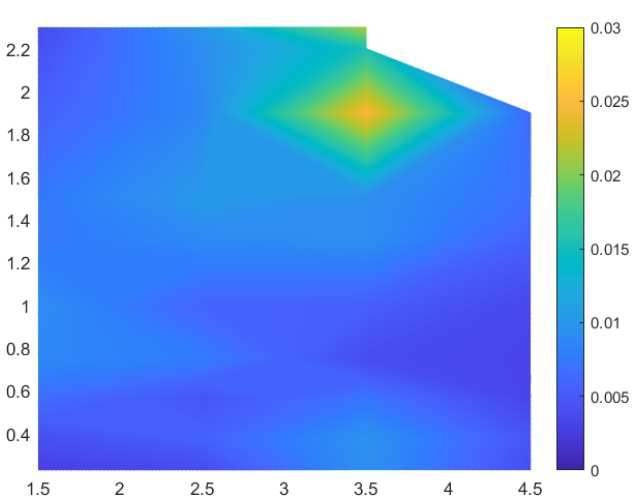

183.a. Amplification ratio n_{std}

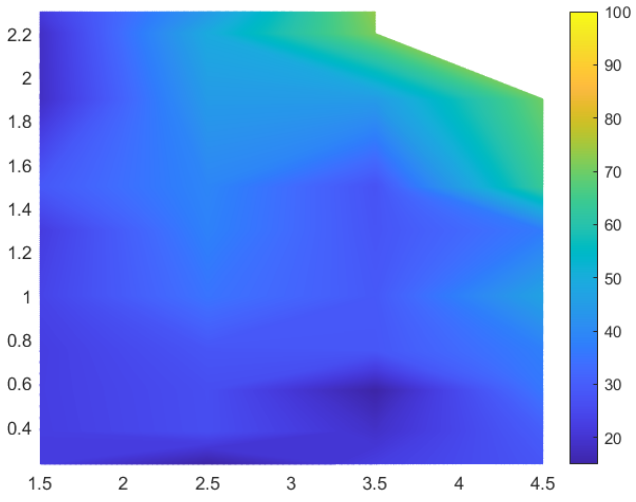

183.b. Standard deviation of F_2

Figure 183: $\omega = 400$ $[rpm]$. x-axis: TG in $[mm]$. y-axis: v_f in $[mm/s]$

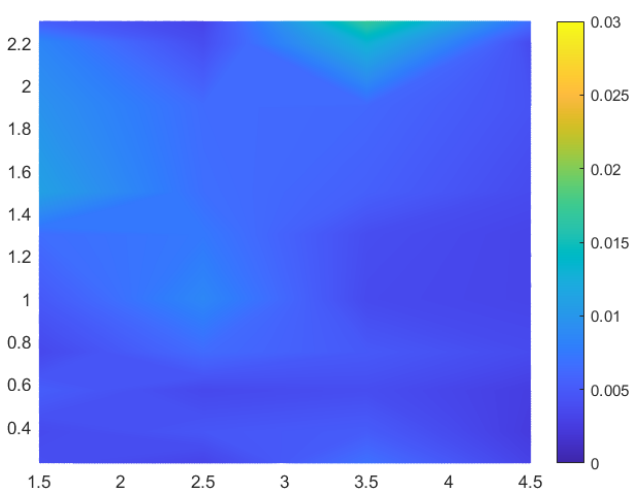

184.a. Amplification ratio n_{std}

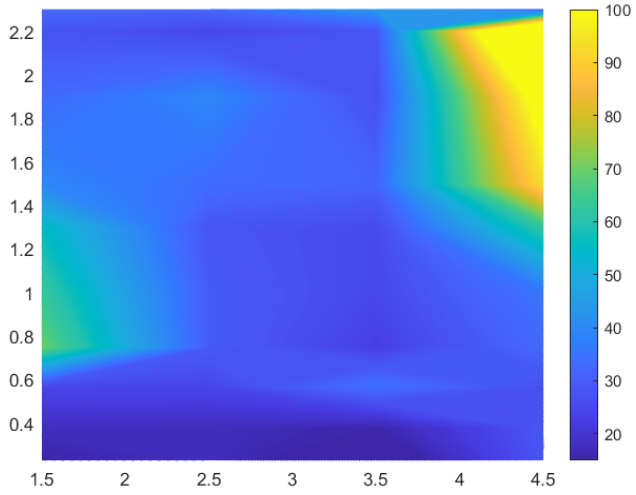

184.b. Standard deviation of F_2

Figure 184: $\omega = 500$ $[rpm]$. x-axis: TG in $[mm]$. y-axis: v_f in $[mm/s]$

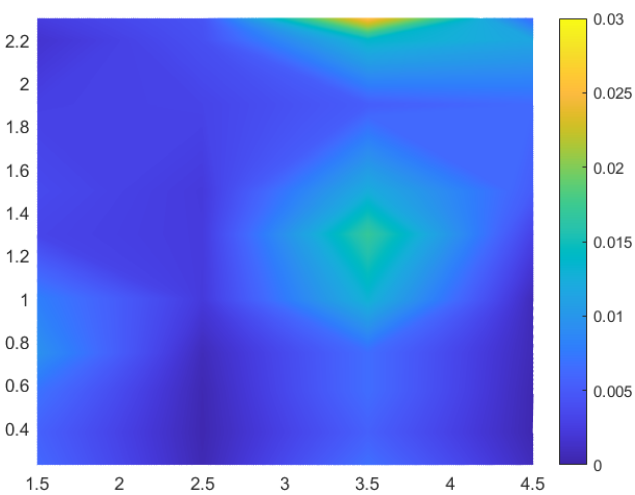

185.a. Amplification ratio n_{std}

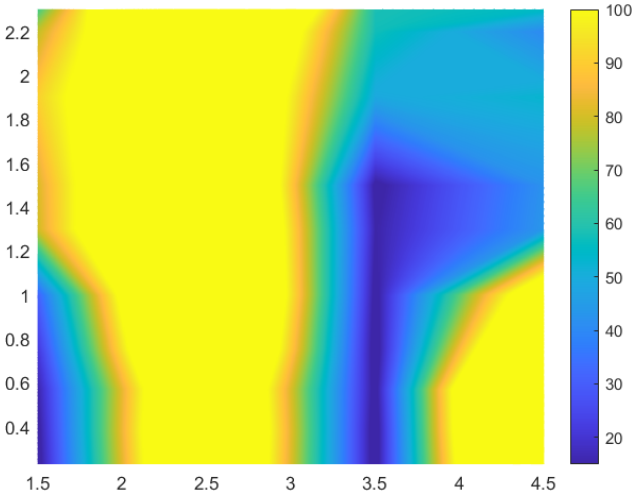

185.b. Standard deviation of F_2

Figure 185: $\omega = 600$ $[rpm]$. x-axis: TG in $[mm]$. y-axis: v_f in $[mm/s]$